

# S L C DESIGN HANDBOOK

STANFORD LINEAR ACCELERATOR CENTER  
STANFORD UNIVERSITY

Stanford, California 94305

December 1984

Prepared for DOE under Contract  
No. DE AC03-76SF 00515

# TABLE OF CONTENTS

PREFACE

CHAPTER 1. INTRODUCTION

CHAPTER 2. LINEAR ACCELERATOR

CHAPTER 3. THE COLLIDER ARC SYSTEM

CHAPTER 4. THE FINAL FOCUS SYSTEM

CHAPTER 5. ELECTRON AND POSITRON SOURCES

CHAPTER 6. DAMPING RING AND BUNCH COMPRESSOR

CHAPTER 7. INSTRUMENTATION AND CONTROL

CHAPTER 8. ALIGNMENT DESIGN

CHAPTER 9. LUMINOSITY AND BACKGROUNDS

CHAPTER 10. EXPERIMENTAL USE

CHAPTER 11. CONVENTIONAL FACILITIES

CHAPTER 12.

CHAPTER 13.

CHAPTER 14. SUMMARY OF PARAMETERS

CHAPTER 15. PUBLICATIONS

## PREFACE

The SLC Design Handbook is intended to be a consistent description of the SLAC Linear Collider project, including explanations of the design criteria and listing the key technical specifications. The precedent set by the PEP Design Handbook during the construction and commissioning of that machine a few years ago leads us to hope that this handbook will have a similar impact on the SLC by serving as a concise and up-to-date reference guide for the design and construction.

Many details of the SLC design are not yet firm and can be expected to evolve as the construction proceeds. Thus, we have chosen a 3-ring loose-leaf format and a page numbering scheme to accommodate the addition or replacement of sections as needed. In order to minimize the confusion that could result from the distribution of multiple versions of some sections, each page is marked with a revision data in the upper right corner.

The task of keeping a large number of widely dispersed copies up to date would be prohibitively difficult. Consequently, we are forced to limit the distribution to a few libraries and group offices and to individuals with a bonafide use for it. We will attempt to maintain a list of all recipients and to provide them with updated sections as they become available. To avoid further delays and to get this book into the hands of those who might find it useful, we have decided to proceed with the first printing and distribution before all sections have been written. Readers may be puzzled by Chapters 12 and 13. Based on our experience with the linear accelerator, we felt it was prudent to provide at least two spares.

This book is the result of the efforts of innumerable SLAC staff members, as well as several interested persons from other institutions. The technical content is ultimately the responsibility of the SLC Parameters Committee, under the chairmanship of John Rees. While it is impossible to acknowledge everyone who has contributed to the production of this handbook, we recognize that it may be useful to list the names of a few persons readers can contact for more information about the various subsystems described here. In that spirit, we list here the names of persons who are not necessarily the sole authors of the

indicated sections, but who provided much of the text and who can redirect inquires to others, as appropriate.

Energy Upgrade	-	G. Leow
Linac Upgrade	-	R. Stiening
Arcs	-	G. Fischer
Final Focus	-	R. Erickson and D. Walz
Sources	-	S. Ecklund
Damping Rings	-	T. Fieguth
I & C	-	M. Crowley-Milling and N. Phinney
Alignment	-	R. Pitthan and R. Ruland

We would like to acknowledge the persons whose special contributions made this book possible. Helmut Wiedemann, who edited the highly successful PEP Design Handbook, began the job of assembling the SLC Design Handbook, established the general format and produced the first drafts of several of the chapters. He was assisted by Jan Adamson, who set up these drafts on the TeX wordprocessor and helped immeasurably in smoothing the transition for the new editor. The final formatting, error checking and mechanics of production have all been the work of Laura Poplin with the assistance of Gretchen Brewer, who implemented several useful features of the new wordprocessor system. The cover design was created by Conrad Ouellette.

Roger Erickson  
 Editor  
 13 November 1984

**CHAPTER 1.  
INTRODUCTION**

- 1.1 THE RATIONALE FOR LINEAR COLLIDERS**
- 1.2 BRIEF DESCRIPTION OF THE PROJECT**
- 1.3 PHYSICS POTENTIAL**
- 1.4 COMPATIBILITY WITH OTHER SLAC OPERATIONS**

## 1. INTRODUCTION

### 1.1 THE RATIONALE FOR LINEAR COLLIDERS

The progress of particle physics has always been intimately connected with the progress of accelerator technology. The past decade has seen the maturation of the electron-positron colliding-beam storage-ring technique, and the machines built to exploit this technique have yielded a wealth of information about the properties of the heavy quarks and leptons, as well as the dynamics of their interactions. The arguments for continuing to higher energy in electron-positron colliding beams are compelling. However, storage rings are becoming evermore costly. While it is clear that higher energies in electron-positron storage rings are technically possible, it is not clear that they are fiscally feasible.

The SLAC Linear Collider (SLC)<sup>1</sup> has two main goals. The first is to serve as the pioneer machine in a new technique to achieve electron-positron collisions at a lower cost per GeV than the storage-ring technique used until now. The other goal is to increase the center-of-mass energy available in the electron-positron system to the level required to investigate the unification of the weak and electromagnetic interactions, now expected to become manifest at approximately 94 GeV.

The SLC is a variant of a new class of accelerator designs called linear colliders.<sup>2</sup> The most straightforward design would use two linear accelerators aimed end-to-end at each other; one for electrons, the other for positrons. A collider of this kind would avoid the two fundamental limitations associated with storage rings. These are synchrotron radiation power loss and the tune shift caused by the interaction of the colliding beams.

Any time a charged particle is deflected from a straight path, it emits synchrotron radiation. The power radiated away increases as the fourth power of the particle's energy (in units of the rest mass) and inversely as the radius of the deflection. In an  $e^+ e^-$  storage ring, the particles are deflected endlessly in closed orbits. The energy lost as synchrotron radiation must be replaced, generally with RF accelerator cavities, or the particles are lost. Replacing the lost

power becomes the primary technical problem in the design of storage rings in the multi-GeV range. The other fundamental limitation of storage rings results from the mutual defocusing effect of the two stored beams as they collide. Since this effect is a function of the electromagnetic force between the beams, it depends on the number of particles per bunch and on how tightly they are focused, and thus limits the maximum current density at the interaction points.

The power lost as synchrotron radiation and the disruption caused by the beam-beam interaction are the ultimate limitations on the peak energy and luminosity, respectively, of the largest existing  $e^+ e^-$  storage rings. In contrast to storage rings, a linear collider with no bends and no stored beams is not limited by either of these effects. A linear collider needs RF power only to accelerate the particles to the desired collision energy, but not to make up for any synchrotron radiation loss. Furthermore, the outgoing beams are discarded after each collision and no attempt is made to store or re-circulate them. Thus, the beam-beam effect does not limit the luminosity, and extremely high current densities can be tolerated. Indeed, under optimum conditions the beam-beam interaction enhances the luminosity by a mutual pinch effect between the crossing beams.

These fundamental differences between linear colliders and storage rings lead to different scaling relations for size and cost vs energy for the two types of machines. It is these different scaling relations that promise lower cost per unit energy for very large linear colliders than for storage rings. The basic argument is as follows. To keep the RF power within practical bounds, storage ring designers are forced to choose a ring diameter, and hence a total machine cost, that increases roughly as the square of the energy. The cost of a linear collider, on the other hand, will be proportional to the length of the accelerators, and thus will increase linearly with energy. At some energy, a first-power scaling relation will result in a less costly device than a quadratic scaling relation.

The highest energy electron-positron storage rings built to date are the PEP project at SLAC and the PETRA project at DESY in Hamburg, West Germany. These machines cost about 80 million dollars each (without experimental apparatus) and achieve center-of-mass energies of approximately 35 and 45 GeV. A

much larger storage ring is being constructed at CERN to achieve a maximum center-of-mass energy of 160 GeV with conventional RF, and 240 GeV with superconducting RF, when the latter technique becomes practical. The version with conventional RF is estimated to cost approximately 1000 million Swiss Francs plus personnel costs. The detailed design studies of the CERN group agree closely with the scaling relation discussed above which shows that the cost of an  $e^+ e^-$  storage ring scales roughly as the square of the center-of-mass energy.

The SLAC linear collider will use the single existing linac to accelerate both electrons and positrons simultaneously. The opposite-sign bunches will be separated and guided to the collision point by long arcs of strong-focusing magnets. Some energy will unavoidably be lost due to synchrotron radiation in the guide magnets, but for beam energies below 70 GeV, the loss is small enough that it can be neglected, and no provision for restoring this energy is needed.

## 1.2 BRIEF DESCRIPTION OF THE PROJECT

The SLC is designed to operate at any center-of-mass energy from that of PEP up to about 100 GeV with a design luminosity of up to  $6 \times 10^{30} \text{ cm}^{-2}\text{sec}^{-1}$ . The maximum energy can be increased at a later time to 140 GeV in the center-of-mass, should that become desirable.

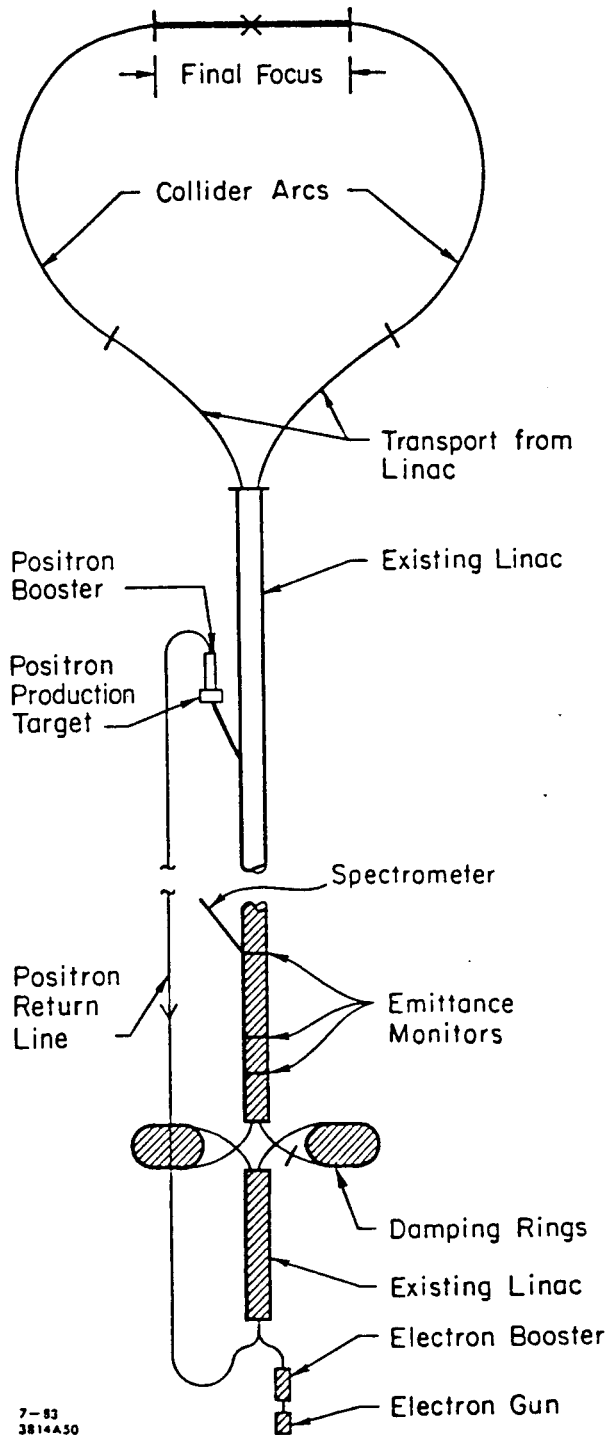
The SLC project entails a major upgrading of the existing linac, as well as the construction of new high-intensity electron and positron sources, damping rings to shrink the transverse size of the beams, arcs of magnets to transport the beams to the interaction point, a final optical system to focus and steer the beams into collision, and facilities to accommodate large experimental detectors. The complete system is shown schematically in Fig. 1.2.1. The important parameters are summarized in Chapter 14. Two essential facets of the project that are not evident in Fig. 1.2.1 are the instrumentation and control system and the unprecedented survey and alignment procedure. These are described in Chapters 7 and 8.

A typical operation cycle proceeds as follows. The cycle begins just before the pulsing of the linac. At this point, the electron and positron damping rings each contain two bunches of  $5 \times 10^{10}$  particles at an energy of about 1.2 GeV. One of the positron bunches is extracted from the damping ring, passes through a pulse compressor which reduces the bunch length from about a centimeter to the millimeter size required for the linac, and is then injected into the linac. Both electron bunches are extracted from the electron damping ring, pass through an independent pulse compressor, and are injected into the linac behind the positron bunch. The spacing between bunches is about 17.6 meters in the linac.

The three bunches are then accelerated through the linac. At the two-thirds point, the trailing electron bunch is extracted from the linac with a pulsed magnet and is directed onto a positron-production target. The positron bunch and the leading electron bunch continue to be accelerated to the end of the linac.

At the end of the linac, the two opposite-charge bunches are separated by a DC magnet and pass through a transport system which matches the focusing of

Figure 1.2.1 Schematic Layout of SLAC Linear Collider



the linac to that of the main collider arcs, the positron bunch traveling along the south arc, the electron bunch along the north. The collider arcs are composed of small-aperture magnets with strong alternating gradient focusing, which is required to hold down emittance growth. After emerging from the arcs, the bunches pass through matching and focusing sections which correct the dispersion and chromatic aberrations of the beams and steer them to the collision point.

The positrons produced by the "scavenger" electron bunch that was extracted at the two-thirds point of the linac pass through a focusing system at the positron source, a 200-MeV linear accelerator booster, a 180° bend, and an evacuated transport pipe located in the existing linac tunnel. This brings the positron bunches back to the beginning of the linac. At this point, the positron bunch passes through another 180° bend and is boosted to an energy of 1.2-GeV in the first sector of the existing linac. From there it is injected into the damping ring.

Because the emittance of the initial positron beam is much too large for acceptable collider operation, each positron bunch must remain in the damping ring for approximately four radiation damping times, which corresponds to twice the time interval between linac pulses. Thus the positron bunch to be used in the next linac cycle is the one that is still stored in the damping ring from the previous cycle.

Electrons for collider operation are produced from a high-intensity gun equipped with a subharmonic buncher. Two bunches of electrons are produced, are boosted to 200 MeV in a dedicated section of linac, and are then injected into the same section of linac used to boost the positron bunch to 1.2 GeV. At the end of this section the 1.2 GeV electrons are injected into a separate damping ring. The electron bunches at the time of injection into this damping ring have an emittance somewhat larger than required for collider operation but considerably smaller than the emittance of the positron bunch and thus need only be damped for two damping times or one interpulse period. The entire cycle repeats 180 times per second.

### 1.3 PHYSICS POTENTIAL

During the past decade, while electron-positron colliding-beam experiments were illuminating the spectra of the charmed and bottom quarks, the fixed-target machines were successfully probing the weak interaction. A new manifestation of the weak interaction, the neutral current, was discovered, and both the electromagnetic and weak structure-functions of the proton were measured.

From all of this experimental work, a new theoretical picture has emerged which interprets both the weak and electromagnetic forces as different manifestations of one basic force. All of the variants of this picture have one or more heavy particles which interact with the electron-positron system in the same basic way as does the ordinary massless photon. The simplest form of this theory has come to be known as the "standard model." It features a neutral boson called the  $Z^0$  with a mass predicted to be about 90 GeV. The  $Z^0$  should be copiously produced in  $e^+ e^-$  annihilations and will have decay modes into all the quarks and leptons with masses less than half the  $Z^0$ .

The standard model has been so successful in explaining apparently unrelated observations, that it is generally believed to be correct. The first direct evidence for the existence of the  $Z^0$  was reported in 1983 by two experimental collaborations studying proton-antiproton collisions at CERN.<sup>3</sup> Based on a handful of events with high-momentum  $e^+ e^-$  pairs in the final states, these collaborations report a  $Z^0$  mass of about  $94 \pm 3$  GeV. In addition, they have recently reported indirect evidence for the existence of a state in the 40-50 GeV range that decays semi-leptonically. This could be the long-sought top quark. These discoveries are the best evidence to date for the correctness of the standard model. The production and storage of antiprotons are certainly a technological triumph for CERN, but the limitations of the  $\bar{p}p$  technique are already becoming evident.  $Z^0$ 's are detected in fewer than one event in ten million. A year of running since the initial discovery has yielded only about a dozen  $Z^0$ 's. The unknown parameters that must be determined experimentally to clarify and extend the theoretical model, namely the width and shape of the  $Z^0$  and the identification of its decay products, seem to be beyond the reach of the  $\bar{p}p$  technique. One conclusion is

clear: an  $e^+ e^-$  collider that covers the 90–100 GeV range is exactly the tool needed to move this frontier forward.

The SLC design is optimized for operation at the  $Z^0$  mass.<sup>4</sup> Operating at the peak of the  $Z^0$  cross section, the SLC will cleanly produce thousands of  $Z^0$ 's per day. The decays of these  $Z^0$ 's are expected to be rich sources of heavy quarks and leptons and perhaps more exotic particles that are predicted by theories seeking to extend the standard model. A careful measurement of the width of the  $Z^0$  resonance will measure the total number of decay modes possible, and thus will reveal the total number of different fermion families that make up the universe. Such a measurement may have profound implications for cosmology as well as for particle physics.

## 1.4 COMPATIBILITY WITH OTHER SLAC OPERATIONS

The operation of the SLAC linac in the era of the collider must be compatible with other programs at SLAC that will use the linac. It is difficult to project a detailed laboratory program for the second half of the 1980's, but present plans would call for operation of the PEP and SPEAR storage rings, test beams in the research area for the development of new detectors and apparatus, and a limited fixed-target program that includes nuclear physics experiments at relatively low energies.

When the linac is set up for 50-GeV collider operation, the focusing system along the machine is capable of delivering beams at the end of the accelerator with any energy greater than about 20 GeV. The storage rings require both electron and positron beams at energies ranging from 2 to 17 GeV, and are therefore not compatible with collider operation on an interlaced pulse-to-pulse basis. Since the storage rings only require the use of the linac for a few minutes per hour for refilling, the linac will be dedicated to the storage rings for those few minutes. This requires only that the quadrupoles on the linac be capable of being reset to their new values in a few seconds. The positron intensity from the new source required for the collider will be much greater than that available at present, and the filling times of the storage rings will be correspondingly reduced.

Test beams for apparatus development require only low intensities. In principle, these beams could be generated as secondary beams from targets struck by the primary collider beam. Although no detailed design exists at present, a pulsed-magnet system capable of diverting pulses as required from the collider to a secondary-beam target is being considered. We estimate that storage-ring operation and test-beam operation will require about 10% of the linac pulses. This does not seriously impact the collider luminosity.

The potential demand for high-energy, high-intensity beams for fixed-target experiments some five years hence is not clear at this time. There is no problem in delivering the two electron bunches that will be used in a collider cycle to the end of the accelerator, and then diverting these bunches down the existing beam

lines. This mode of operation will give  $10^{11}$  electrons per pulse (150 kW at 50 GeV, 180 pps). Should longer duty cycle beams be required, the damping system can be by-passed, and thus beams with energy up to 50 GeV can be generated up to the full pulse length of SLED II (approximately 200 nsec), but this mode of operation will be incompatible with SLC operation.

## REFERENCES

1. SLAC Linear Collider Conceptual Design Report SLAC-229, June 1980. B. Richter, *The SLAC Linear Collider*, 11th International Conference on High Energy Accelerators, Geneva, Birkhauser Verlag Basel (1980), p. 168. H. Wiedemann, *The SLAC Linear Collider Project*, IEEE, Vol. NS - 28, No. 3, p. 2016 (1981). B. Richter, *The SLAC Linear Collider, The Machine, The Physics, The Future*, SLAC-PUB-2854 (1981).
2. M. Tigner, *Possible Apparatus for Electron Clashing Beam Experiments*, Nuovo Cimento 37, 1228 (1965). J. E. Augustin, N. Dikanski, Ya. Derbenev, J. Rees, B. Richter, A. Skrinski, M. Tigner and H. Wiedemann, *Limitations on Performance of  $e^+ e^-$  Storage Rings and Linear Colliding Beam Systems at High Energy*, Proceedings of the Workshop on Possibilities and Limitations of Accelerators and Detectors FNAL, Batavia, Illinois (1979). Several reports on Colliders in Proceedings of the 2nd ICFA Workshop on Possibilities and Limitations of Accelerators and Detectors, Les Diablerets, Switzerland, edited by U. Amaldi (1979). H. Wiedemann, *Linear Collider*, Proceedings of the Summer Institute on Particle Physics, SLAC Report-245 (1981). P. Wilson, *High Energy Electron Linacs: Applications to Storage Ring RF Systems and Linear Colliders*, Physics of High Energy Particle Accelerators, American Institute of Physics, New York, edited by R. A. Carrigan, F. R. Huson and M. Month (1982).
3. G. Arnison *et al.*, Phys. Lett. 126B, 398 (1983). B. Sadoulet *et al.*, Proceedings of 1983 Symposium on Lepton and Photon Interactions, Cornell University, August 1983, p. 27. P. Bagnaia *et al.*, CERN-EP/84-39 (1984).
4. Proceedings of the SLC Workshop on Experimental Use of the SLAC Linear Collider, SLAC Report-247 (1982).

## **CHAPTER 2. LINEAR ACCELERATOR**

### **2.1 LINAC ENERGY UPGRADE TO 50 GeV**

### **2.2 SPACE CHARGE EFFECTS IN THE LINEAR ACCELERATOR**

#### **2.2.1 Introduction**

#### **2.2.2 Calculation of Longitudinal and Transverse Wake Fields**

#### **2.2.3 Longitudinal Wake-Field Effects and Control Measures**

#### **2.2.4 Transverse Wake-Field Effects**

### **2.3 UPGRADED BEAM GUIDANCE SYSTEM**

#### **2.3.1 Introduction**

#### **2.3.2 Tolerances and Corrections**

#### **2.3.3 Control of Beam Center Line**

#### **2.3.4 Computer Support**

#### **2.3.5 Beamline Status**

### **2.4 TOLERANCES AND BEAM QUALITY**

#### **2.4.1 Linac Tolerances**

#### **2.4.2 Computer Simulation**

## CHAPTER 2. LINEAR ACCELERATOR

### 2.1 LINAC ENERGY UPGRADE TO 50 GEV

Operating in the conventional unSLEDed mode, the SLAC linac is presently capable of producing 1.6  $\mu$ sec electron beam pulses with a maximum energy of about 24 GeV. This energy is obtained with a complement of about 240 klystrons, each supplying 2.5  $\mu$ sec RF pulses to a 12.5 m girder supporting four 3.05 m constant gradient accelerator sections. The present klystron population contains a mixture of about 115 older tubes with nominal peak powers of 20 and 30 MW, and about 128 newer tubes of 35 MW nominal peak power. Each station produces a maximum energy given by the simple expression

$$E_{\text{MeV}} = 20\sqrt{P_{\text{MW}}}$$

or about 100 MeV with an average klystron peak power of 25 MW. The maximum repetition rate is 360 pps. The SLED I mode of operation increases the total no-load energy by a factor of 1.4 to about 33.5 GeV. This energy is not reached in practice because of beam loading and because one of the 30 linac sectors (Sector 9) has been temporarily set aside for SLC development tests. The maximum reachable energy with SLED I at this time is about 31 GeV. The SLC program requires that the linac be upgraded to deliver 50 GeV beams.

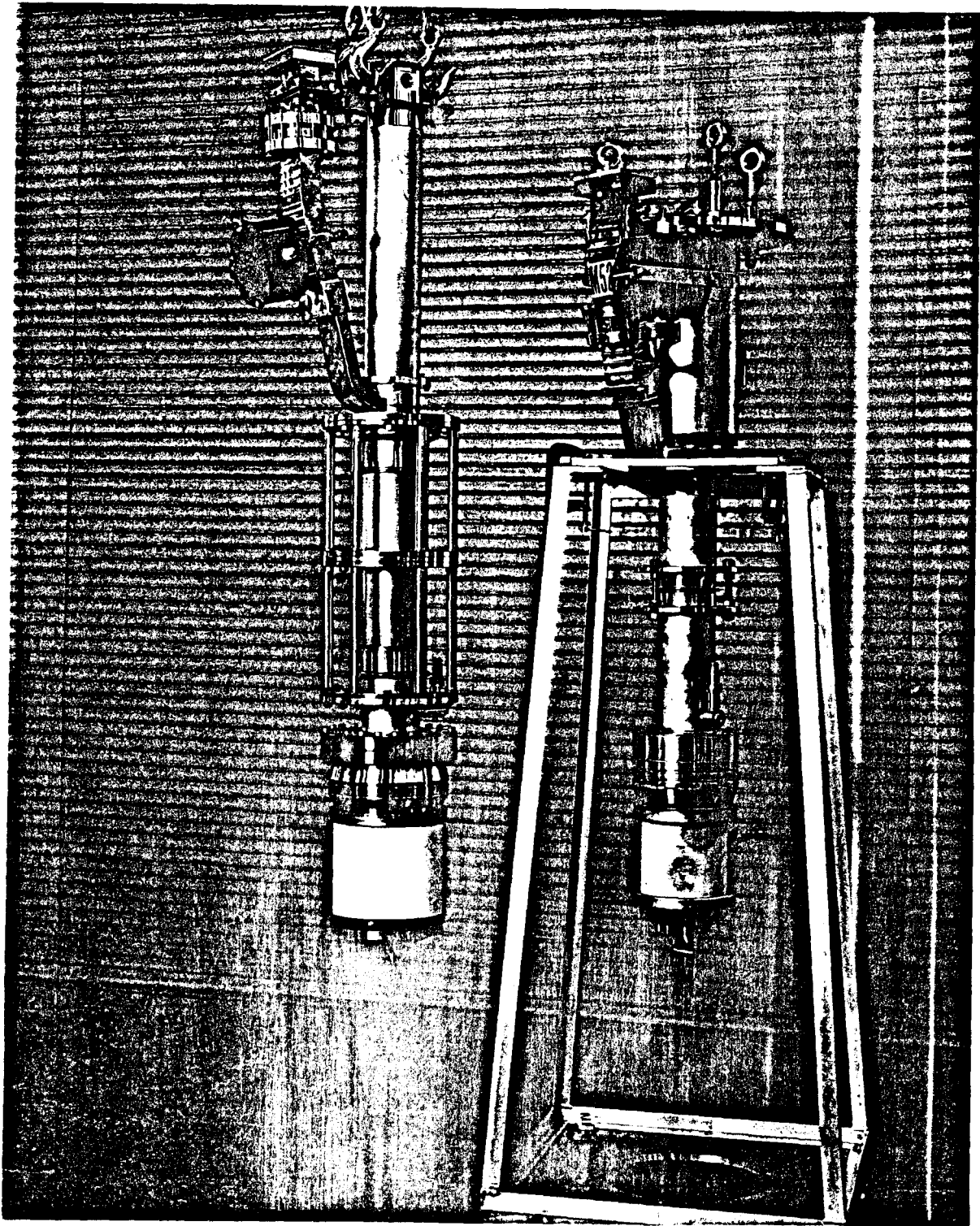
The 50 MW klystron is an upgraded version of the 36 MW tube now being built and used at SLAC. For comparison, the specifications of these two tubes and the modulators which go with them are shown in Table 2.1.1. Figure 2.1.1 shows a photograph of the two klystrons. Note that the 50 MW tube is somewhat longer than the 36 MW tube and in its present design incorporates 6 rather than 5 cavities. The focusing magnet for the 50 MW klystron is an electromagnet rather than the permanent magnet presently in use with the 36 MW tube. A series of prototypes of the 50 MW tube has been constructed and tested. The primary objective is to obtain running experience in order to demonstrate reliability and a low fault rate. Several recent tubes have achieved full rated

power at 315 kV and have been sufficiently stable for use on the accelerator. Use of a dispenser cathode and higher quality materials, such as vacuum-melted low-carbon stainless steel, OFHC copper and molybdenum, has resulted in tubes with a much lower fault rate. If it is assumed that 5% of the SLC pulses can be lost, each klystron may miss one pulse in 5000 or 200 pulses in  $10^6$ . At 180 pps operation this translates into 130 missing pulses per hour being permitted on a given tube.

Klystron Peak Output Power	36 MW	50 MW
Frequency	2856 MHz	2856 MHz
Perveance	$2.1 \times 10^{-6}$	$2 \times 10^{-6}$
Peak Beam Voltage	265 kV	315 kV
Peak Beam Current	286 A	354 A
Peak Beam Power	75.8 MW	111.5 MW
Average Beam Power	91.5 kW	120.3 kW
Klystron Impedance	926 $\Omega$	890 $\Omega$
RF Pulse Width	2.5 $\mu$ sec	5 $\mu$ sec
Modulator Pulse Width	3.35 $\mu$ sec	6 $\mu$ sec
Repetition Rate	360 pps	180 pps
Klystron Efficiency	0.47	0.45
Pulse Transformer Ratio	1:12	1:14
PFN Impedance	6 $\Omega$	4.6 $\Omega$
dc Power	107.6 kW	141.6 kW
ac Power	119.5 kVA	157.5 kVA
Focusing Magnet	Permanent	Electromagnet
Cathode Type	Oxide	Dispenser

There are two types of klystron faults. One is a single missing or partially missing pulse, called a fast forward energy fault (FFE). Several tubes to date have had less than 10 of these faults per hour. The other type of fault is a tube arc, which shuts the modulator off for 1 to 3 seconds when the fault occurs. The

Figure 2.1.1



best tubes to date have had 0.1 to 0.25 of these per hour. Depending on the modulator recycle time this also is an acceptable fault rate. Other tests are still in progress to demonstrate reliability.

After completion of the present series of tests, the Klystron Group will switch its regular production program of 36 MW models to 50 MW tubes and these, together with their pulse transformer tanks, will then be installed gradually along the accelerator as the SLC construction program progresses and the older tubes fail. The necessary modulator modifications and new ac power equipment which goes with them will be added accordingly. The same is true for the cooling water and mechanical support modifications which are necessary for the new klystrons. Figure 2.1.2 illustrates the modulator and ac power equipment changes. The modulator changes to accommodate the energy upgrade consists of changing the klystron pulse transformers, the PFNs (pulse forming network), and the power supplies. The longer pulse duration and the 20% higher beam voltage combine to require a pulse transformer with 2.1 times the voltsecond capability of the present transformer. The longer pulse duration and higher peak power of the klystron results in 2.8 times more energy in the PFN requiring the replacement of the PFN capacitors. The average kVA and power of the modulator at 180 PPS will increase by 32% over the present modulators designed for 360 PPS. This increase in average power requires the replacement of the modulator rectifier, filter network, and charging choke.

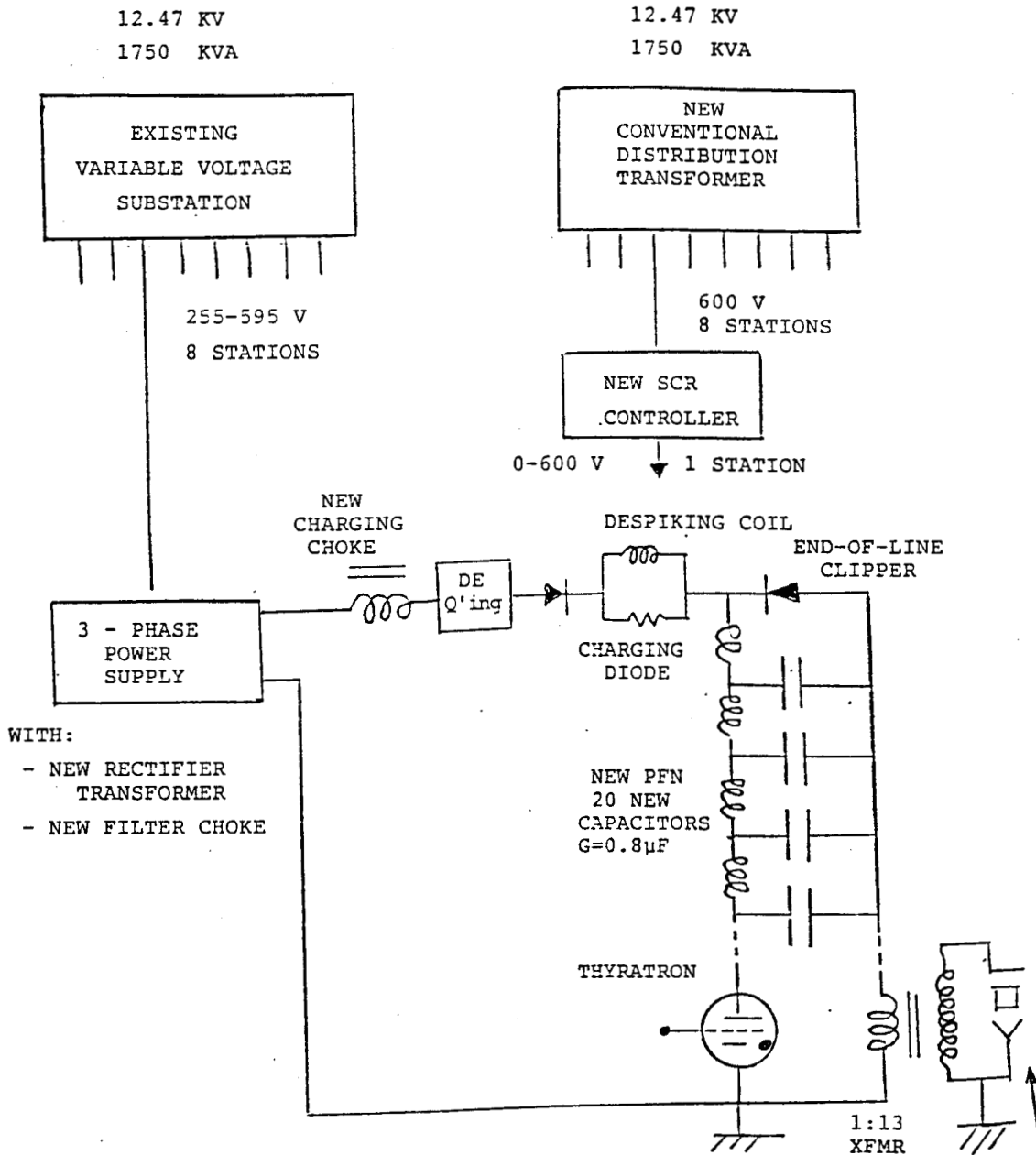
The modulator cabinet and most of the other equipment will be reused and rebuilt in place. The ac distribution will be rebuilt to accommodate the increased power requirements.

To minimize the conversion and future power costs, the rise time of the modulator pulse will be used to reduce the flat top pulse duration. Measurements made on the accelerator indicated that the flat top could be reduced to 4.6  $\mu$ sec and still produce the required RF power.

A pulse transformer turns ratio of 14/1 was chosen to keep the voltage on the modulator thyatron as low as practical. This leaves open the option of higher voltage operation in the future.

Figure 2.1.2

Block diagram showing, at the top, the existing Variable Substation and the new Distribution Transformer with eight individual SCR controllers (one per modulator) and at the bottom, one typical modulator with the modifications required for the 50 MW klystron operating in the SLED II mode.

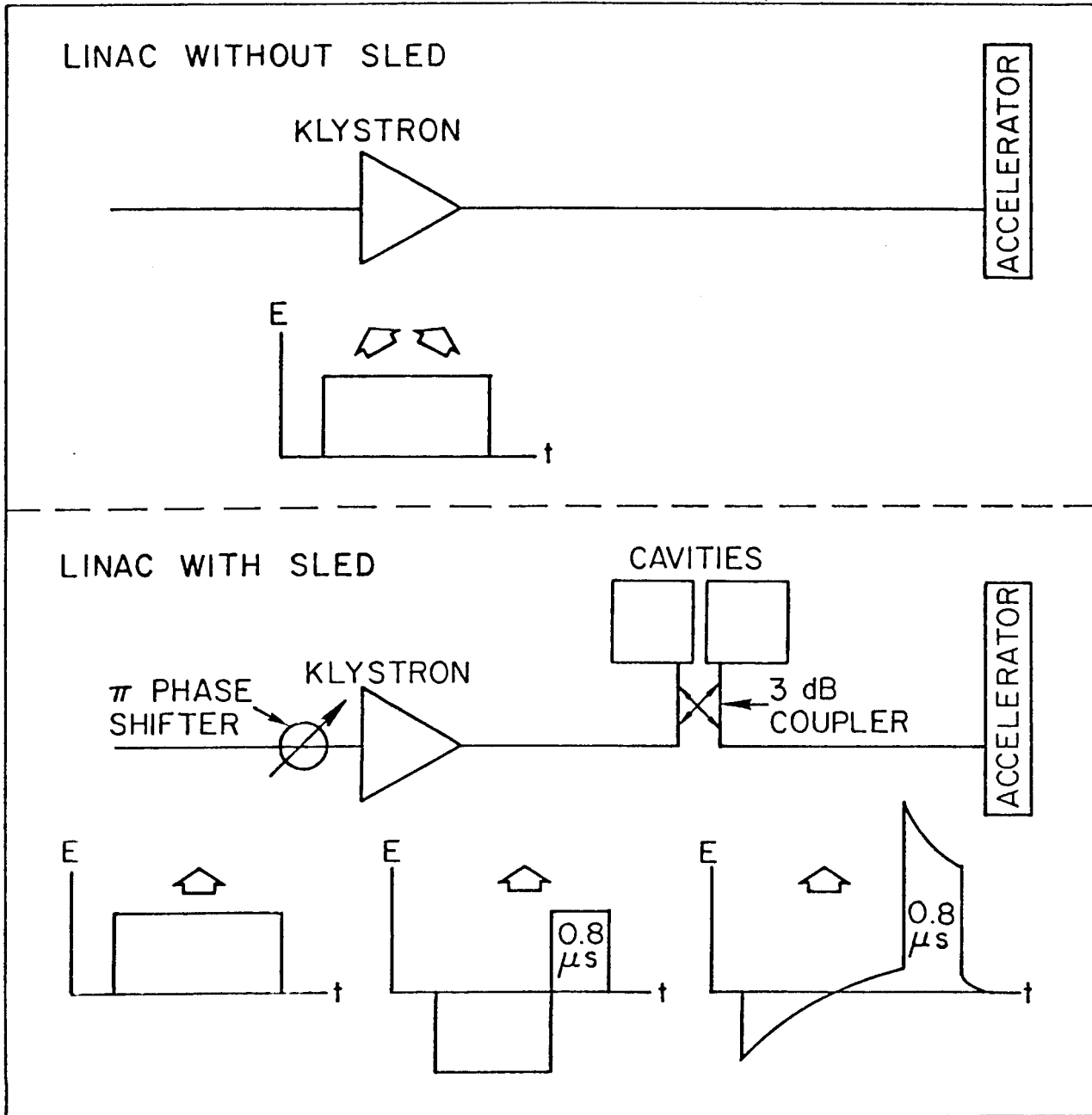


The variable voltage transformers (VVT's) are to be replaced with individual modulator primary control phase back thyristors. The open wye connection of these will result in individual voltage control capability for each klystron (minimizing the deQing loss) and will reduce the current during a thyatron fault and shorten the recovery time. The primary controller and the deQing circuit will be controlled by the MK package and the computer system to control the individual klystron voltages.

The principle and operation of SLED have been described in great detail in several published documents<sup>1-4</sup> and are only briefly summarized here. Referring to the top of Figure 2.1.3, we see that under normal non-SLED operation, the RF pulse, which is amplified by the klystron, is directly transmitted to the linear accelerator. The SLED system which is shown at the bottom of Figure 2.1.3 has two major components: a 180° fast phase shifter on the drive side of the klystron and two high-Q ( $Q_o = 100,000$ ) cavities on the output side of the tube with a 3 db coupler connected as shown. During the first part of the pulse, the phase of the RF drive signal is reversed and the RF cavities fill up with energy with that phase. Because of the 3 db coupler, no energy is reflected toward the klystron. The fields emitted by the cavities add algebraically with the fields reflected by the cavity coupling irises and the power flows toward the accelerator. Exactly one linac filling time ( $0.8 \mu\text{sec}$ ) before the end of the pulse, the phase of the drive signal is flipped back by 180°; as a result both cavities discharge their energy into the accelerator. The discharging pulse amplitude is increased by the fact that the klystron pulse adds to it. The output pulse length is tailored exactly to fill the accelerator sections at one instant of time.

There is no qualitative difference between SLED I and SLED II, only a quantitative one. In SLED I, the RF pulse length is  $2.5 \mu\text{sec}$  and the time devoted to charging the cavities is  $1.7 \mu\text{sec}$ . In SLED II, the RF pulse length is doubled to  $5 \mu\text{sec}$  and the charging time is  $4.2 \mu\text{sec}$ . As a result, the effective pulse height is increased as shown in Figure 2.1.4. This explains the respective energy gains of 1.4 for SLED I and 1.78 for SLED II. The only penalty for going from SLED I to SLED II without increasing the ac power input to each modulator is that the repetition rate must be cut from 360 pps down to 180 pps.

Figure 2.1.3 The Elements of SLED



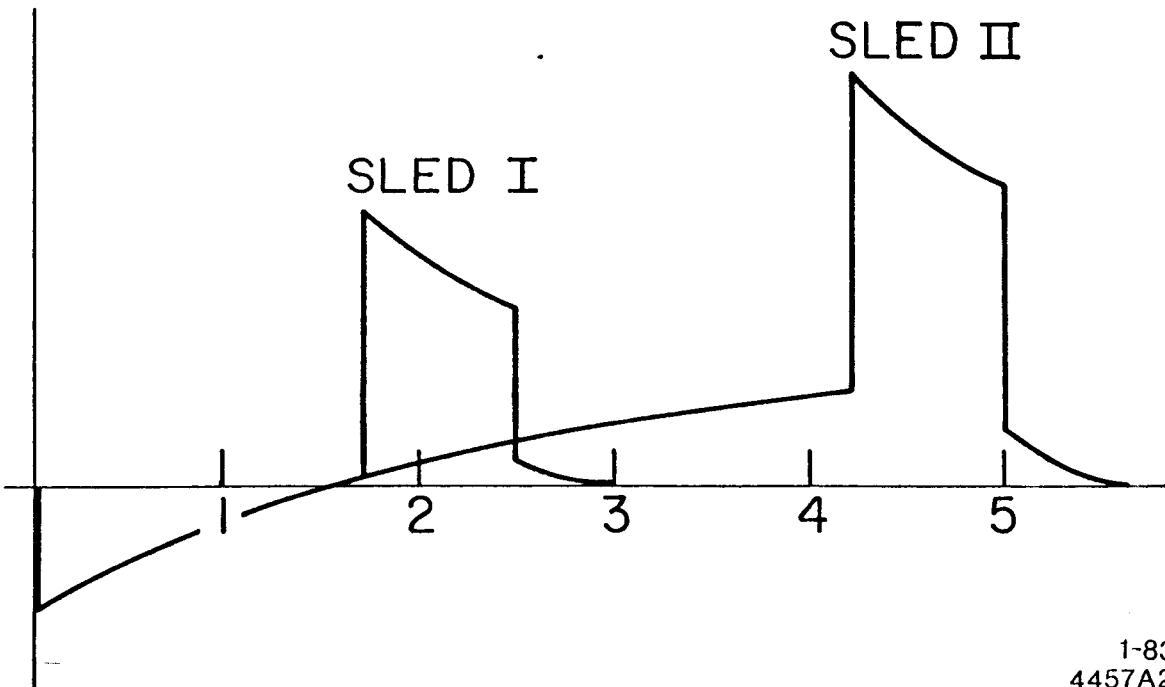
1-83

4457A1

Figure 2.1.4

SLED OPTIONS

	I	II
PULSE LENGTH	$2.5\mu s$	$5\mu s$
EFFECTIVE POWER GAIN	2	3.15
ENERGY GAIN	1.4	1.78
REPETITION RATE	360 pps	180 pps

1-83  
4457A2

The linac, from Sector 2 to Sector 30, contains about 230 stations. Most of these are standard but a few are made of shorter accelerator sections and a few have only two or three sections instead of four. An overall 1% energy derating factor must be applied because of these non-standard girders. Let us assume that 226 stations are available at any given time (i.e., two stations are out of order and two are on standby). To obtain 100 GeV of energy in the center-of-mass, each bunch must emerge from the linac with at least 51 GeV since 1 GeV will be lost by synchrotron radiation in the SLC arcs. In addition, it is estimated that an extra 3.6 GeV must be available to compensate for beam loading. The energy budget for the first bunch ( $e^+$ ) then comes out as follows:

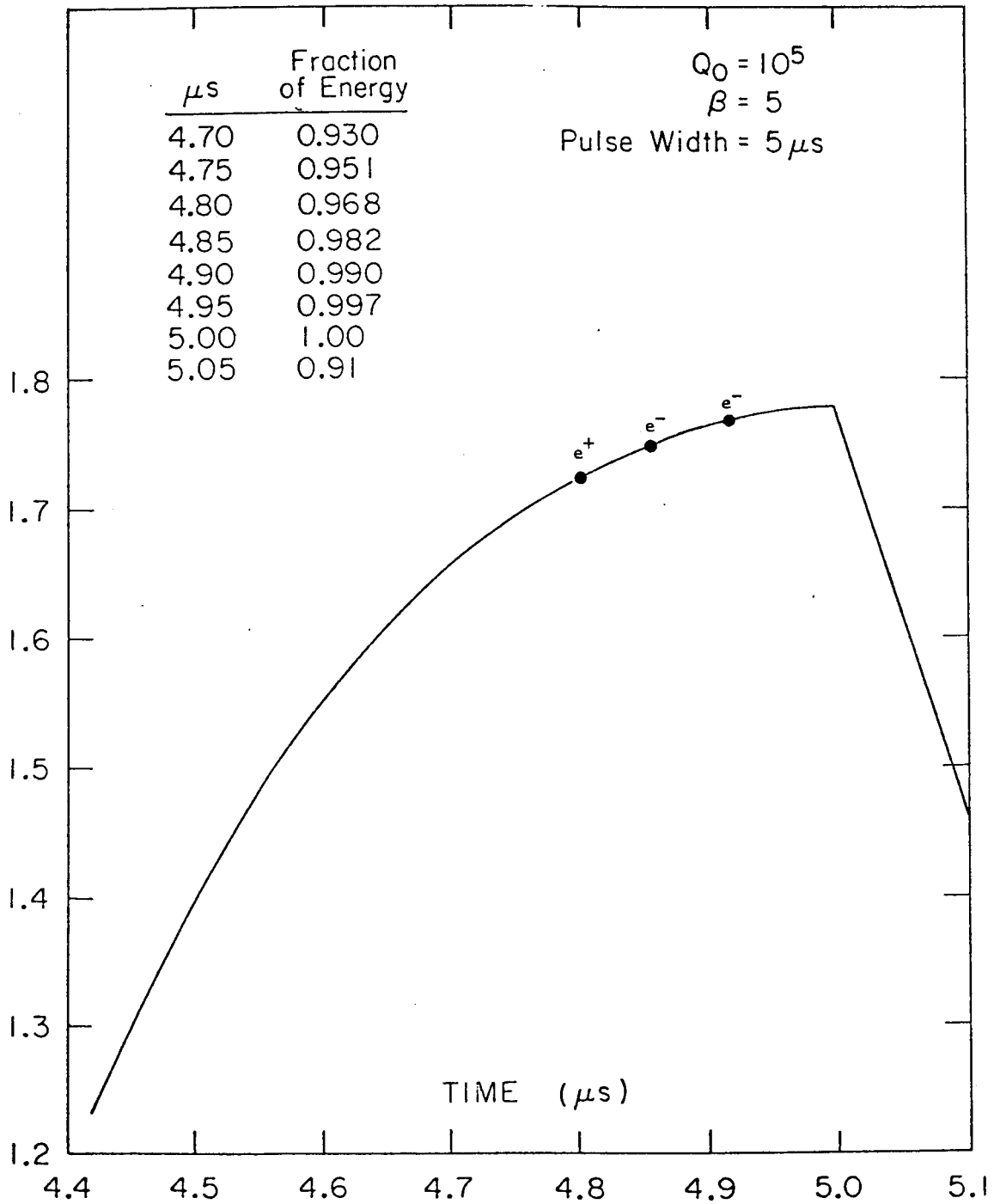
$$\begin{array}{ccccccc}
 E+226 \times 1.78 & \times & 0.99 & \times & 0.968 & \times & 20\sqrt{P_{MW}} \times 10^{-3} \text{ GeV} \\
 \uparrow & \uparrow & \uparrow & & \uparrow & & \uparrow \\
 \text{No. of Stations} & \text{SLED II Multiplier} & \text{Derating because of non-standard girders} & & \text{Derating because of SLED II slope} & & \text{Net girder contribution} \\
 \\ 
 + 1.21 \text{ GeV} & - & 1 \text{ GeV} & - & 3.6 \text{ GeV} & & \\
 \uparrow & & \uparrow & & \uparrow & & \\
 \text{Sector 1, Damping Rings} & & \text{Synchrotron Radiation Loss} & & \text{Beam Loading Compensation} & & 
 \end{array}$$

For  $P = 50$  MW, there results an energy of 51.13 GeV at the interaction point. Each station contributes a no-load energy of about 250 MeV with an average gradient of about 20 MeV/m.

The energy derating of 0.968 due to the SLED II slope can be understood by looking at Figure 2.1.5. This curve shows the energy gain profile versus time as the SLED II pulse progressively fills the accelerator. The  $e^+$  and following two  $e^-$  bunches are made to ride on this curve roughly as shown, with a spacing of 58.8  $\mu\text{sec}$  corresponding to half the going-around time in the damping rings.

The energy of the  $e^+$  bunch injected at  $t = 4.800 \mu\text{sec}$  is 0.968 of the SLED II maximum. When the subsequent  $e^-$  comes along at time  $t = 4.800 + 0.0588 \mu\text{sec}$ , it would acquire an energy of  $\approx 0.983$  of the SLED II maximum, or roughly 800 MeV more than the  $e^+$  bunch. However, the  $e^+$  bunch has just wiped out 408 J or so of the roughly 14,000 J stored in the accelerator. This energy

Figure 2.1.5 SLED II Energy Gain vs. Time



reduction results in an 800 MeV decrease. In addition, it should be noted that to compensate for beam loading due to the generation of higher-order modes resulting in longitudinal wake-fields, the gaussian bunches are made to ride with their centers  $15^\circ$  ahead of the accelerating wave crest. This has the effect of reducing their final energy by about 3.6 GeV. The  $e^+$  and  $e^-$  bunches thus reach the final interaction point, each with an energy of 51.1 GeV. The third bunch, coming at time  $t = 4.800 + 0.118 \mu\text{sec}$ , would have an energy of 0.992 of the SLED II maximum, again reduced by another 800 MeV. The energy of this bunch would then be 50.9 GeV at the interaction point. In actual fact it is deflected for positron generation at the end of Sector 19 at which point its energy is about 33 GeV.

In summary, we see that with the 50 MW klystrons and SLED II, we have a small energy reserve of 1.1 GeV per beam above the design requirement of 50 GeV. This reserve must be kept to make up for other possible shortcomings in the overall system such as imperfect klystron phasing and timing.

## 2.2 SPACE CHARGE EFFECTS IN THE LINEAR ACCELERATOR

### 2.2.1 Introduction

Space-charge forces cause the effective emittance and energy spread of particle bunches to grow as they pass through the linear accelerator. The properties of the optical system which focuses the bunches have been chosen on the assumption that the energy spread of the particle bunches leaving the linear accelerator is  $\pm 0.5\%$  and that the effective emittance of the bunches is  $3 \times 10^{-10}$  radian-meters.

It is a simple matter to produce a low-intensity beam exceeding this specification. As the current is increased, however, the emittance and energy spread of the beam will grow. The maximum current which can be accelerated subject to the conditions on maximum usable emittance and energy spread is determined by the space-charge-control measures which are adopted.

The space-charge effects which are important here are the head-to-tail type which are common in particle accelerators. The leading particles at the head of the bunch leave behind fields in the linac RF structure which act on particles which follow in the tail of the bunch. Once the distribution of fields which a single particle leaves behind is known, it is a straightforward matter to compute the space-charge disruption of the ensemble of particles which constitute a bunch.

Two types of wake-field trail behind a particle passing through the linac RF structure. There is a longitudinal wake which decelerates and a transverse wake which deflects particles that follow. The longitudinal wake-field depends only on the distance between the particles generating the wake-field and the particle upon which the wake-field acts. The transverse wake-field is more complicated. Like the longitudinal wake this wake depends on the distance between the particle which generates it and the particle on which it acts. It is also proportional to the distance between the path of the generating particle and the geometrical center line of the linac RF cavities, but is independent of the transverse position of the particle on which it acts. There are other higher order wake-fields which depend on higher powers of the distance between the path of the generating and following particle and the axis of the RF cavities. These fields are unimportant

in the present application.

The transverse wake-field that causes growth in the effective transverse emittance of the bunches and the longitudinal wake-field that causes growth in energy spread differ in their dependence on the distance between the leading particle that generates the wake and the following particle that is acted on by the fields. For the range of bunch lengths appropriate to the Collider, the transverse wake increases with increasing separation between the particles, while the longitudinal wake decreases. For this reason, the energy spread increases when the bunch is made shorter, while the transverse emittance growth decreases. The bunch length, which is a controllable parameter, must be chosen to best balance these two space-charge effects. For the present Collider parameters, a gaussian bunch with a rms length of 1.0 mm is consistent with the acceleration of  $5 \times 10^{10}$  particles/bunch with the required limits on energy spread and transverse emittance.

The effects of the longitudinal wake-field are partially controlled by placing the bunch ahead of the crest of the RF wave in the linac and thus compensating the energy loss due to the wake. This procedure will be discussed in Section 2.2.3.

The effects of the transverse wake-field are controlled by making a precise trajectory correction for the beams so that they pass very close to the center of the RF structure. This procedure minimizes the wake-field. The effect of the residual wake-field is minimized by the choice of a very tightly focused linac quadrupole lattice. There is one more condition which can only be satisfied by a tuning procedure. It is necessary to inject the beam into the linac with a very small component of free betatron motion. This will be accomplished by empirical tuning of injection conditions using emittance detectors at the end of the linac as monitors. This procedure has been tried successfully with short trains of bunches during accelerator physics experiments. The theory of transverse emittance growth will be discussed in Section 2.2.4.

## 2.2.2 Calculation of Longitudinal and Transverse Wake Fields

We consider an axisymmetric periodic structure to have a geometry as shown

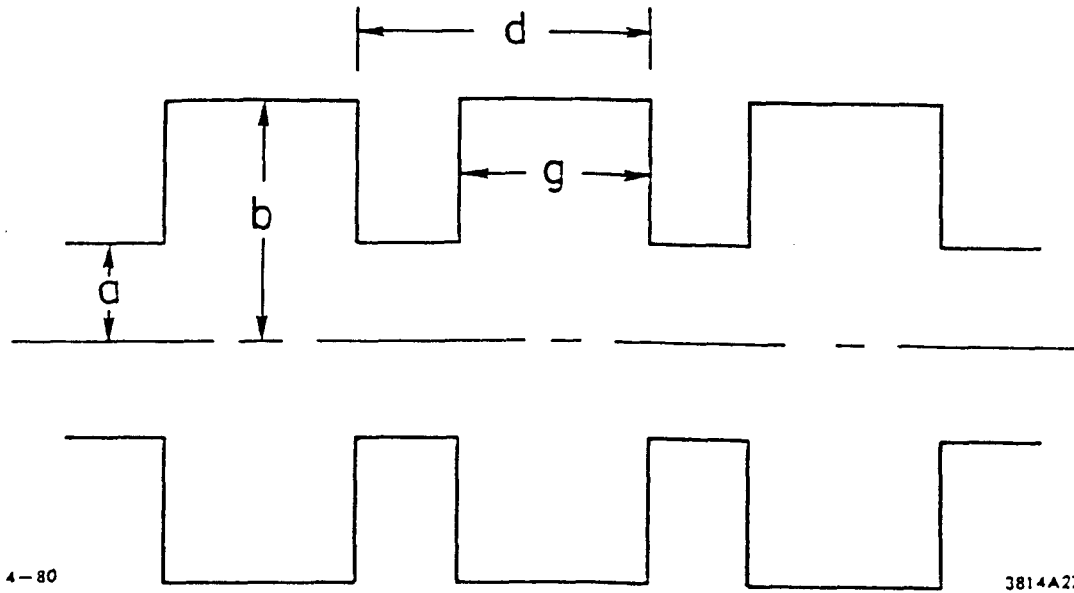


Figure 2.2.2.1

Structure geometry analyzed by the program TRANS.

in Fig. 2.2.2.1. It can be shown<sup>6</sup> that for this structure a synchronous mode (traveling-wave mode with phase velocity equal to  $c$ ) has an axial electric field that varies with radial position and azimuthal  $\angle \phi$  as

$$E_z = E_0 \left( \frac{r}{a} \right)^m \cos m\phi \quad , \quad (1)$$

where  $a$  is the beam-hole radius, and  $m$  is an integer. In terms of the "cold" (no charges present) electromagnetic properties of the structure, we can define a loss parameter  $k_n$  for each mode by

$$k_n = \frac{(E_{0n}d)^2}{4W_n} \quad , \quad (2)$$

where  $d$  is the periodic length, and  $W_n$  is the energy stored per period. For a point charge  $q$  traveling parallel to the axis of the structure at  $r = r_e$  and  $\phi = 0$ , the beam-induced energy deposited in the  $n$ th mode per period is<sup>7</sup>

$$W_n = k_n q^2 \left( \frac{r_e}{a} \right)^{2m} \quad .$$

Eliminating  $W_n$  using the preceding two expressions, we have

$$E_{0n}d = -2 \left( \frac{r_e}{a} \right)^m k_n q \quad . \quad (3)$$

The minus sign indicates that the phase of the induced field is such as to oppose the motion of the charge. As a function of distance  $\Delta z = c\tau$  behind the exciting charge, the field varies as  $E_z \sim \cos \omega_n \tau$ . Using this, together with Eq. (3) in Eq. (1), we obtain

$$E_{zn}(r, \phi, \tau)d = -2k_n q \left( \frac{r}{a} \right)^m \left( \frac{r_e}{a} \right)^m \cos m\phi \cos \omega_n \tau \quad . \quad (4)$$

For longitudinal modes ( $m = 0$ ), we define the wake potential for the  $n$ th mode as the voltage per period, per unit exciting charge,

$$w(\tau) \equiv E_{zn}d/q = -2k_n \cos \omega_n \tau \quad .$$

By superposition, the total wake potential for  $N$  modes is

$$w(\tau) = -2 \sum_{n=1}^N k_n \cos \omega_n \tau \quad . \quad (5)$$

For deflecting modes ( $m > 0$ ), we define the wake potential seen by a relativistic ( $v = c$ ) particle with charge  $e$ , following at a distance  $c\tau$  behind a unit point charge, by

$$w(\tau) = (c/e) \vec{\Delta} p_{\perp} = \left( \vec{E}_{\perp} + c\vec{B}_{\perp} \right)^{(f)} d \quad ,$$

where  $\Delta p_{\perp}$  is the transverse momentum kick per period. The superscript  $(f)$  indicates that the electric and magnetic fields are evaluated in a frame moving with the particle. For a synchronous particle, the momentum kick can be expressed in terms of the  $E_z$  field component alone:<sup>8</sup>

$$\left( \vec{E}_{\perp} + c\vec{B}_{\perp} \right)^{(f)} = j(c/\omega) \vec{\Delta}_{\perp} E_z^{(f)} \quad .$$

Assuming  $E_z = -|E_z|e^{j\omega\tau}$ , the preceding two relations give

$$\vec{W}(\tau) = d(c/\omega) \sin \omega\tau \left( \hat{r} \frac{\partial |E_z|}{\partial r} + \hat{\phi} \frac{1}{r} \frac{\partial |E_z|}{\partial \phi} \right) ,$$

where  $\hat{r}$  and  $\hat{\phi}$  are unit vectors. From Eq. (4) we now obtain

$$\begin{aligned} \hat{r} : W_n(r, \phi, \tau) &= 2m \left( \frac{k_n}{\omega_n a/c} \right) \left( \frac{r}{a} \right)^{m-1} \left( \frac{r_e}{a} \right)^m \cos m\phi \sin \omega_n \tau \\ \hat{\phi} : W_n(r, \phi, \tau) &= -2m \left( \frac{k_n}{\omega_n a/c} \right) \left( \frac{r}{a} \right)^{m-1} \left( \frac{r_e}{a} \right)^m \sin m\phi \sin \omega_n \tau \end{aligned} \quad (6)$$

for the components of the wake in the  $\hat{r}$  and  $\hat{\phi}$  directions. The  $\hat{r}$  component of the wake at  $\phi = 0$  for dipole ( $m = 1$ ) modes is of the most interest:

$$w_n(\tau) = 2 \left( \frac{k_n}{\omega_n a/c} \right) \left( \frac{r_e}{a} \right) \sin \omega_n \tau . \quad (7)$$

Analogous to Eq. (5), the total wake for  $N$  modes is the sum of the individual wakes.

Two computer programs are available for finding the values of  $\omega_n$  and  $k_n$  required in Eqs. (5) and (6). The program KN7C<sup>9</sup> can be used for longitudinal modes ( $m = 0$ ). More recently, a program TRANS has been developed<sup>6</sup> which can find the modes in the structure shown in Fig. 2.2.2.1 for any value of  $m$ . The real SLAC structure is a constant-gradient structure. The beam-hole size varies from 1.31 cm to 0.96 cm along the length of the structure. For the computer runs, the dimensions of an average cavity (cavity No. 45 in the middle of the structure) were used:

$$\begin{aligned} a &= 1.163 \text{ cm} \\ b &= 4.134 \text{ cm} \\ g &= 2.915 \text{ cm} \\ d &= 3.499 \text{ cm} \end{aligned}$$

Because of the varying beam-hole size, the wake for the actual structure is estimated to be about 5% larger than the wake computed using the average cell.

There will also be a small error due to the fact that in the real structure the disks are rounded, as opposed to right-angled as assumed in Fig. 2.2.2.1.

Both programs have been checked for agreement with the analytic modes for a pillbox cavity in the limit of vanishing beam aperture. In addition, TRANS gives agreement with the measured frequency and  $k$  for the lowest frequency deflection mode in the SLAC structure. TRANS also gives the same result (Brillouin diagram, stored energy per period) for an RF-separator structure analyzed previously by Hereward and Bell.<sup>10</sup>

If an accurate knowledge of the wake is required down to times on the order of  $\tau_0$ , then modes to frequencies on the order of  $\omega_0 \simeq 1/\tau_0$  must be known. The bunch length for the Collider will be on the order  $\sigma_z \simeq 1$  mm, or  $\sigma_t \simeq 3$  ps. The wake should be accurate to at least  $\tau_0 \simeq 0.1$   $\sigma_t \simeq 0.3$  ps. Thus modes with angular frequencies up to about  $3 \times 10^{12}$  ought to be computed. Because the density of modes increases in proportion to frequency, there is a practical limit on the frequency that can be reached with reasonable computation time. As an example, 450 modes have been computed for the SLAC structure for  $m = 1$ , up to a maximum frequency  $\omega_0 = 4.8 \times 10^{11}$ . Since this is considerably lower than the desired frequency of about  $3 \times 10^{12}$ , there appears to be a problem. Fortunately, the situation is saved by the fact that at higher frequencies the statistical properties of the modes follow simple scaling laws. For example, by summing the  $k_n$ 's within bins of equal width in frequency and making a log-log plot of the result as a function of frequency, it is found that

$$\Delta k = \frac{A_m}{\omega^{3/2}} \Delta \omega \quad . \quad (8)$$

This result is in fact, predicted analytically by the optical resonator model<sup>11</sup> of a disk-loaded structure. Using this frequency variation for  $dk/d\omega$ , analytic expressions can be found for the wake due to frequencies greater than  $\omega_0$ . For the case  $m = 0$ , we obtain

$$w_0(\tau) = \frac{4A_0}{\omega_0^{1/2}} \left\{ \cos x - \sqrt{\pi x/2} \left[ 1 - 2S \left( \sqrt{2x/\pi} \right) \right] \right\} \quad , \quad (9)$$

where  $x = \omega_0\tau$  and  $S$  is the Fresnel integral. A similar expression is obtained for  $m = 1$ :

$$\frac{w_1(\tau)}{\left(\frac{re}{a}\right)} = \frac{4A_1c}{a\omega_0^{3/2}} \left\{ \frac{x}{3} \left[ 2\cos x + \frac{\sin x}{x} - \sqrt{2\pi x} \left( 1 - 2S\left(\sqrt{2x/\pi}\right) \right) \right] \right\} . \quad (10)$$

The constants  $A_0$  and  $A_1$  are found by fitting a line with slope  $-3/2$  on a log-log plot to the binned mode results versus frequency. The total wake is then obtained by adding the analytic extension, as given by Eqs. (9) and (10), to the computation of discrete mode up to  $\omega_0$ . It is found that the total wake using 50 modes plus analytic extensions agrees well with the total wake using 450 modes plus analytic extension. The relative contribution of the analytic extension is, of course, much larger in the 50-mode case.

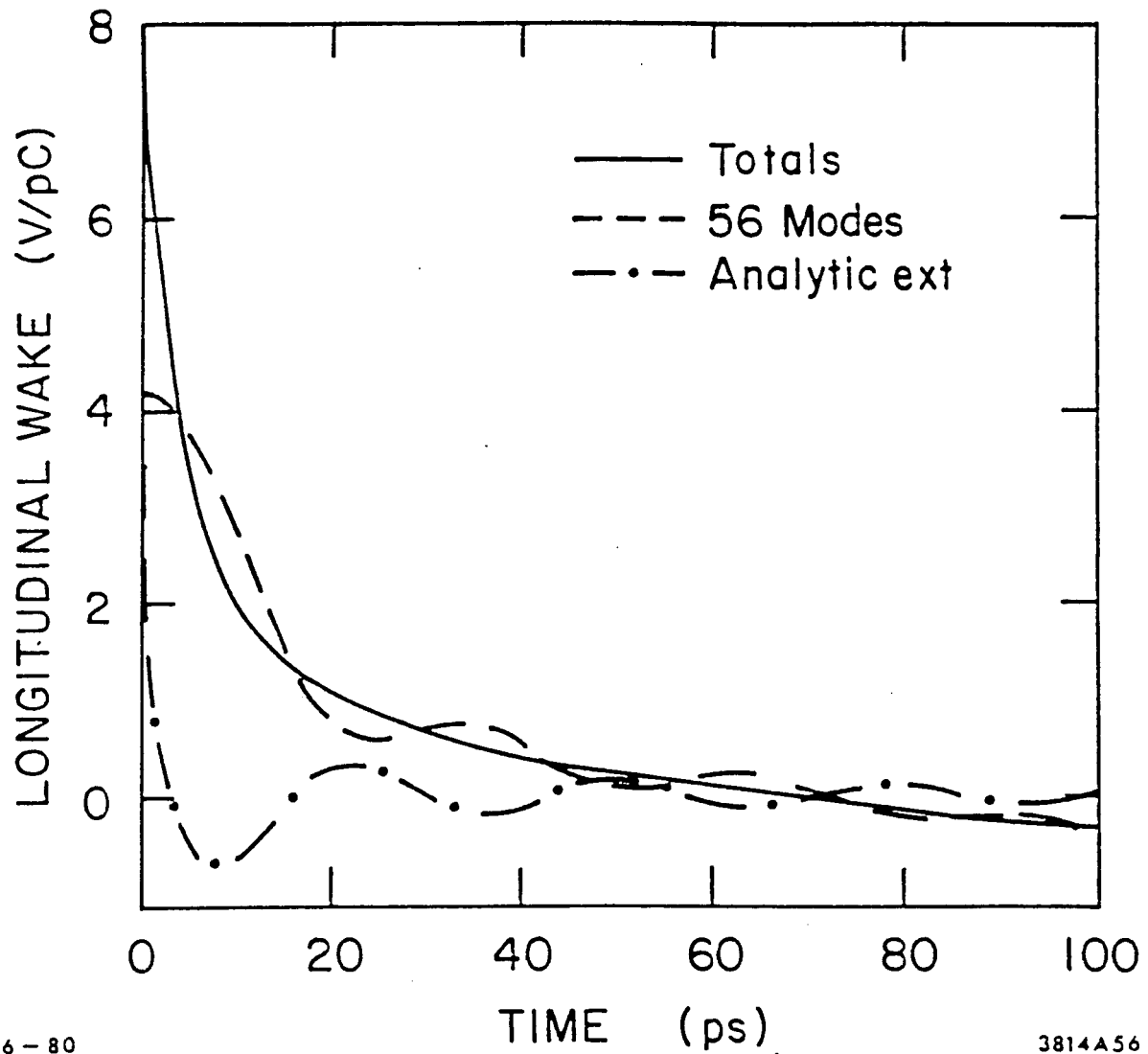
Figure 2.2.2.2 shows how, for the  $m = 0$  case, the wake from the analytic extension adds to the wake from discrete modes to give the total wake for the SLAC structure. Note that the slope of the analytic extension, and hence the slope of the total wake, becomes infinite as  $\tau \rightarrow 0$ . The intercept, however, is finite and from Eq. (5) is equal to twice the average loss per particle, per period, per picocoulomb of total charge. The validity of this wake for the SLAC linac has been checked experimentally in single-bunch beam-loading experiments.<sup>12</sup> The model predicts, first of all, the average energy loss per particle:

$$\Delta U = \text{eq} \left[ \sum_{n=1}^N k_n e^{-\omega_n^2 \sigma_t^2} + \int_{\omega_0}^{\infty} \frac{A_0 e^{-\omega^2 \sigma_t^2}}{\omega^{3/2}} d\omega \right] \quad (11)$$

where  $\sigma_t$  is the bunch length. For  $10^9$  electrons, the measured<sup>12</sup> average energy loss per electron for the total length of the SLAC structure ( $\simeq 81500$  cells) was 50 MeV. The loss computed from Eq. (1) is 40 MeV, which is about 20% lower. A more detailed test of the wake function is obtained by examining the shapes of the single-bunch energy spectra. In Ref. 12 the measured and computed spectra are plotted for three phase angles of the bunch center with respect to the crest of the accelerating wave and for four values of bunch charge. Very good agreement is obtained between the calculated and measured shapes. Again, the computed values give lower total energy widths for the spectra as compared to

Figure 2.2.2.2

Contributions from the analytic extension and wake from discrete modes to the total longitudinal wake per cm for the SLAC linac structure.



6-80

3814A56

the measured widths. The computed widths are lower by about 25%. Since the length of the bunch used in these experiments was three times shorter than the Collider design length ( $\sigma_z = 1$  mm) we expect that this discrepancy will be less when the experiment is repeated with a Collider-type bunch.

Figures 2.2.2.3 and 2.2.2.4 show the total SLAC wake per cell for dipole ( $m = 1$ ) modes for  $\tau = 0 - 10$  ps and  $\tau = 0 - 100$  ps. An important parameter for the dipole case is the slope of the wake as  $\tau$  approaches zero. From Eq. (10), we see that this slope is finite, even taking into account modes to infinite frequency. From Fig. 2.2.2.3 the slope for small  $\tau$  is about 0.33 V per pico-second, per picocoulomb per cell.

### 2.2.3 Longitudinal Wake-Field Effects and Control Measures

The effect of the longitudinal wake is to increase the energy spread of the beam by decelerating particles at the tail of the bunch. The control measure we have adopted is to place the bunch ahead of the crest of the accelerating RF wave in order to achieve a partial compensation of this effect of the wake-field.

There is an analytic expression which closely approximates the longitudinal wake-field calculated in Section 2.2.2. Let  $z$  be the distance between an electron that generates the wake and the point at which the wake is measured. Then:

$$W(z) = -0.115 e^{-\sqrt{z/1.62}} \text{ volts} \quad . \quad (12)$$

In this expression  $z$  is measured in millimeters. The minus sign signifies deceleration. This expression is a good approximation for the wake field only over the range of  $z$  from 0 to 10 mm. In Fig. 2.2.3.1 we have shown the convolution of the total wake given in expression (1) with a gaussian bunch with a rms length of 1 mm. The bunch contains  $5 \times 10^{10}$  electrons. The maximum energy loss caused by wakefield deceleration in this bunch takes place at a point 1 mm behind the bunch centroid. The loss in energy at this point is 2.2 GeV.

The complete wake approximated in (12) is made up of the contributions of many modes in the RF structure. It is useful to give a separate (and exact) expression for the lowest frequency mode. This is the mode which is also excited

Figure 2.2.2.3

Dipole wake per cell for the SLAC linac structure for  $\tau = 0$  to  $\tau = 100$  ps.

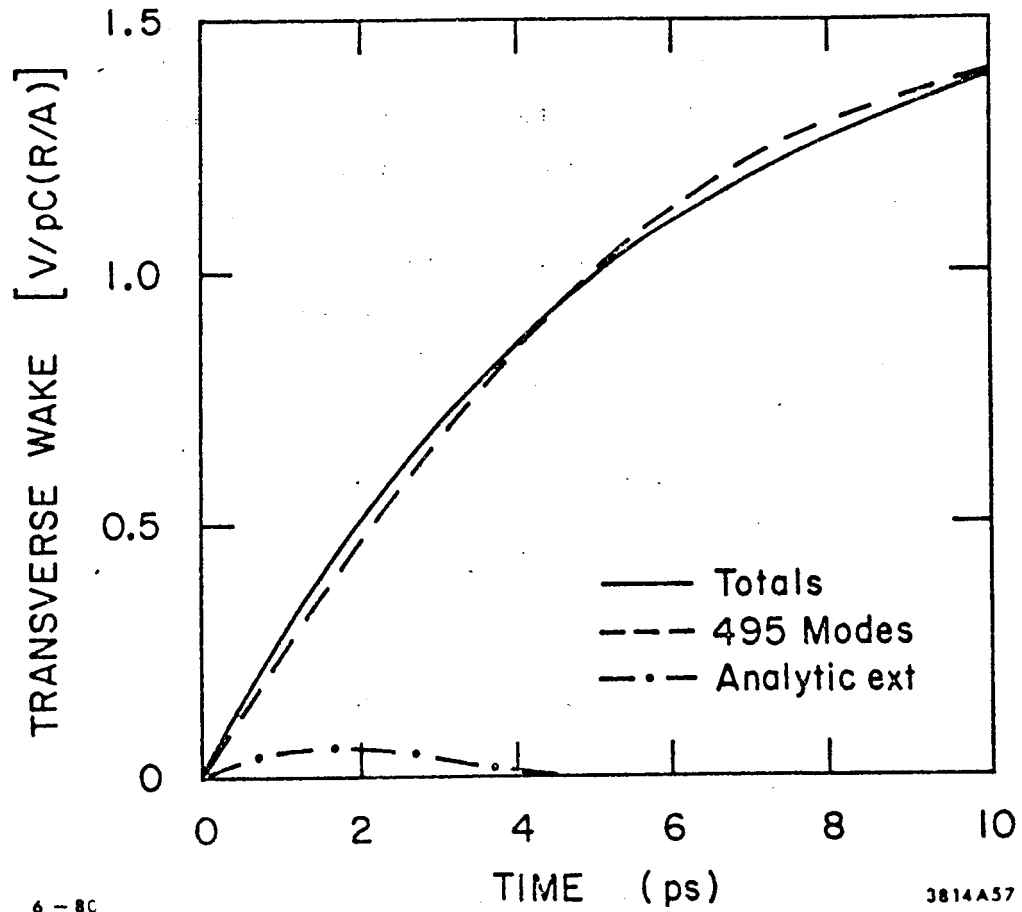
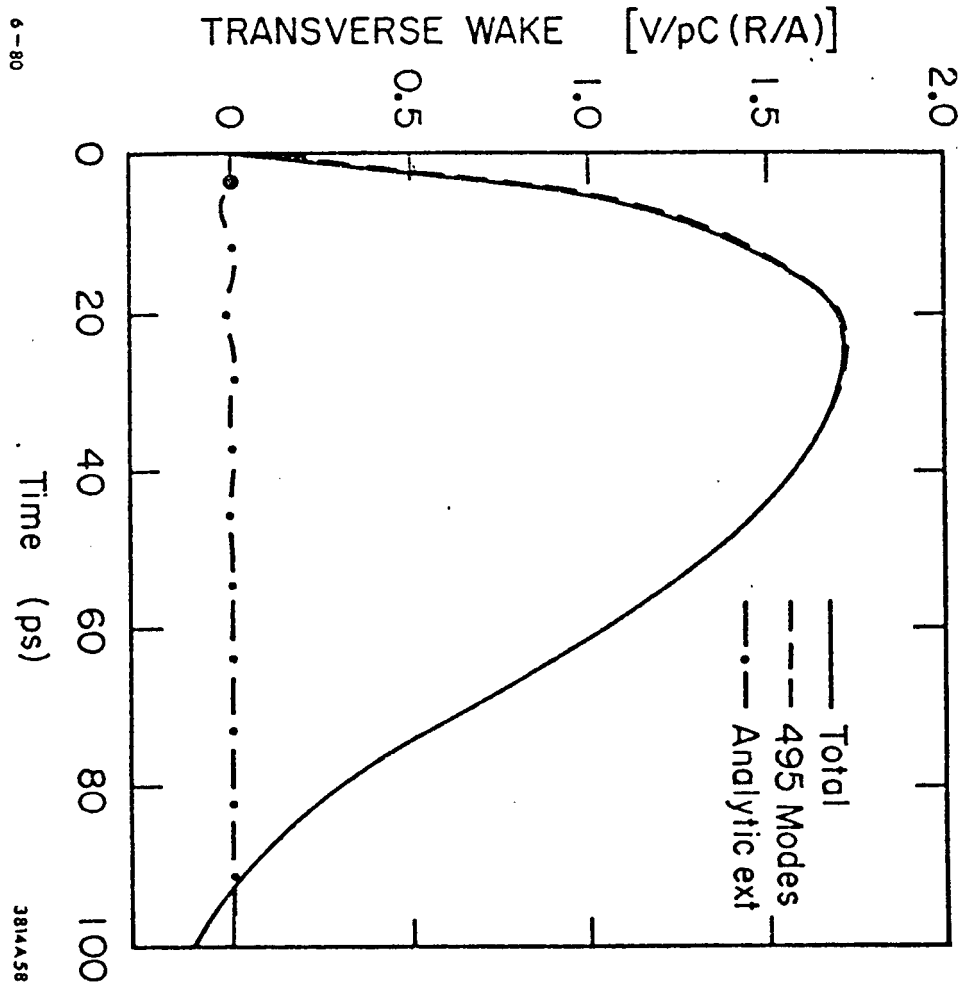


Figure 2.2.2.4

Dipole wake per cent for the SLAC linac structure for  $\tau = 0$  to  $\tau = 100$  ps.



by the external RF power sources.

$$W(z) = -0.0177 \cos(0.0598z) \text{ volts} \quad . \quad (13)$$

The total field which acts on an electron in the linac is the linear sum of the wake-field that has been stored in the RF structure before the bunch enters. The energy gain from this latter field is:

$$E(z) = E_0 \cos(0.0598 z + \delta) \text{ volts} \quad . \quad (14)$$

The greatest energy can be extracted from the stored energy in the RF structure if the phase  $\delta$  between the stored field and the bunch centroid is chosen to be such that the fundamental part of the wake field given by the convolution of (13) with the bunch distribution interferes destructively with the stored field. Unfortunately, the energy spread within the bunch would be too large if this choice of phase were made. In order to make a partial compensation for the wake-field induced energy spread, the phase of the stored field is chosen such that the centroid of the bunch is located 3.5 mm ahead of the crest of the stored field. To accelerate the centroid of the bunch to 50 GeV, the parameter  $E_0$  in (14) must be 52.73 GeV. For this choice of parameters the energy distribution of the particles within the bunch is shown in Fig. 2.2.3.2.

A typical energy distribution  $dN/dE$  of electrons in a bunch is shown in Figure 2.2.3.3. The energy gain of a single electron passing through the linac would be 50 GeV for the case shown in the figure. The mean energy of the bunch shown in the figure is 2.4 GeV lower than 50 GeV because of the compensation described earlier. Much smaller energy spreads  $\Delta E$  are possible at some expense in the number of electrons within the range  $\Delta E$ . Figure 2.2.3.4 shows that 80% of the particles in the bunch can be held within  $\pm 0.15\%$  of SLC operation when a very narrow energy spread is desired. There is some energy penalty in operation with small energy spread. The difference in mean energy of the bunch in the two cases described above is 1 GeV. The above figures were taken from CN-110.

It is interesting to note that of the 12 500 J stored in the fundamental

**Figure 2.2.3.1**

The longitudinal wake for the design intensity of  $5 \times 10^{10}$  particles/bunch and the design bunch shape, a gaussian with  $\tau = 1.0$  mm. The current in the bunch is 950 amperes.

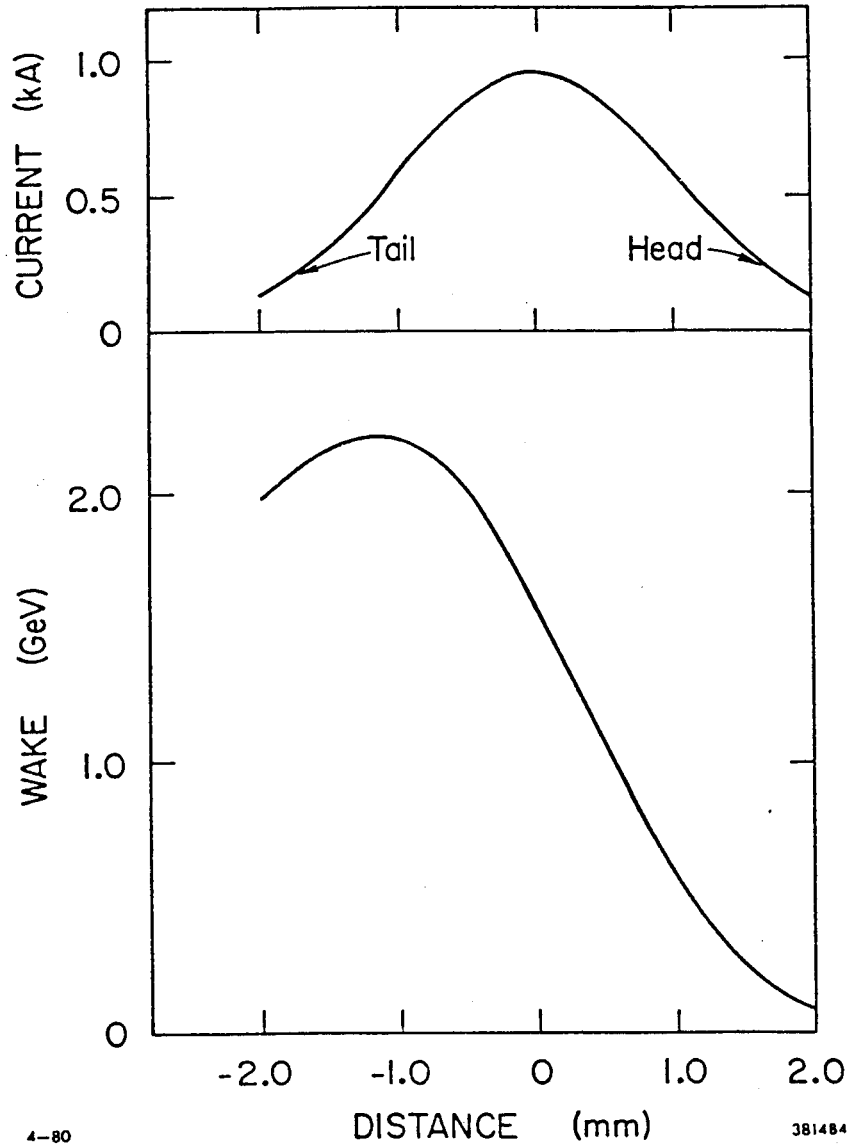
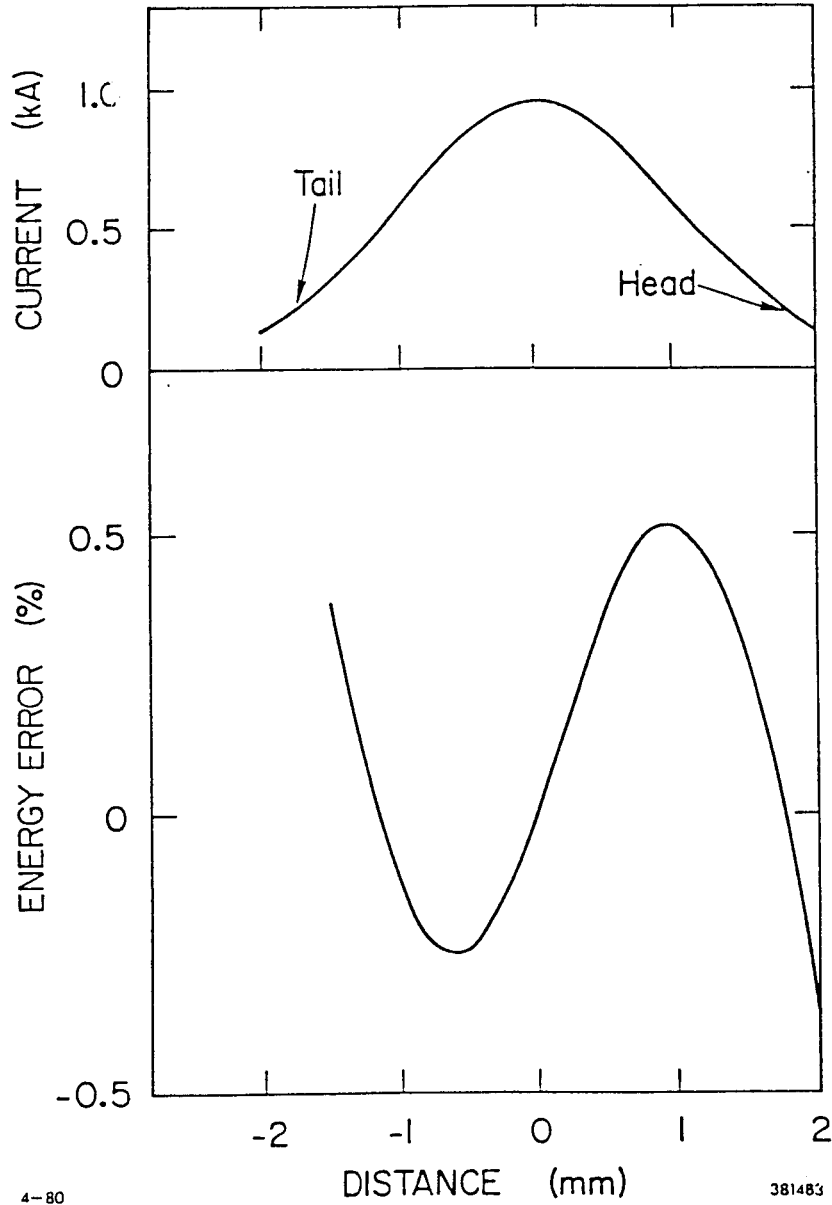


**Figure 2.2.3.2**

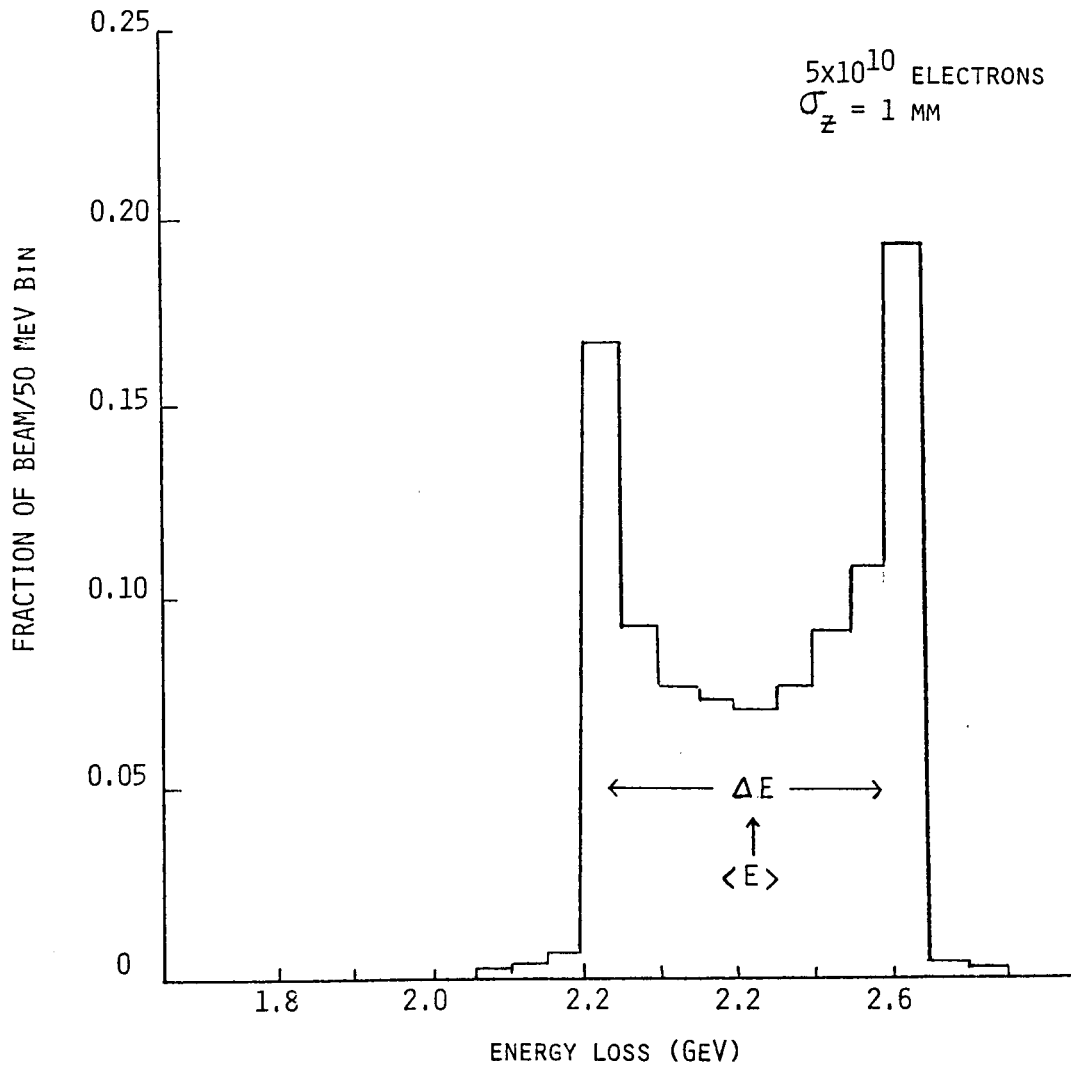
The fractional energy error as a function of position within the bunch after partial compensation has been made by placing the bunch-center 3.5 mm ahead of the crest of the RF wave.



4-80

381483

Figure 2.2.3.3 Typical Energy Distribution



RF mode in the linac structure, 415 J have been converted into bunch kinetic energy, and 7.8 J have been left behind in the structure in the form of higher order modes.

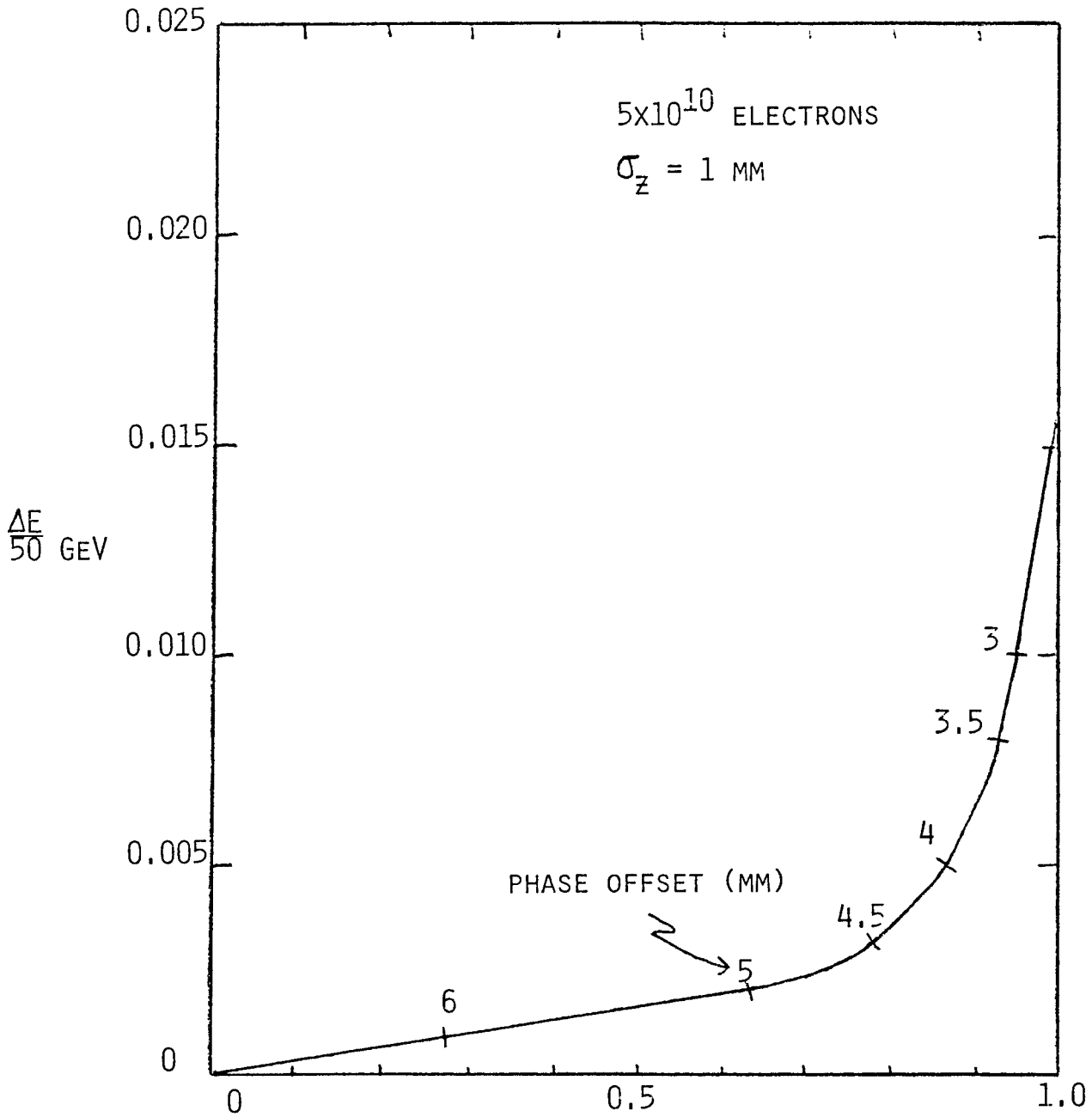
If we wished to accelerate more charge in a bunch of the same length and if we wished to maintain the same limit on energy spread it would be necessary to add compensating sections to the linac which operate at higher frequency than the 2856 MHz fundamental. This option is not considered to be practical at the present time.

The electron and positron bunches leaving the high energy end of the linac will not necessarily have the same energy. There are three contributions to the energy difference and one control measure which can be employed. The first bunch leaves behind a 2856 MHz wake-field which retards the second bunch. For  $5 \times 10^{10}$  positrons the wake is 890 MeV. This wake is independent of the energy to which the positrons are accelerated and is proportional to the number of positrons in the bunch. It is independent of bunch shape for the range of practical possibilities. The higher order mode compensation causes a reduction in mean energy. If the bunches differ in shape or number of particles the compensation is different. If one bunch contains  $5 \times 10^{10}$  particles and the other contains  $1 \times 10^{10}$ , the difference in compensation causes an energy difference of 1.113 GeV. The intense bunch is lower in energy. The shape of the RF pulse from the klystrons/sled system will cause a difference in energy. This can be estimated for the SLED-II case from the figure shown earlier.

A control measure which may be employed is to time the RF pulses from the klystrons so that the accelerating waveguide is not full when the first bunch passes through the linac. This measure is adequate to compensate for all of the effects given above. The penalty for using this control measure is that it reduces the center of mass energy at the collision point.

#### **2.2.4 Transverse Wake Field Effects**

When a point charge travels off-axis down a linac structure it interacts with the walls of the structure and leaves behind a transverse wake-field which will deflect particles traveling behind the point charge. If an intense bunch of parti-

Figure 2.2.3.4 Fraction of Beam within  $\Delta E$ 

cles travels through a structure whose transverse dimensions are large compared to the length of the bunch, the transverse wake-field will be such that all particles behind the head of the bunch are deflected further away from the axis of the structure. Thus, as the bunch travels along the linac, the projected area in transverse phase space will increase.

To estimate the magnitude of these effects we shall first derive the equation of motion for particles in the bunch and then solve this equation by a perturbation method. The results of this analysis will then be applied to the SLAC linac for bunches of  $5 \times 10^{10}$  electrons.

### Equation of Motion

In what follows, we treat the bunch as if its transverse dimensions were zero. We calculate the displacement of a particle in the bunch,  $x(z, s)$ , as a function of  $z$ , the longitudinal position relative to the center of the bunch.  $z$  is positive toward the head of the bunch, and  $s$  is the distance from the beginning of the linac. The approximation of zero transverse dimensions for the bunch is a good one for the Collider, since the transverse dimension of the bunch is very much less than the diameter of the linac irises. Thus, the transverse wake-field is uniform across the bunch. In effect,  $x(z, s)$  is the displacement of the center of a slice through the bunch at the position  $z$ . The transverse force at  $z$  depends on the displacement of all charges with  $z' > z$  and is given by

$$F_x(z, s) = e^2 \int_z^\infty dz' \rho(z') W(z' - z) x(z', s) \quad (15)$$

where  $\rho$  is the line density of particles in the bunch ( $\int \rho dz$  is normalized to the total number of particles in the bunch), and  $e \cdot W \cdot x$  is the transverse field produced by a point charge displaced from the axis by  $x$  at a distance  $z' - z$  behind the point charge. All of the properties of the linac structure are contained in  $W$ . We have assumed that the displacement of a particle changes sufficiently slowly with  $s$  so that the average  $W$  of the structure can be used. We also assume that the bunch length is much shorter than the betatron wavelength so

that the retardation in the transverse field from the head to the tail of the bunch can be ignored.

The equation of motion for  $x(z, s)$  can be written as

$$\frac{d}{ds} \left\{ \gamma(s) \frac{d}{ds} x(z, s) \right\} + \left( \frac{2\pi}{\lambda(s)} \right)^2 \gamma(s) x(z, s) = r_0 \int_z^{\infty} dz' \rho(z') W(z' - z) x(z', s) \quad (16)$$

where  $\gamma(s)$  is the energy of the beam at position  $s$  in units of  $mc^2$ ,  $m$  being the rest mass of the particle,  $\lambda(s)$  is the instantaneous wavelength of betatron focusing at position  $s$ , and  $r_0 = e^2/mc^2$  is the classical radius of the particle. We have assumed that the betatron focusing is provided by a smooth function rather than coming from a series of discrete quadrupoles.

We assume that the energy of the beam increases linearly with  $s$  as a result of acceleration in such a way that  $\gamma(s) = \gamma_0 (1 + Gs)$  with  $\gamma_0 mc^2$  the beam energy at injection and  $G$  the acceleration gradient. We assume that the strength of the focusing force in the linac scales with beam energy so that the instantaneous betatron wavelength remains constant  $\lambda(s) = \lambda_0$ .

We first make a change of variable in the equation of motion (16) from  $s$  to a new variable  $u = 1 + Gs$ . Eq. (16) then becomes

$$\frac{d^2 x}{du^2} + \frac{1}{u} \frac{dx}{du} + \left( \frac{k_0}{G} \right)^2 x = \frac{r_0}{\gamma_0 G^2 u} \int_z^{\infty} dz' \rho(z') W(z' - z) x(z', u) \quad , \quad (17)$$

where we have defined  $k_0 = 2\pi/\lambda_0$ . This equation will be solved by an iteration procedure. The solution  $x(z, s)$  is expanded in a series of powers in terms of the wake field

$$x(z, s) = \sum_{n=0}^{\infty} x^{(n)}(z, s) \quad . \quad (18)$$

The 0th order solution  $x^{(0)}$  is first obtained by setting the wake-field  $W$  equal to 0 in Eq. (17) and demanding the initial conditions  $x(z, u) = x_0$  and  $dx(z, u)/du =$

0 at  $s = 0$  or  $u = 1$ . The  $n$ th order term  $x^{(n)}$  is then obtained from the  $(n-1)$ th order term  $x^{(n-1)}$  by solving Eq. (17) with the  $x$ 's on the left-hand side replaced by  $x^{(n)}$  and the  $x$  on the right-hand side replaced by  $x^{(n-1)}$ . The solution can be obtained using a Green's function.

$$x^{(n)}(z, u) = \int_1^u du' G(u, u') \frac{r_0}{\gamma_0 G^2 u'} \int_z^\infty dz' \rho(z') W(z' - z) x^{(n-1)}(z', u') \quad (19)$$

with  $G(u, u')$  the Green's function. For the Collider, the betatron oscillation wavelength is much shorter than the distance required to double the energy i.e.,  $k_0 \gg G$ . The acceleration is then adiabatic, and we have

$$x^{(0)}(z, s) \simeq \frac{x_0}{\sqrt{u}} \cos \left[ \frac{k_0}{G} (u - 1) \right] = \frac{x_0}{\sqrt{1 + Gs}} \cos k_0 s \quad , \quad (20)$$

and

$$G(u, u') \simeq \frac{G}{k_0} \sqrt{\frac{u'}{u}} \sin \left[ \frac{k_0}{G} (u - u') \right] \quad . \quad (21)$$

The factor  $\sqrt{1 + Gs}$  in Eq. (20) is the usual adiabatic damping factor.

Substituting Eqs. (20) and (21) into Eq. (19), we find that the terms in the series solution (18) are

$$x^{(n)}(z, s) = \frac{x_0}{\sqrt{1 + Gs}} \left( \frac{r_0}{\gamma_0 k_0} \right)^n I_n(s) R_n(z) \quad , \quad (22)$$

where we have defined

$$R_n(z) = \int_z^\infty dz_1 \rho(z_1) W(z_1 - z) \int_{z_1}^\infty dz_2 \rho(z_2) W(z_2 - z_1) \dots \int_{z_{n-1}}^\infty dz_n \rho(z_n) W(z_n - z_{n-1}) \quad , \quad (23)$$

and

$$I_n(s) \simeq \frac{1}{n!} e^{ik_0 s} \left[ \frac{1}{2iG} \ln(1 + Gs) \right]^n \quad . \quad (24)$$

In the derivation, we have assumed that the beam energy at the end of acceleration is much higher than the beam energy at injection, and taking the real part is understood in Eq. (24).

A closed form can be obtained for  $R_n$  if we approximate  $\rho$  by a rectangular distribution and  $W$  by a linear function, i.e.,

$$\rho = \begin{cases} N/\ell & \text{for } |z| < \ell/2 \\ 0 & \text{for } |z| \geq \ell/2 \end{cases} \quad (25)$$

$$W = W_0 \frac{z}{\ell} . \quad (26)$$

Both approximations are close enough for the Collider to allow a good assessment to be made of the importance of higher order terms. We find

$$R_n(z) = \frac{1}{(2n)!} \left[ NW_0 \left( \frac{1}{2} - \frac{z}{\ell} \right)^2 \right]^n . \quad (27)$$

Knowing  $R_n(z)$  and  $I_n(s)$ , we can substitute Eq. (22) into Eq. (18) to obtain

$$x(z, L) = \frac{x_0}{\sqrt{1 + GL}} e^{ik_0 L} \sum_{n=0}^{\infty} \frac{1}{n!(2n)!} \left( \frac{\eta}{2i} \right)^n , \quad (28)$$

where we have evaluated  $x$  at the end of linac  $s = L$  and have defined

$$\eta = \frac{Lr_0NW_0}{k_0(\gamma_f - \gamma_0)} \ell n \frac{\gamma_f}{\gamma_0} \cdot \left( \frac{1}{2} - \frac{z}{\ell} \right)^2 . \quad (29)$$

There is no closed form for Eq. (28), but one can find an asymptotic expression in the strong-wake-field limit  $|\eta| \gg 1$ . This asymptotic expression is

$$x(z, L) \simeq \frac{x_0}{\sqrt{6\pi(1 + GL)}} |\eta|^{-1/6} \exp \left( \frac{3\sqrt{3}}{4} |\eta|^{-1/3} \right) \cos \left[ k_0 L - \frac{\eta}{|\eta|} \left( \frac{3}{4} |\eta|^{1/3} - \frac{\pi}{12} \right) \right] . \quad (30)$$

In Fig. 2.2.4.1, we have plotted  $x(z, L)$  across the bunch for values of  $k_0 L = 0, \pi/2, \pi$  and  $3\pi/2$  (Modulus  $2\pi$ ). The wake field strength is such that the value of  $\eta$  at the very tail of the bunch is equal to 150. The vertical scale is in units of  $\sqrt{\gamma_0/\gamma_f} x_0$ . It is clear from Fig. 2.2.4.1 that the distortion of the bunch can be very large.

### Misalignment Effects

In the previous analysis, we have assumed that the accelerator structure is perfectly aligned, and the wake-field is produced as a consequence of beam injection with a displacement error. In this section, we will study the effect caused by misalignment of the accelerator pipe. We assume the beam is injected into the linac with precision and it travels down the linac in a straight line in the limit of weak beam intensity. We will study the case with acceleration under the approximation that the acceleration is adiabatic. The equation of motion can be written as:

$$\frac{d^2 x}{du^2} + \frac{1}{u} \frac{dx}{du} + \left(\frac{k_0}{G}\right)^2 x = \frac{r_0}{\gamma_0 G^2 u} \int_z^\infty dz' \rho(z') W(z' - z) [x(z', u) - d(s)] \quad , \quad (31)$$

where  $d(s)$  is the transverse position error of the linac structure at position  $s$ . If there are  $N_c$  sections with the  $i$ th section misaligned by a distance  $d_i$ , one has

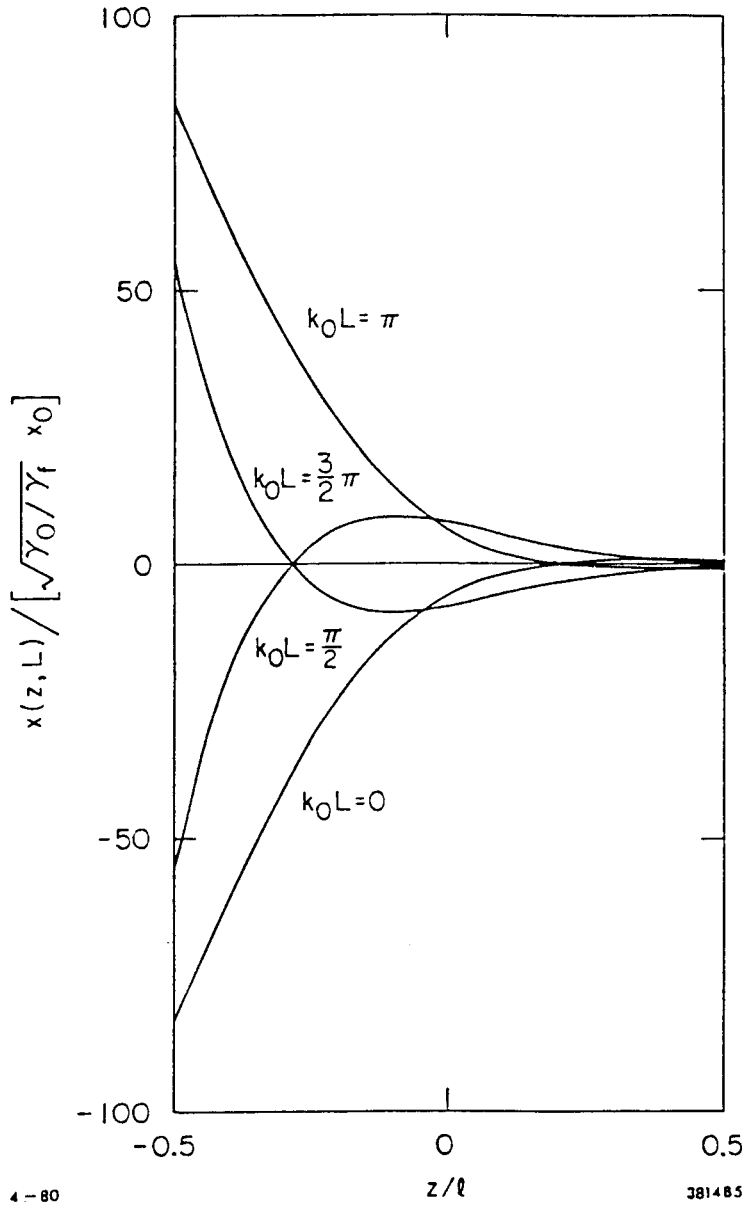
$$d(s) = \sum_{i=1}^{N_c} d_i l_i \delta(s - s_i) \quad ,$$

where  $l_i$  and  $s_i$  are the length and the position of the  $i$ th section respectively. Compared with Eq. (17), Eq. (31) contains an additional force term on the right-hand side that comes from the pipe misalignment.

The 0th order solution to Eq. (31) is  $x^{(0)} = 0$ , instead of Eq. (20) since the beam is assumed to be injected without error. The trajectory of the head of the bunch strictly follows  $x^{(0)}$  and is, therefore, a perfect straight line. The first-order perturbation term comes solely from the linac structure misalignment

**Figure 2.2.4.1**

The transverse bunch shape at the end of acceleration for four different values of total betatron phase:  $0, \pi/2, \pi,$  and  $3\pi/2$ . the wake-field strength parameter  $\eta = 150$  at the tail of the bunch.



$d_i$ :

$$x^{(1)}(z, s) = \sum_{\substack{i \\ (s > s_i)}} \frac{r_0 d_i \ell_i}{\gamma_0 k_0} \cdot \frac{1}{(1 + Gs)^{1/2} (1 + Gs_i)^{1/2}} \cdot \sin [k_0 (s - s_i)] \cdot R_1(z) \quad , \quad (32)$$

where the quantity  $R_n(z)$  has been defined in Eq. (23).

In order to apply this to the Collider, it is necessary to carry out the perturbation calculation up to the second order in the wake field. The second-order term can be obtained through the use of Eq. (19). Substituting Eq. (32) in Eq. (19) we find

$$x^{(2)}(z, s) = \sum_{\substack{i \\ (s > s_i)}} \frac{r_0^2 d_i \ell_i}{2\gamma_0^2 k_0^2 G} \cdot \frac{\ln[(1 + Gs)/(1 + Gs_i)]}{\ln[(1 + Gs)/(1 + Gs_i)]^{1/2}} \cdot \cos [k_0 (s - s_i)] \cdot R_2(z) \quad . \quad (33)$$

If we assume the misalignment errors  $d_i$  are uncorrelated from one linac section to the next, we can make an rms estimate to obtain

$$\begin{aligned} \langle x^{(1)2} \rangle &= \frac{1}{2N_c} \langle d^2 \rangle \left( \frac{r_0 L}{\gamma_f k_0} \right)^2 \ln \left( \frac{\gamma_f}{\gamma_0} \right) R_1^2(z) \quad , \\ \langle x^{(2)2} \rangle &= \frac{1}{24N_c} \langle d^2 \rangle \left( \frac{r_0 L}{\gamma_f k_0} \right)^4 \ln^3 \left( \frac{\gamma_f}{\gamma_0} \right) R_2^2(z) \quad , \end{aligned} \quad (34)$$

where  $\langle d^2 \rangle^{1/2}$  is the rms value of the misalignment and we have assumed that all linac sections have the same length  $\ell_i = L/N_c$ . We have also made the approximation that  $\gamma_f \gg \gamma_0$ .

If we assume a square distribution (25) and a linear wake-field (26), we can use Eq. (27) to obtain the quantities  $R_n(z)$ . The ratio of  $\langle x^{(2)2} \rangle$  to  $\langle x^{(1)2} \rangle$  under these assumptions is  $\eta^2/1728$ . The emittance growth due to misalignment can be substantially reduced by empirically controlling the injection offset  $x_0$  and  $x'_0$  at the beginning of the linac. The corresponding first and second order

contributions have been obtained in Eq. (22):

$$\begin{aligned}
 x^{(1)}(z, L) &= \frac{1}{\sqrt{1+GL}} \left( \frac{r_0}{\gamma_0 k_0} \right) R_1(z) \frac{\ell n(1+GL)}{2G} \left( x_0 \sin k_0 L - \frac{x'_0}{k_0} \cos k_0 L \right) \\
 x^{(2)}(z, L) &= \frac{-1}{\sqrt{1+GL}} \left( \frac{r_0}{\gamma_0 k_0} \right)^2 R_2(z) \frac{\ell n^2(1+GL)}{8G^2} \left( x_0 \cos k_0 L + \frac{x'_0}{k_0} \sin k_0 L \right).
 \end{aligned} \tag{35}$$

By choosing proper values of  $x_0$  and  $x'_0$ , it is possible to cancel either the first-order misalignment contribution, Eq. (32), or the second-order misalignment contribution, Eq. (33), by a corresponding contribution from (35). For example if the second-order misalignment term dominates, one might choose

$$\begin{pmatrix} x_0 \\ x'_0 \end{pmatrix} = \frac{4G}{\ell n^2(1+GL)} \sum_i d_i \ell_i \frac{\ell n [(1+GL)/(1+Gs_i)]}{(1+Gs_i)^{1/2}} \begin{pmatrix} \cos k_0 s_i \\ k_0 \sin k_0 s_i \end{pmatrix}, \tag{36}$$

so that the second-order contribution from the injection offset and angle cancels the second-order contribution from the misalignments. The required  $x_0$  and  $x'_0$  have rms values given by

$$\langle x_0^2 \rangle = \frac{8}{3N_c} \frac{\gamma_f/\gamma_0}{\ell n(\gamma_f/\gamma_0)} \langle d^2 \rangle = \frac{1}{k_0^2} \langle x'^2_0 \rangle. \tag{37}$$

With  $x_0$  and  $x'_0$  given by Eq. (36), the first-order term obtained by the sum of misalignment and injection contributions is

$$\begin{aligned}
 x^{(1)} &= \frac{1}{\sqrt{1+GL}} \left( \frac{r_0}{\gamma_0 k_0} \right) R_1(z) \sum_i \frac{d_i \ell_i}{\sqrt{1+Gs_i}} \\
 &\quad \left[ 1 - 2 \frac{\ell n(1+GL)}{\ell n(1+Gs_i)} \right] \sin [k_0(L-s_i)].
 \end{aligned} \tag{38}$$

The rms value of this  $x^{(1)}$  is given by

$$\langle x^{(1)2} \rangle = \frac{1}{6N_c} \langle d^2 \rangle \left( \frac{r_0 L}{\gamma_f k_0} \right)^2 \ell n \left( \frac{\gamma_f}{\gamma_0} \right) \cdot R_1^2(z), \tag{39}$$

which is  $1/3$  of that for the case with no injection cancellation effort. Thus this scheme of minimizing the emittance growth due to misalignment by controlling the injection conditions not only cancels the second-order misalignment contribution but also significantly reduces the first-order contribution.

## 2.3 UPGRADED BEAM GUIDANCE SYSTEM

### 2.3.1 Introduction

The design value of the beam emittance at the end of the SLAC linac is  $3 \times 10^{-10}$  radian-meters at 50 GeV or 1.5 (keV/c) cm. If there were no risk of emittance growth from the damping ring-compressor through the end of the linac, the present linac focusing system would probably be adequate. The present system consists of dc singlets every 12.5 m from Sectors 1 through 6, pulsed singlets every 12.5 m from Sectors 7 through 10, and pulsed doublets (28 m spacing) every 100 m from Sectors 11 through 30. The betatron wavelength is about 130 m in the first ten sectors and 400 m beyond that point. This focusing system was designed to allow multiple interlaced beam operation up to 30 GeV (SLED I) and to control multibunch beam breakup for pulses up to 200 mA and 200 nsec. Successful operation at these levels has now been verified experimentally.

The focusing system for the SLC has to be strengthened considerably above these levels because the beta-function must be minimized in order to control single-bunch beam breakup caused by the excitation of transversely deflecting wake-fields when the bunches wander off-axis. Stronger focusing is planned, as well as steering and position detection at each quadrupole, in order to control the effects of all transversely acting fields. These include (a) the wake-field produced by the bunches themselves, (b) the stray dc fields produced by quadrupole misalignments which deflect the electrons and positrons in opposite directions, and (c) the RF fields from accelerator misalignments and coupler effects which deflect the electrons and positrons in the same direction.

### 2.3.2 The Linac Lattice

The main consideration that influenced our choice of linac lattice has been the need to minimize the beta function in order to reduce the disruption caused by transverse wake-fields. Another important consideration has been that the trajectories of simultaneous beams of electrons and positrons passing through the lattice must be well-centered on the linac axis to suppress the generation of transverse wake-fields.

The lattice we have adopted is a  $90^\circ$  per-cell FODO array with a quadrupole placed at the end of each 12.3-m linac girder. Each sector will contain eight quadrupoles, leading off with a horizontally focusing (for electrons) element and ending with a defocusing magnet. A 3-m long drift section at the end of the linac sectors has necessitated the rematching of the beam at the beginning of each subsequent sector. The refitting is accomplished by increasing the strengths of the first four quadrupoles of a sector by about 13% from their nominal FODO array values. Figure 2.3.2.1 illustrates the horizontal and vertical beta functions in two adjacent sectors for the  $90^\circ$  lattice. The maximum in  $\beta$  occurs in the matching region and is 50% larger than the value for a regular FODO array. Table 2.3.2.1 lists the required element strengths and beta functions values in a standard linac sector.

A nominal phase advance of  $90^\circ$  per cell is maintained through Sector 13 to a beam energy of 22.4 GeV by scaling the quadrupole strengths appropriately with beam energy. A power limitation of the quadrupoles requires that the maximum focusing fields are kept below 9.7 Tesla in the remainder of the linac. The phase advance per cell thus tapers between Sectors 13 and 30, down from the  $90^\circ$  to  $43^\circ$  at a beam energy of 50 GeV.

**Figure 2.3.2.1**

Linac  $\beta$  functions for two adjacent sectors in the  $90^\circ$  per cell phase shift region. The  $n$ th sector begins at  $Z = 0.0$  m; the  $n + 1$  sector begins at  $z = 101.6$  m.

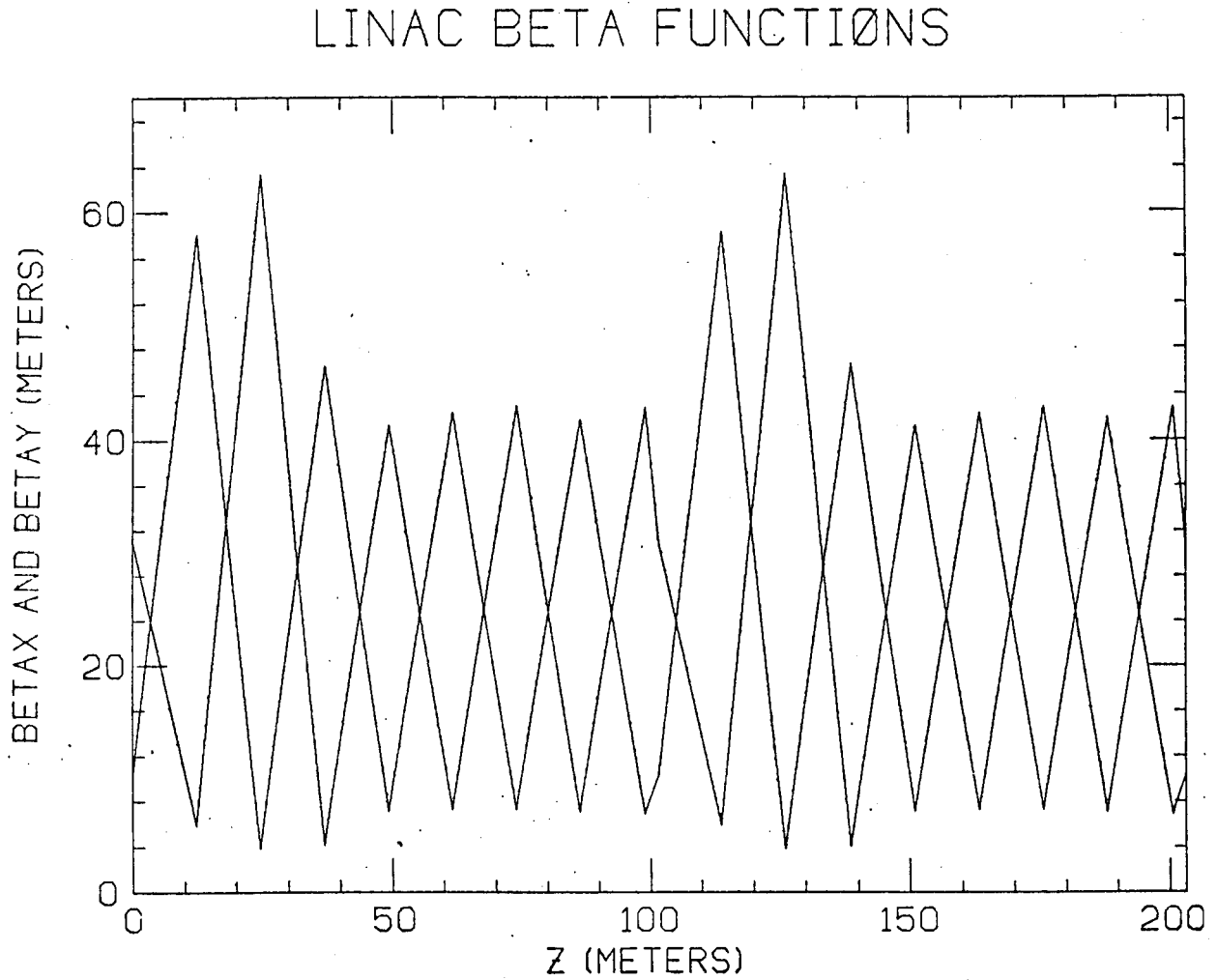


Figure 2.3.2.2

The measured integrated field strength for a prototype QD strong quadrupole.

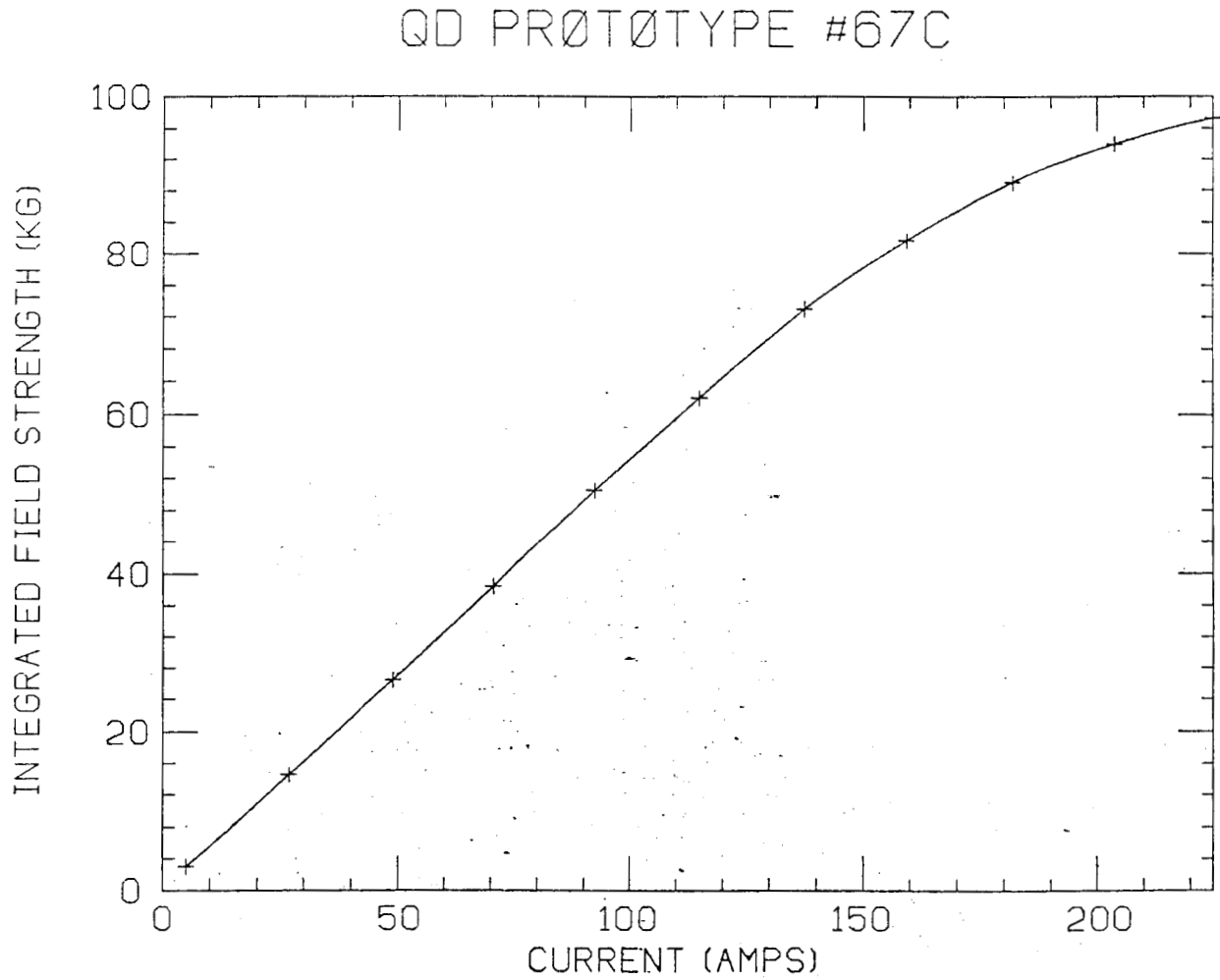


Table 2.3.2.1 Linac Lattice Parameters				
Location	Distance from Beginning of Sector	Quadrupole Strength (kg/GeV)	$\beta_x$ (m)	$\beta_y$ (m)
Entrance	0.00		10.52	30.40
Q21F	12.34	+4.02	59.28	5.95
Q31D	24.60	-4.33	3.87	63.33
Q41F	36.95	+4.32	45.36	4.11
Q51D	49.30	-4.33	7.21	40.95
Q61F	61.64	+3.82	43.11	7.28
Q71D	73.99	-3.82	7.26	42.55
Q81F	86.33	+3.82	40.54	7.19
Q91D	98.99	-3.82	7.00	42.40
Exit	101.60		10.52	30.57

Four different types of quadrupoles are used to construct the focusing lattice. Table 2.3.2.2 lists the properties of these magnets. The QA quadrupoles are used in the first two linac sectors, type QCH magnets in the third and fourth sectors; type QC are used for Sectors 5 through 10, and the strongly focusing model, QD, are used throughout the remainder of the linac. Two prototypes of the strong QD quadrupole have been built and tested. Figure 2.3.2.2 shows the measured integrated field strength as a function of excitation current.

The quadrupoles in the first four linac sectors are driven by individual power supplies. For Sectors 5 through 28, a single "large power supply" (LGPS) is used to drive the quadrupoles of a given sector in series. In addition, each quadrupole on an LGPS string has an independently controlled current shunt, thereby affording individual adjustments to the magnets. Separate current supplies are required for the quadrupoles in Sectors 29 and 30 to provide matching for low

energy beams into the SPEAR transport line. Several other separate supplies are needed in the vicinity of the existing Sector 11 positron source to insure proper beam transport onto and away from the target.

Table 2.3.2.2 Linac dc Quadrupole Specifications				
	QA	QCH	QC	QD
Maximum Gradient				
Length Product (kG)	14.5	22.0	87.0	97.0
Effect Length (cm)	10.2	8.3	8.3	10.0
Aperture Radius (cm)	1.5	1.4	1.4	1.4
Maximum Current (Amps)	8	12	195	225
Cooling Mechanism	Air	Air	Water	Water

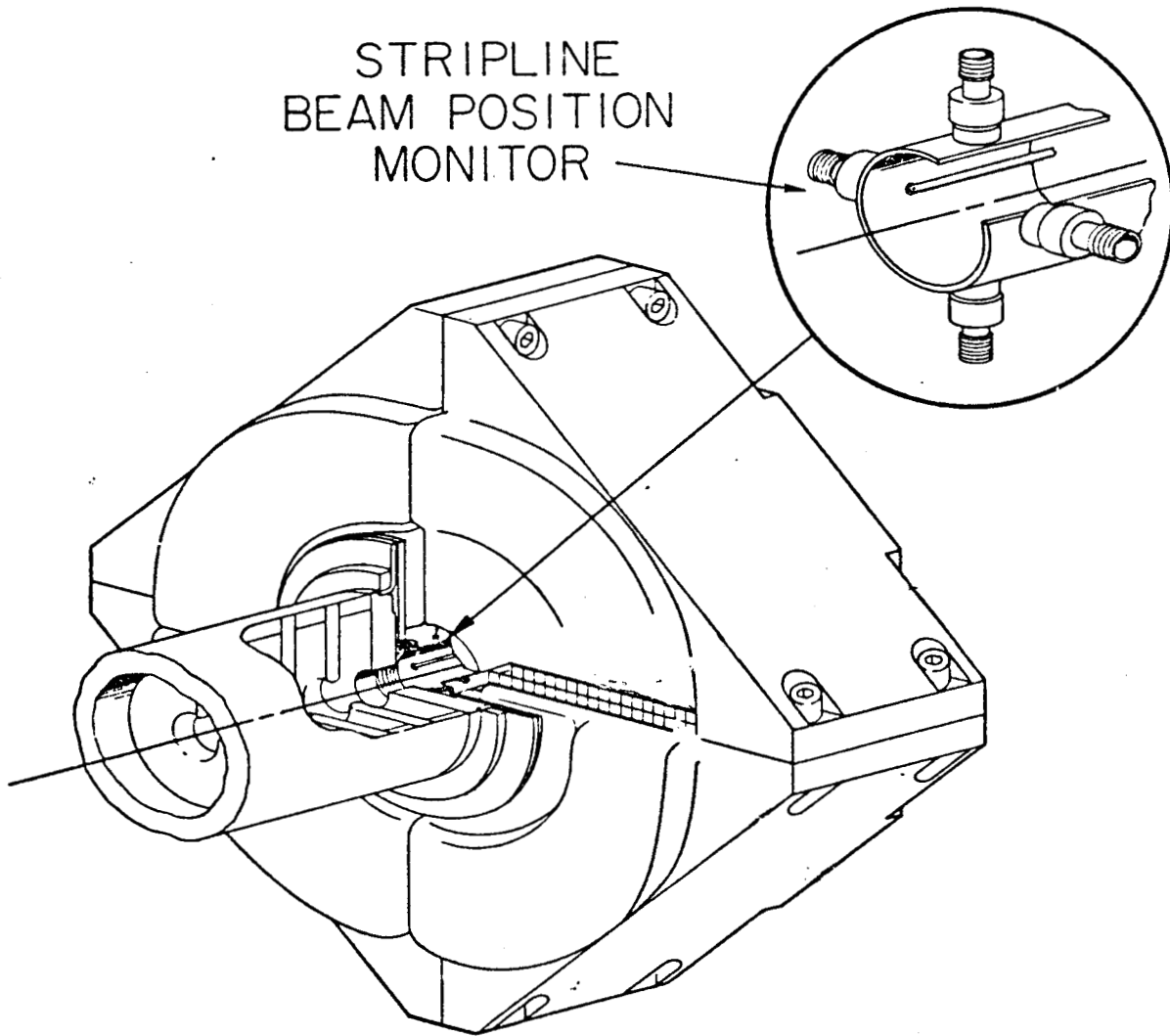
### 2.3.3 Control of Beam Center Line

Because of the severity of the effects of single bunch transverse wake-field on emittance growth, it is necessary to always keep beams in the linac steered to within  $100\ \mu\text{ms}$  of the iris center line. To accomplish this, a collection of beam position measuring devices and steering magnets have been incorporated into the linac design.

Within each quadrupole of the SLAC lattice will be a beam position monitor (a set of four strip lines) which is electrically gated so that the transverse position (in two dimensions) of the electron and the positron beams can be measured separately with a relative accuracy of  $25\ \mu\text{m}$ . The position monitors have been designed to be self-jigging to their host quadrupoles to insure proper alignment. Figure 2.3.3.1 illustrates the placement of a monitor inside its quadrupole. Alignment of the centers of the position monitors to the centerline of the quadrupoles is better than  $50\ \mu\text{ms}$ . Quadrupoles will be placed on the linac axis with an absolute rms tolerance of  $50\ \mu\text{ms}$ .

Associated with each quadrupole is a pair of horizontally and vertically bending dipole magnets for use in correcting the beam trajectory. Typically, these dipoles are placed around the RF accelerating sections, less than one meter

Figure 2.3.3.1 Linac dc Quadrupole Assembly



downstream of their neighboring quadrupoles. Three types of dipoles will be used, increasing in maximum bending strength down the length of the linac. The properties of the corrector magnets and their placement in the linac are listed in Table 2.3.3.1. The dipoles are individually controlled from bipolar current supplies.

There are two kinds of forces that cause trajectory errors: static fields (such as those caused by quadrupole misalignments) deflect positrons and electrons in opposite directions, while RF fields (such as those caused by a tilted linac girder or by waveguide end-couplers) deflect positrons and electrons in the same direction. We shall show that it is possible to simultaneously correct the trajectory distortions caused by both sources of error with the static dipole windings on the quadrupoles.

We have made a computer model of the linac lattice in order to study the trajectory-correction problem. We model the RF error deflections by giving the beam a single random kick at the center of each 12.5-m girder, the same point at which the accelerator has been introduced. The static error problem has been modeled by introducing a random displacement of each quadrupole and another random displacement of each position monitor.

We have chosen the following distributions for random errors for our study. Quadrupole displacements and beam-position-monitor errors have been uniformly distributed between  $-0.1$  and  $+0.1$  mm. The RF kicks are uniformly distributed between  $-3 \times 10^{-5}$  and  $+3 \times 10^{-5}$  GeV and are assumed to be centered in each 12.5-m girder. This distribution is consistent with measurements which have been made on the SLAC linac.

Our correction scheme is as follows. Let the correctors be specified by index  $j$  ( $j = 1, 2, \dots, N$ ) and the monitors by index  $i$  ( $i = 1, 2, \dots, M$ ). Let  $x_i^+$  and  $x_i^-$  be the measured positions of the  $e^+$  and  $e^-$  at the  $i$ th monitor before corrections are applied. If we turn on the  $j$ th corrector the orbit at the  $i$ th monitor will change by  $C_{ij}^+ \theta_j$  for the  $e^+$  beam and  $-C_{ij}^- \theta_j$  for the  $e^-$  beam.  $\pm \theta_j$  are the kicking angles for the  $e^+$  and  $e^-$  beams.  $C_{ij}^\pm$  are the response matrices determined by the linac lattice.  $C_{ij}^\pm$  will be zero if the  $j$ th corrector is downstream of  $i$ th monitor.

Table 2.3.3.1 Linac Corrector Dipole Specifications			
	SLC Type 2*		SLC Type 3**
	Long	Short	
Strength (Kg/Amp)	3.629	3.116	8.77
Maximum Current (Amps)	5.5	5.5	8.0
Physical Length (Meters)	0.438	0.381	0.200
Turns/coil	130	130	170
Installation	Sectors 2-5		Sectors 6-10
<p>*This is a nested pair of iron-free dipoles with orthogonal fields. The longer dipole deflects the beam in the horizontal direction as presently installed.</p> <p>**This is a dipole with an iron outer return path. Separate dipoles are used for horizontal and vertical correction.</p>			

We wish to find a solution ( $j = 1, 2, \dots, N$ ) which minimizes the rms value ( $S$ ) of the orbit after correction:

$$S = \sum_{i=1}^M \left( x_i^+ + \sum_{j=1}^N C_{ij}^+ \theta_j \right)^2 + \left( x_i^- - \sum_{j=1}^N C_{ij}^- C_{ij}^- \theta_j \right)^2 \quad (40)$$

If we group the constants  $C_{ij}^+$  and  $C_{ij}^-$  to form two  $M \times N$  matrices  $C^+$  and  $C^-$ , and group  $x_i^+$  and  $x_i^-$  to form two  $M$ -dimensional vectors  $\vec{x}^+$  and  $\vec{x}^-$ , the solution for  $\vec{\theta}$  which minimizes  $S$  is given by the following expression:

$$\vec{\theta} = - (\tilde{C}^+ C^+ + \tilde{C}^- C^-)^{-1} (\tilde{C}^+ \vec{x}^+ - \tilde{C}^- \vec{x}^-) \quad (41)$$

$\tilde{C}$  is the transpose of  $C$ . Thus a solution can be easily determined.

### 2.3.4 Computer Support

A set of online computer models have been developed to calculate the settings of lattice magnet strengths. These programs take various input parameters (such as injected beam phase space distribution, beam energy gain profile along the linac, and beam position monitor readings) to calculate the quadrupole strengths required for optical matching and efficient beam transport as well as to determine corrector strengths needed to steer the beam onto the linac axis. Other models have been written to compensate for random field errors in the linac.

An important concern has been consideration of changes in the beam when individual klystrons cycle on and off. Computer simulations and operating experience have demonstrated that changes in the beam energy can be effectively dealt with by rescaling the extant compliment of magnet strengths linearly to the new beam energy. At the beginning of the linac (the first four sectors) an addition or deletion of a klystron typically requires the rematching of the sector in which the change occurred and appropriate rescaling in the downstream sectors. Beyond Sector 4, simple magnet field rescaling appears to be adequate. The changes in transverse beam kicks corresponding to RF steering when klystrons are cycled might need compensation in the early sections of the machine. We plan to tabulate the effective steering associated with each klystron and store the results in the control computer database. This table will then be referenced for setting the appropriate dipole magnets for trajectory correction in response to klystron power changes.

Once magnet strengths have been calculated, a series of control and monitoring routines are used to set and maintain the required magnet currents. These programs are also used to investigate hardware problems. In addition, normal sorts of software has been written to save and restore configurations of magnet strengths to facilitate restarting of machine operations after shutdowns. Ultimately, all aspects of linac operations will be controlled using a central computer in conjunction with a network of distributed microcomputers.

### 2.3.5 Beamline Status

At present, the first ten sectors of the linac have been fully instrumented with SLC type quadrupoles, corrector dipoles, and beam position monitors.

Since September, 1982, the SLC type magnetic elements in the injector region and first ten linac sectors have been controlled with the recently developed software. For standard beams (PEP, SPEAR, and 90° per cell SLC lattice) the new focusing system has been successfully tested during the special SLC machine physics runs. A combination of SLC dc corrector dipoles and the linac pulsed steering dipoles (located in the injector region and at the end of the sectors) are used for trajectory correction. Readouts of klystron parameters (e.g. power, phase, and beam steering effects) along with position monitor signals into the SLC computer have been completed in the first ten sectors.

## 2.4 TOLERANCES AND BEAM QUALITY

### 2.4.1 Linac Tolerances

The design parameters for the SLC mode of operation are:

$$\begin{aligned}
 N &= 5 \times 10^{10} & \sigma_x &= 70 \mu\text{m} \\
 \gamma_0 &= 2.4 \times 10^3 \text{ (1.2 GeV)} & \ell &= 3.5 \text{ mm} \\
 \gamma_f &= 10^5 \text{ (50 GeV)} & W_0 &= 5.9 \times 10^5 m^{-3} \\
 L &= 3 \times 10^3 \text{ m} & N_k &= 240 \\
 \lambda_0 &= 100 \text{ m} & &
 \end{aligned} \tag{42}$$

Under these conditions, the asymptotic expression must be used in order to find the proper tolerance criterion.

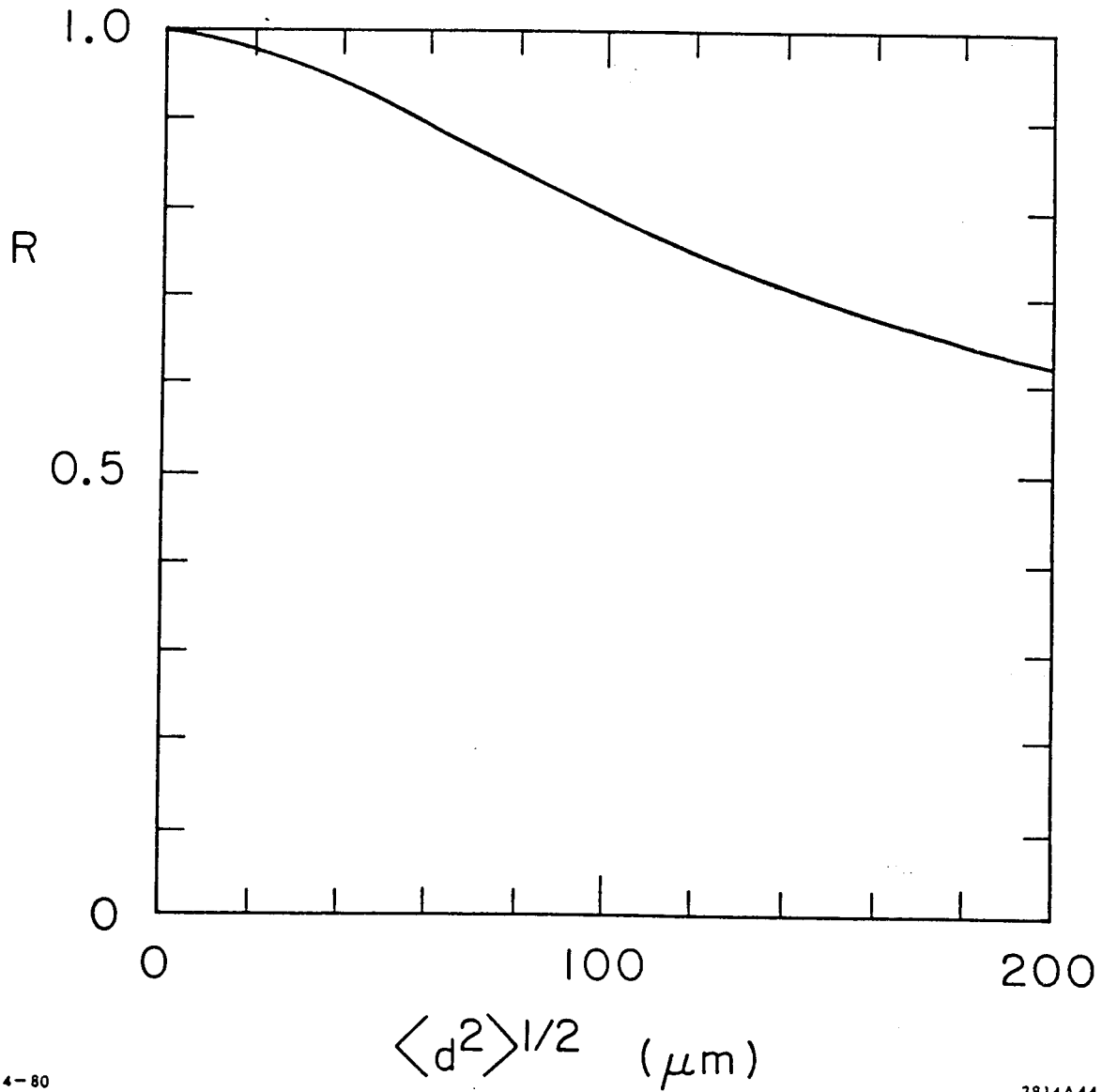
The value of  $\eta$ , according to Eq. (29) in 2.2.4, is 37 at  $z = 0$ , 94 at  $z = -\sigma_z = -\ell/2\sqrt{3}$ , and 150 at  $z = -\ell/2$ . The bunch shape for this case has been shown in Fig. 2.2.4.1. The corresponding values of the magnitude of  $x(z, L)$  are  $1.5 x_0$  for  $z = 0$  and  $6.1 x_0$  for  $z = -\sigma_z$ . If we choose  $z = -\sigma_z$  for our beam-quality requirements, we obtain the tolerance on the injection displacement  $|x_0| < \sigma_x/6.1 = 11 \mu\text{m}$ . This tolerance on injection error  $x_0$  is a criterion on the injection jittering since a static injection error can always be compensated by a set of trajectory kickers before injection. The corresponding tolerance on the jittering of the injection angle is  $\pm 1 \mu\text{rad}$ .

Substituting the SLAC linac data into Eq. (34) in Section 2.2.4, it turns out that the misalignment effect is dominated by the second-order perturbation rather than the first-order perturbation. For a particle at  $z = -\sigma_z$  the ratio  $x_{\text{rms}}^{(2)}$  to  $x_{\text{rms}}^{(1)}$  is about 2.2.

The misalignment effect can be minimized by injecting the beam with empirically determined offset  $x_0$  and angle  $x'_0$ . Since the second-order contribution dominates, the optimum choice of  $x_0$  and  $x'_0$  is given by Eq. (36) of 2.2.4. The expected rms value of the required injection offset, given by Eq. (37) of 2.2.4, is  $\langle x_0^2 \rangle^{1/2} = 0.35 \langle d^2 \rangle^{1/2}$ . After optimizing control of the injection conditions, the resultant beam-size growth,  $\langle x^{(1)2} \rangle^{1/2}$ , is given by Eq. (39) in 2.2.4, which

Figure 2.4.1.1

The luminosity reduction factor  $R$  vs. the misalignment tolerance of the accelerator pipe  $\langle d^2 \rangle^{1/2}$



is found to be  $0.25 \langle d^2 \rangle^{1/2}$  at the bunch center and  $0.62 \langle d^2 \rangle^{1/2}$  at  $\sigma_z$  behind the bunch center. For this beam-size growth at  $z = -\sigma_z$  to be less than the transverse beam size  $\sigma_x$  at the end of the linac, we demand a misalignment tolerance of  $\langle d^2 \rangle^{1/2} = 0.11$  mm.

The effect of misalignment is determined by examining the reduction in luminosity arising from the emittance growth. Since the luminosity is inversely proportional to the emittance, the reduction factor  $R$  is approximately given by

$$R = \int_{-\ell/2}^{\ell/2} \frac{dz/\ell}{1 + \langle x^{(1)2} \rangle \sigma_x^2} \quad (43)$$

with  $\langle x^{(1)2} \rangle$  given by Eq. (39) in 2.2.4. In Fig. 2.4.1.1 we have plotted  $R$  versus  $\langle d^2 \rangle^{1/2}$ . For  $\langle d^2 \rangle^{1/2} = 0.1$  mm, the reduction in luminosity is about 20%. The third-order term is appreciable only at the very tail of the bunch and thus does not affect the luminosity noticeably.

Another mechanism that relaxes both the injection and the misalignment tolerances is the following: different particles have slightly different energies and thus different betatron frequencies. The resonant driving situation is therefore pessimistic. This Landau damping effect will become significant if  $\Delta k_0 L > \pi$ , where  $\Delta k_0$  is the spread in the betatron wave number in the bunch.

Trajectory distortions will tend to disperse the beam as a function of energy and thereby increase the effective transverse emittance. The cumulative effect of the random dispersions caused by trajectory errors  $\delta x_i$  may be found by an adiabatic perturbation method. Under the assumptions that the acceleration, the phase advance/cell and the energy deviation are all constant, we find that the expectation value for the emittance increase is

$$\overline{\Delta \epsilon} = \frac{2n (\delta x_{\text{rms}})^2}{\ell^2} \left[ \left( \sqrt{\beta_F} - \sqrt{\beta_D} \cos \frac{\mu}{2} \right)^2 + \left( \sqrt{\beta_D} - \sqrt{\beta_F} \cos \frac{\mu}{2} \right)^2 \right] \times \left( \delta^2 + \frac{n^2}{6} x^2 \delta^4 \right) \quad (44)$$

where  $n$  is the number of FODO cells,  $\delta x_{\text{rms}}$  is the trajectory error,  $\ell$  is the half-cell length,  $\beta_F$  and  $\beta_D$  are the betatron functions at the  $F$  and  $D$  quadrupoles,  $\mu$  is the phase advance/cell, and  $x$  is the betatron chromaticity per cell.

For the linac lattice we have described we find

$$\overline{\Delta\epsilon} = 79 (\delta x_{\text{rms}})^2 (\delta^2 + 9600\delta^4) \quad . \quad (45)$$

With  $\delta = 0.005$  and  $\delta x_{\text{rms}} = 10^{-4}$  m, we find an emittance growth of  $2.2 \times 10^{-11}$  radian-meters, which is small compared to our design value of  $3 \times 10^{-10}$  radian-meters.

#### 2.4.2 Computer Simulation

We have made a computer model of the accelerator in order to study transverse wake-field effects. From our study we have concluded that the most critical parameters are the position and angle of the 1.2 GeV bunches injected into the linac. These parameters must be very stable from pulse to pulse.

Our model contains the following features: the linac lattice (a FODO array with 12.4 m between quadrupoles) is divided into 480 sections or 4 sections per lattice cell. The quadrupoles are adjusted so that the betatron phase advance per cell is  $90^\circ$  in the energy range from 1.2 to 26 GeV. From the 26 GeV point to the end of the linac the quadrupole strength is constant (100 kG is the maximum value consistent with the design of the quadrupole). At the end of the linac the phase advance has dropped to  $44^\circ$  per cell.

Moving along with the bunch is a grid of 61 slices, each 0.1 mm long. The bunch is simulated by populating slices with electrons according to the desired distribution. The results described here were obtained with gaussian bunches cut off at  $\pm 2\sigma$ .

We denote the position along the linac by index  $j$  (section number), and the position in the grid moving with the bunch by index  $m$  (slice number). The state vector which describes the position of slice  $m$  in transverse phase space at

location  $j$  in the linac is defined as follows:

$$\begin{aligned} \operatorname{Re} (x_j^m) &= \text{position at point } j / \sqrt{\beta_j} \quad ; \\ \operatorname{Im} (x_j^m) &= \text{angle at point } j \times \sqrt{\beta_j} \quad . \end{aligned} \quad (46)$$

If the slice is perturbed by an angular deflection at point  $j$ , the state vector at point  $j + 1$  is given as follows:

$$x_{j+1}^m = \left\{ (x_j^m) + \delta (x_j^m) \right\} \sqrt{\frac{E_j}{E_{j+1}}} e^{-i(\phi_{j+1} - \phi_j)} \quad . \quad (47)$$

In this expression  $\phi_j$  and  $E_j$  are the betatron phase and particle energy. The angular deflection of slice  $m$  at position  $j$  is determined by the position relative to the axis of the waveguide of all slices ahead of slice  $m$ . The wake deflection that is generated by these slices is

$$\delta (x_j^m) = i \sum_{k>m}^{61} n_k \frac{W(k-m)}{E_j} \left\{ \beta_j \operatorname{Re} (x_j^k) - \sqrt{\beta_j} d_j \right\} \quad . \quad (48)$$

In this expression  $d_j$  is the displacement of the RF structure relative to the axis of the accelerator, and  $n_k$  is the number of electrons in slice  $k$ .  $W(k-m)$  is the wake-field per electron at a distance of  $0.1 \times (k-m)$  mm. The displacement errors  $d_j$  can be controlled by accurate alignment. The wake field is fixed by the linac structure.

There are two effects we have studied. The first is the effect of an error in injection position or angle on the final emittance of the bunch. The second effect is that of the random misalignment of the linac sections. We shall show that the former effect is the most important and that the effects of random section misalignment are removed by the empirical tuning procedure used to optimize the injection angle and position.

We describe the injection error in a phase-independent manner by giving the corresponding value of the Courant and Snyder invariant. Figure 2.4.2.1 shows the evolution of the Courant and Snyder parameter for the central slice of the

bunch as it passes through the linac. When the bunch has few electrons in it, the parameter damps as  $1/E$ . When the bunch is well populated, the injection error is no longer damped. It should be noted that the various cases shown in Fig. 2.4.2.1 differ in bunch length as well as in the number of electrons per bunch. The bunch has been shortened as the current is reduced in order to maintain a constant energy spread. This reduction in length reduces the transverse wake-field while maintaining constant the longitudinal wake-field.

The injection error must be tuned empirically through the use of emittance monitors at the end of the linac. For the tuning to be successful the jitter in the injection conditions must be limited. If we require that the jitter in injection conditions have no more effect than to displace the slice of the bunch  $0.5 \sigma$  behind the center to  $3 \times 10^{-10}$  radian-meters, the following tolerance must be maintained (a  $\beta$  of  $42 m$  is assumed):

Tolerance on Injection Stability		
NUMBER	POSITION ERROR	ANGLE ERROR
$5 \times 10^{10}$ /bunch	$13 \mu\text{m}$	$0.3 \mu\text{rad}$
$4 \times 10^{10}$ /bunch	$30 \mu\text{m}$	$0.7 \mu\text{rad}$
$3 \times 10^{10}$ /bunch	$57 \mu\text{m}$	$1.6 \mu\text{rad}$

The 50 GeV phase-plan distribution of a bunch of  $5 \times 10^{10}$  electrons injected into the linac with a position error of  $13 \mu\text{m}$ s is shown in Fig. 2.4.2.2. The figure shows that the disruption of the bunch increases rapidly as the point of observation is moved back from the head of the bunch.

Random misalignment of the linac sections can cause the bunch to be disrupted even if it is injected without error. In our model we have assumed that the waveguide at each quadrupole has been randomly misaligned in the range  $-0.2$  to  $+0.2$  mm relative to the axis of the linac. In Fig. 2.4.2.3 the curve marked "no correction" shows the evolution of the Courant and Snyder invariant for the central slice of the bunch. The final position of  $10^{-9}$  radian-meters is greater than our design emittance. To correct for the misalignment, the in-

**Figure 2.4.2.1**

The curves show the evolution of an injection error for the central slice of the bunch. Then the number of electrons in the bunch is small, the Courant and Snyder invariant damps as  $1/E$ .

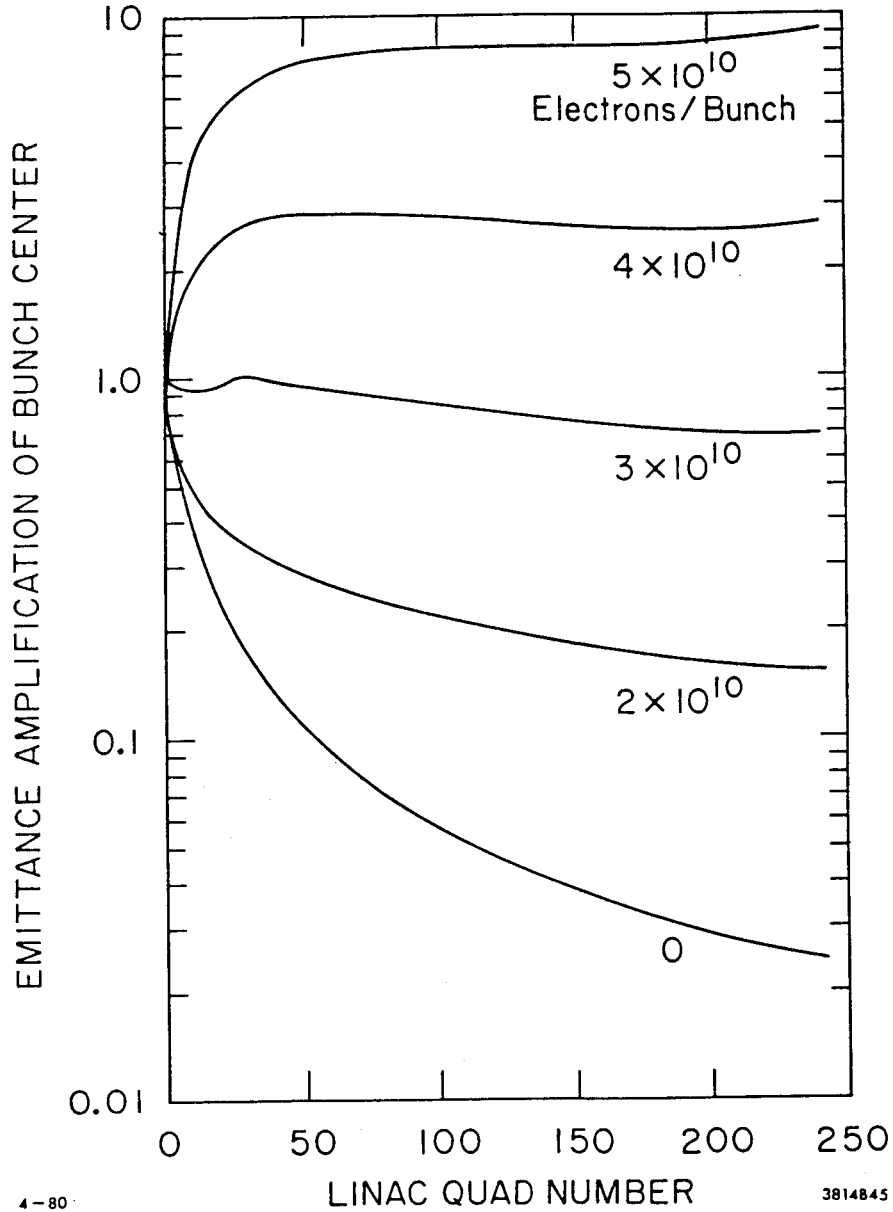
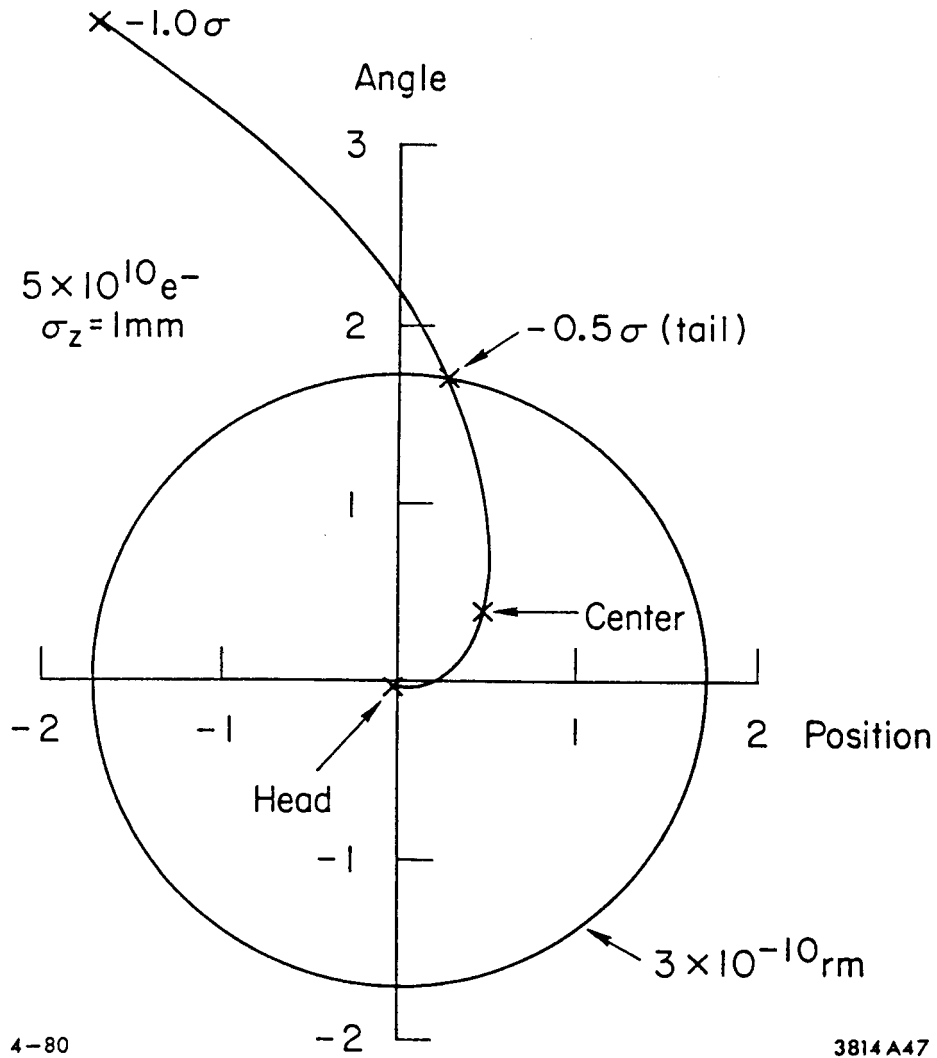


Figure 2.4.2.2

The transverse phase space at 50 GeV of a bunch of electrons injected into the linac with a position error of  $14\ \mu\text{m}$



jection conditions have been empirically tuned (by a computer operator in this case). The procedure was terminated when the curve marked "with correction" was obtained. In Fig. 2.4.2.4 we show the phase-plane distribution of the bunch after the tuning correction was made.

If the injection jitter is held to the tolerance shown above, the effects of the linac waveguide random misalignment should not be important.

Figure 2.4.2.3

The curve marked "no correction" shows the Courant and Snyder invariant of the center of a bunch that has been injected without error into a misaligned linac. The misalignment of the linac sections has been uniformly distributed between  $-0.2$  and  $+0.2$  mm. The "with correction" curve shows the improvement made by empirical tuning of the injection conditions to compensate for the misalignment.

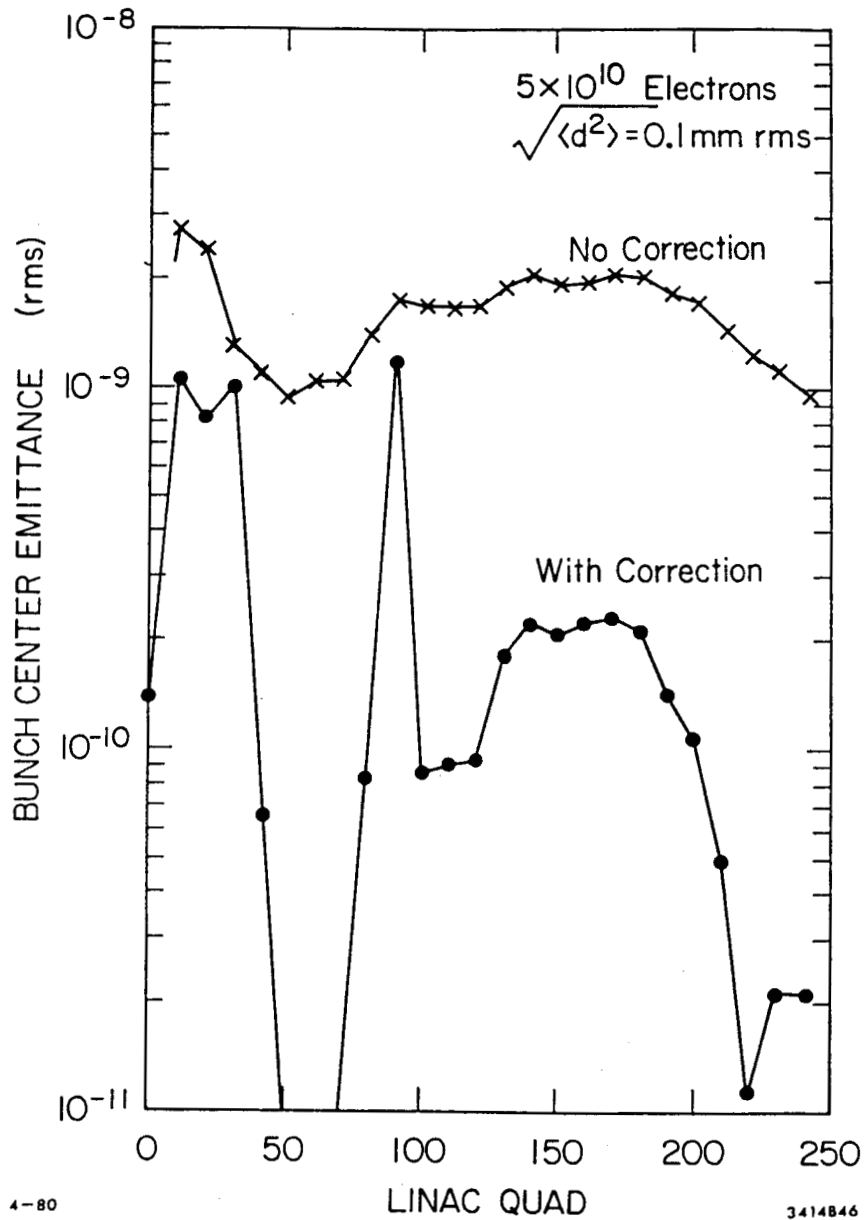
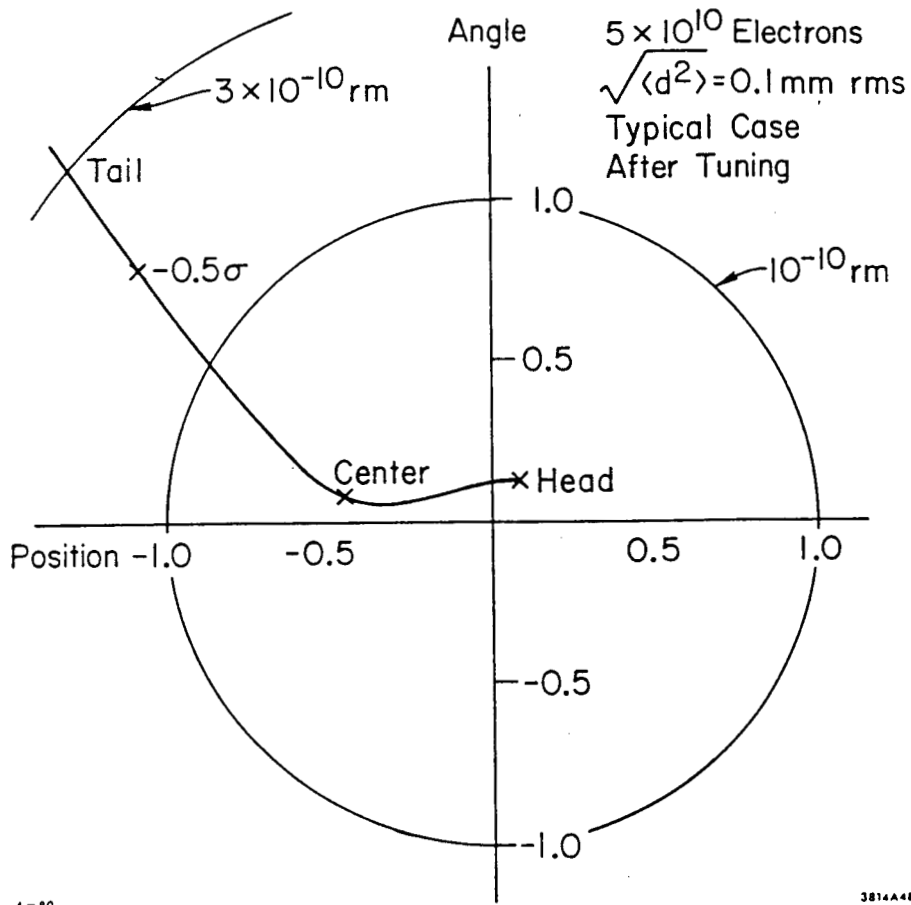


**Figure 2.4.2.4**

The transverse phase space of the bunch shown in Figure 2.4.2.3 at 50 GeV after empirical tuning of the injection conditions.



## REFERENCES

1. Z.D. Farkas, H.A. Hogg, G.A. Loew, and P.B. Wilson, Proc IXth Int. Conf. on High Energy Accel., SLAC (1974), p. 576.
2. Z.D. Farkas, H.A. Hogg, G.A. Loew, and P.B. Wilson, IEEE Trans Nucl. Sci. NS-22, No. 3, 1299 (1975)
3. Z.D. Farkas, H.A. Hogg, G.A. Loew, and P.B. Wilson, IEEE Trans Nucl. Sci. NS-22, No. 3, 1827
4. G.A. Loew, Proc. Xth Int. Conf. on High Energy Accel, Serpukhov, USSR (1977), 1, p. 58
5. G.A. Loew, "Ideas on Linac for Colliding Beams," AATF/79/4
6. B. Zotter and K. Bane, PEP Note-308 (1979)
7. See for example P. Wilson, PEP Note-276 (1978)
8. W.K.H. Panofsky and W.A. Wenzel, Rev. Sci. Instr. 27, 967 (1956)
9. E. Keil, Nucl. Instr. Meghods 100, 419 (1972)
10. M. Bell and H.G. Hereward, AR Division Report 65-67, CERN (1965)
11. Reported in E. Keil, Nucl. Instr. Meghods 100, 419 (1972), Sec. 4.3
12. R.F. Koontz, G.A. Loew, R.A. Miller and P.B. Wilson, IEEE Trans. Nucl. Sci. NS-24, 1493 (1977)

## **CHAPTER 3. THE COLLIDER ARC SYSTEM**

### **3.1 INTRODUCTION**

### **3.2 LINAC - ARC TRANSITION**

#### **3.2.1 Layout**

#### **3.2.2 Optical Considerations**

#### **3.2.3 Measurement of Energy and Energy Spread**

### **3.3 ARCS**

#### **3.3.1 Layout**

#### **3.3.2 Emittance Growth**

#### **3.3.3 General Philosophy for the Mitigation of Second Order Effects**

#### **3.3.4 Optics of the Reverse Bend and Instrument Sections**

#### **3.3.5 Vacuum Requirements**

#### **3.3.6 Arc Magnet Field Specification**

#### **3.3.7 Energy Loss due to Synchrotron Radiation**

### **3.4 TOLERANCES**

#### **3.4.1 Ground Motion**

#### **3.4.2 Orbit Distortions**

#### **3.4.3 Correction Schemes**

#### **3.4.4 Wake Field Effects in the Vacuum Chamber**

### **3.5 COMPONENTS**

#### **3.5.1 Arc Magnets**

##### **3.5.1.1 Magnet Profile**

##### **3.5.1.2 Construction Parameters**

##### **3.5.1.3 Measurement of Models**

#### **3.5.2 Magnet Support System**

#### **3.5.3 Arc Vacuum Pipe and Pumping System**

#### **3.5.4 Beam Position Monitors**

#### **3.5.5 Special Magnets**

#### **3.5.6 Power Supplies**

##### **3.5.6.1 Main Supply**

##### **3.5.6.2 Special Magnet Supplies**

##### **3.5.6.3 Trim Supplies**

#### **3.5.7 Diagnostics**

##### **3.5.7.1 Momentum Spectrometers and Collimators**

##### **3.5.7.2 Emittance Monitors and Collimators**

##### **3.5.7.3 Machine Protection**

### 3. COLLIDER ARCS

#### 3.1 INTRODUCTION

It is the function of the magnet lattice in the Collider arcs to bend the high energy  $e^+$  and  $e^-$  beams from the SLAC accelerator in such a manner that they will collide head-on with as little dilution of phase space and loss of energy as possible. Quantum effects in the synchrotron-radiation energy-loss mechanism, coupled with the finite amplitude ( $\beta$ ) and dispersion ( $\eta$ ) functions of the lattice, will cause some emittance growth. For a given gradient in an alternating-gradient structure, the growth is roughly proportional to  $L^3/r^4$ , where  $L$  is the length of a single focusing ( $F$ ) or defocusing ( $D$ ) magnet, and  $r$  is the bending radius. This speaks for a lattice of large radius containing many short high-gradient magnets of small aperture. In the adopted design, capable of transporting beams of energy up to 70 GeV with acceptable dilution,  $r$  is a site-limited  $\sim 279$  meters. The guide field at 50 GeV is  $\sim 5.98$  KG, with a corresponding gradient of  $\sim 7.02$  KG/cm. For a phase advance of  $108^\circ$  per FD cell, the magnets are  $\sim 2.5$  meters in effective length. The present design assumes  $a \sim 10$  cm effective drift length between magnets.

## 3.2 LINAC-ARC TRANSITION

The purpose of this system is to carry the two beams emerging from the linac through the switchyard to the start of the collider arcs. This should be done in a manner that minimizes costs and the disruption of existing SLAC experimental facilities. Figure 3.2.1 a,b,c shows the general scheme that has been chosen to achieve this end.

### 3.2.1 Layout

The starting point of the optical TRANSPORT system has now been defined to be in the center of the last regular linac quadrupole (Q81) which is located 50.0971 feet upstream of the official beginning of the beam research yard (BSY) whose  $z$  coordinate along the axis of the linac is often designated station  $100 + 00.0$ . Positrons and electrons are separated by a DC magnet 50B1 whose vertex coordinate is  $100 + 68.4715$  ft. From thereon the two beams traverse the remainder of optical matching sections to enter the arc lattice about 93 ft. later. Both north and south arc trains leave the BSY via glancing saw-cut penetrations to emerge some 237 ft. from the start of the BSY. Care has been taken that the new equipment will not infringe on the space presently occupied by such important components as the PEP extraction lines or the series of pulse magnets that feed End Stations A and B. Other rearrangements of BSY equipment are feasible and relatively minor.

### 3.2.2 Optical Considerations

Some rather special constraints apply to the matching sections. For example, as long as the two beams share common beamline elements and because they have opposite charges, focusing lenses for one beam are defocusing for the other. Moreover, it is quite important to observe certain symmetry properties in the matching design. These considerations as well as the desirability of avoiding existing equipment and minimizing breakout construction costs have led to a unique design.

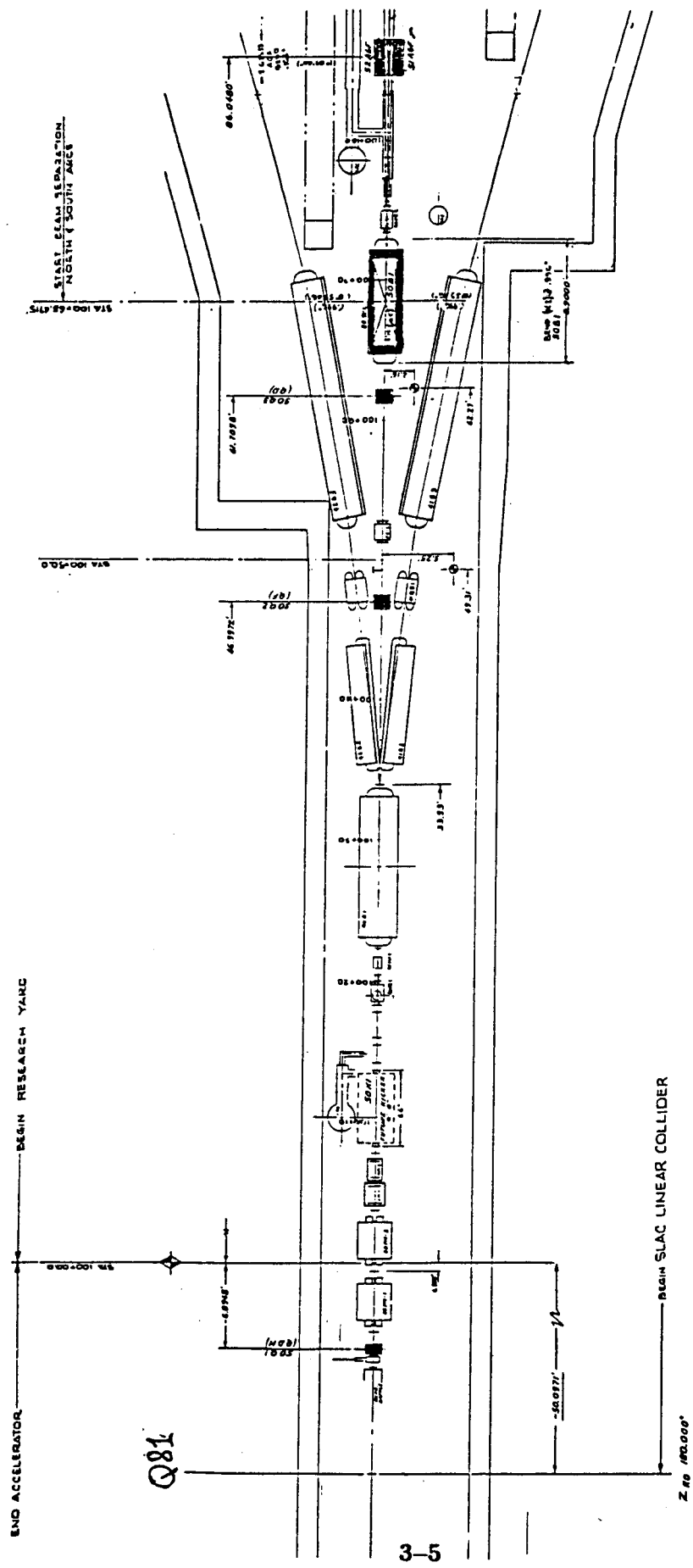


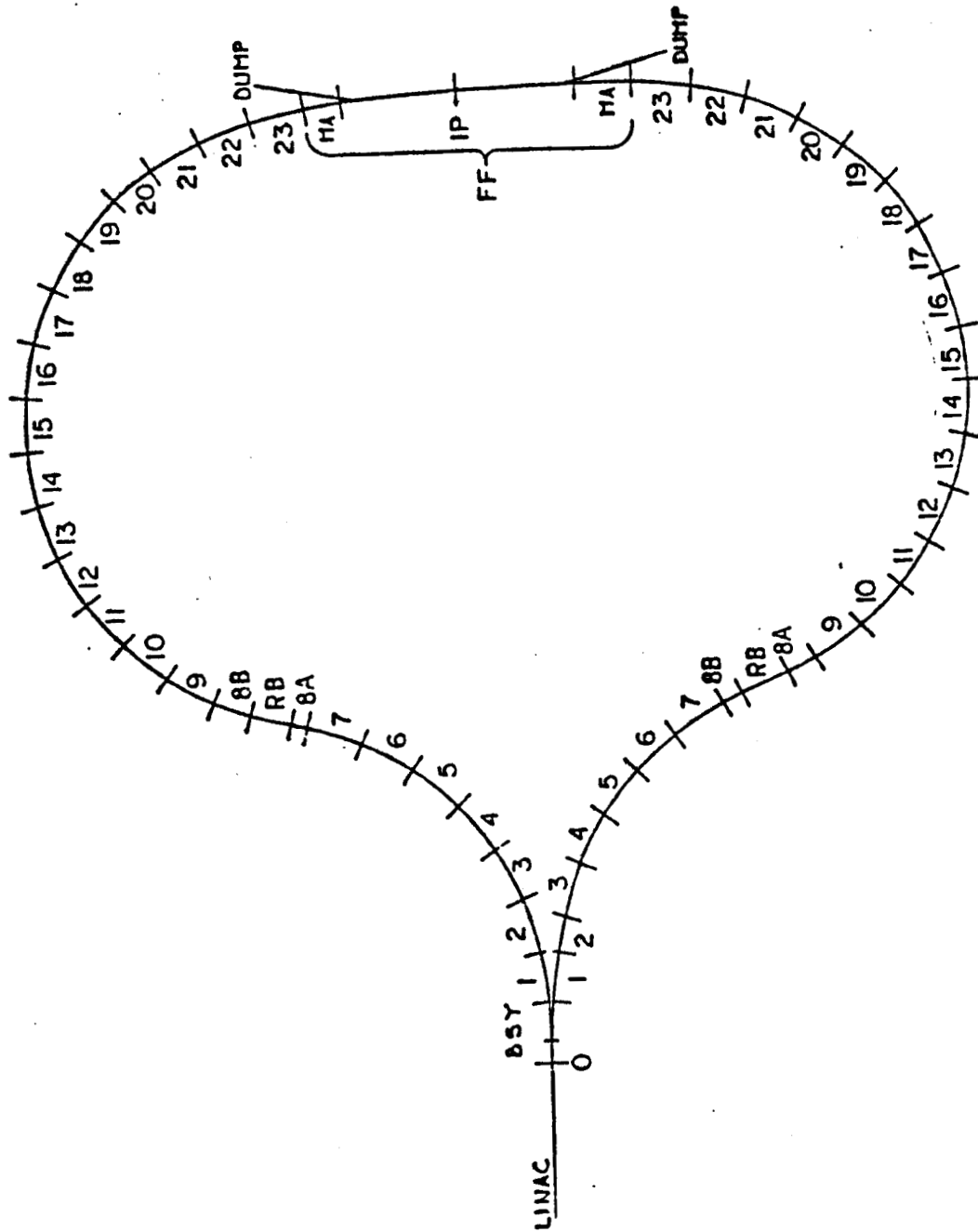
Figure 3.2.1 a: Layout, Linac-Arc Transition in BSY  
Sheet 1

STANFORD LINEAR ACCELERATOR CENTER		SHEET	
P.O. BOX 20080, STANFORD, CALIF. 94303-5080		DATE	
PROJECT: BE-M & NE LAYOUT		DRAWING NO.	
SUBJECT: INJECTION LINES 50.51.52		DATE	
DRAWN BY: [Name]		SCALE: 1/8" = 1'-0"	
CHECKED BY: [Name]		PROJECT NO. GP 363-001-15-RO	
APPROVED BY: [Name]		SHEET NO. E	





Figure 3.2.2: Layout of Arcs to Interaction Point  
(numbers refer to achromats)



The first three lenses, labelled QDH (50Q1) QF (50QD) and QD (50Q3) continue the linac focusing lattice and transform to a point at which both beams are round and their ellipses are erect, i.e.,  $\beta_{x+} = \beta_{x-} = \beta_{y+} = \beta_{y-}$ ,  $\alpha_x = \alpha_y = 0$ . At this point, the properties of both beams are identical; one might think of this point as a "swivel" in phase space. The fact that this point is virtual in the design (it is located after the splitting bend 50B1) is of no consequence as long as the condition  $\beta_x = \beta_y$  is maintained. Note:  $\alpha_x = \alpha_y$ , but they are no longer zero.

The north and south linac to arc transition lines can now be made mirror symmetric about the linac axis with parameters suitably adjusted for geometry and to match the  $\beta$  and  $\eta$  values of the arcs. The flat field 50B1 is followed by an alternate gradient magnet to focus and bend early on.

### 3.2.3 Measurement of Energy and Energy Spread

The maximum value of  $\eta_x = 150$  mm is reached inside of Q3 (51Q3, 52Q3). This value is as high as it will ever get in the arcs and is, therefore, a good region for an energy defining spectrometer. Although  $\beta_x$  also peaks in Q3, the resolution at the instrument would be about .14%, good enough to provide the operator with a tool to set up the linac and set the currents in the arc magnets. A spectrometer is needed in each arc since the energy of the positron and electron beams may differ by as much as 2% depending on how the linac is operated.<sup>1</sup> (see Section 2.)

Because of this fact, and because (50B1) is common to both beamlines, a small steering compensation is called for in the arms. This will be accomplished by small correcting coils in each arm in the vicinity of Q3.

### 3.3 ARCS

#### 3.3.1 Layout

Figure 3.2.2 depicts the general layout including the BSY breakouts, reverse bend sections, final focus matching sections and the final focus. The geometry is determined by site boundaries and the proposed location of the interaction region hall. It has been found possible to accommodate the vertical tunnel profile (see Conventional Facilities) by bending magnet rolls about the beam direction no larger than about 14 degrees with respect to the tunnel floor.

The general principles outlined in the Conceptual Design Report<sup>2</sup> have led to a lattice design containing some 940 alternate gradient magnets. Realizable specifications for magnets<sup>3</sup> and overall geometry<sup>4</sup> were used and became the basis for tunnel layout. Late in 1983<sup>5</sup> it was decided to study the effects of changing the height of the beam above the tunnel floor in order to accommodate simplifications in the magnet support system but without changing the existing tunnel contract drawings. It was decided that the beam height should be 42". At the date of this writing, January 1984, the current layout is called ARCN Final (12/27/83) and ARCS FINAL (12/27/83).<sup>6</sup>

#### 3.3.2 Emittance Growth

Emittance growth has been calculated by means of the program TURTLE<sup>7</sup> which is as realistic a computational tool as exists at present. Additional programs such as DIMAT are under development to further simulate the arc optics. All of these studies have shown that lattices having phase shifts per cell of 108°, 135° and 144° yield quite similar results as far as emittance growth is concerned, but that a 90°/cell has a 20% additional emittance growth relative to the 108° cell.<sup>9</sup> Work continues to develop arc lattices which incorporate the best of engineering features, simplicity of construction and alignment, and ease of operation. The optical drift space between magnets has been recently increased from 5cm to 10cm. This modification results in ease of vacuum chamber assembly permitting installation or replacement of beam position monitors after the magnets have been mounted in the tunnel. The effect of this change on emittance growth at

50 GeV is immeasurably small. Lattice functions for the current solution (not necessarily the final solution to be adopted) for the north arc are shown in Figs. 3.3.1 to 3.3.18, those for the south arc in Figures 3.3.19 to 3.3.36. Note: emittance growth from the arcs is not included in the envelope function but has been calculated using TRANSPORT for the actual lattice in detail. For beams having no orbit errors and no optical distortions (i.e., linear theory) the dilution is

$$\Delta\epsilon_x = 1.3 \times 10^{10} \text{ radian meters at 50 GeV}$$

$$\Delta\epsilon_y = 0.5 \times 10^{10} \text{ radian meters at 50 GeV}$$

In addition, some minor effects should be included. They are about 5.6% due to radiation anti-damping<sup>10</sup> and about 5 to 10% due to transverse wake fields.<sup>11</sup>

Instruments to measure emittance on line and thereby permitting the correction of growth effects in the linac will be located in the reverse bend section where  $\eta$  is driven to zero before being matched to the arcs with opposite signs.

### 3.3.3 General Philosophy for the Mitigation of

#### Second Order Effects in the Arcs

The transport of beams having  $3 \times 10^{-10}$  radian meters transverse phase space and with a momentum spread  $\Delta p/p = \pm 0.5\%$  require careful attention to second and higher order effects. The philosophy adopted in this design is derived from a theorem<sup>12</sup> restated below:

“If one combines four or more identical cells consisting of dipoles and quadrupoles with their parameters chosen so that the overall first order transfer matrix is equal to unity, then it follows that such a system will have vanishing second order geometric aberrations and with an appropriate distribution of sextupoles in the cells, all second order chromatic aberrations may be eliminated without the reintroduction of second order geometrics.”

The arcs should, therefore, in their simplest approximation consist of a train of such second order achromats. The achromats are numbered in Figure 3.2.2. In practice, it turns out that the properties of the system are not appreciably compromised if the train is interrupted at any point, provided the insertion itself

has a unit matrix, i.e., +1. This permits, for example, the insertion of a section to reverse the sign of the dispersion function as is required in the reverse bending match. Moreover, any particular achromatic section (in this design 10 cells or 20 magnets) may be rolled (within limits set by vertical  $\eta$ ) about the beam axis without disturbing the properties of the achromats. It should be noted that all magnets within an achromat are in a plane although this plane has both pitch and roll. This permits the flexible tailoring of the vertical projection of the beam as required by the terrain and other constraints which the tunnel alignment must follow.

BKUP ARCN GEO B (11/18/82): BEGINNING TO 1000 FT

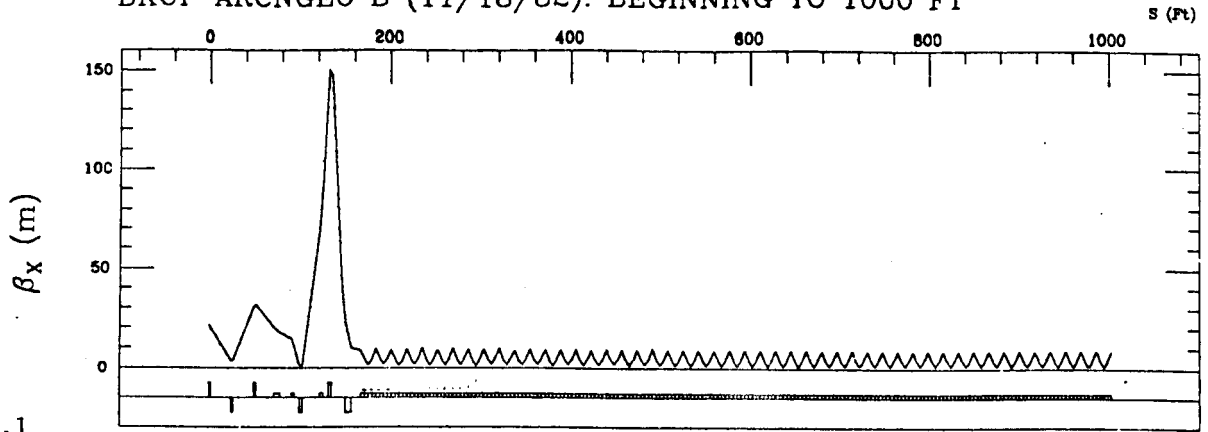
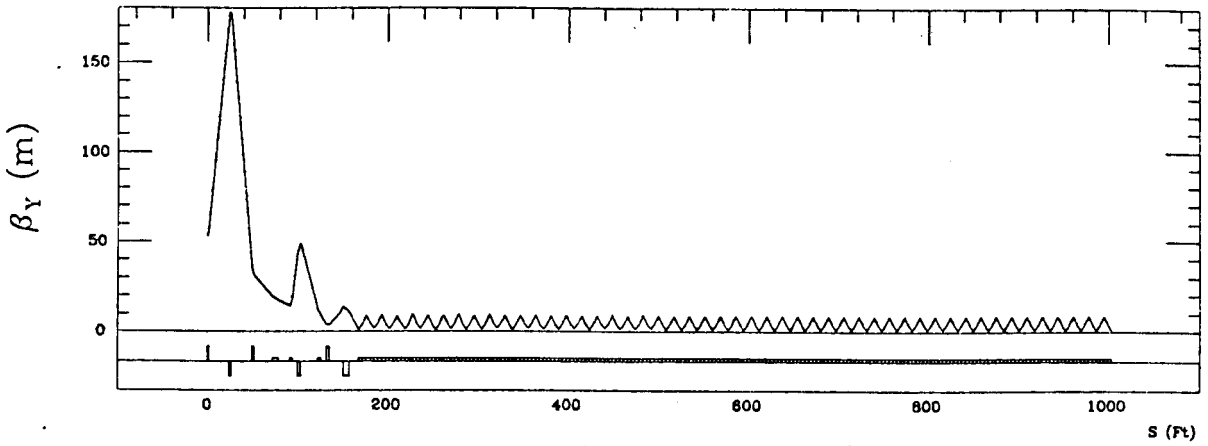


FIG. 3.3.1



BKUP ARCN GEO B (11/18/82): 1000 FT TO 2000 FT

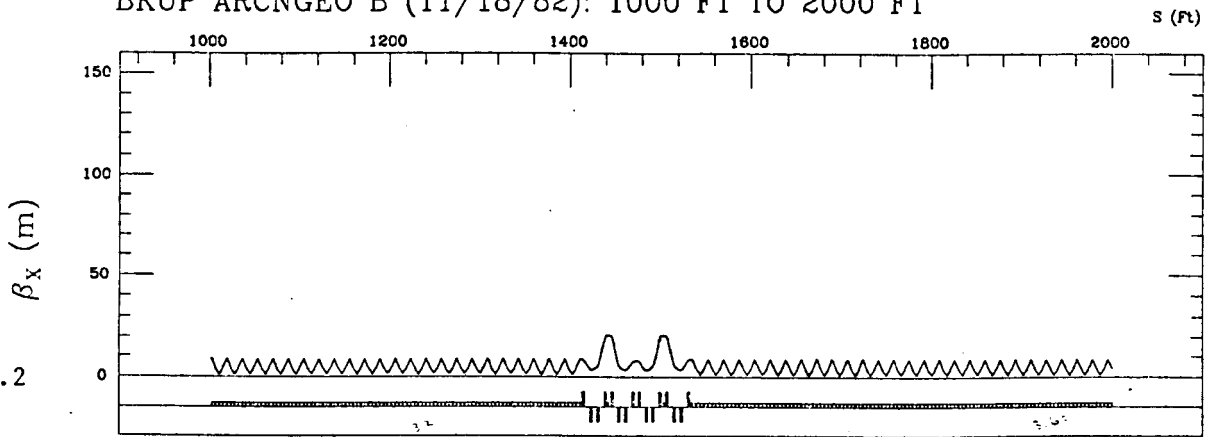
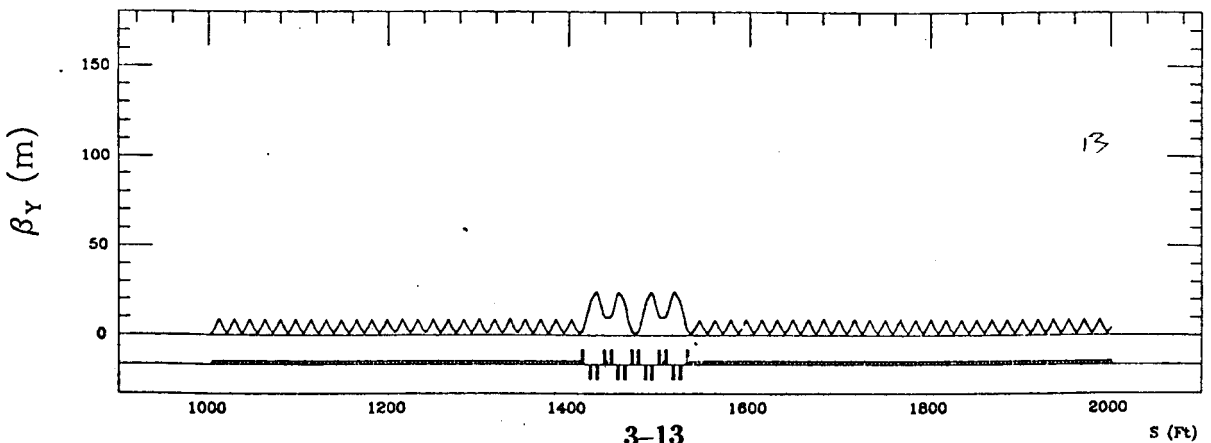


FIG. 3.3.2



BKUP ARCN GEO B (11/18/82): 2000 FT TO 3000 FT

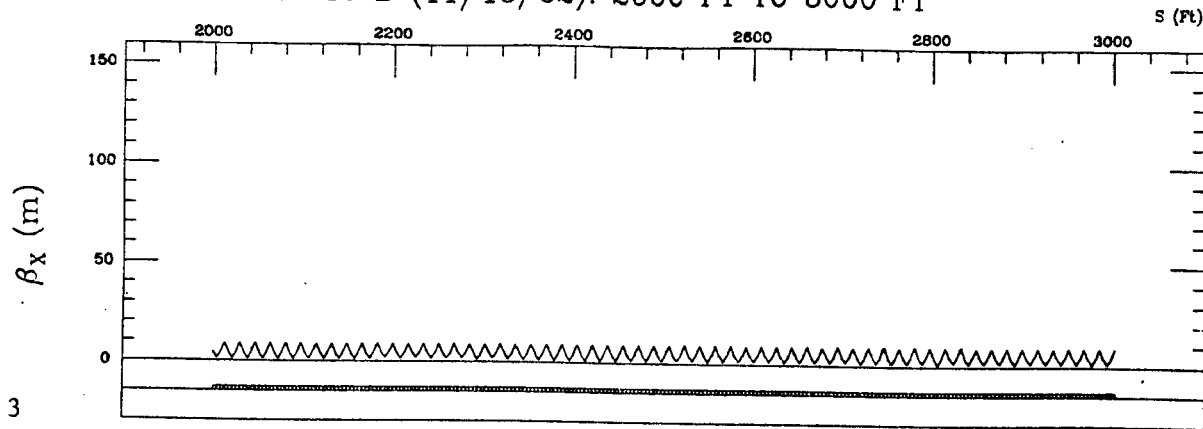
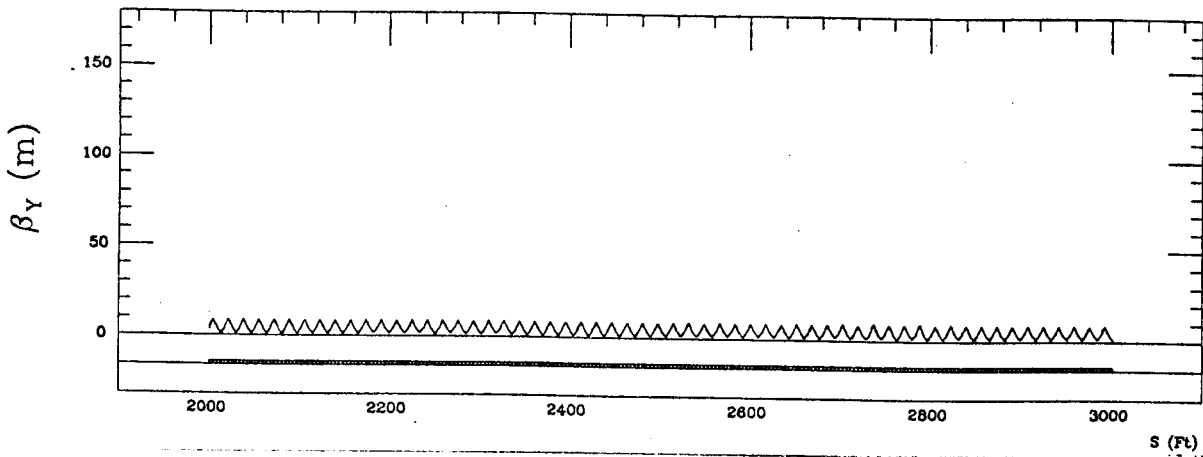


FIG. 3.3.3



BKUP ARCN GEO B (11/18/82): 3000 FT TO 4000 FT

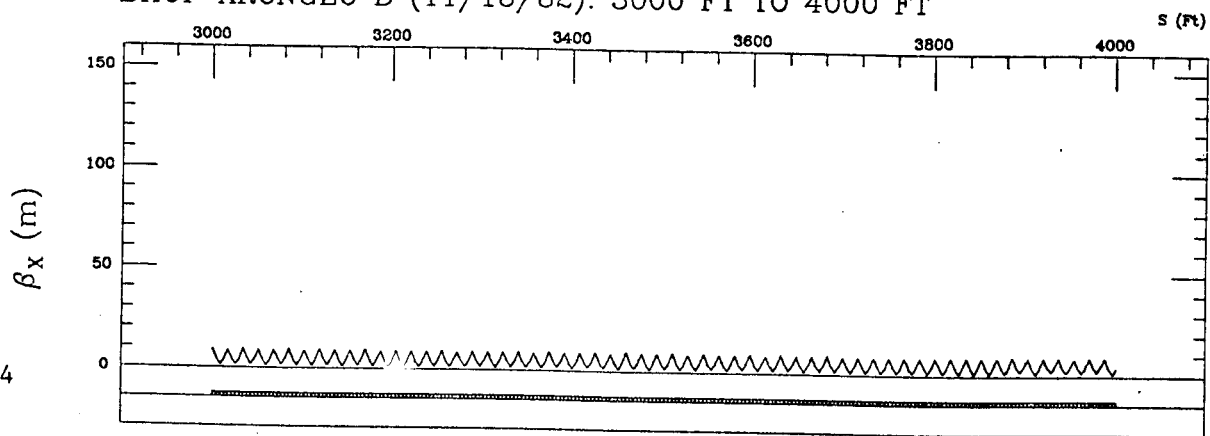
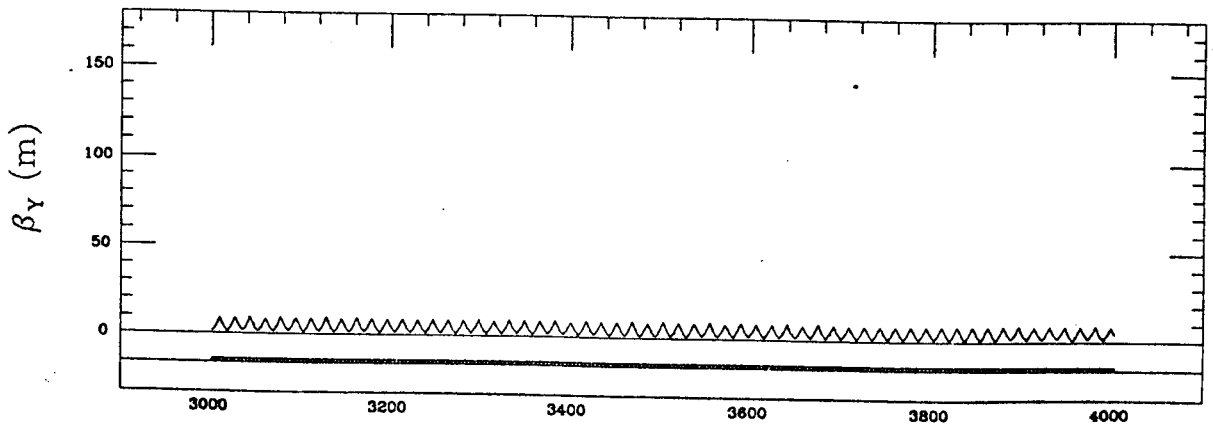


FIG. 3.3.4



BKUP ARCNGEO B (11/18/82): 4000 FT TO ARC END

S (Ft)

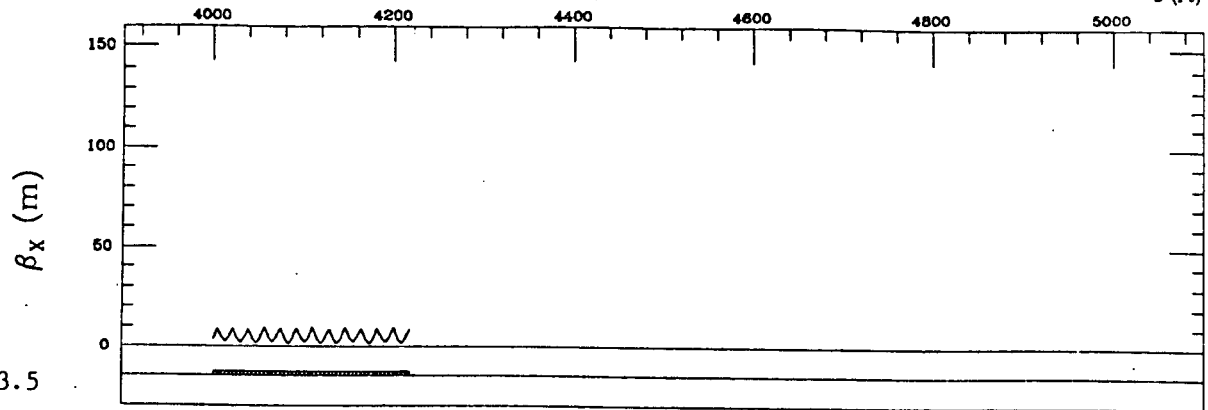
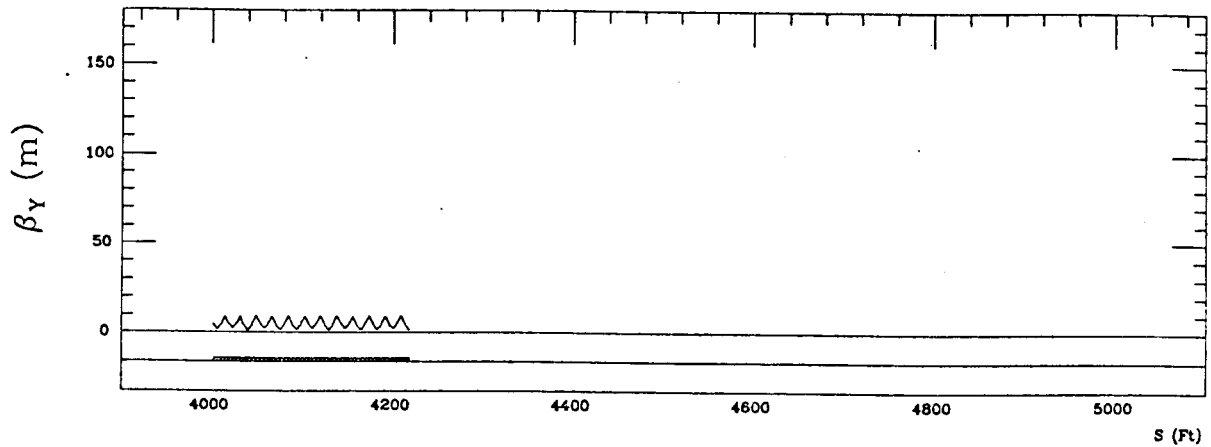


FIG. 3.3.5



BKUP ARCNGEO B (11/18/82): ARC END TO I.P.

S (Ft)

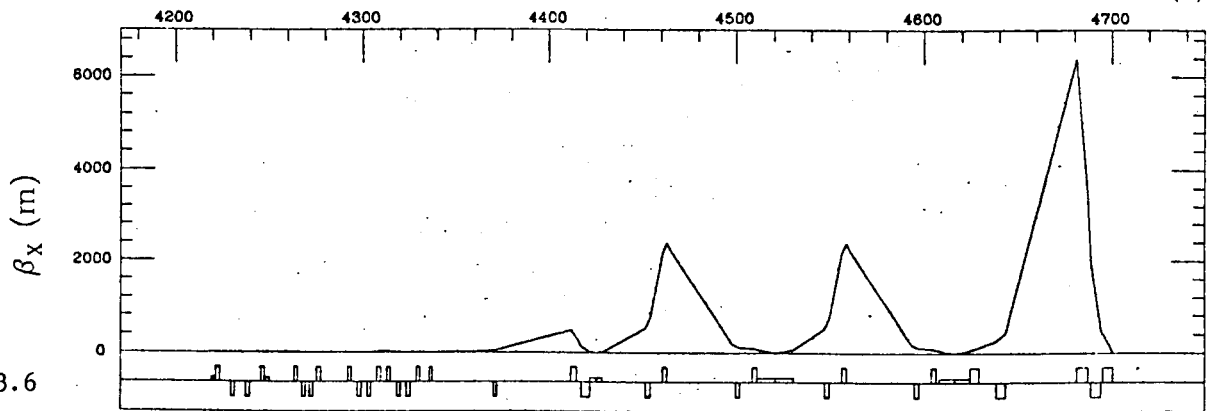
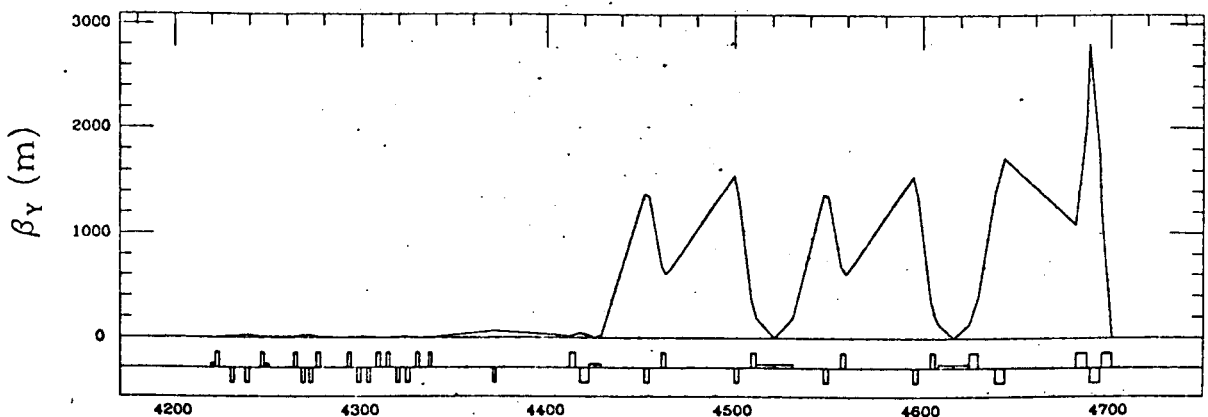


FIG. 3.3.6



S (Ft)

BKUP ARCNGEO B (11/18/82): BEGINNING TO 1000 FT

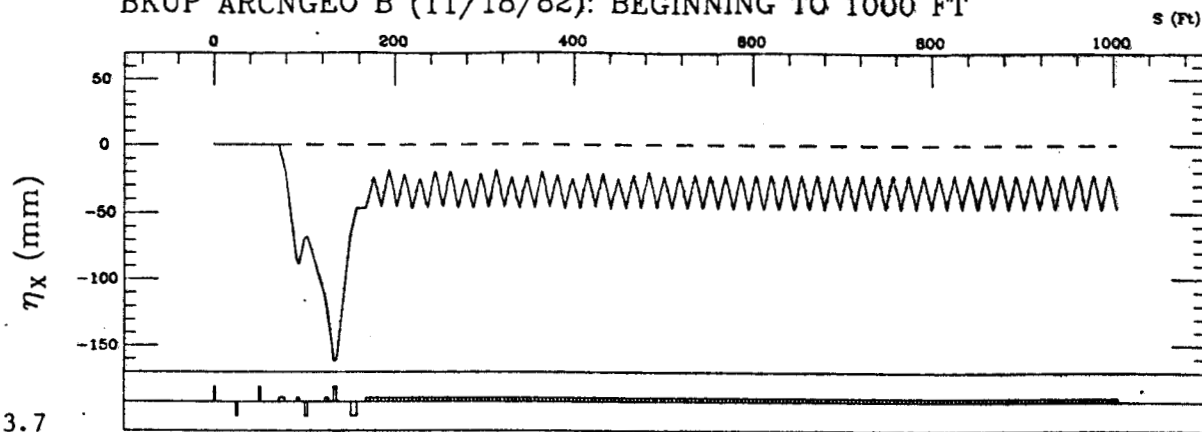
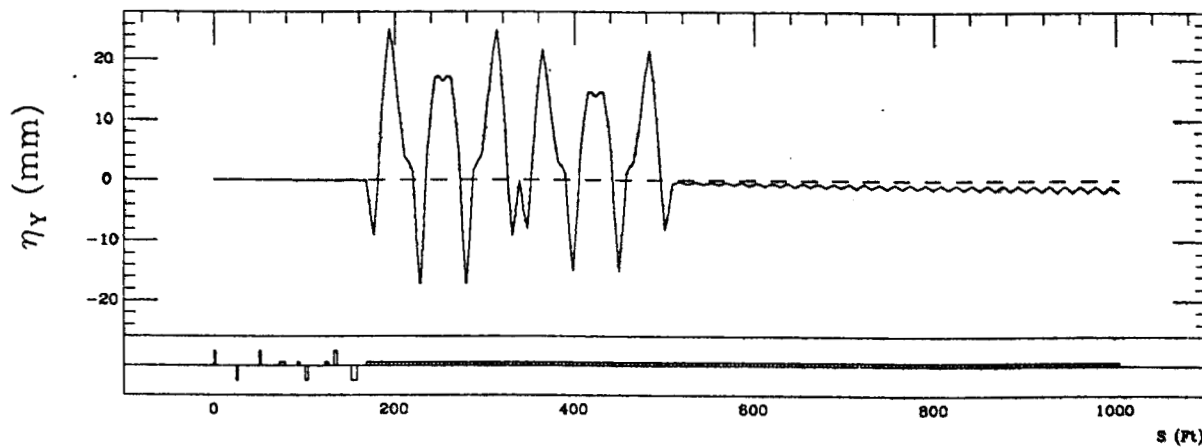


FIG. 3.3.7



BKUP ARCNGEO B (11/18/82): 1000 FT TO 2000 FT

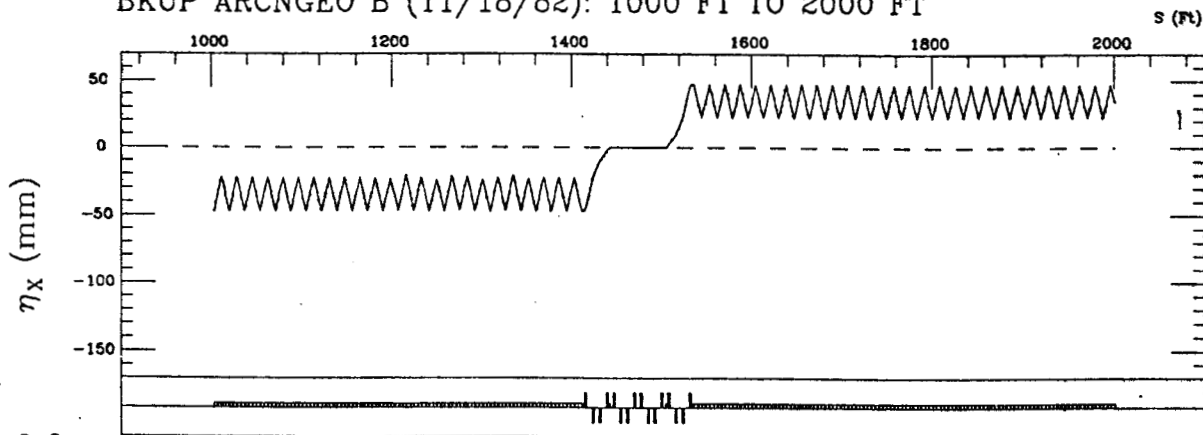
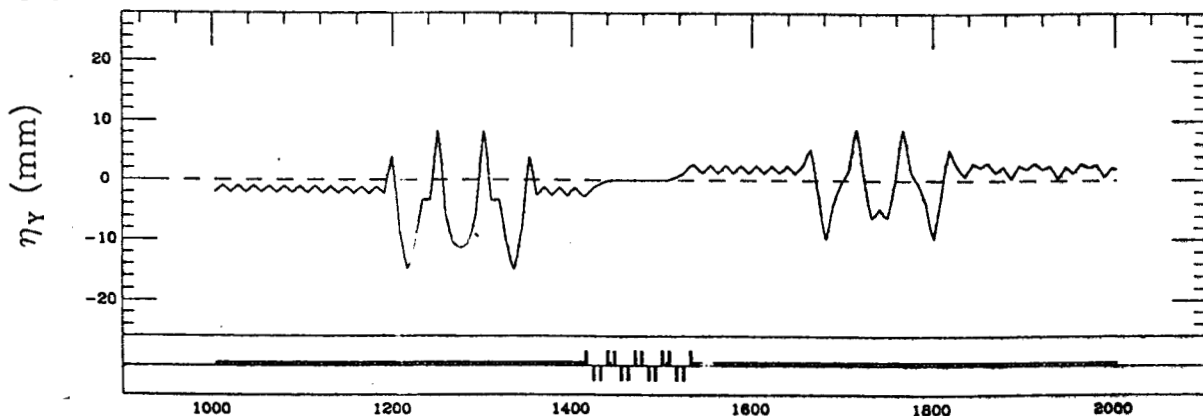


FIG. 3.3.8



BKUP ARCNGEO B (11/18/82): 2000 FT TO 3000 FT

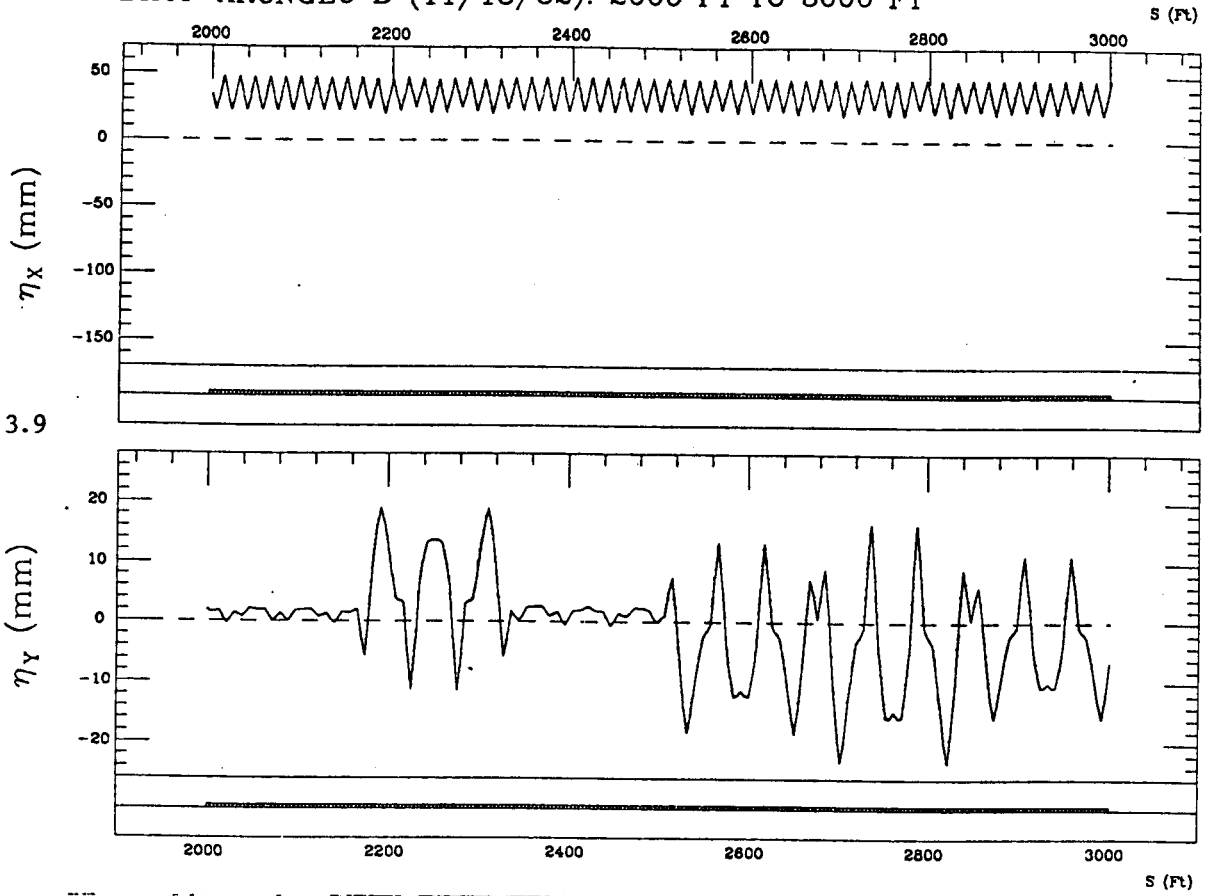


FIG. 3.3.9

BKUP ARCNGEO B (11/18/82): 3000 FT TO 4000 FT

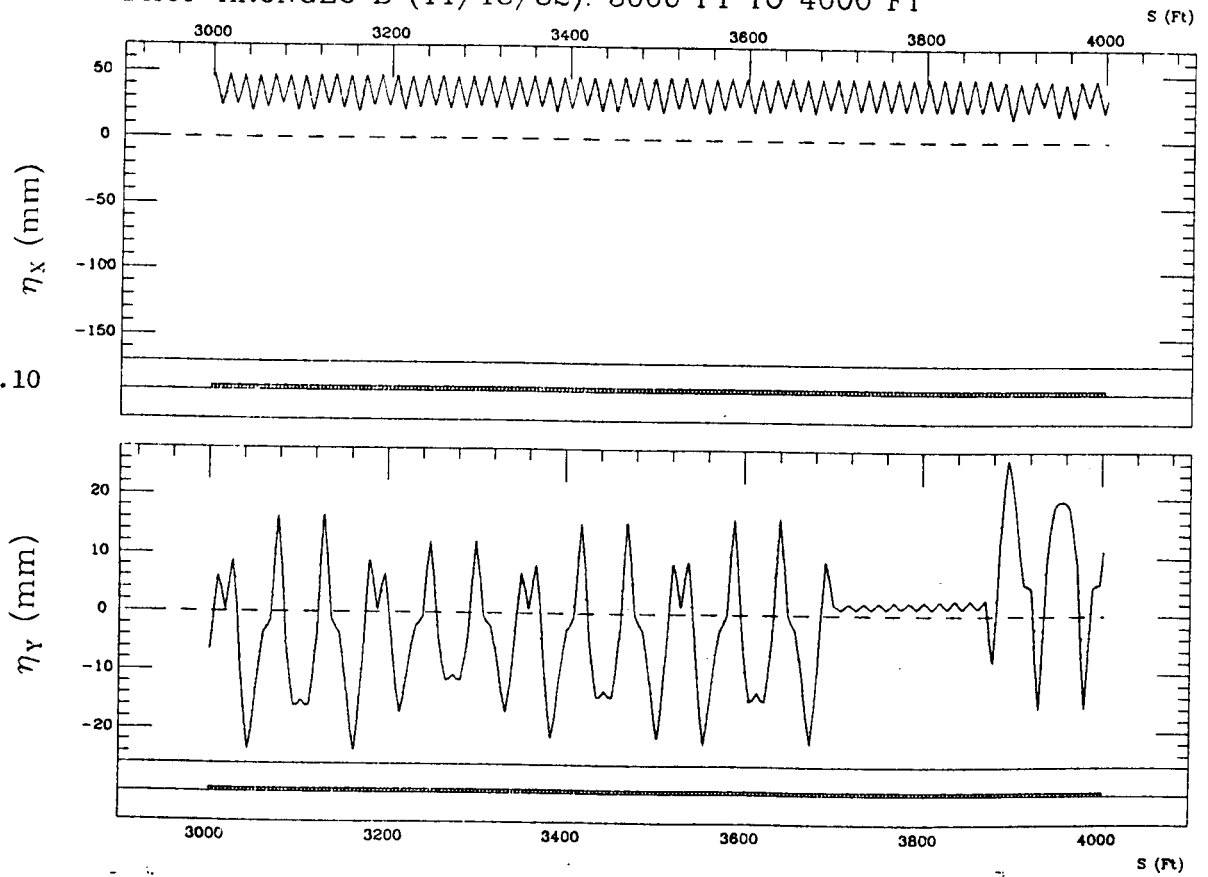


FIG. 3.3.10

BKUP ARCNGEO B (11/18/82): 4000 FT TO ARC END

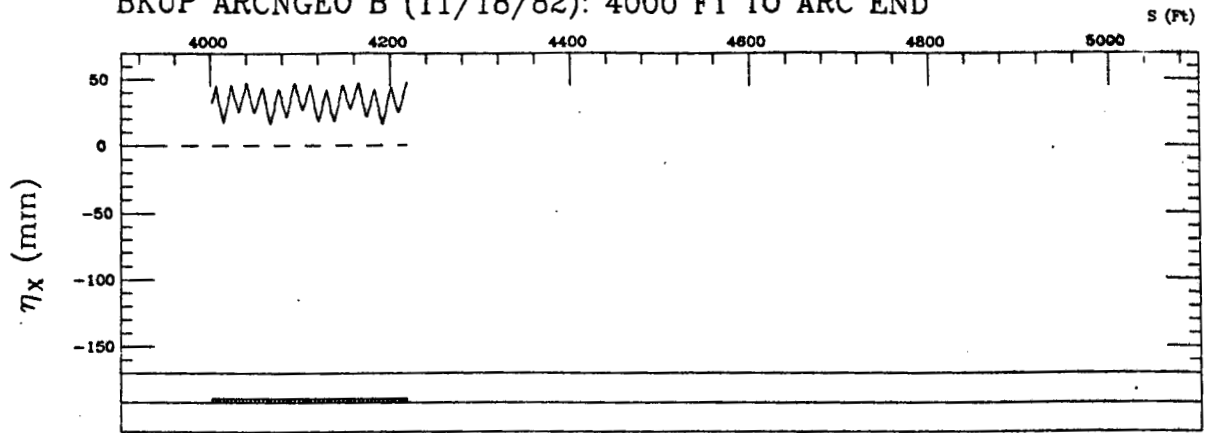
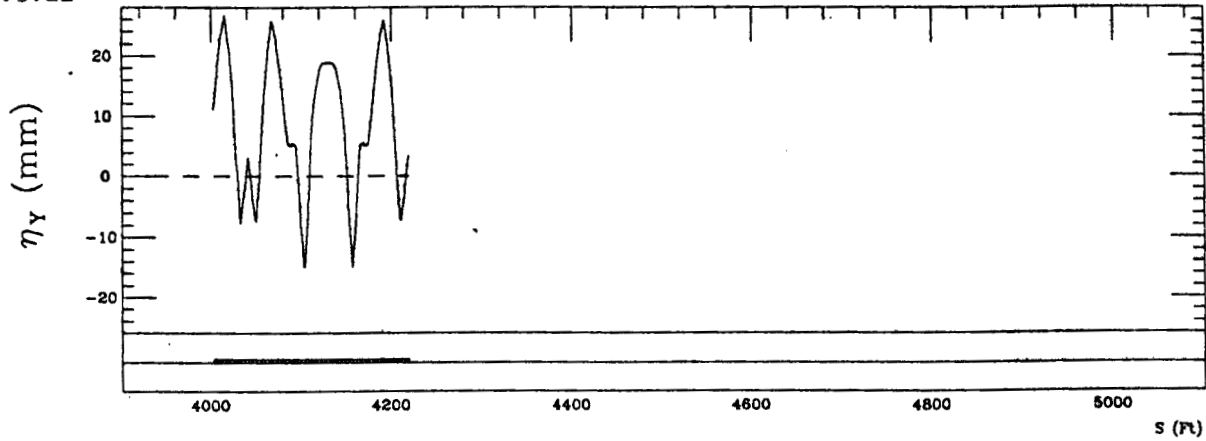


FIG. 3.3.11



BKUP ARCNGEO B (11/18/82): ARC END TO I.P.

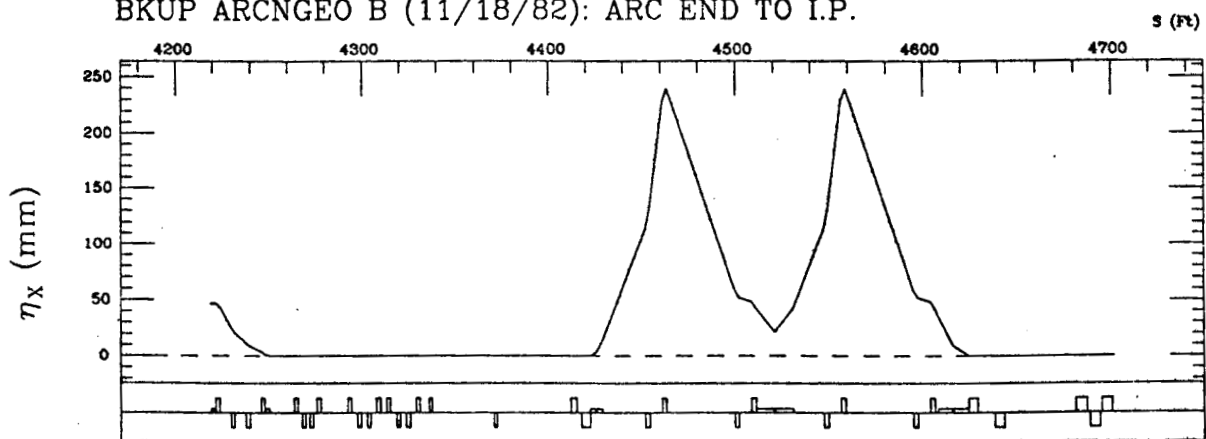
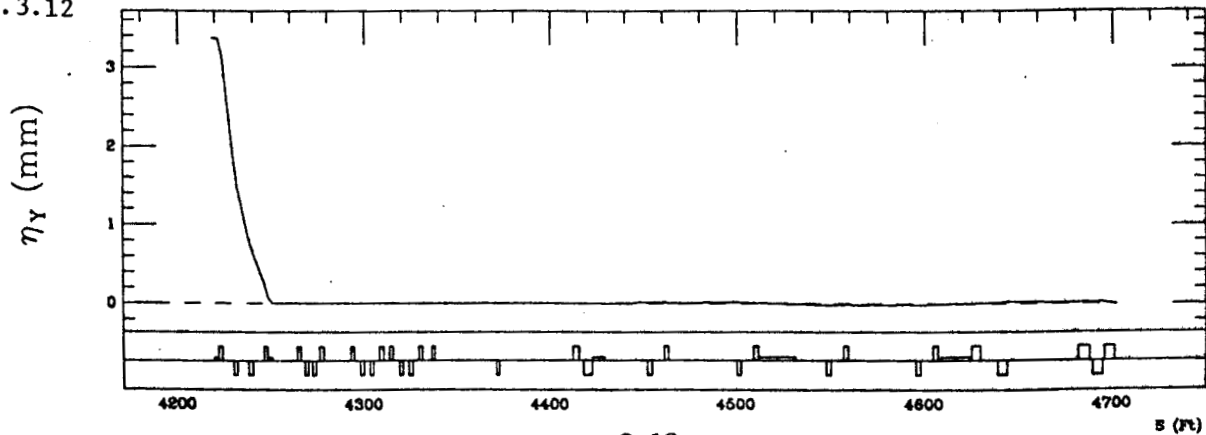


FIG. 3.3.12



BKUP ARCNGEO B (11/18/82): BEGINNING TO 1000 FT

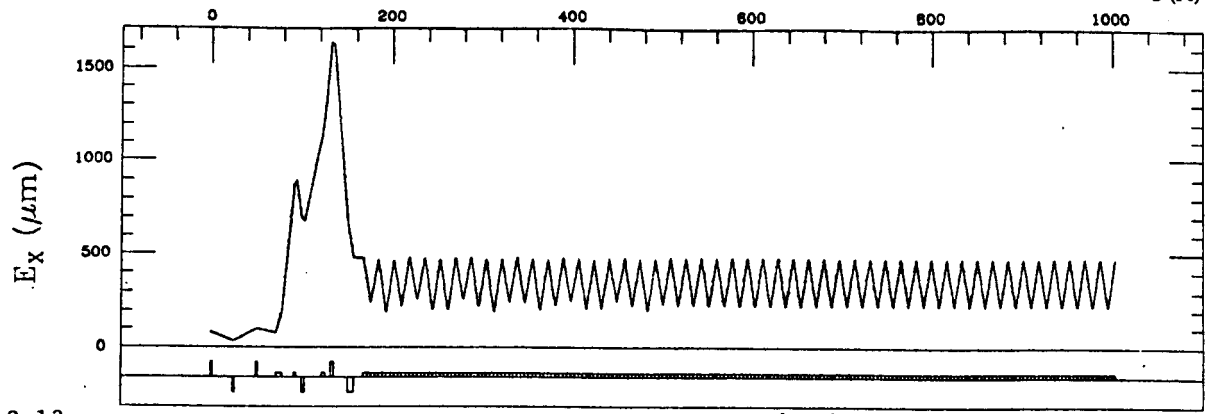
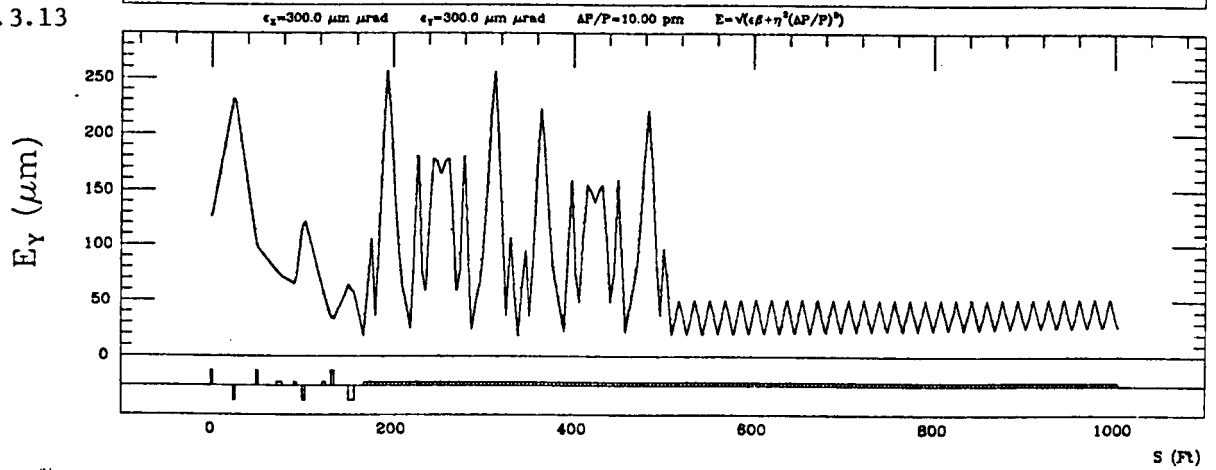


FIG. 3.3.13



BKUP ARCNGEO B (11/18/82): 1000 FT TO 2000 FT

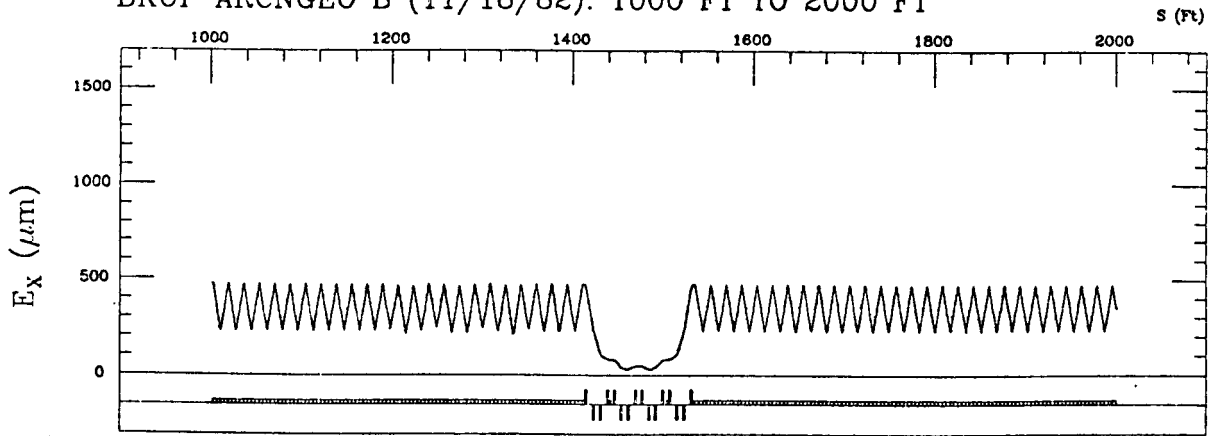
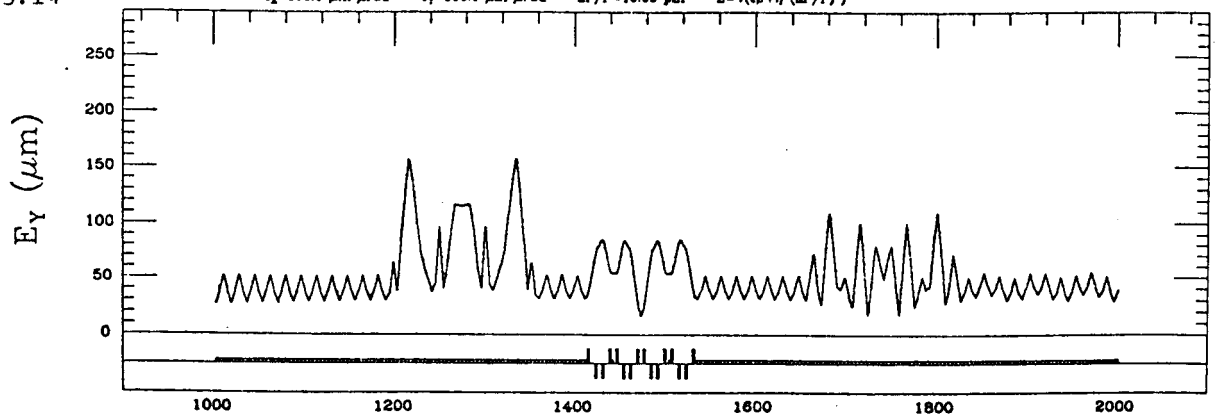


FIG. 3.3.14



BKUP ARNGEO B (11/18/82): 2000 FT TO 3000 FT

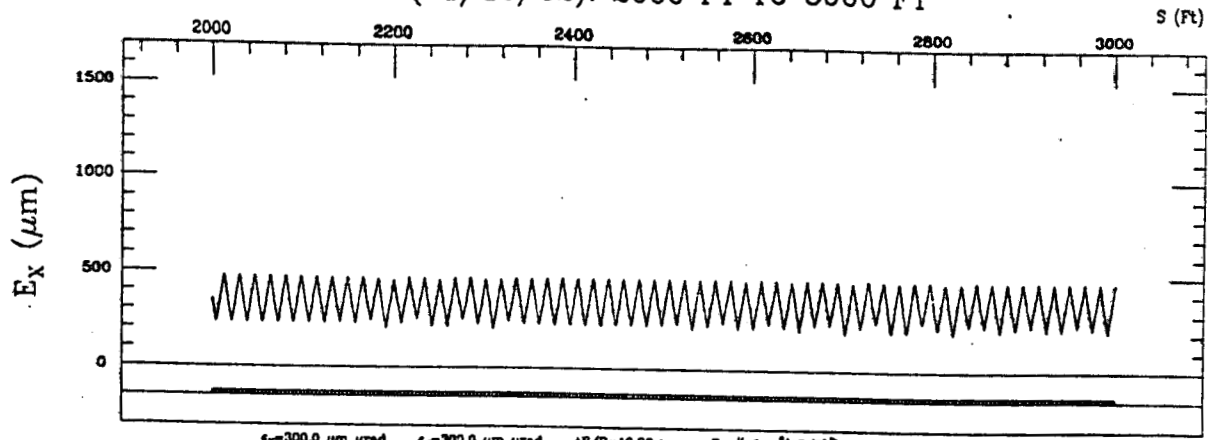
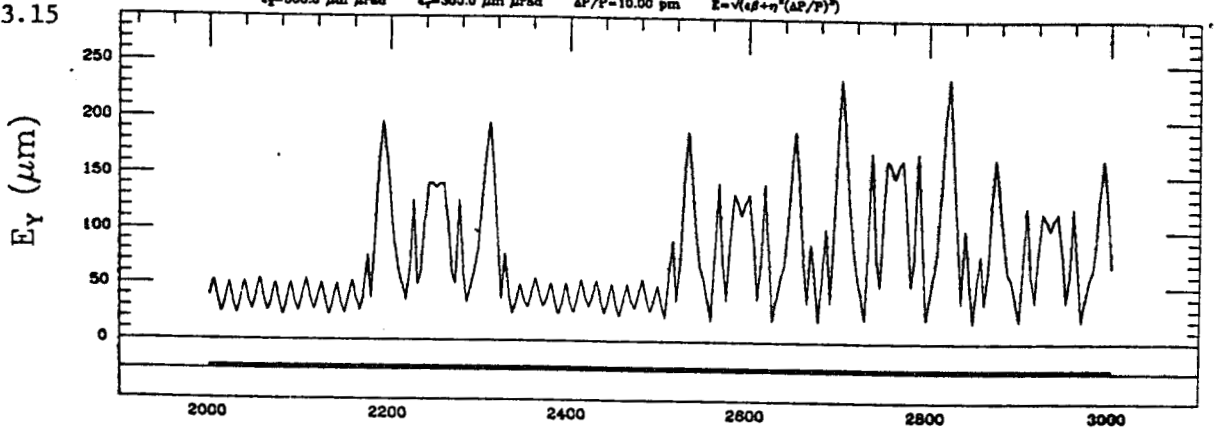


FIG. 3.3.15



BKUP ARNGEO B (11/18/82): 3000 FT TO 4000 FT

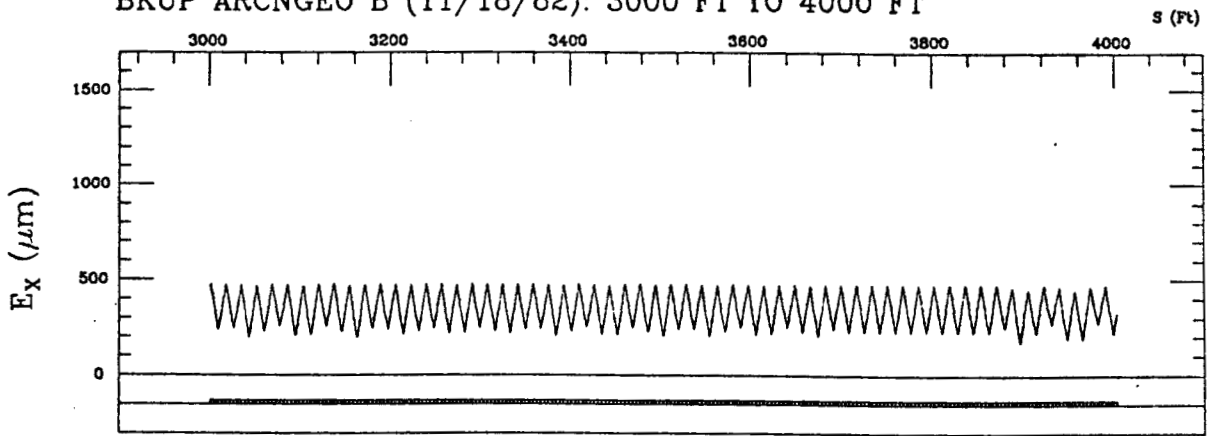
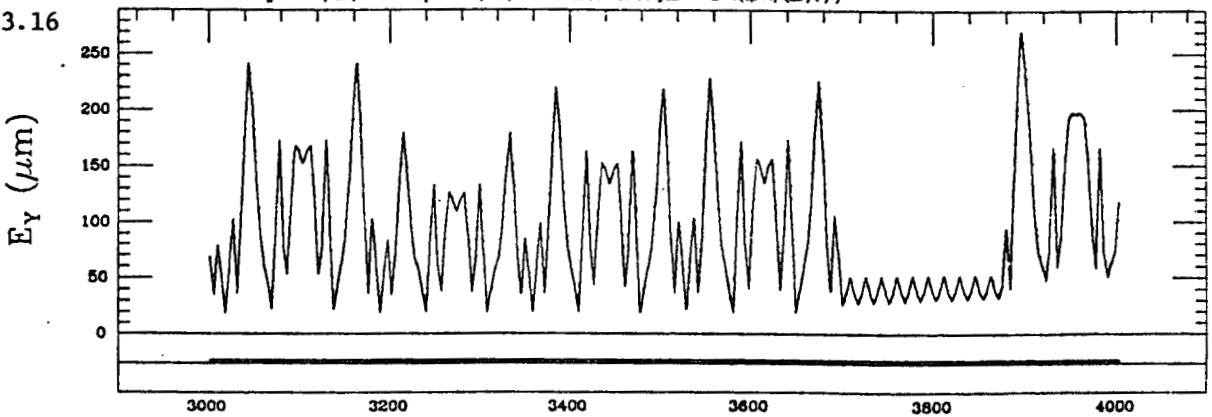
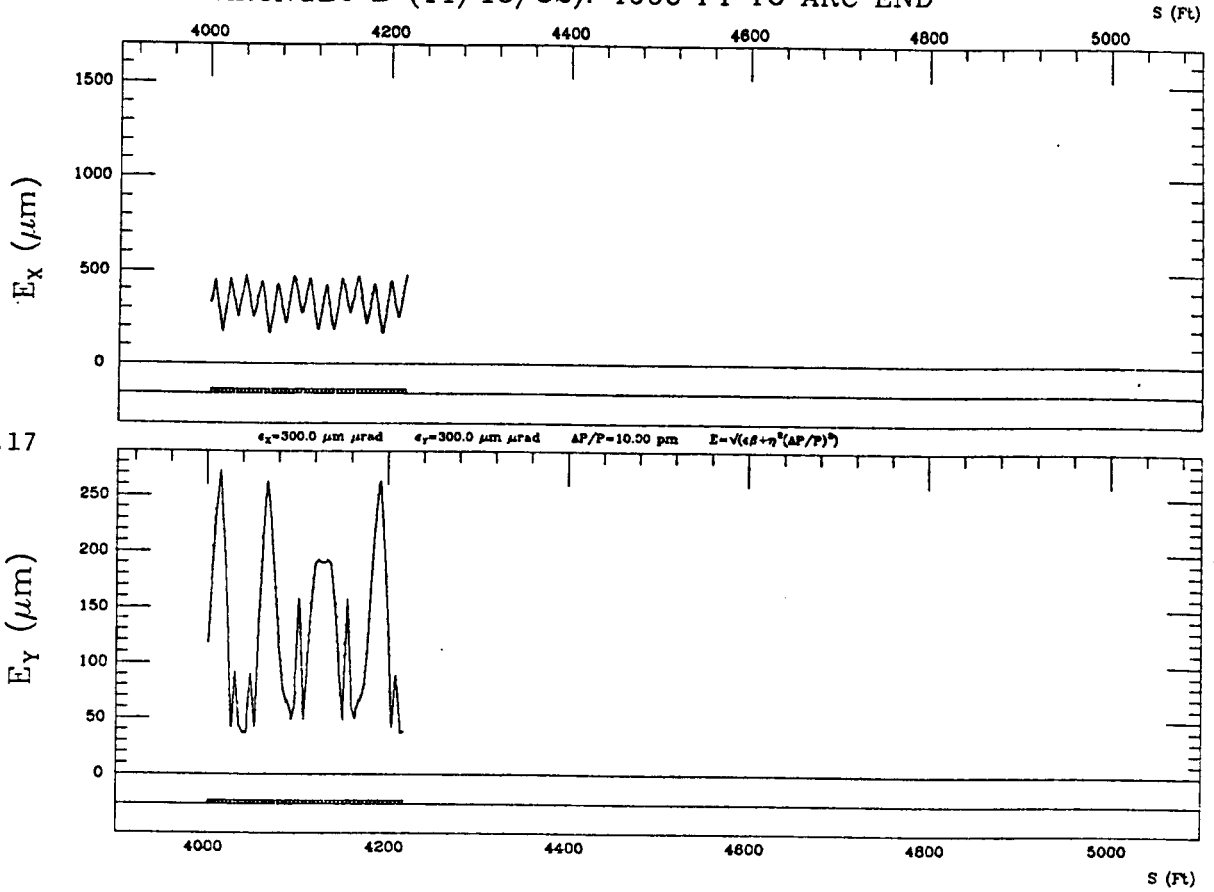


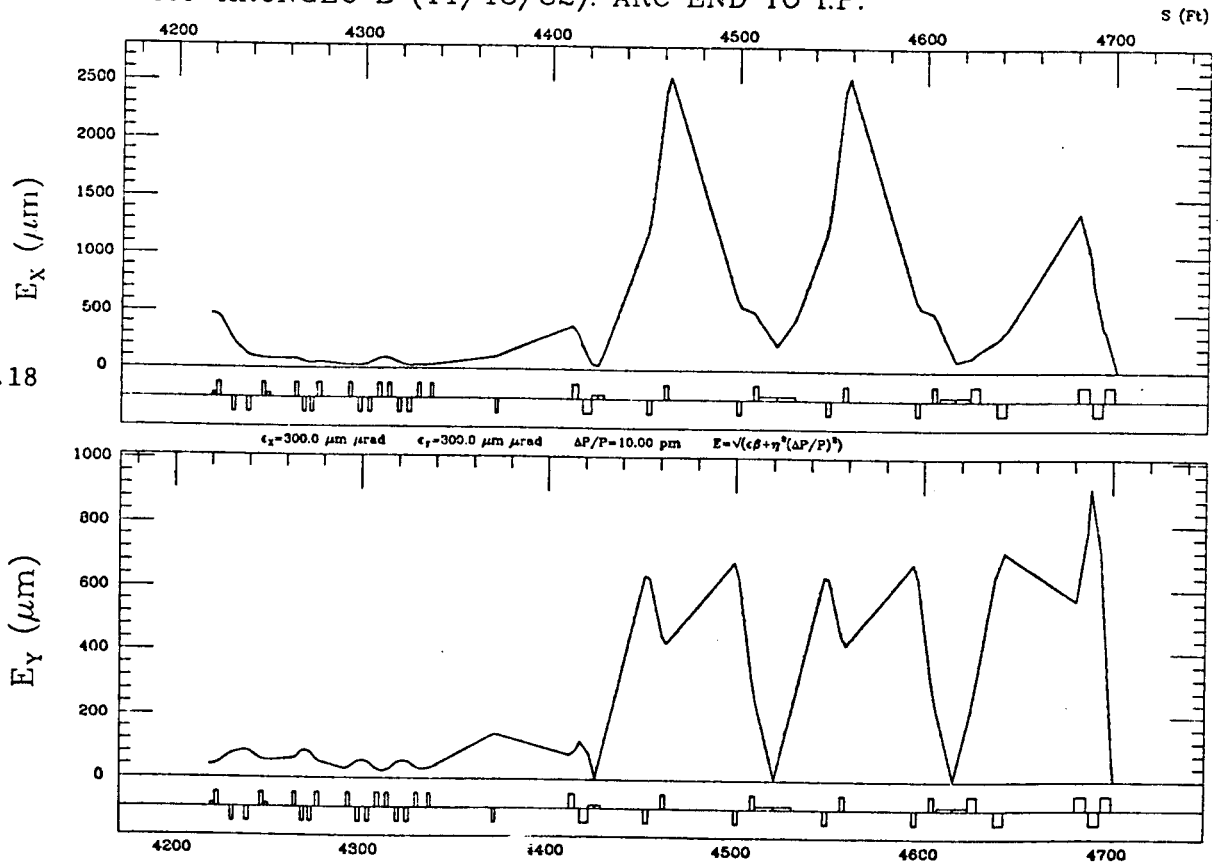
FIG. 3.3.16



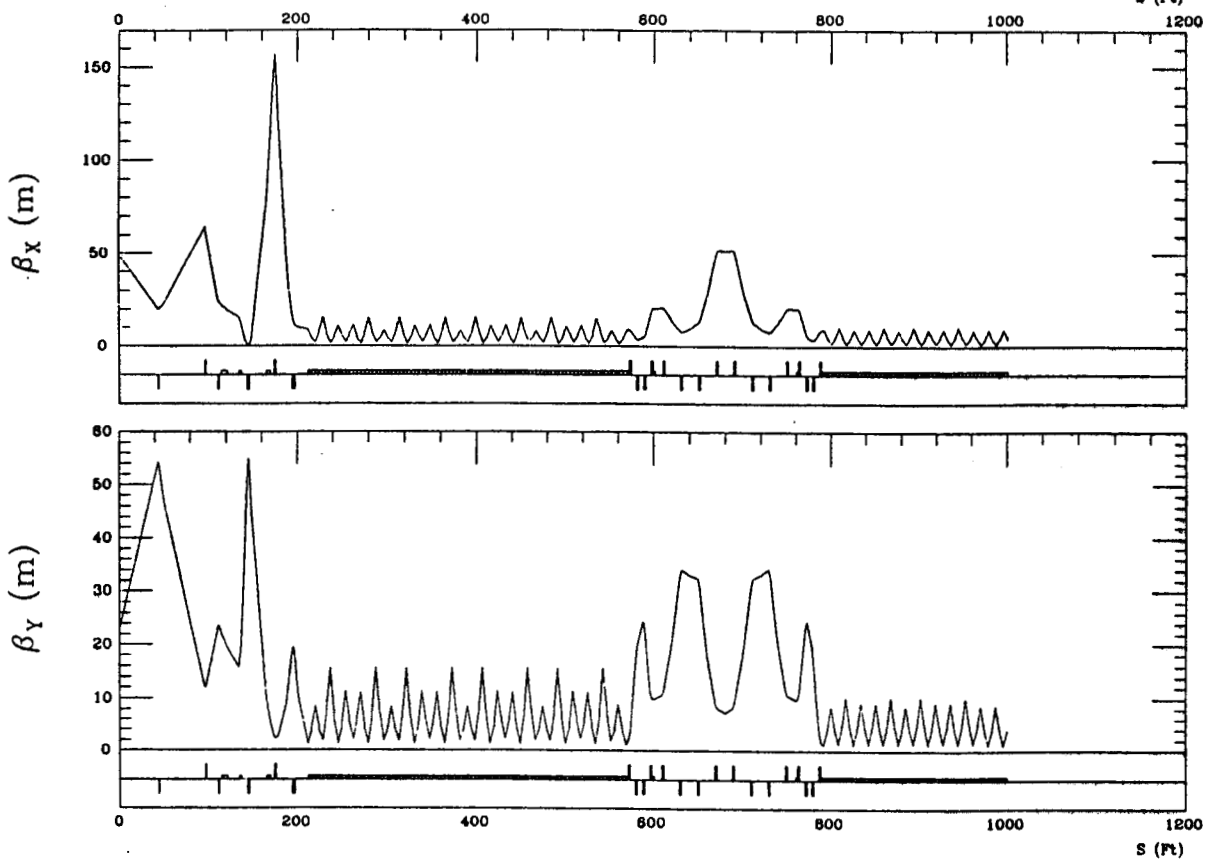
BKUP ARCNGEO B (11/18/82): 4000 FT TO ARC END



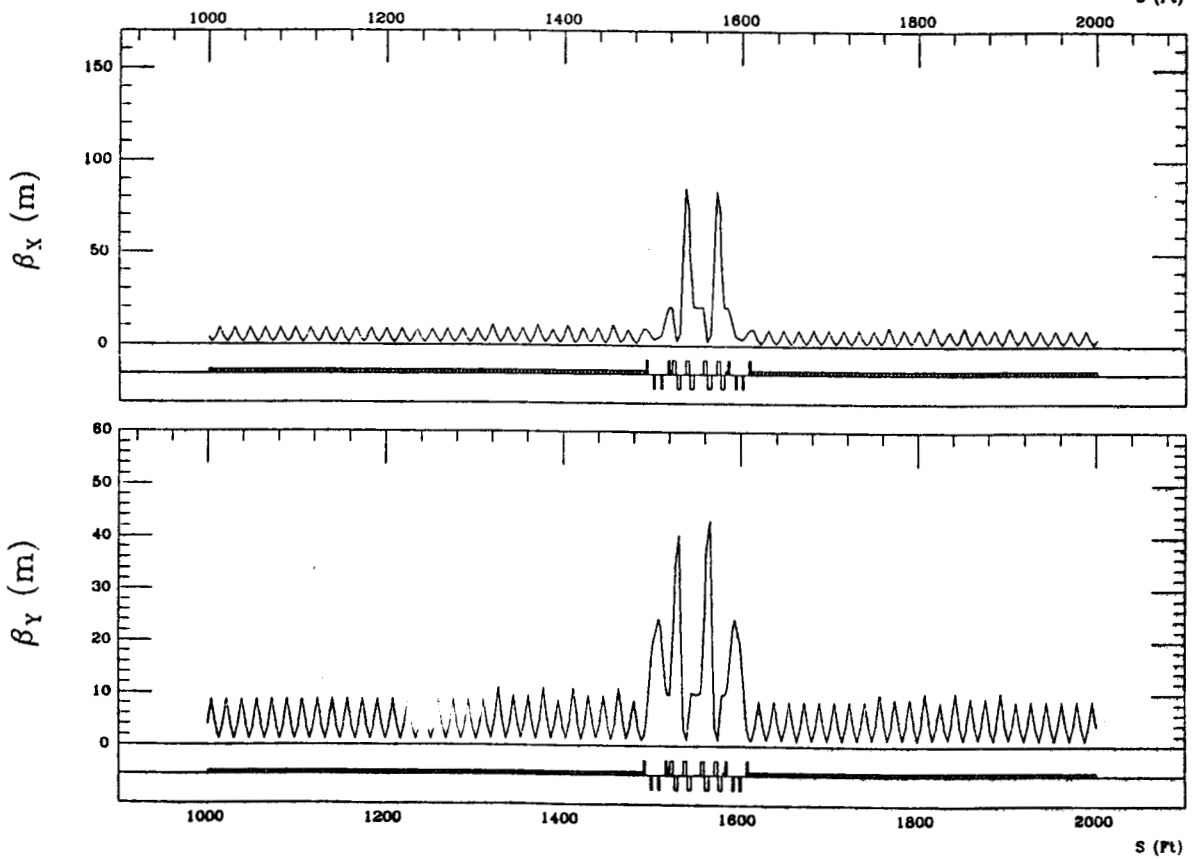
BKUP ARCNGEO B (11/18/82): ARC END TO I.P.



ARCS FINAL (12-27-83): BEGINNING TO 1000 FEET Fig.3.3.19

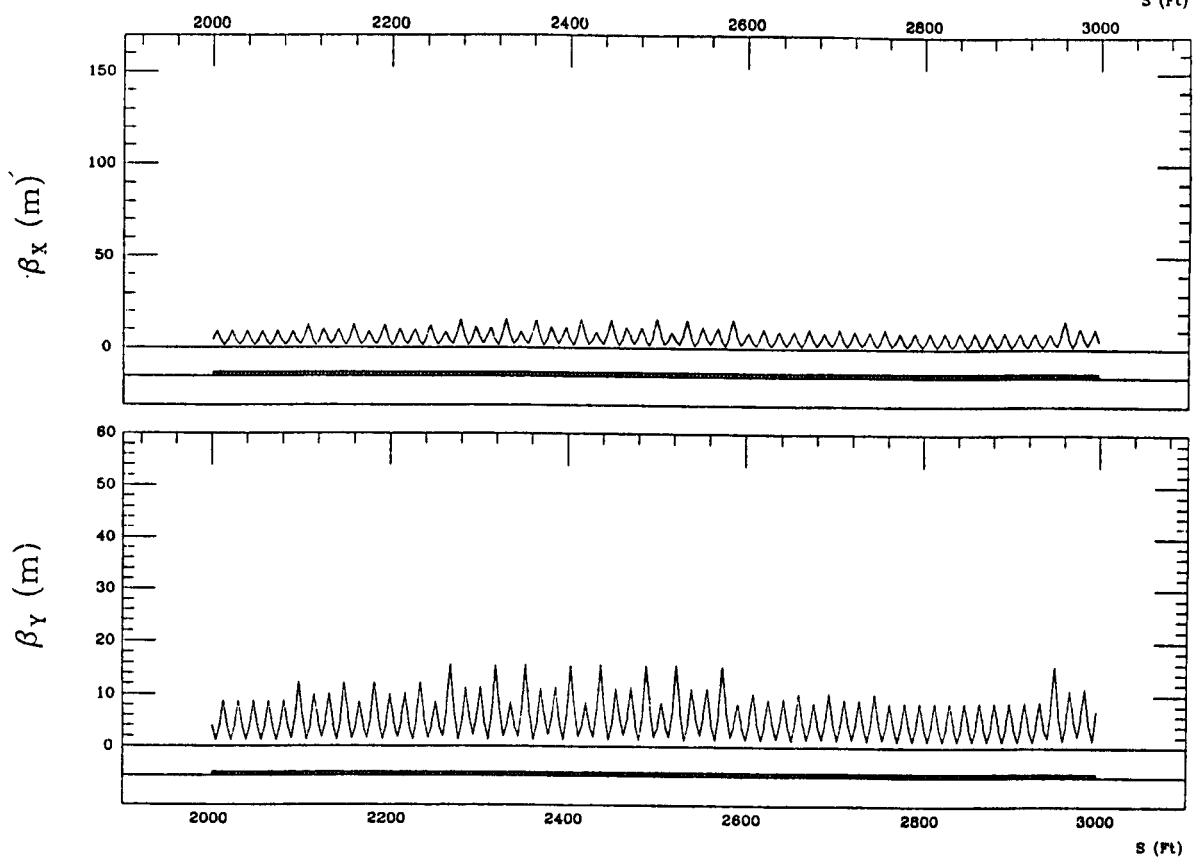


ARCS FINAL (12-27-83): 1000 FEET TO 2000 FEET Fig.3.3.20



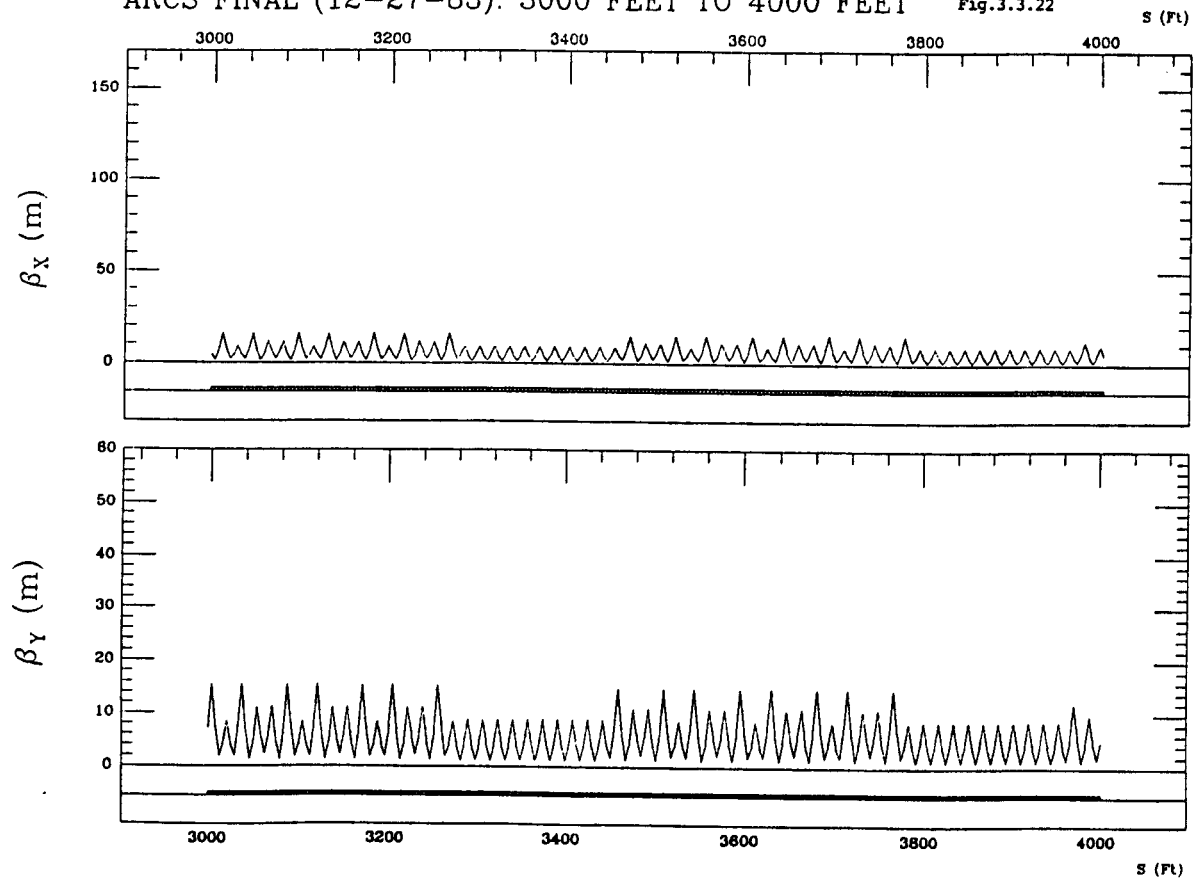
ARCS FINAL (12-27-83): 2000 FEET TO 3000 FEET

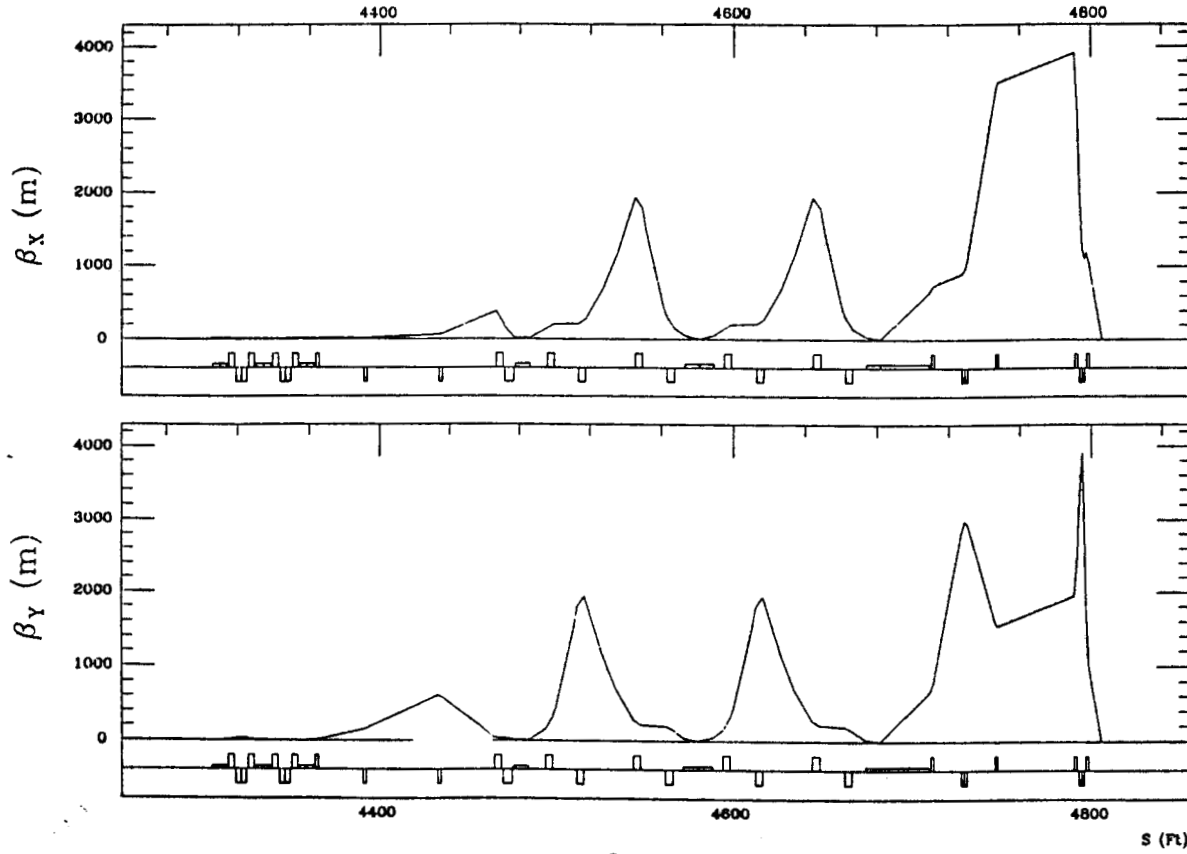
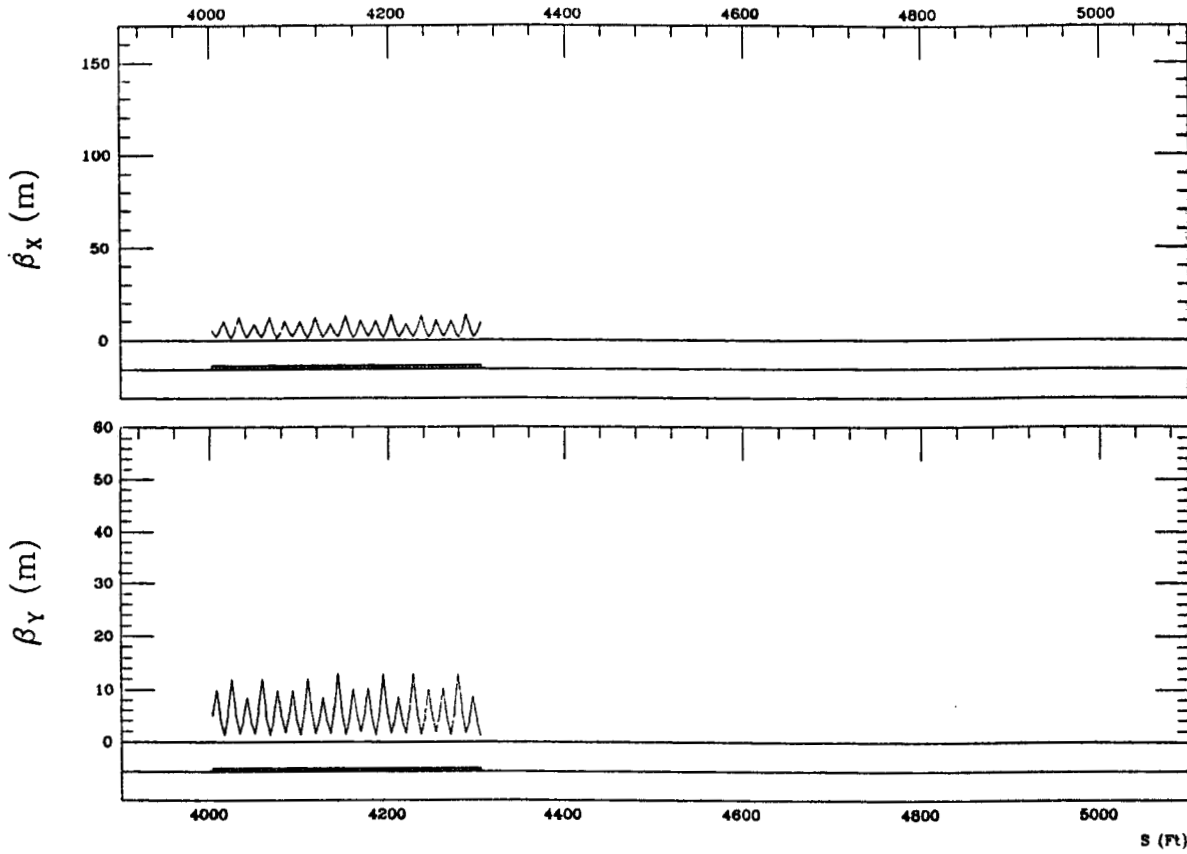
Fig.3.3.21



ARCS FINAL (12-27-83): 3000 FEET TO 4000 FEET

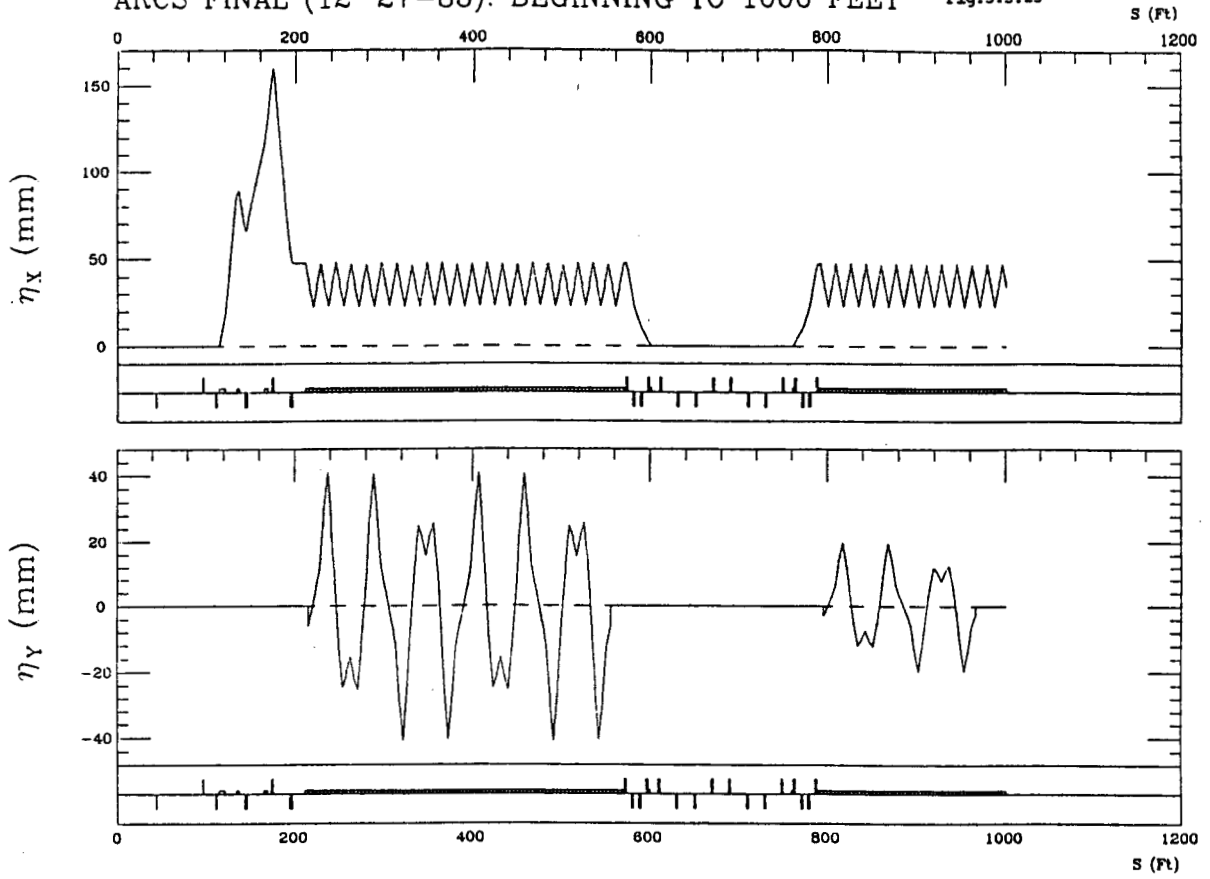
Fig.3.3.22





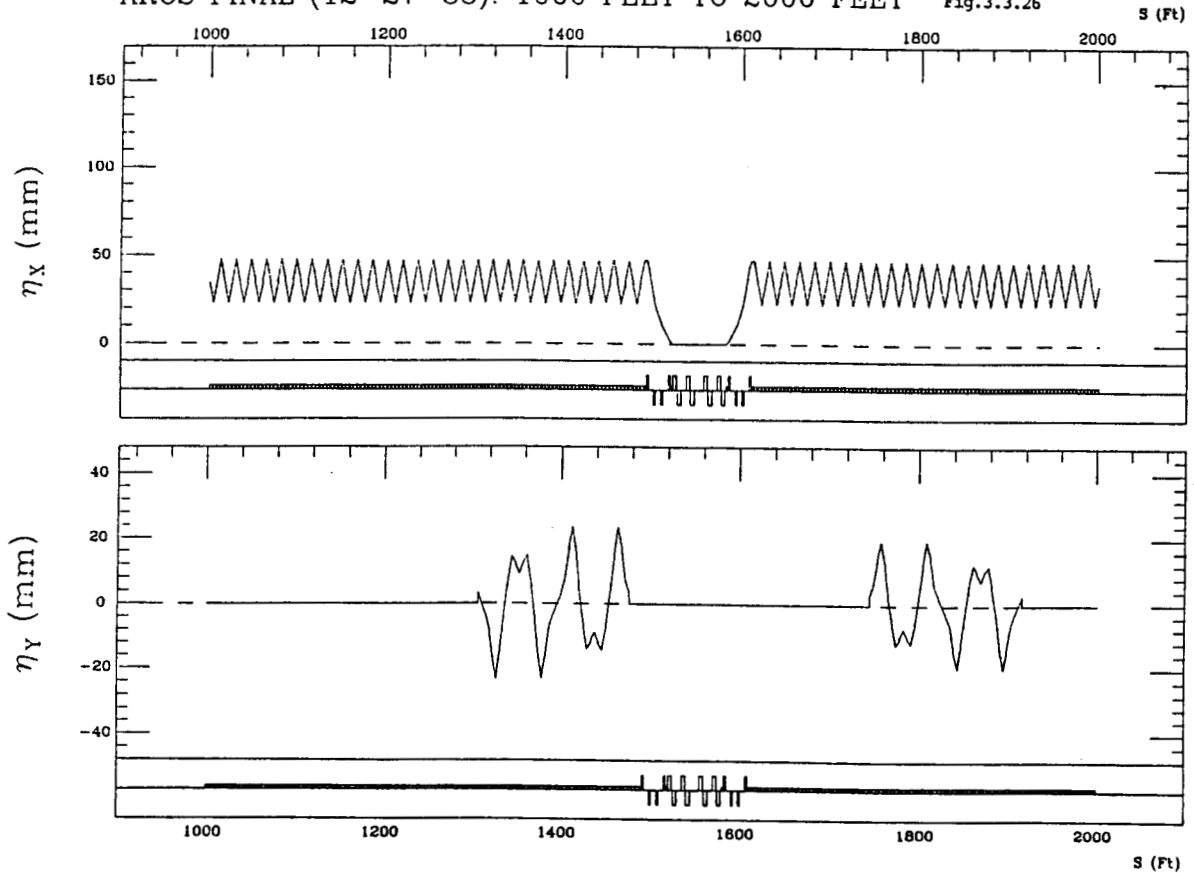
ARCS FINAL (12-27-83): BEGINNING TO 1000 FEET

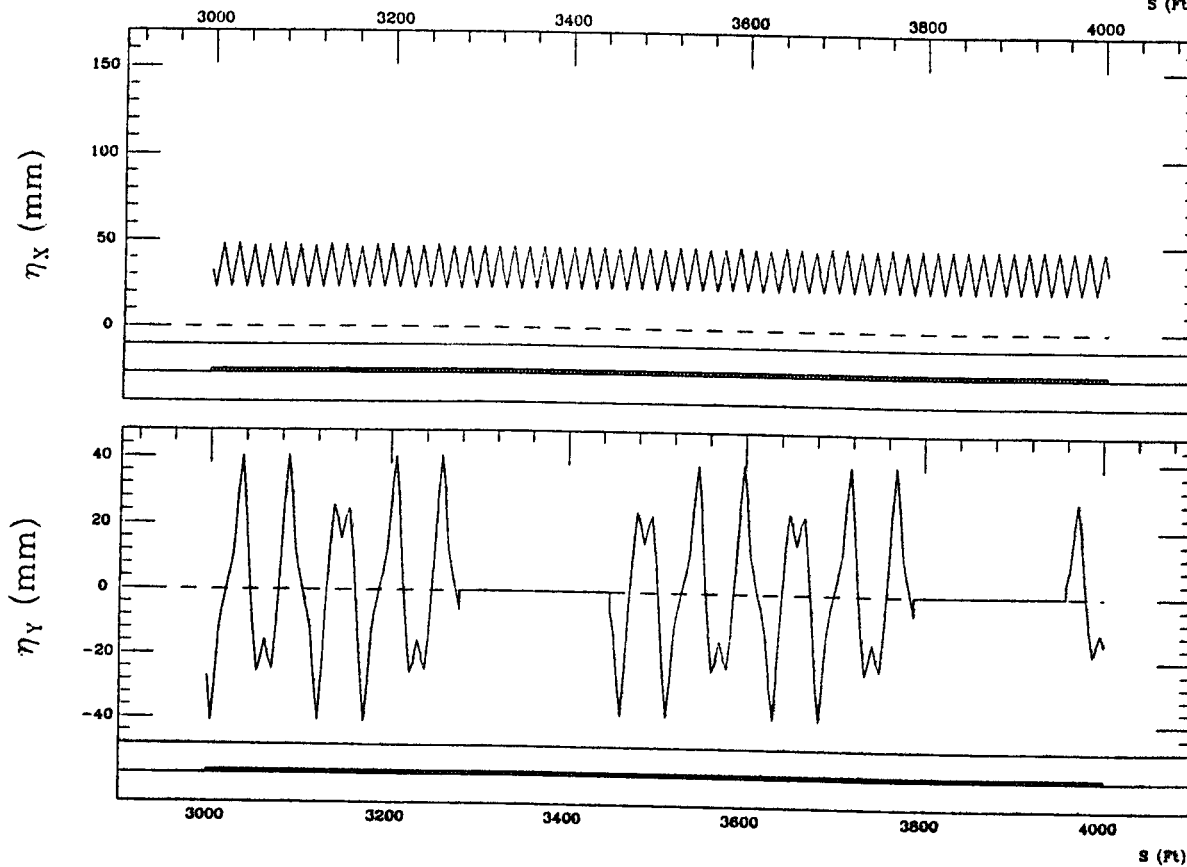
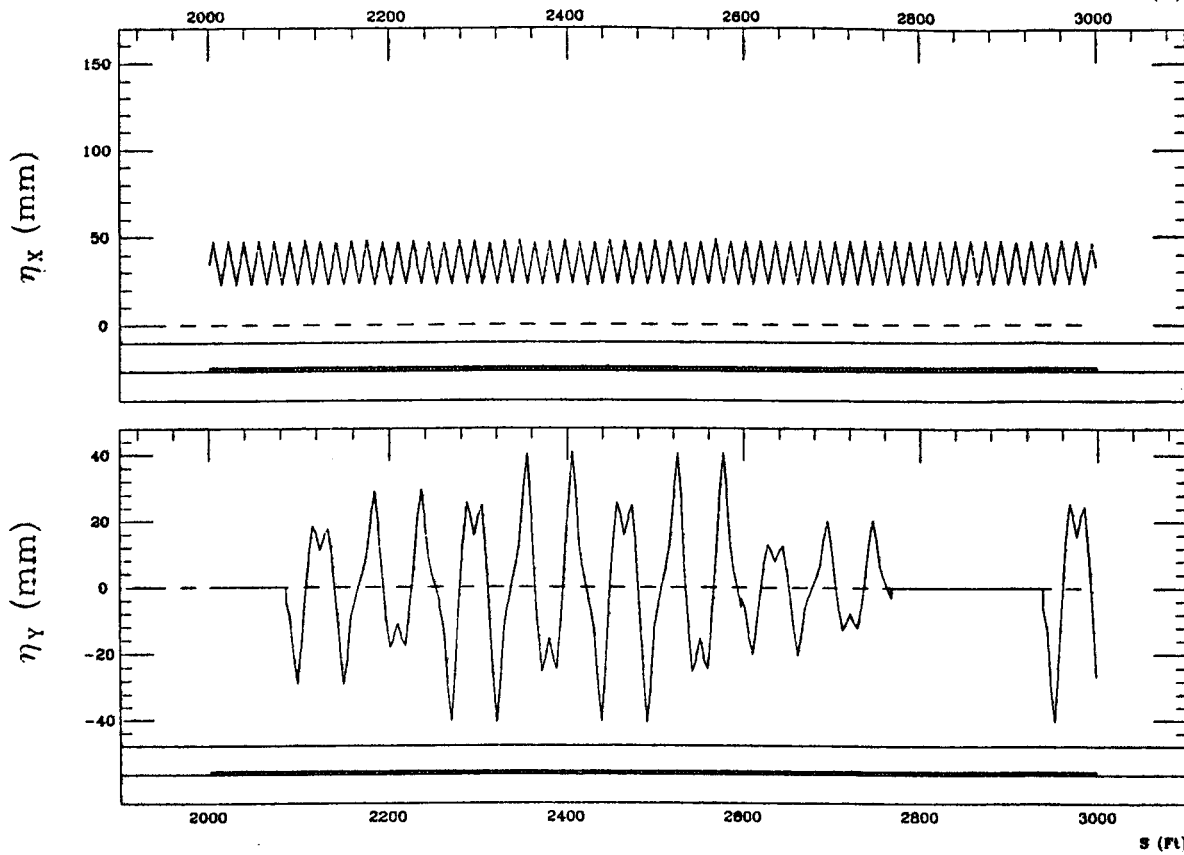
Fig.3.3.25



ARCS FINAL (12-27-83): 1000 FEET TO 2000 FEET

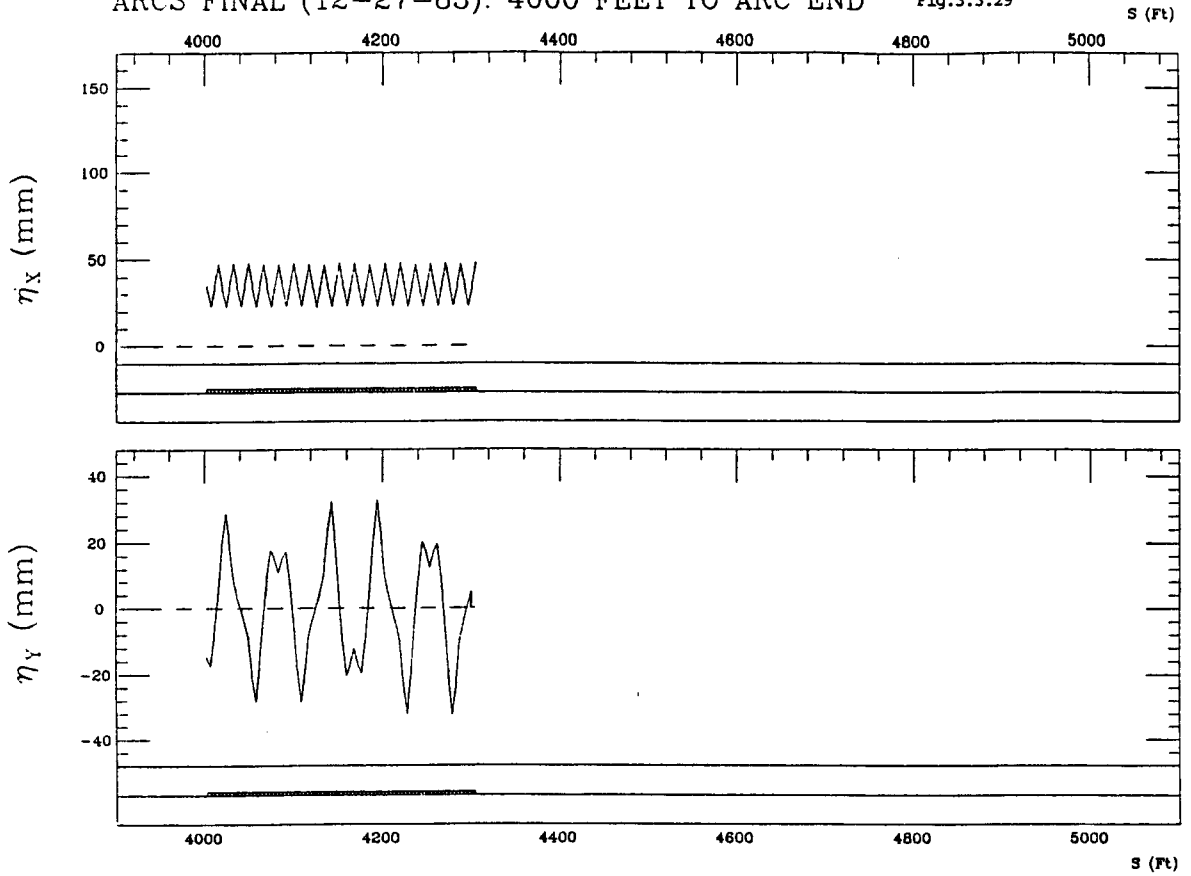
Fig.3.3.26





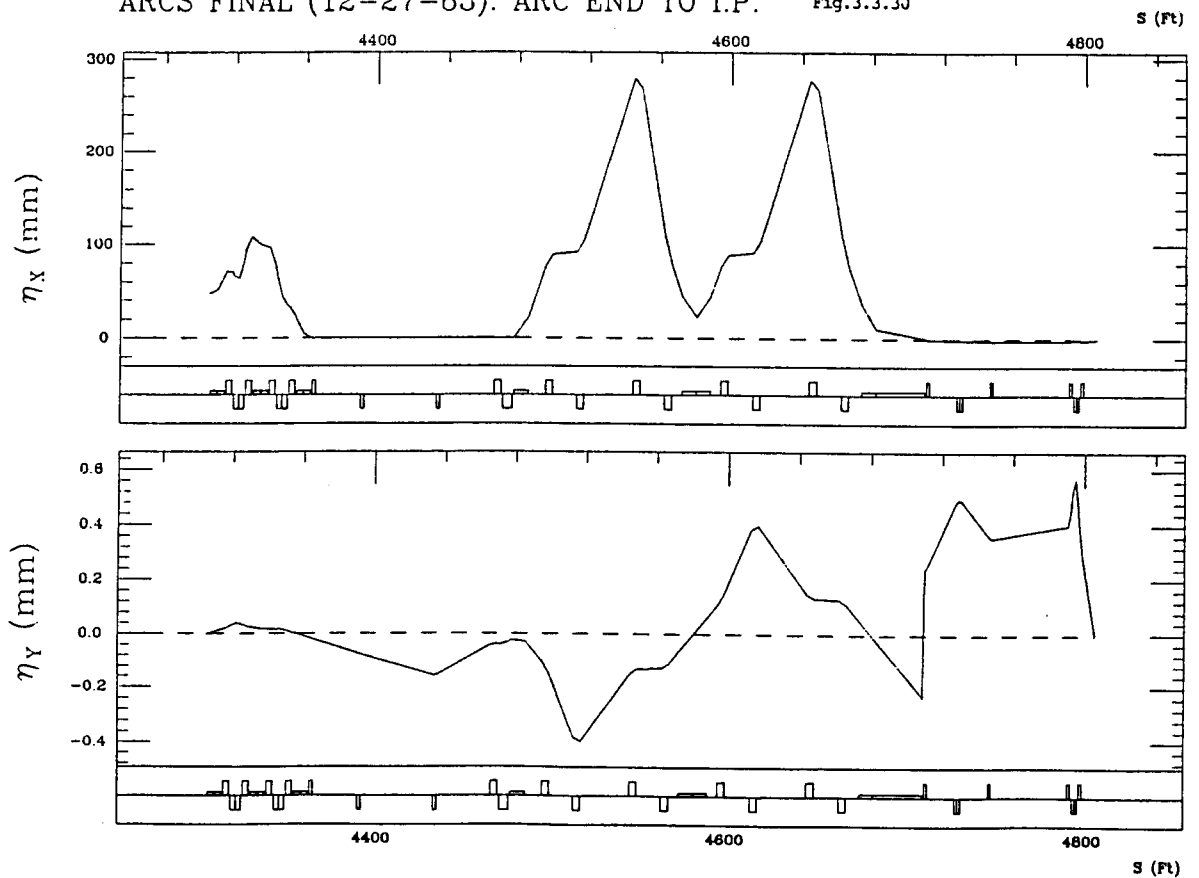
ARCS FINAL (12-27-83): 4000 FEET TO ARC END

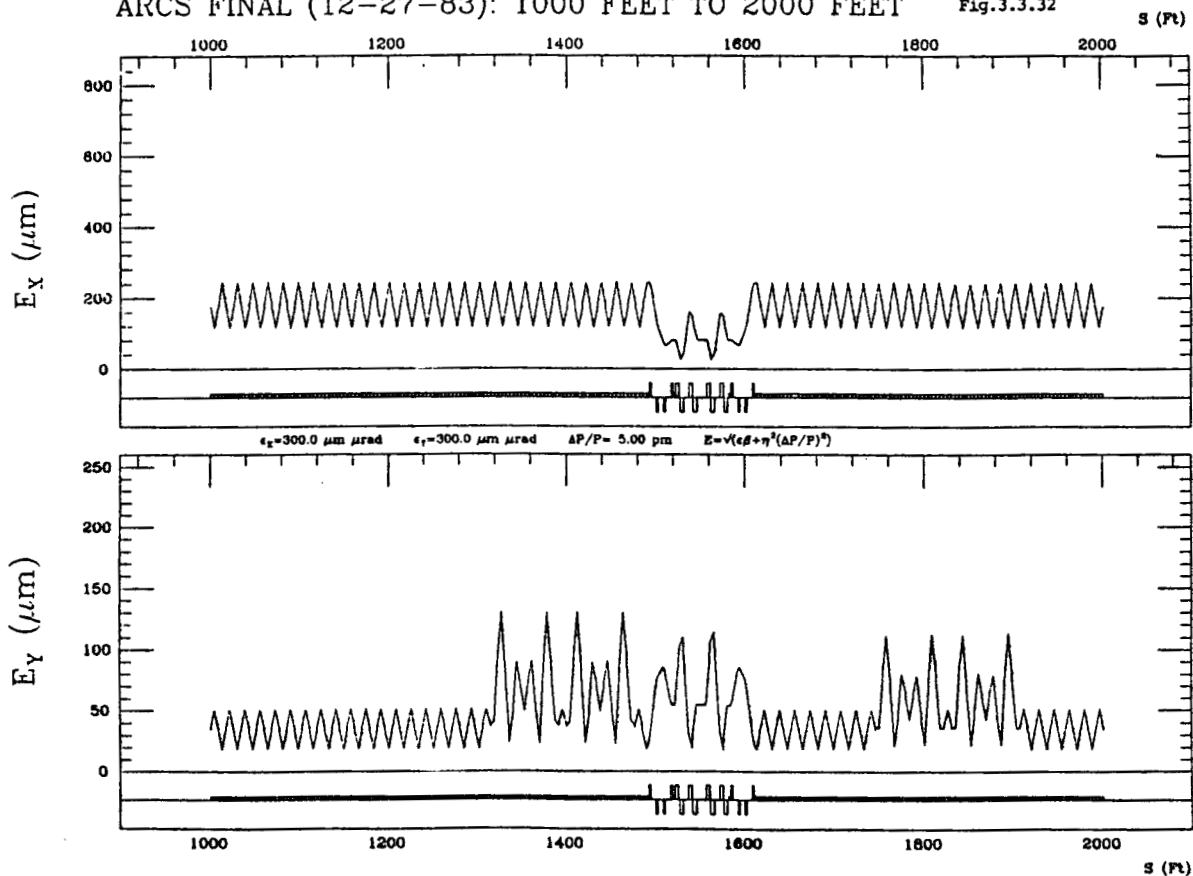
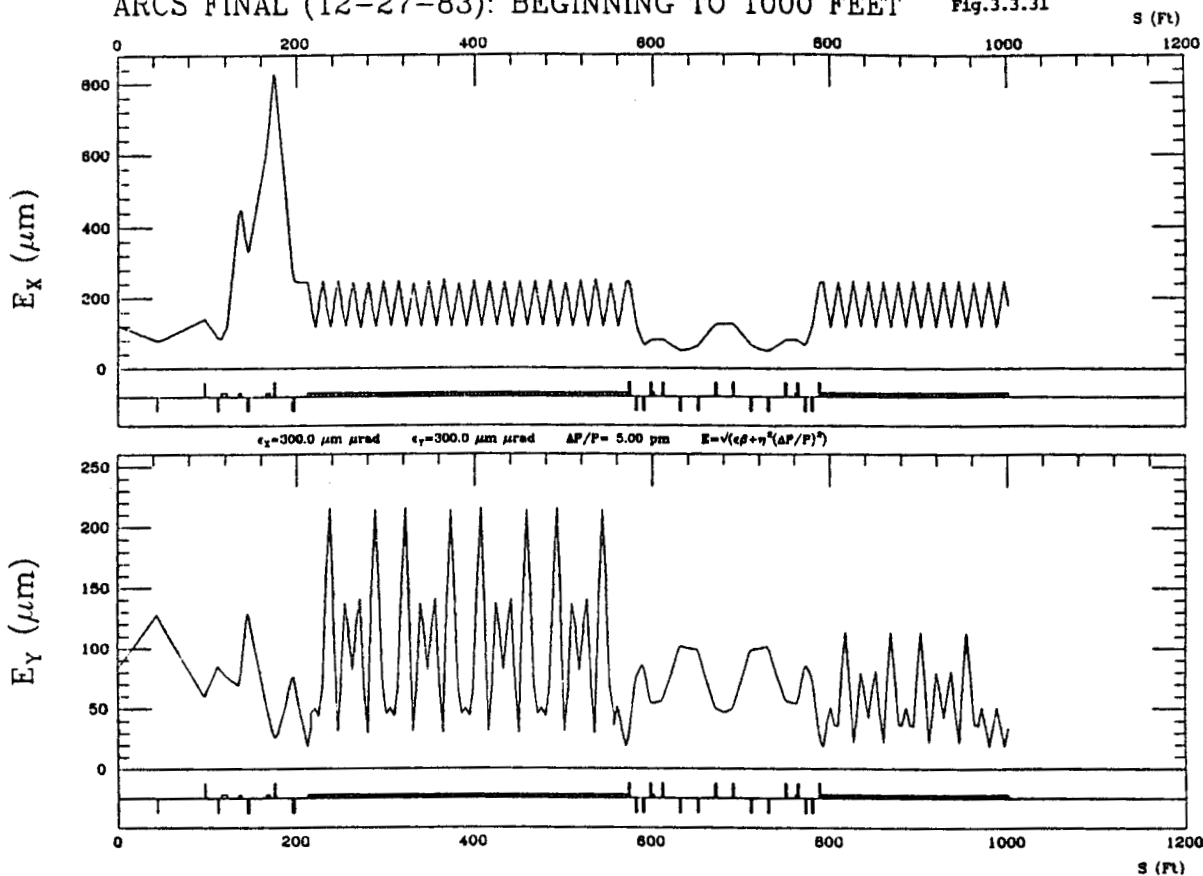
Fig.3.3.29



ARCS FINAL (12-27-83): ARC END TO I.P.

Fig.3.3.30

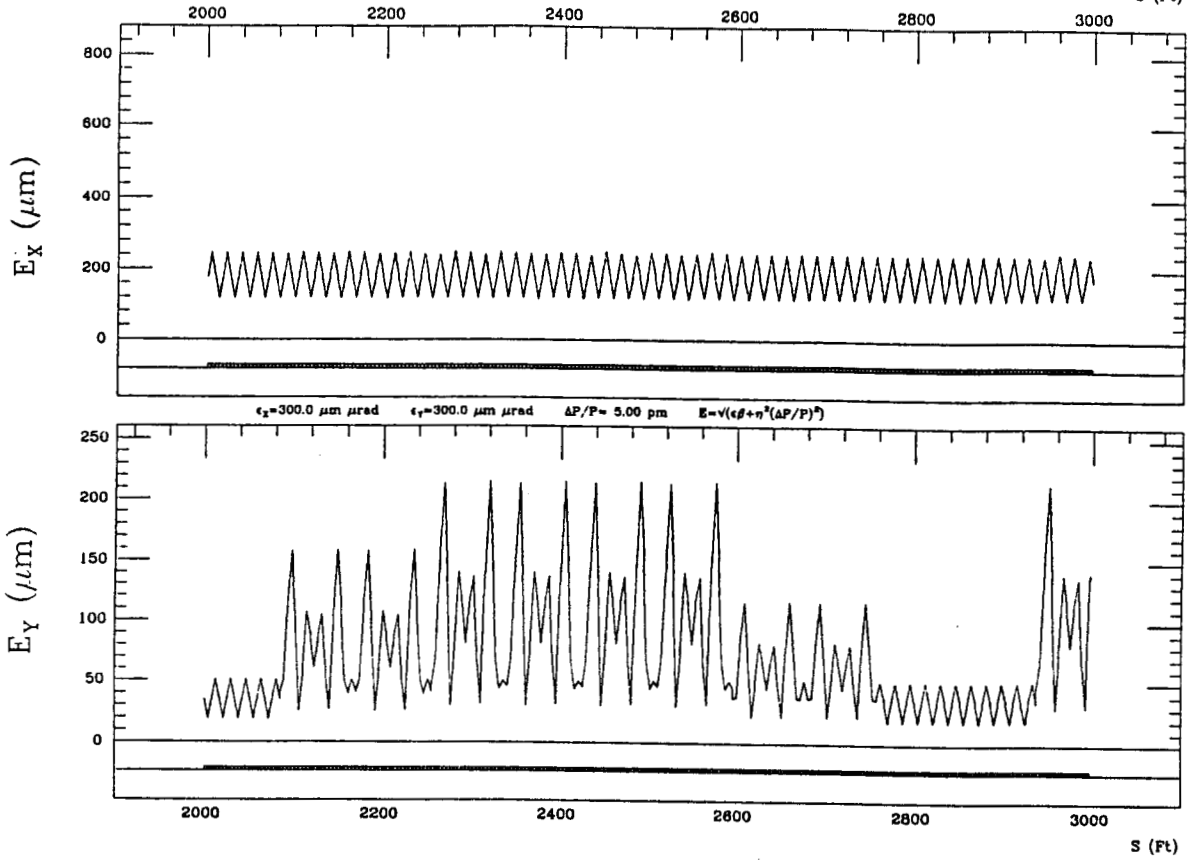




ARCS FINAL (12-27-83): 2000 FEET TO 3000 FEET

Fig.3.3.33

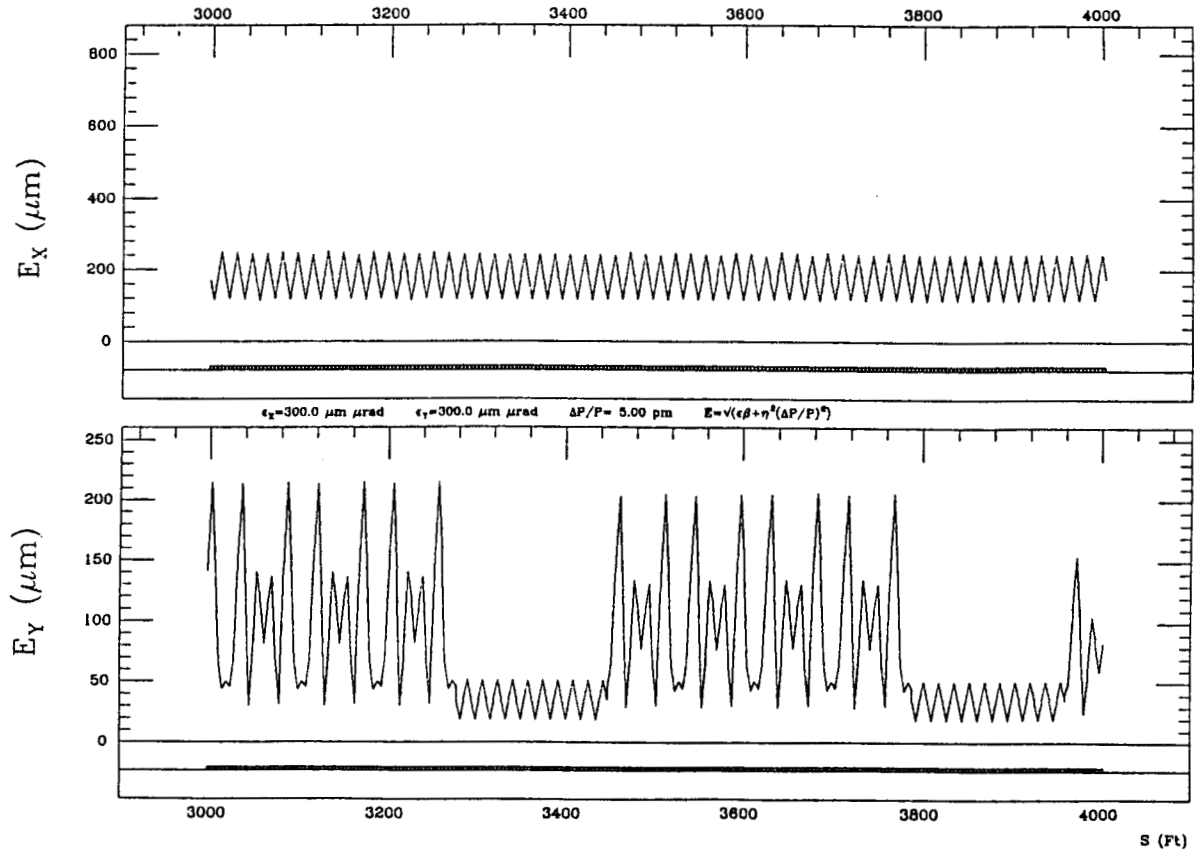
S (Ft)

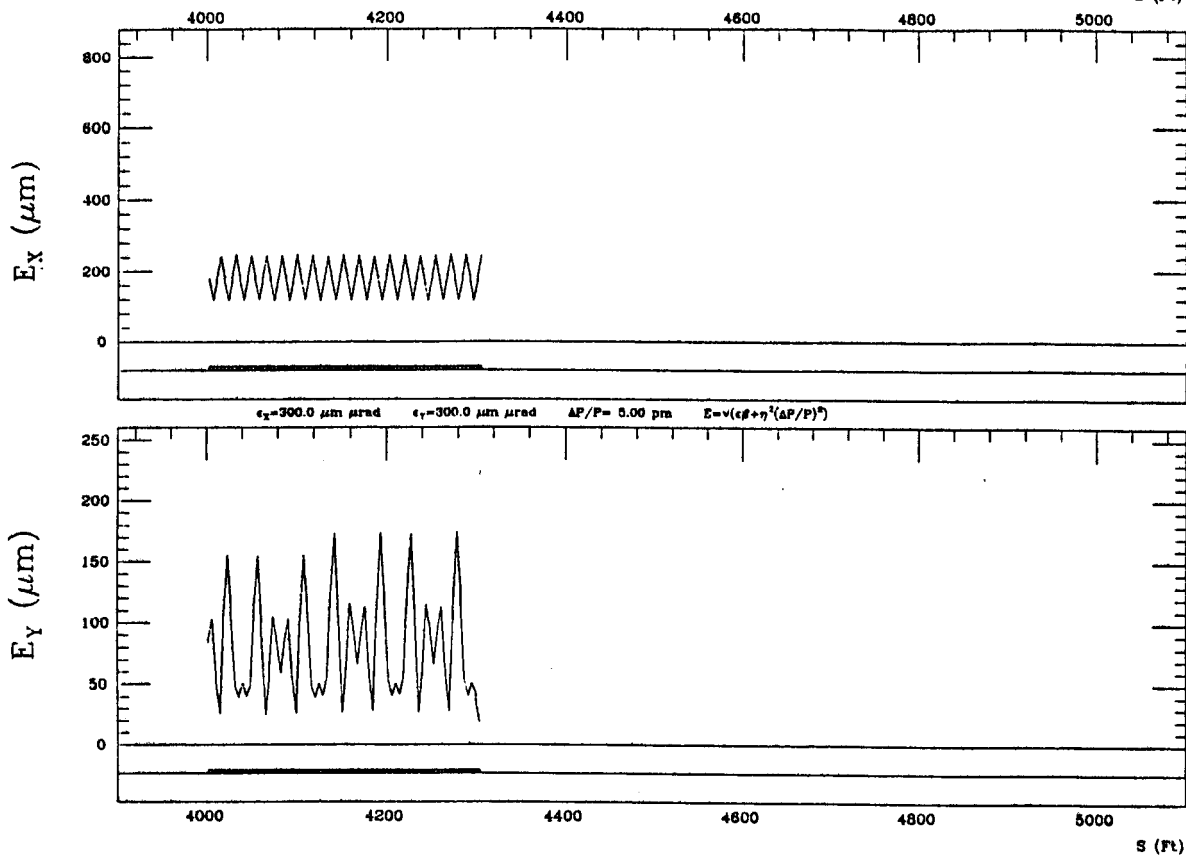


ARCS FINAL (12-27-83): 3000 FEET TO 4000 FEET

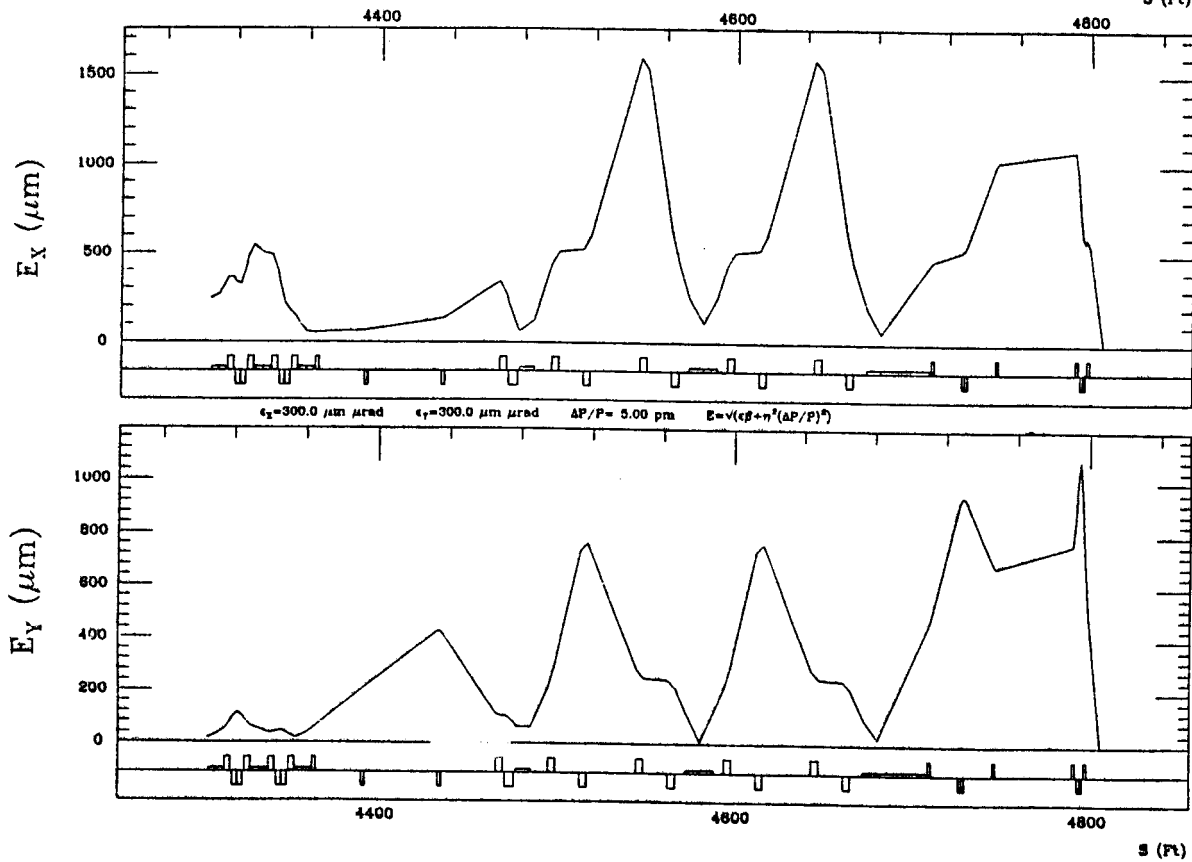
Fig.3.3.34

S (Ft)





ARCS FINAL (12-27-83): ARC END TO I.P.   Fig.3.3.36



# ENERGY LOSS IN COLLIDER ARCS

$\rho = 279.4\text{m}$ ,  $\phi$  north = 236 degrees.

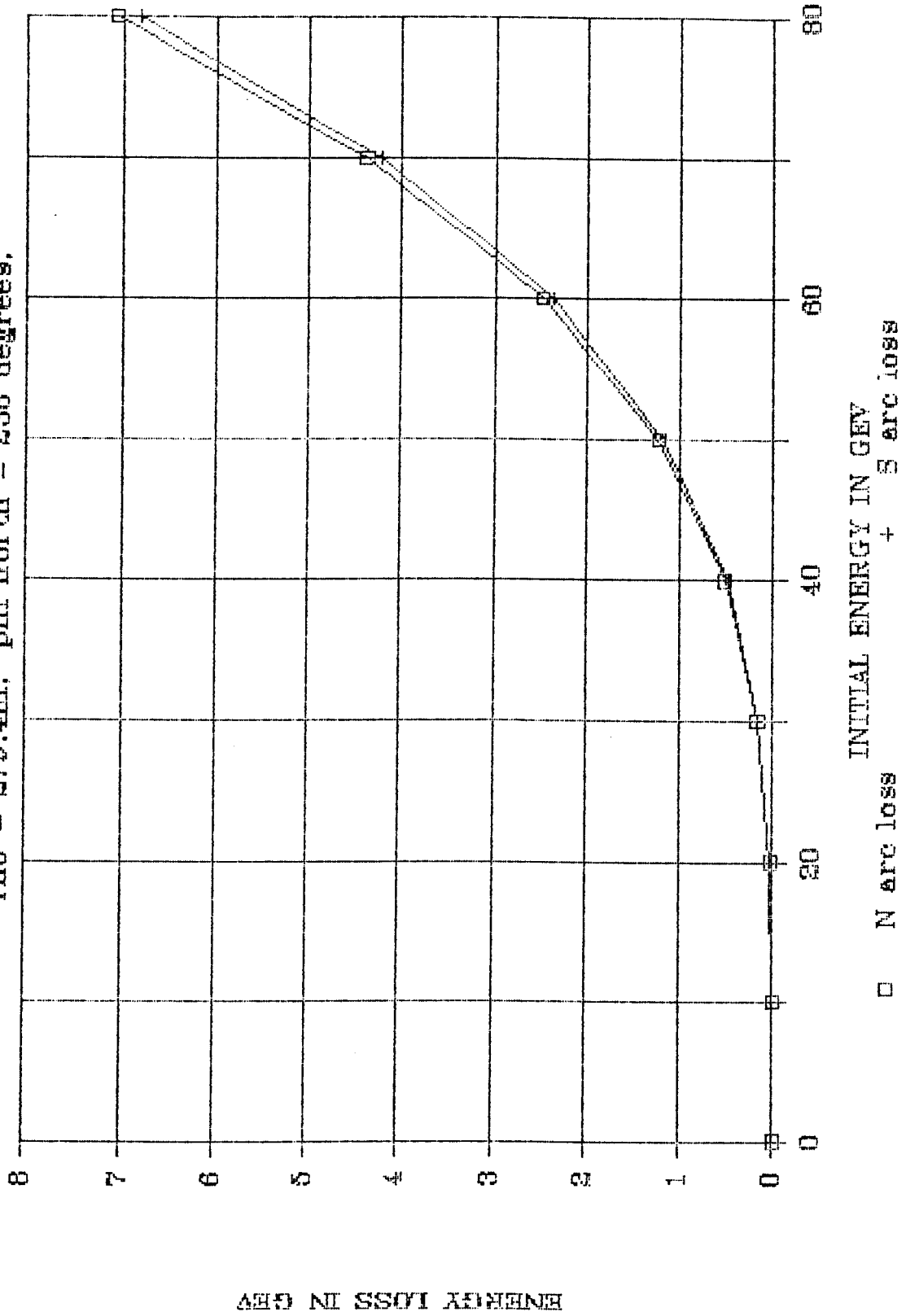


Figure 3.3.37

### 3.3.4 Optics of the Reverse Bend and Instrument Sections

On examining Figure 3.2.2 the reader will notice that following achromat No. 7 the bending radius must reverse its sign which will give rise to a reversal in sign of the dispersion function ( $\eta_x$ ). It is the function of the reverse bend matching sections (RB) to provide this match in a proper way. Following the principles outlined above, this is accomplished by the insertion of a unit (+1) optical transform. The effects can be seen, for example, in Figure 3.3.8. Notice that the vertical dispersion function resulting from rolls is also zero. As stated earlier, that since the dispersion functions have been suppressed, portions of these regions are therefore suitable for a measurement of the beam size due to purely betatron motion. For this reason, the beta functions have been increased as much as is practicable, the limits being set by realizable focusing strengths and the lengths at the insertion. The resulting beta functions are depicted in Figure 3.3.2.

The north and south reverse bend matching sections each contain four dipoles and sixteen quadrupoles arranged symmetrically about the center of the insertion. For reasons of terrain layout, the south arc contains an additional non-bending dummy insertion of similar design but with considerable drift space, (see achromat 3 south on Figure 3.2.2), which happens to pass directly below the building housing the main control center (MCC). For these reasons it has been called the Instrument section.

### 3.3.5 Vacuum Requirements

The collisions of electrons and positrons with the residual gas in the arcs gives rise to a number of processes which cause phase space dilution and extra energy spread. Among these are single and multiple coulomb scattering and bremsstrahlung.<sup>13-14</sup> These considerations are outweighed by the an effect<sup>15</sup> in which ions produced by particles in the head of a bunch defocus the tail. At present the average arc pressure is designed to be about  $10^{-4}$  torr.

### 3.3.6 AG Magnet Specifications

The current lattice design calls for a combined function dipole, quadrupole

and sextupole field distribution in the standard arc magnets of the form,

$$B_y = B_{y0} \left[ 1 - \frac{n}{\rho} x + \frac{\beta}{\rho^2} x^2 + \dots \right] \text{ for } y = 0.$$

The sextupole term in the expansion is needed to increase the momentum pass band of the system.

In general, TRANSPORT assumes a "hard edge" magnet model in which the effects of both bending and focusing are constant over the same constant length. The actual physical magnet on the other hand is described by an equivalent effective length which is larger than the iron core and takes into account the way the fields fall off at the ends of the magnet. Since in this combined function magnet the effective dipole and gradient lengths are not equal, adjustments to the central (i.e., two dimensional) field parameters, which are needed for profile design, need to be made. TRANSPORT fitted parameters of the expansion above, relevant to the recently adopted "10 cm" drift configuration are listed both for the "hard edge" and "physical corrected" magnet in order to avoid confusion on the part of those who wish to use these values. In the TRANSPORT listed values the hard edge bending length is used.

For  $E = 50 \text{ GeV}/c$  beam momentum we have, assuming  $c=2.99792458$   
and  $B\rho \text{ (KGm)} = 33.35640952 \text{ Po (GeV}/c)$

	Values for TRANSPORT Simulation	Values for Physical Magnet Design
Dipole Field in KGauss	$B_{y0} = 5.96976$	5.96976
Bending Radius in Meters	$\rho = 279.378$	279.378
Field Index	$n_f = -32823.7$	-32847.5
	$n_d = + 32824.7$	+32848.5
Field Gradient KG/cm at Equil. Orbit	$g_{av} = 7.0139$	7.0189
Sextupole Terms:	$B_s = 1/2 g^l x^2$	
in focusing magnet:		
	$\frac{\beta_F}{\rho^2} = +0.0013580 \text{ mm}^{-2}$	0.001357
	$g^l = + 1.629 \text{ kG/cm}^2$	+1.629
in defocusing magnet:		
	$\frac{\beta_D}{\rho^2} = -0.0022697 \text{ mm}^{-2}$	-0.0022748
	$g^l = -2.701 \text{ kG/cm}^2$	-2.702
Eff. Arc Length of Magnet $\ell$	$= 2.502999 \text{ m}$	$L_b = 2.50300 \text{ m}$ $L_g = 2.48565 \text{ m}$ iron $L = 2.47935 \text{ m}$
1/2 cell arc length	2.596201936 m	
Total Arc Cell Length	5.192402112 m $= 17.03544 \text{ feet}$	
1/2 Cell Bend Angle	0.513323348°	

### 3.3.7 Energy Loss Due to Synchrotron Radiation

The usual formula of energy loss per turn applies only in the approximation in which the loss portion is small. This may not be the case for the collider.<sup>16</sup>

The differential loss equation

$$\frac{dU}{d\phi} = \frac{8.85 \times 10^{-5}}{2\pi\rho} (E_o - U)^4$$

in which  $E_o$  is the initial energy,  $\rho$  the bending radius and  $\phi$  the bending angle travelled since the start has the solution

$$U = E_o \left[ 1 - (1 + 3\alpha\phi)^{-\frac{1}{3}} \right]$$

in which  $\alpha = 8.85 \times 10^{-5} E^3 / 2\pi\rho$ . To give the reader a feeling for the magnitude of effect, Figure 3.3.37 displays some numerical results for the case in which  $\rho = 279$  m and the north angle turned is 236.12 degrees. Since the south angle is 225.55 degrees, the effect is slightly smaller. At the time of this writing, the feeling is that it will be necessary to compensate the AG lattice for this effect by reducing the fields in the magnets along the arcs on an achromat by achromat basis.

### 3.4 TOLERANCES

#### 3.4.1 Ground Motion

Since the invention of strong focusing, it has been recognized that severe tolerances are placed on the position of magnetic elements. We assume below that a steady-state correction system will be effective in steering the beams around the transport arcs at the fractional millimeter level. In order to collide beams successfully at the interaction point at the micron level, however, a dynamic position feedback system is called for. If this system derives its positional information (i.e., error signal) from a previous beam pulse, its bandwidth is limited by the sampling theorem.<sup>17</sup> Suppose the Collider operates at 180 pps, then the upper limit of the band is 30 Hz. One must examine, therefore, whether disturbances occur around and above this frequency of sufficient amplitude to be injurious to the attainment of good luminosity. This has been done. Ground motion in the PEP tunnel and near the boundaries of the Collider site has been measured<sup>18</sup> in the frequency range of 0.1 to 100 Hz. These studies lead to the following conclusions.

1. Ground motions arising from natural causes, earth tides, earthquakes, microseismic noise due to storm action, etc., have either on-going amplitudes above 2 Hz that are negligible compared to the 0.2 micron rms tolerances<sup>19</sup> required, or else they occur very infrequently. Below 2 Hz, the wavelengths of the disturbances are larger than the Collider site and, therefore, not of importance in relative magnet motion. In addition, a slow feedback system can generally cope with them.
2. Careful design of buildings, structures and nearby equipment is indicated to suppress the effects of wind and of steady-state noise generated by pumps, ventilation fans, transformers, compressors and the like.<sup>20</sup> Control of on-site traffic of vehicles or heavy mobile equipment may be indicated.<sup>21</sup>

#### 3.4.2 Orbit Distortions

Because of the high field gradients in the magnets, the aperture in the Collider arcs is only a few millimeters. This requires good correction of the central beam

trajectory in order to stay inside the vacuum chamber. Accurate correction is also required because distortion of the central path would cause an additional growth in beam emittance due to synchrotron radiation, an effect which should be minimized. Finally, it is important to minimize higher order optical distortions which arise from large centroid displacements.

### 3.4.3 Correction Schemes and Tolerable Errors

Several correction schemes<sup>22</sup> remain under intensive investigation. All viable systems make use of numerous beam position monitors (500x and 500y indicators).

A distinctive property of an achromat, composed of combined function magnets, is that a transverse displacement of the magnet does not introduce residual dispersion into the system. It causes a centroid shift of the beam but it is independent of momentum. Current simulation studies indicate, therefore, that transverse magnet misalignments are best handled via "moving magnets." Residual dispersions in the total system are best corrected via a combination of "moving magnets" and backleg winding correctors in selected locations.

Magnet alignment errors that should be adequately correctable are:

Transverse displacements in $x$ and $y$	0.01 mm rms
Rotation about beam line	1 mr rms

and for the beam positions monitors:

Transverse displacements in $x$ and $y$	0.10 mm rms
---	-------------

After correction, the beam path distortions are then typically less than:

Horizontal = 0.5 mm rms	Vertical = 0.4 mm rms
-------------------------	-----------------------

Typical tolerable random magnetic errors are:

$$\Delta B\ell/B\ell \text{ rms} = 0.5\%$$

$$\Delta g\ell/g\ell \text{ rms} = 0.2\%$$

$$\Delta s\ell/s\ell \text{ rms} \approx < 4\%$$

#### 3.4.4 Wakefield Effects in the Vacuum Chamber

The electromagnetic field of the beam bunch induces in the walls of the vacuum chamber an image current which will then react back on the beam in a calculable way via the so called "wake-field" formalism. If the beam is not centered in the chamber, transverse forces on the bunch particles will result in addition to resistive longitudinal energy loss caused by the finite conductivity of the pipe.

Transverse forces will give rise to emittance growth, making it necessary to evaluate a "centering tolerance" of the beam with respect to the chamber. These can then be related to the mechanical tolerances of the chamber with respect to the magnet to which it is attached.

Interpretation of the calculation<sup>11</sup> is not straight forward, however, since potentially dangerous disturbances occur only at or very near the effective betatron frequency of the particles as they traverse the system. (Recall: 1 betatron wavelength is 56.78 feet of exactly  $20/3=6\ 2/3$  magnets.) For a chamber material of high conductivity, a transverse centering tolerance of about 1 millimeter appears to be adequate.

### 3.5 COMPONENTS

#### 3.5.1 Arc Magnets

**3.5.1.1 Arc Magnet Profile** The first published article on strong focusing<sup>23</sup> contains the design concepts of a magnet having the characteristics required for the SLC arcs. A suitable magnet cross section is shown in Figure 3.5.1.1. The distance between the position of the equilibrium orbit and the neutral pole is about 8 mm.

Detailed studies of the magnetic field quality with the program POISSON have been performed. First the approximate original configuration has been mapped into dipole geometry via the conformal transformation:

$$Z_{\text{dipole}} = X + iY = z_{\text{quad}}^2 = (x + iy)^2$$

Hence  $X = x^2 - y^2$  and  $Y = 2xy$

Figure 3.5.1.2 shows the resultant dipole which has been optimized for aperture and uniformity in the usual manner by shimming corners. The resultant "perfect" dipole is now mapped back into quadrupole geometry using the transformation:

$$z_{\text{quad}} = x + iy = Z_{\text{dipole}}^{\frac{1}{2}} = [X + iY]^{\frac{1}{2}}$$

$$\text{Hence } x = \left[ \frac{(X^2 + Y^2)^{\frac{1}{2}} + X}{2} \right]^{\frac{1}{2}}$$

$$y = \left[ \frac{(X^2 + Y^2)^{\frac{1}{2}} - X}{2} \right]^{\frac{1}{2}} \Rightarrow \frac{Y}{2x}$$

to produce a "perfect" quadrupole. The coordinates of such a profile are shown in Figure 3.5.1.3. An overall flux plot is shown in Figure 3.5.1.4. The second step of this process is now modified in order to introduce the required perturbative sextupolar content. The resulting pole shapes for the focusing magnet containing a positive sextupole and the defocusing containing a negative sextupole are shown in Figure 3.5.1.5 for the old 5 cm drift space configuration. Profiles for the new 10 cm drift solution will appear in the next update of this report.

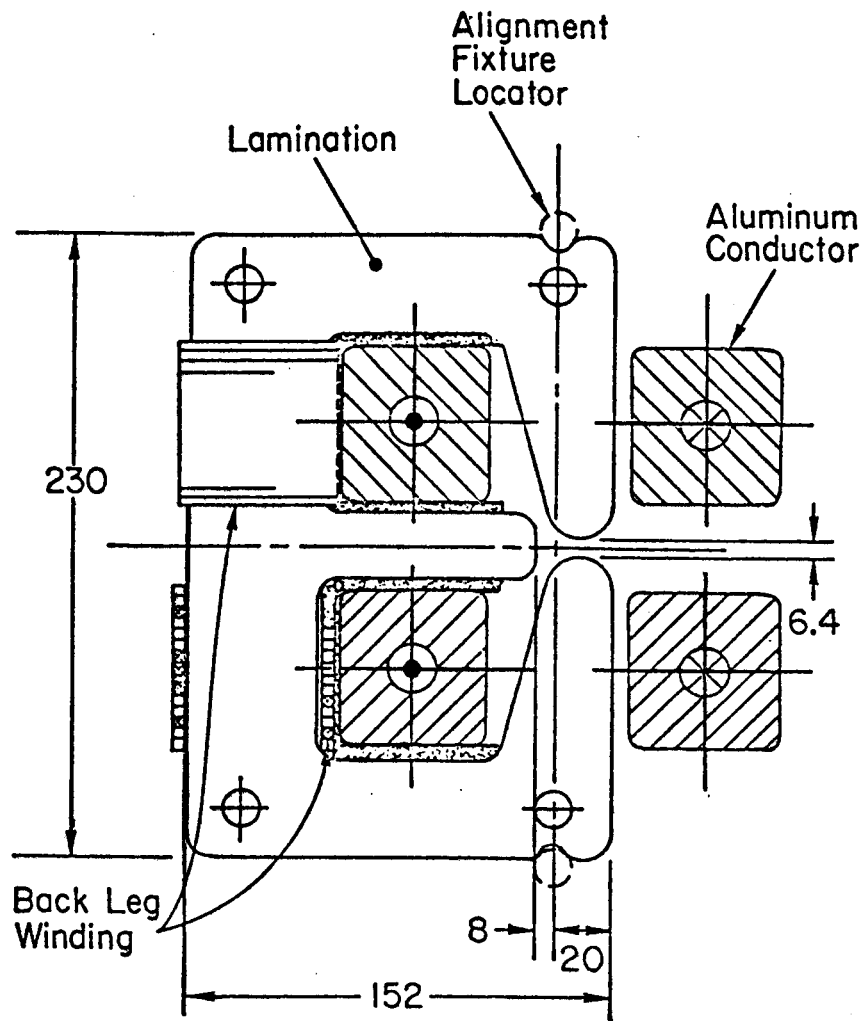


**Figure 3.5.1.1 Crosssection of Alternate Gradient Arc Magnet (Schematic)**

**TABLE 3.5.1.1**

**ALTERNATE FOCUSING MAGNET PARAMETERS AT 50 GEV**

Magnet designation		6AG2500
Number of Magnets		940
Field at 50 GeV	KG	5.986
Field Integral at 50 GeV	KGm	14.9423
Gap Height		
a) at equilibrium orbit	mm	16.4
b) minimum focusing	mm	7.344
c) minimum defocusing	mm	8.060
Width of Good Field Region	mm	+/- 4.0
Core Length	mm	2479.353
Core Weight	lbs	1100
Lamination Width	mm	152.5
Lamination Height	mm	230.0
Ampere-turns/pole	Amps	3982
Turns/pole		1
Conductor Cross Section	inches	2.190x2.060
Conductor area	mm <sup>2</sup>	2840
Cooling Hole Diameter	in	.375
Resistance at 55°C	milliohms	0.12
Power/Magnet	KW	1.65
Voltage Drop/Magnet	Volts	0.44
Current Density	Amps/mm <sup>2</sup>	1.37
Coil Weight	lbs	158
Number of Water Circuits		4
Water Flow Rate/Magnet	gpm	0.59
Water Velocity in Each Conductor	ft/sec	3.5
Temperature Rise per Circuit	Degrees C	11.5
Trim Windings		
No. of Coils		2
Turns/Coil		30
Maximum Current Rating	Amps	5

**3.5.1.2 Construction Parameters** An analysis of capital construction costs in relation to operating power costs indicates the use of aluminum as a conductor material and a generous coil window. Some parameters of the arc magnets are listed in Table 3.5.1.1

**3.5.1.3 Measurement of Models** Models of these designs have been constructed. Figures 3.5.1.6 and 3.5.1.7 depict laminated cores and show the arrangement of the four conductors which thread through the cores.

Figure 3.5.1.8 shows a full scale magnet under magnetic test. Measurements of the field are performed by moving a thin full length coil of appropriate curvature through the open side of the aperture. The resolution of coordinate setting is 1 micron. The device is computer controlled.

Figure 3.5.1.9 is a computer generated plot of the integrated strength per unit current as a function of distance from the equilibrium orbit at various levels of excitation of an early model which was designed to have a zero sextupole component. Analysis of the data shows (a) that the magnet is a very linear quadrupole over at least  $\pm 4$  mm, (b) that the ratio  $K = B/g$  (dipole/gradient) is very nearly independent of current, (c) that the sextupolar content is very nearly zero and higher order coefficients are virtually nonexistent.

Figure 3.5.1.10 is a plot of the saturation characteristics of the core up to 6000 amp turns/pole. At 50 GeV the magnet is still in the linear region.

Figure 3.5.1.11 is a plot of the raw magnetic data of a magnet model recently constructed of trial laminations whose profile contains the calculated sextupolar content required for a defocusing magnet of the so-called "5 cm drift" solution. Notice the curvature produced by the negative sextupole. Fits to the data show that the precise values of required dipole and gradient content can be achieved by minor adjustments to the excitation current and position of equilibrium orbit. After this is done the remaining parameter, namely the sextupole strength is within a few percent of that specified and hence well within the required tolerance.

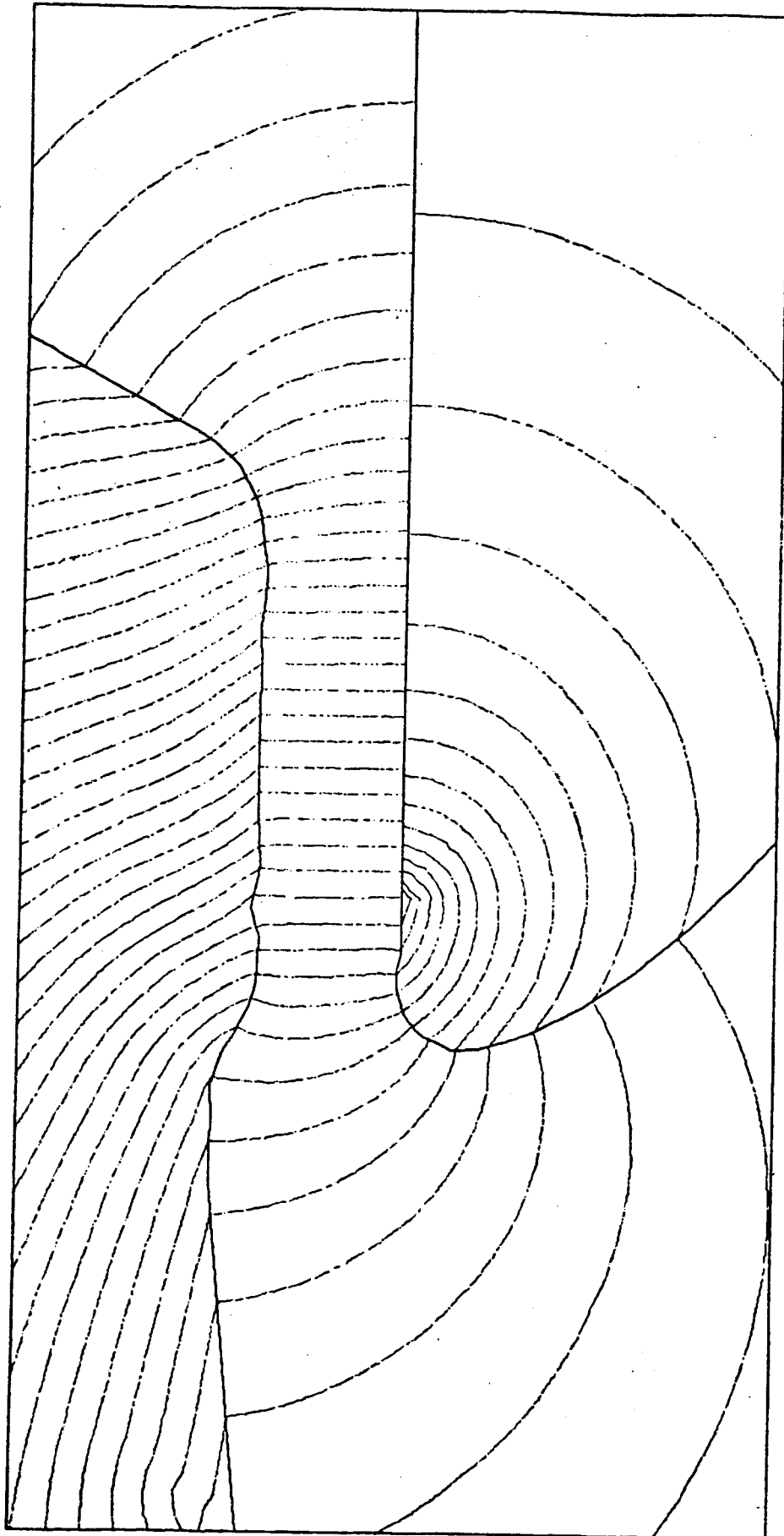
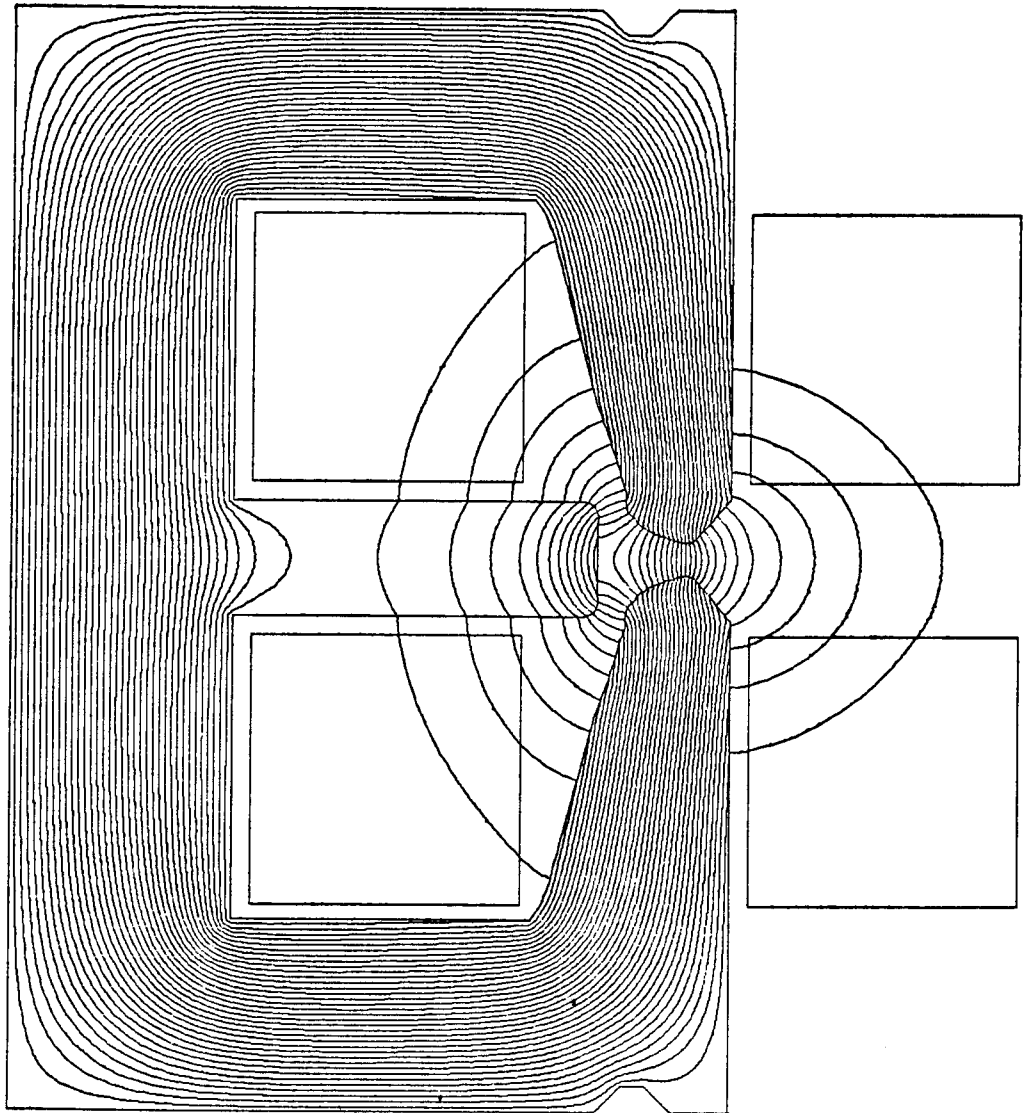


Figure 3.5.1.2: AG Magnet Transformed into Dipole Geometry





**Figure 3.5.1.4: Field Distribution in the SLC Arc Magnets**

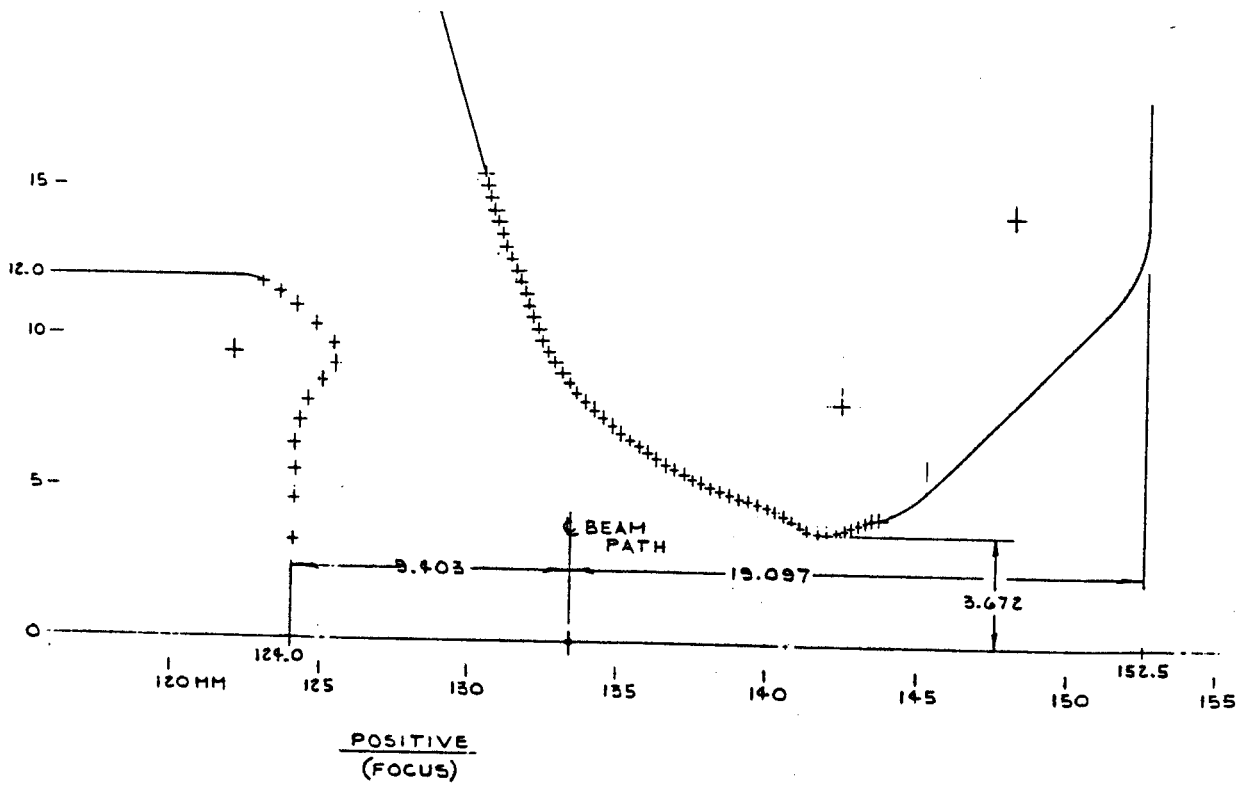
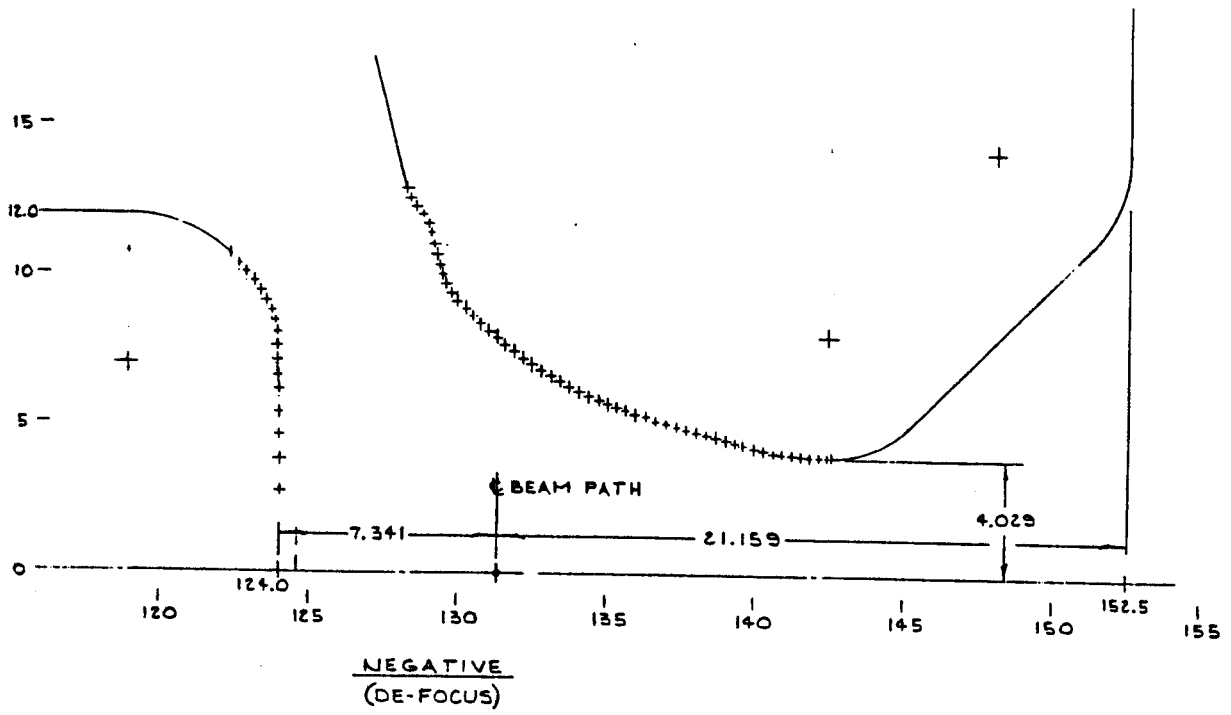


Figure 3.5.1.5 a,b, Pole profiles for Focus and Defocus AG Magnets  
(5 cm drift solution)

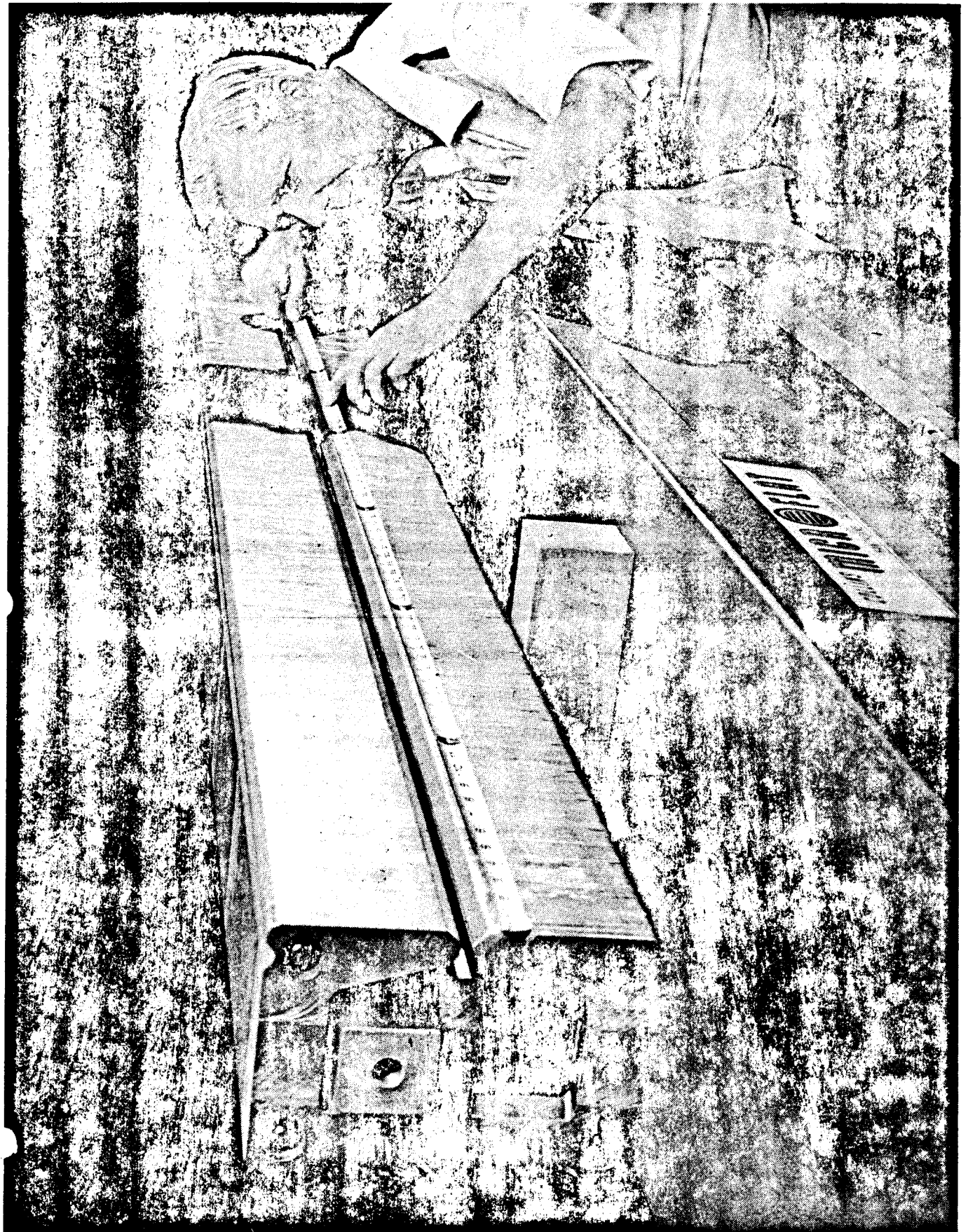


Figure 3.5.1.6: Full Scale Model of Arc Magnet

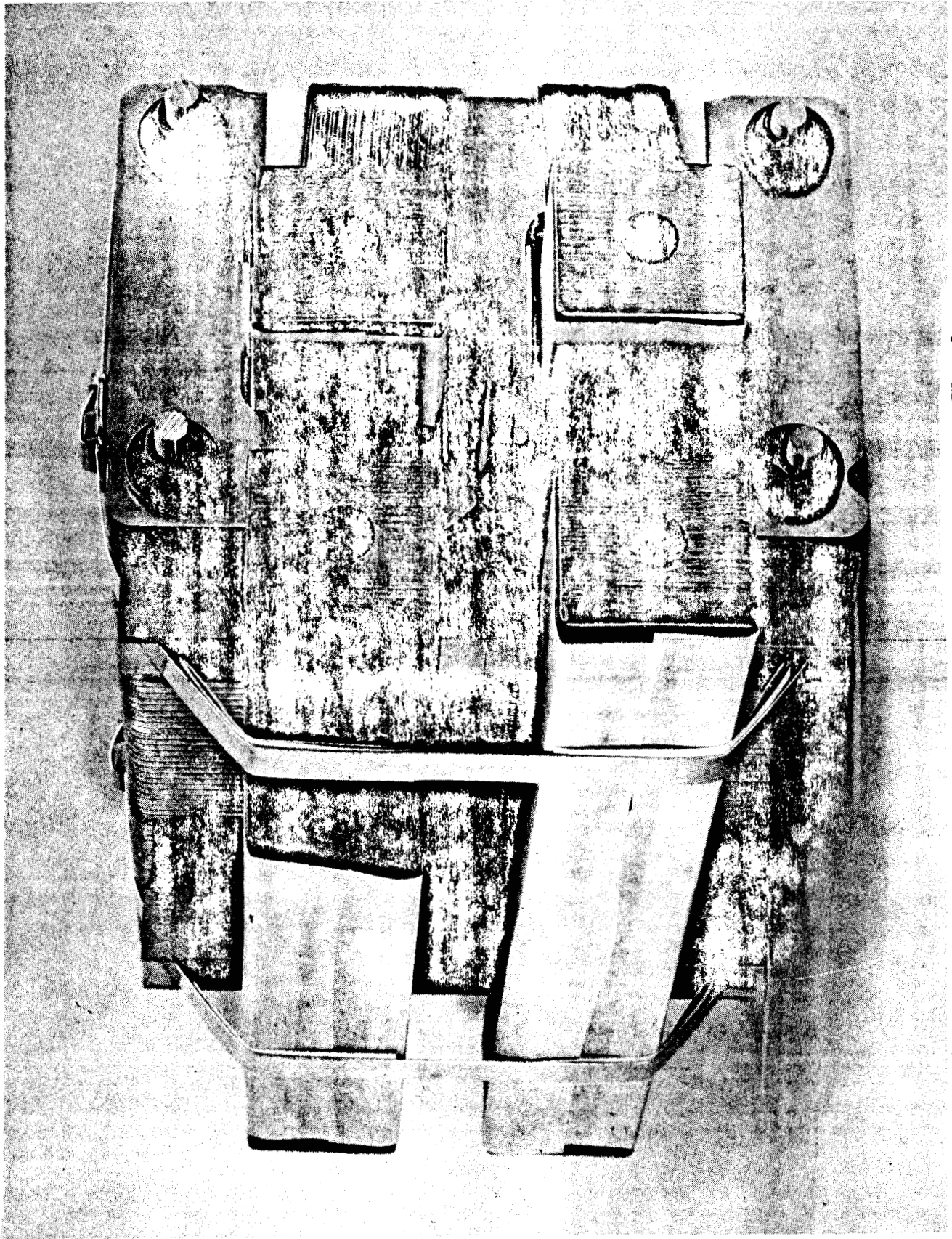


Figure 3.5.1.7: Bus Bar Coils and Vacuum Chamber  
in Arc Magnet

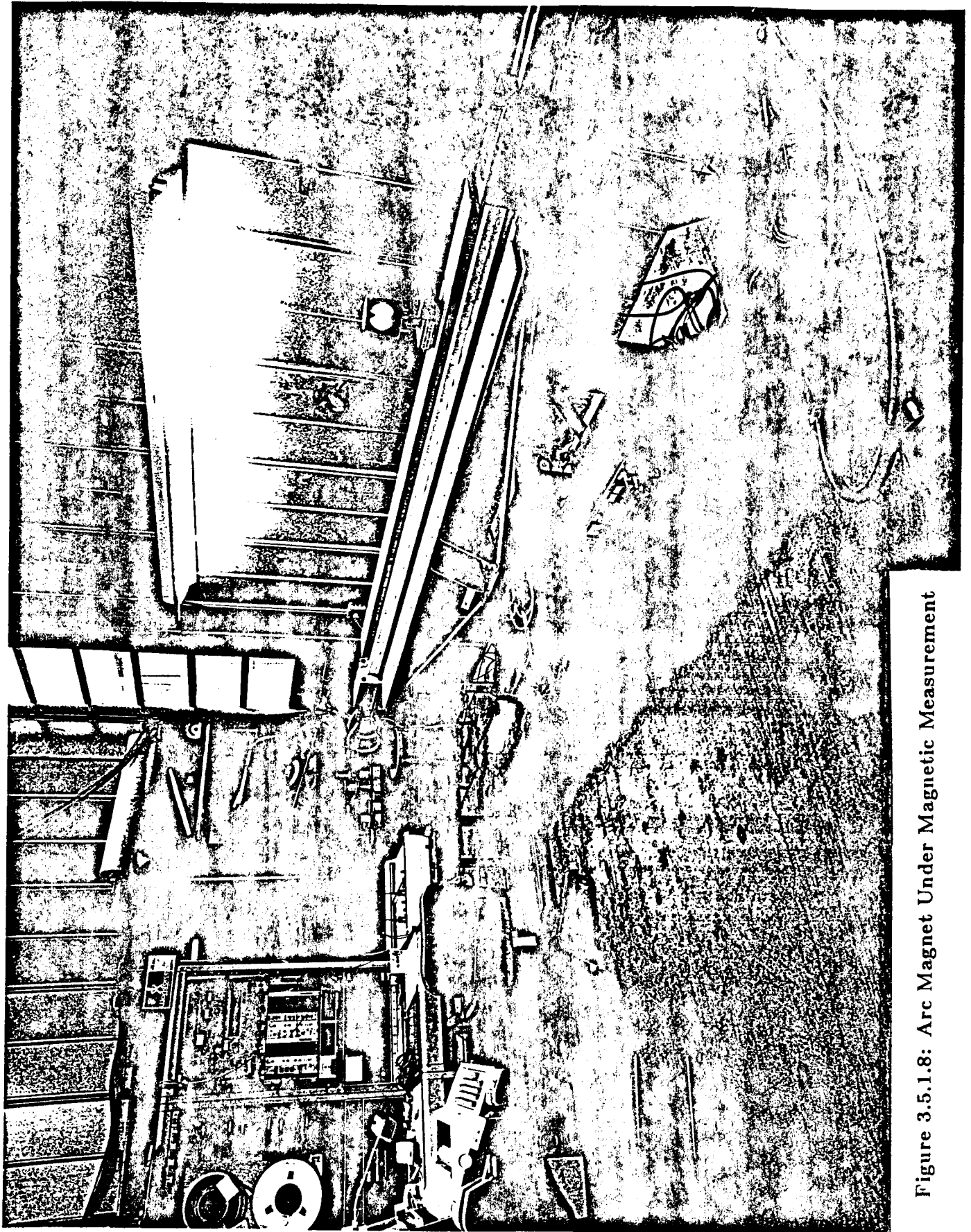


Figure 3.5.1.8: Arc Magnet Under Magnetic Measurement

# SLCARC MODEL I B LIGHT ASSEMBLY BLDG 1/18/83

6000 - 5000 - 4000 - 3000 - 2000 AMP-TURNS/POLE

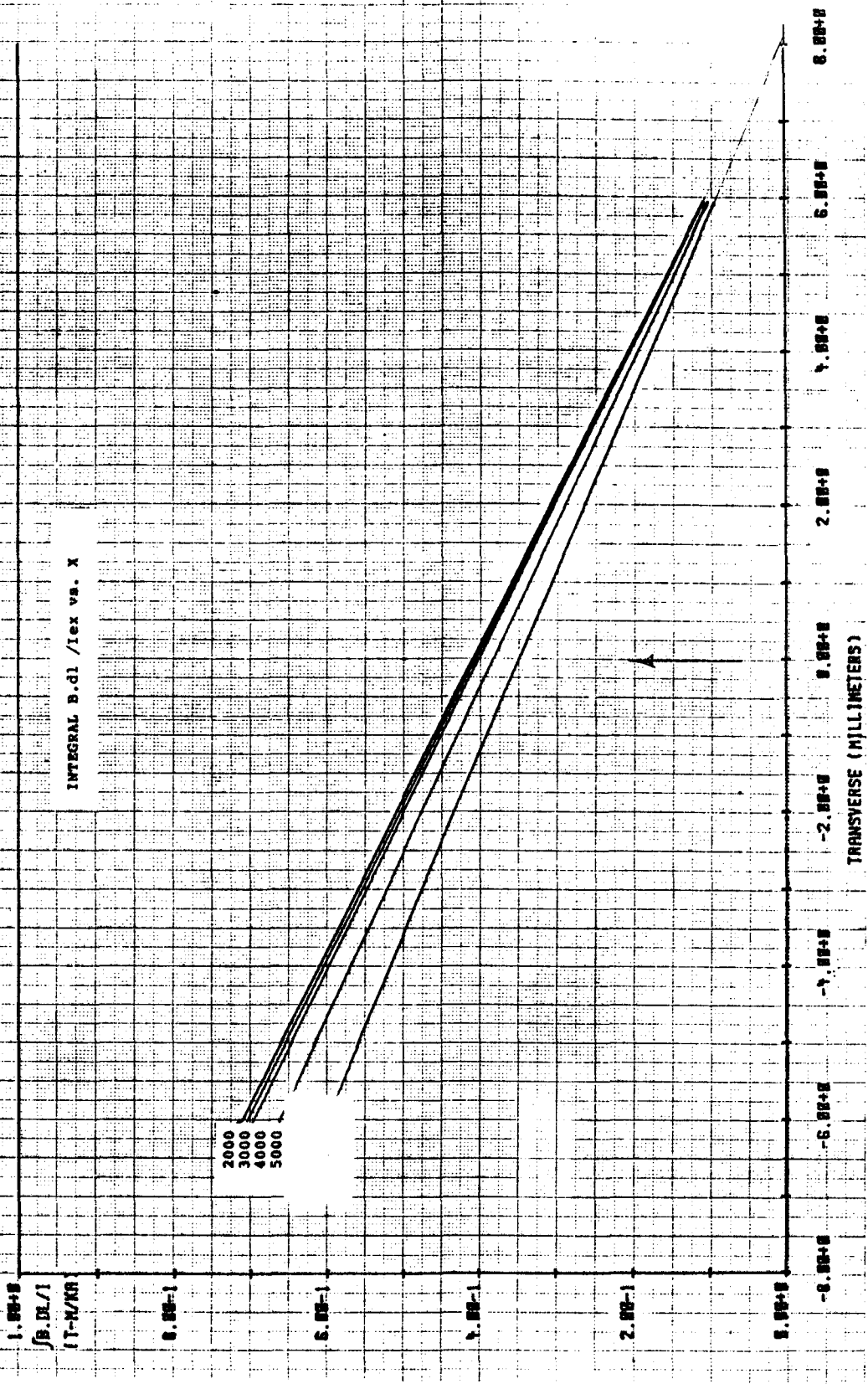


Figure 3.5.1.9:  $\int B dl / I$  vs. X

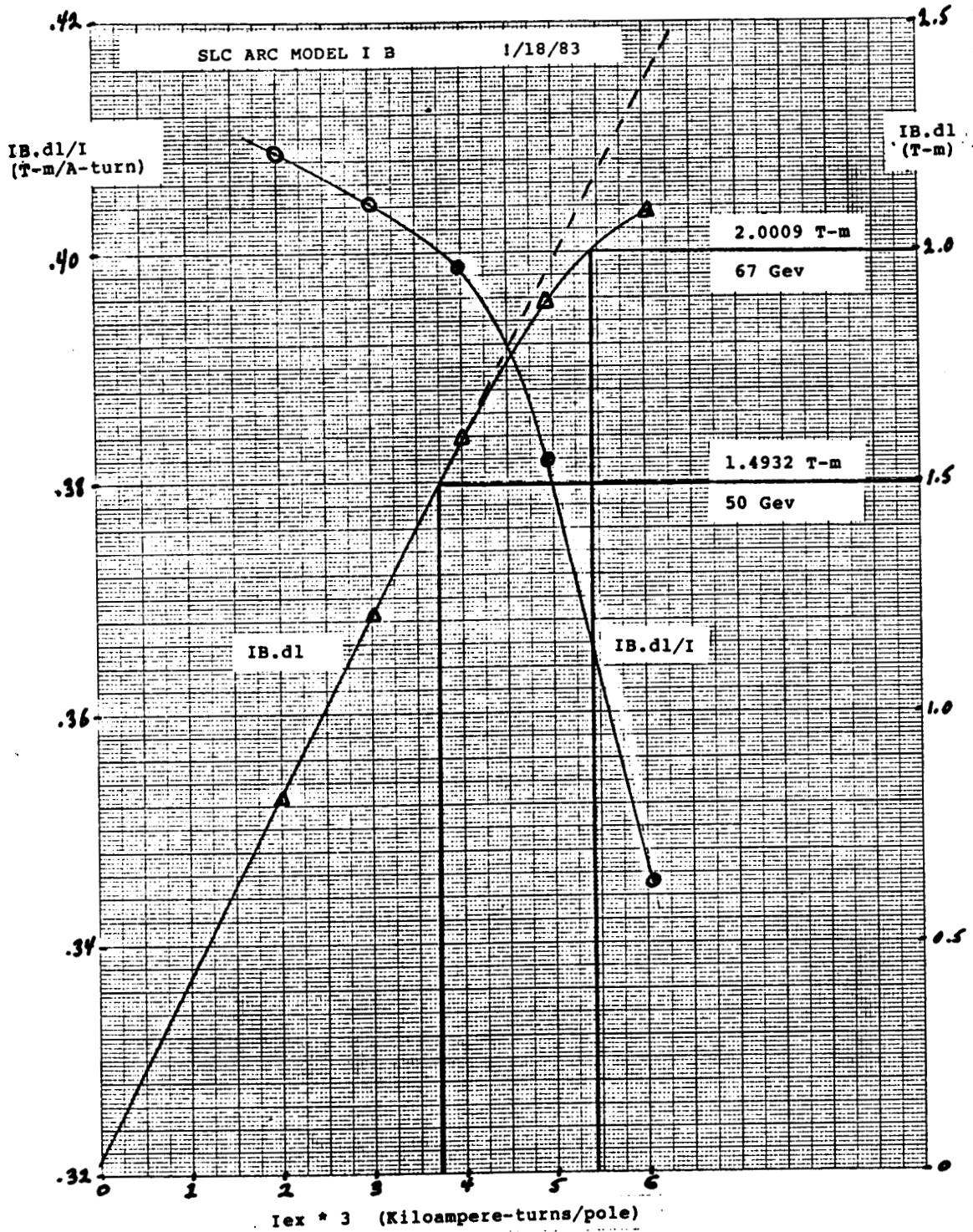


Figure 3.5.1.10:  $\int B \cdot dl$  and  $\int B \cdot dl / I$  vs.  $I$

# SLC MAIN ARC DEFOCUS MODEL EM3-001

1/5/84 6K-5K-4K-3K AMPERE-TURNS/POLE

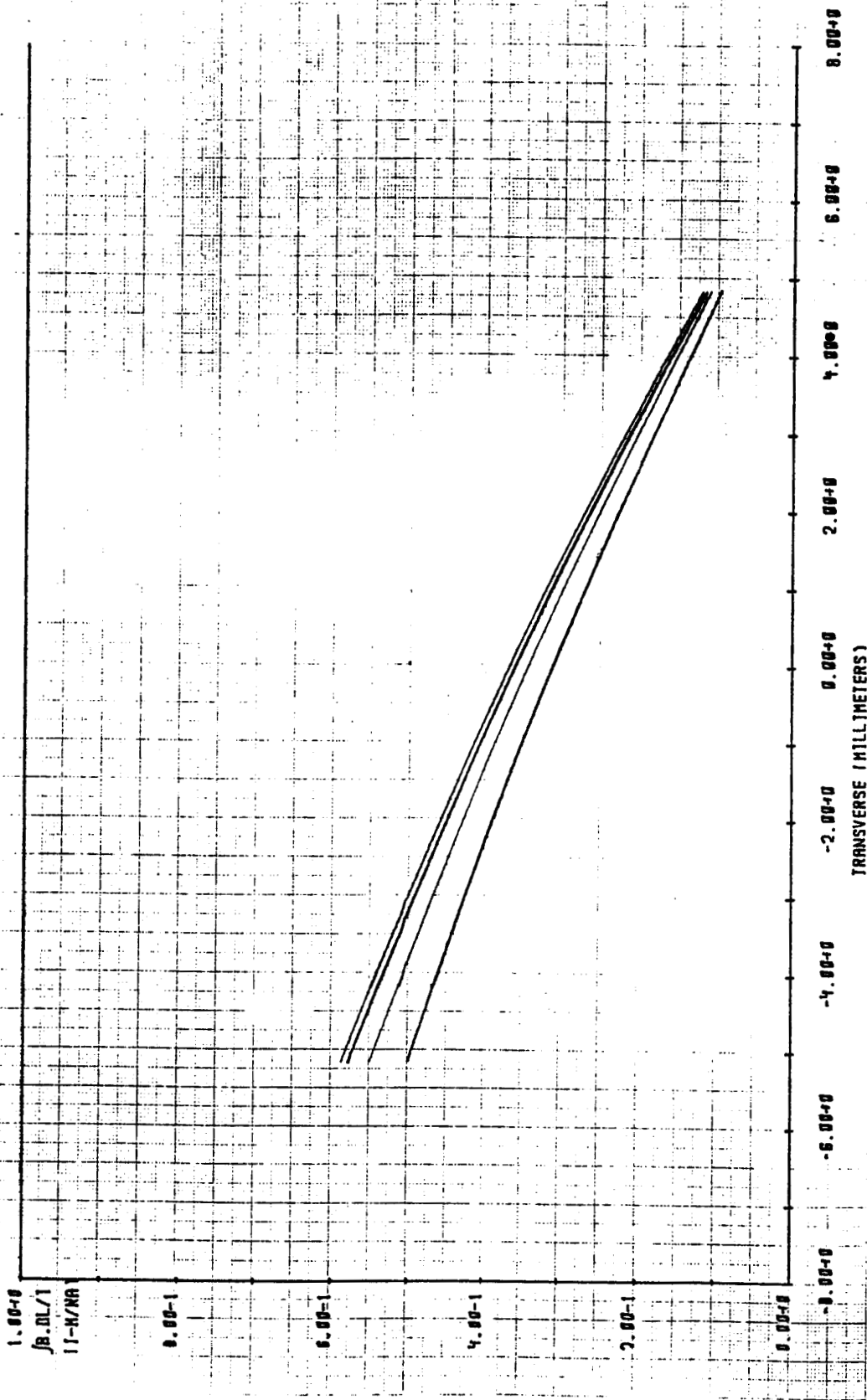


Figure 3.5.1.11

# MAGNETIC MEASUREMENT RESULTS

DEFOCUS MAGNET MODEL 5cm drift

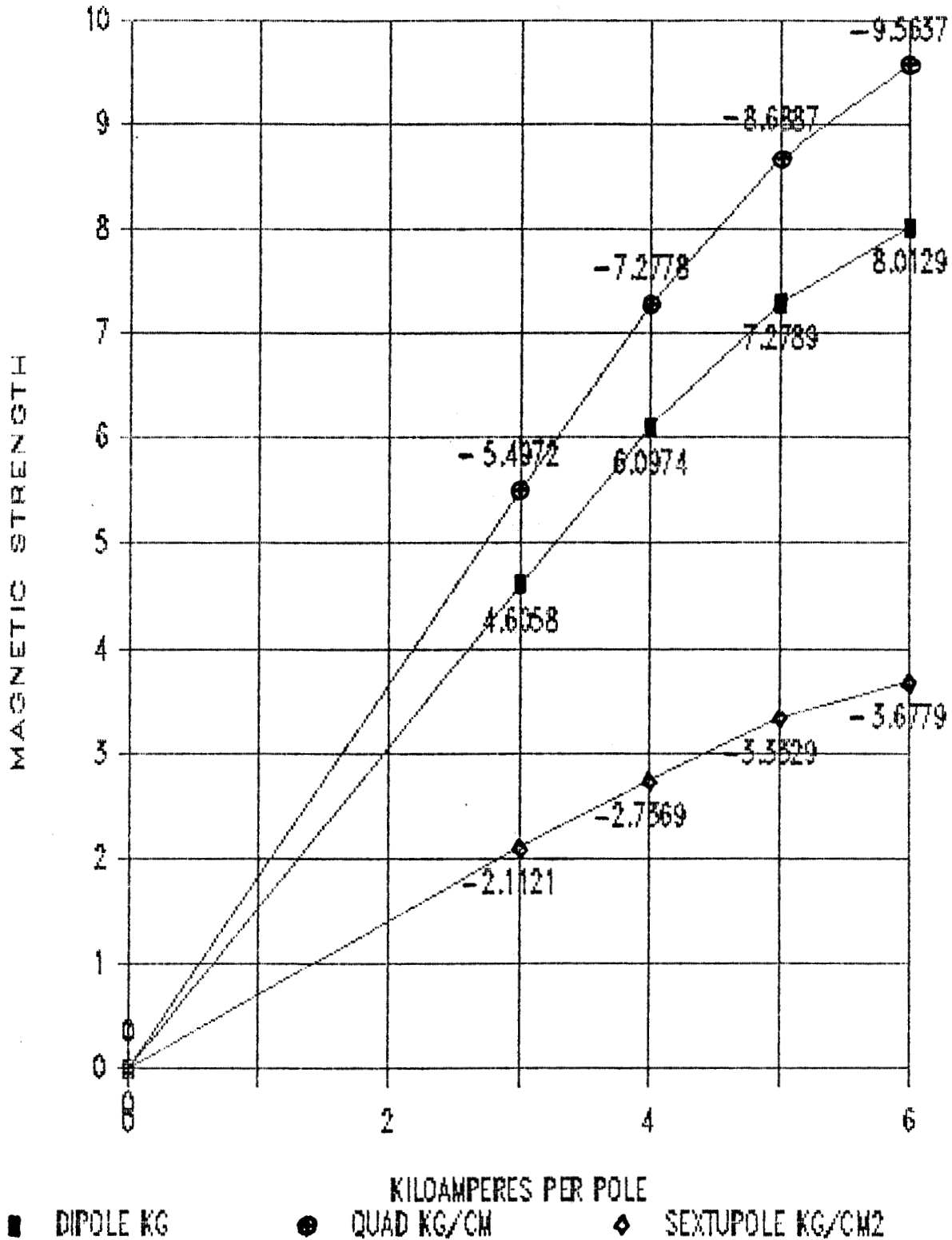


Figure 3.5.1.12: Measured Magnetic Parameters vs. I  
(Fit to Requirements)

Figure 3.5.1.12 shows these results as a function of current.

Each of the some 907 magnet cores will be measured for conformance with their mechanical specifications using a specially constructed computer-driven measuring apparatus. The device is capable of measuring very rapidly along the full length of the magnet: 1. Vertical height and straightness, 2. Horizontal curvature with a resolution of .001", 3. Minimum gap to .0001" and 4. roll (i.e., twist) to 0.1 milliradians. Each core will thereby be subjected to stringent mechanical tolerance tests and if passed given a mechanical "pedigree." Since there must exist a correlation between mechanical and magnetic properties of an "iron gap magnet" constructed of randomized laminations, it is the intent to establish this correlation experimentally over a statistically significant sample and subsequently be able to substantially reduce the numbers of magnets that will have to be measured magnetically.

Figure 3.5.1.13 shows an early arc magnet core being fabricated using a technique of stacking and welding similar to that employed for the PEP bending magnets.

### **3.5.2 Magnet Support System**

The scheme by which the magnets are supported in the tunnel has recently undergone a major conceptual change. For reasons of mechanical stability against microseismic disturbances the "four magnet girder" concept has been abandoned in favor of a system of pedestals as shown, for example, in Figures 3.5.2.1 and 3.5.2.2. The new concept is particularly well suited to the moving magnet correction system mentioned in Section 3.4.3. Moreover, pedestals can be installed and quite accurately surveyed into place with respect to the three dimensional vertex points prior to magnet installation. This procedure also decouples the logistics of alignment and magnet fabrication. These advantages are believed to outweigh considerably the logistic disadvantages of final magnet assembly in the tunnel.

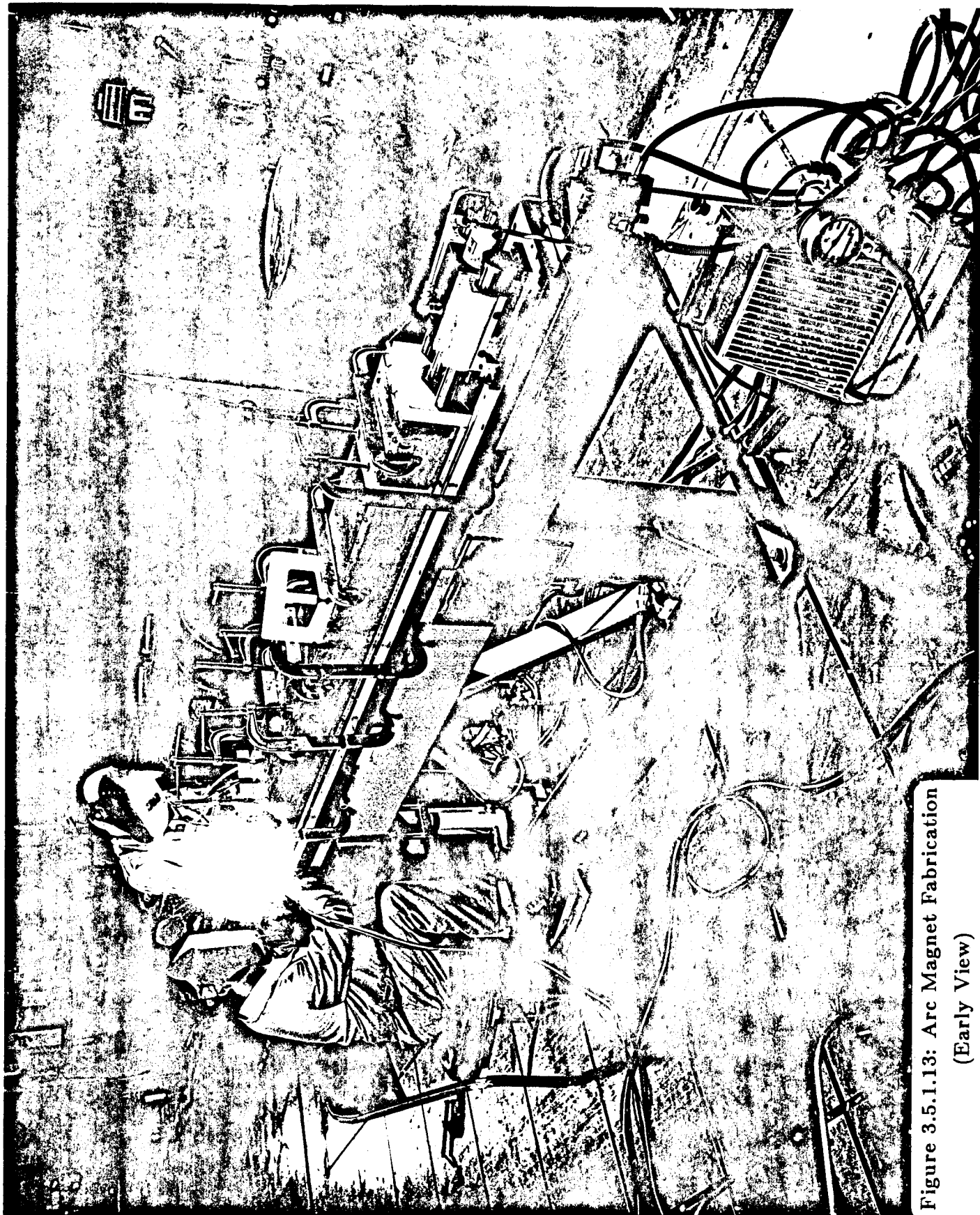


Figure 3.5.1.13: Arc Magnet Fabrication  
(Early View)

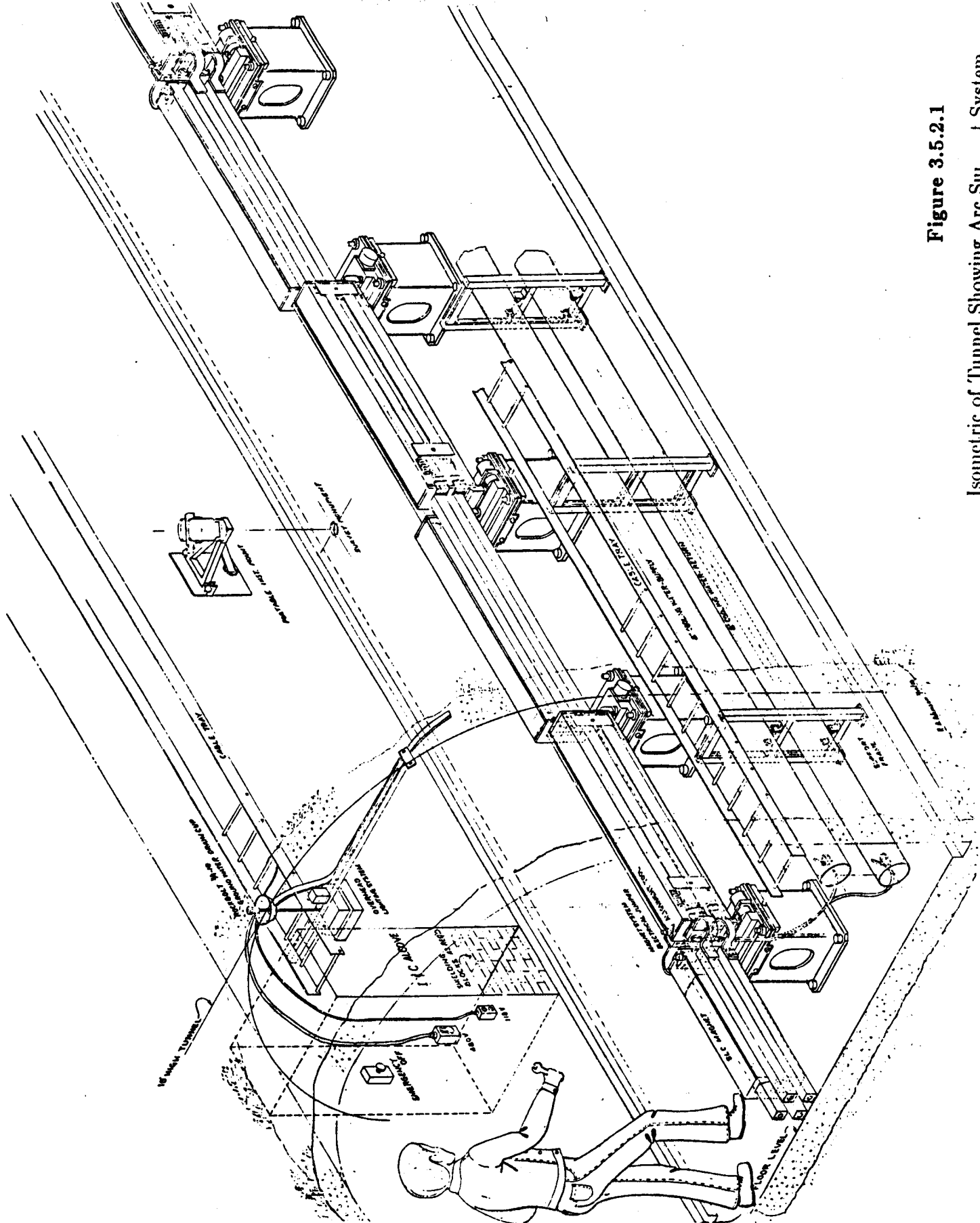


Figure 3.5.2.1  
Isometric of Tunnel Showing Arc Support System

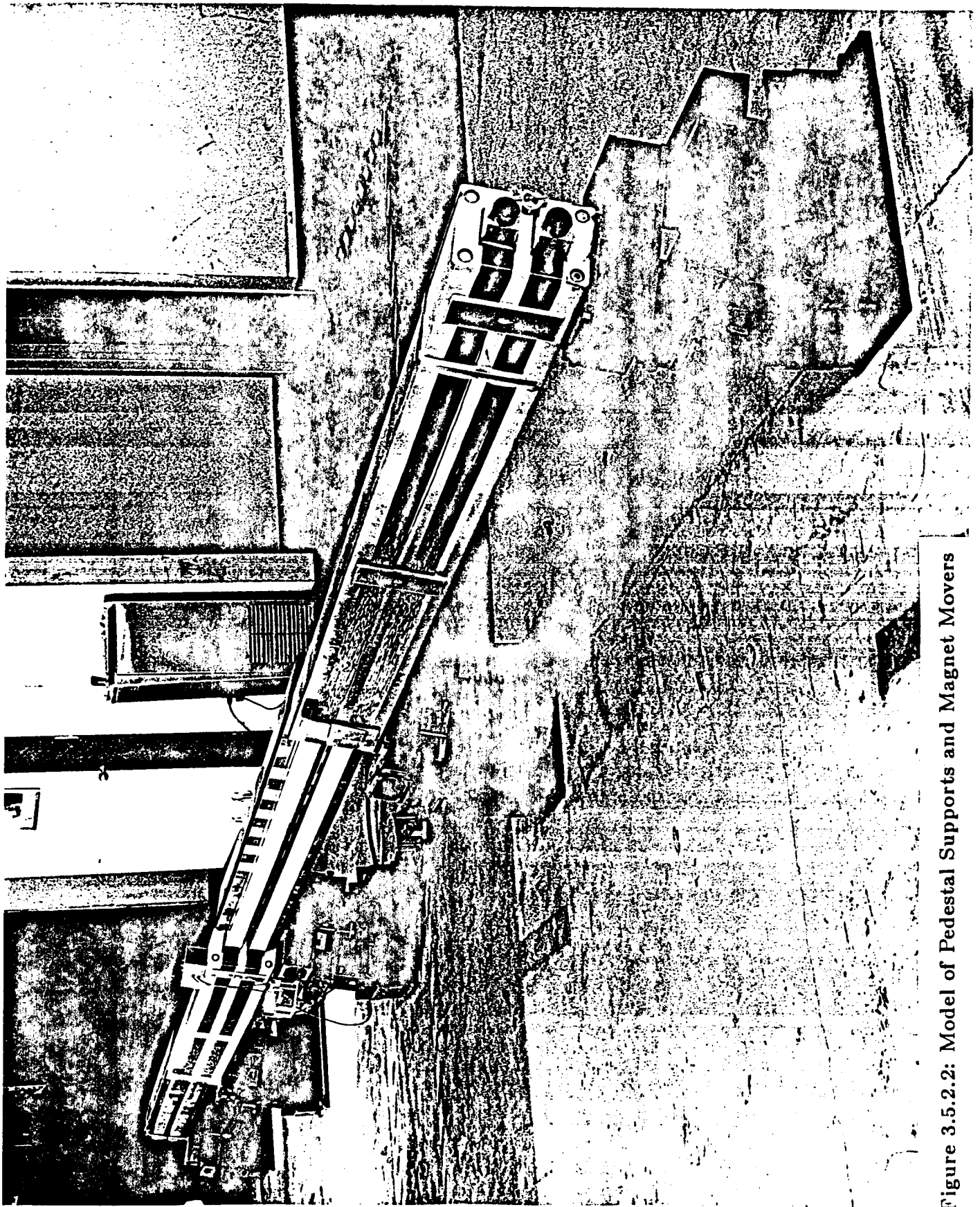


Figure 3.5.2.2: Model of Pedestal Supports and Magnet Movers

### 3.5.3 SLC-Arc Beampipe and Pumping System

The arc beampipe includes the injection, or front end, arc and reverse bend systems. The total length is approximately 8900 ft. of which the arc makes up 92%.

The design pressure for these systems is  $1 \times 10^{-4}$  torr average. To attain this pressure, 20 litre per second ion pumps will be located at intervals of 170 feet, or one pump per achromat. Due to conductance limitation in the pipe, the pressure will vary from approximately  $1 \times 10^{-7}$  torr at the pump to  $1.5 \times 10^{-4}$  torr midway between pumps as shown in Figure 3.5.2.1.

The arc beampipe is being designed in modular form so that gaps between AG magnets are filled with either a beam position monitor or a pump port/bellows module. The design is simplified, and additional pumping could be added at a later date with minimal rework of the beampipe if a lower operating pressure is required. The material of the chamber is aluminum, chosen for its low electrical resistance<sup>11</sup> and long radiation length.<sup>28</sup>

### 3.5.4 Beam Position Monitors

A BPM module consists of four stripline electrodes (50 ohms)<sup>24</sup> housed in an accurately machined body with attached bellows and is shown in Figures 3.5.4.1 and 3.5.4.2. The rationale of this design is contained in Reference 25.<sup>25</sup> Based on recent experimental results with a model of this design one would expect to be able to measure beam coordinates ( $x, y$ ) with a spatial resolution of 26 micrometers rms at an intensity of  $5 \times 10^{10}$  electrons/pulse. (See letter J.L. Pellegrin, dated Nov. 14, 1983). It should be noted that the discontinuities in the vacuum chamber wall caused by the monitors and bellows causes a minor emittance growth.<sup>11</sup>

# SLC-ARC PRESSURE PROFILE

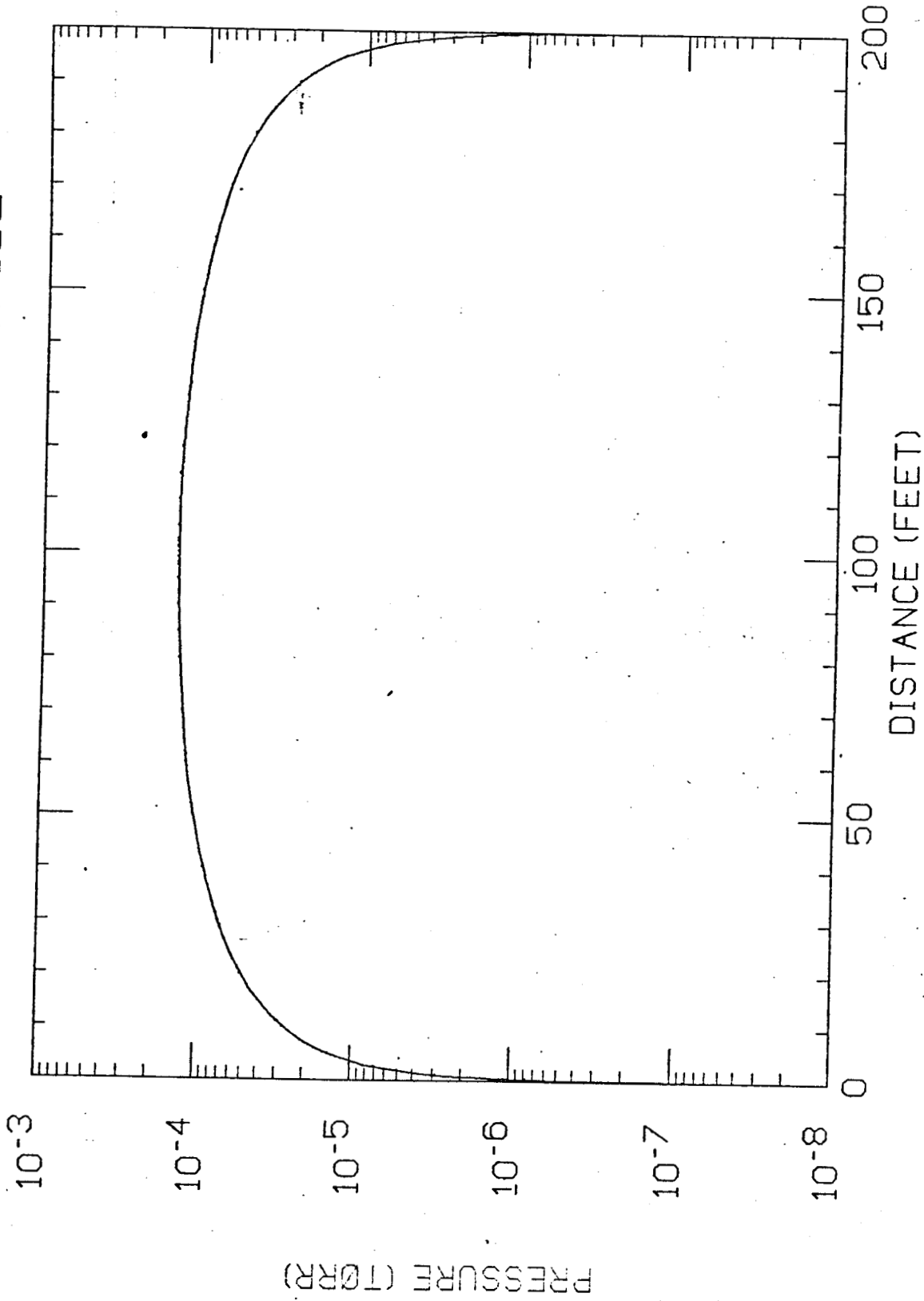
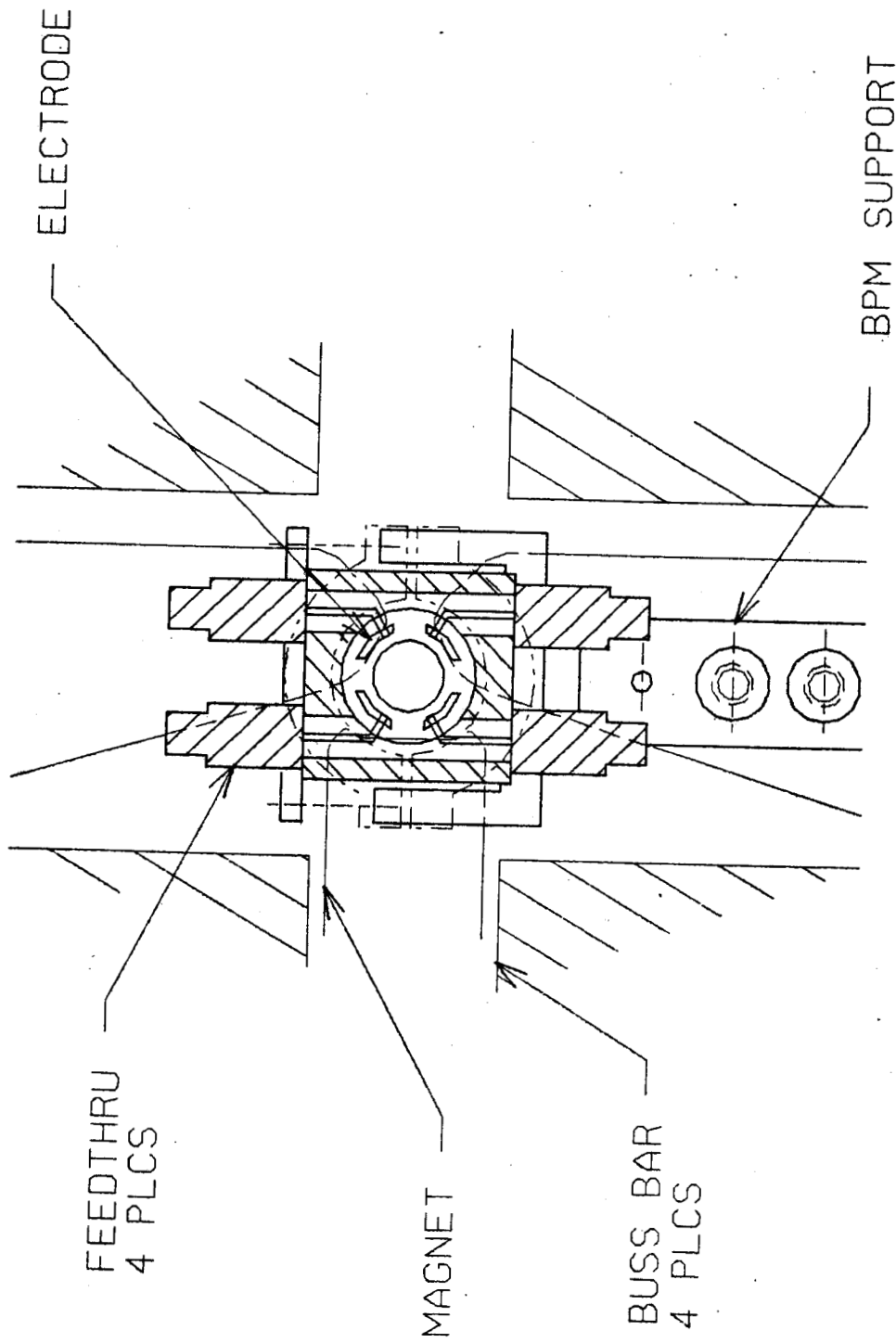


Figure 3.5.3.1: Pressure Profile in Arc Vacuum Chamber



CROSS SECTION BEAM POSITION MONITOR

Figure 3.5.4.1: SCALE: FULL

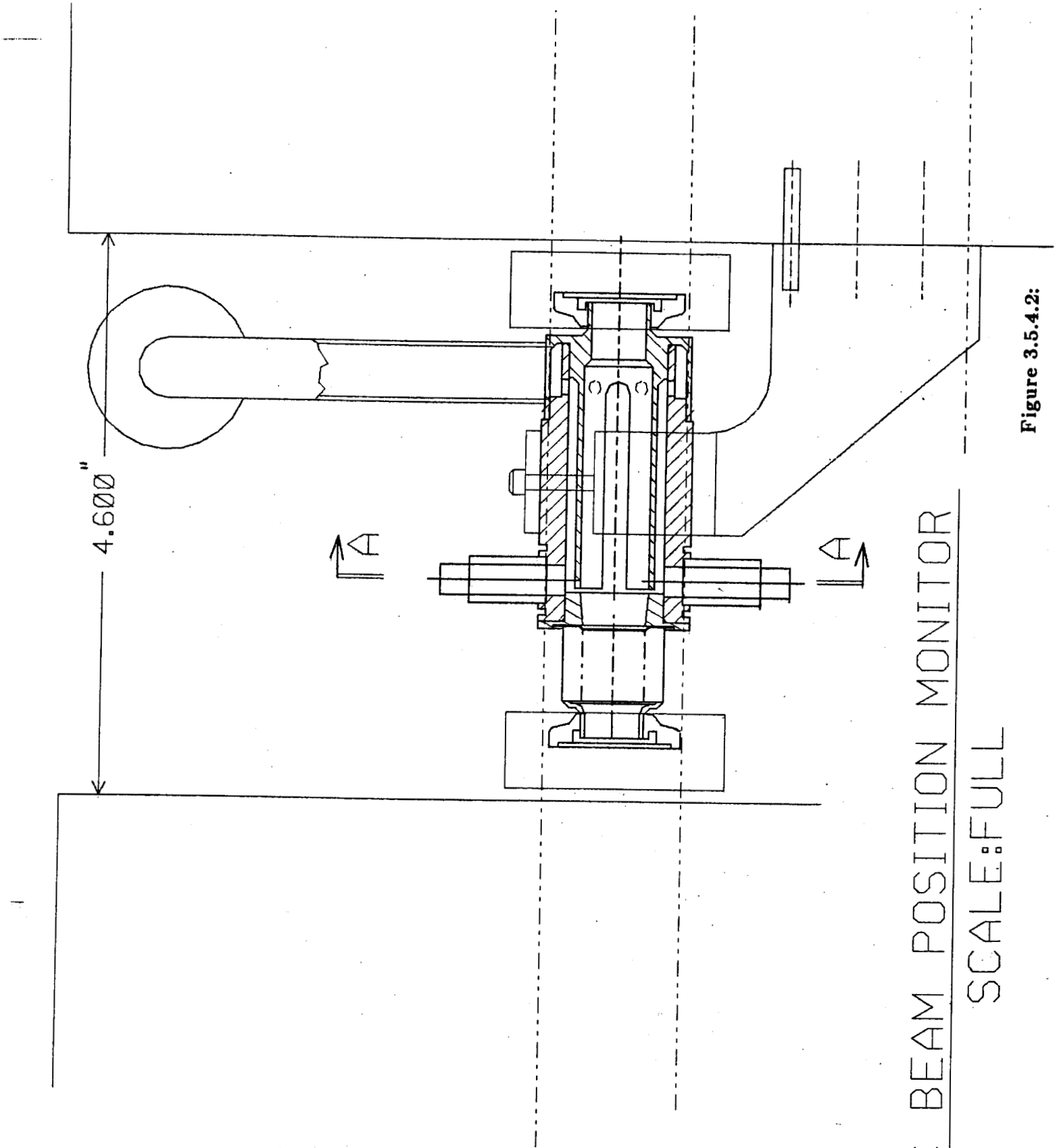


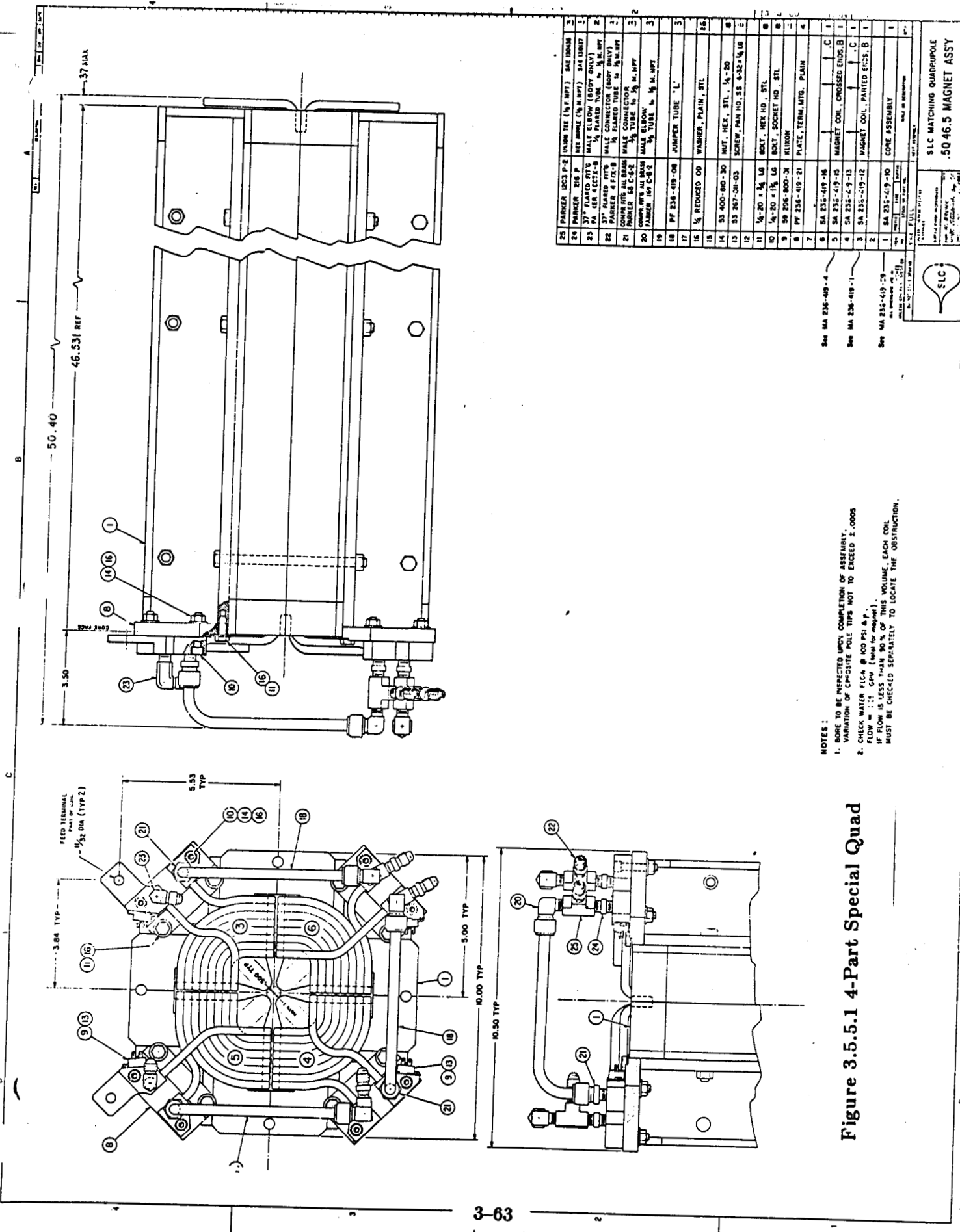
Figure 3.5.4.2:

ARC BEAM POSITION MONITOR  
SCALE:FULL

### 3.5.5 Special Magnets

Aside from the alternate gradient magnets described above, the arc system also contains a number of magnets of a more special variety. The front end system has already been described in Section 3.2. We note here the more unusual quadrupoles of the reverse bend and instrument sections.

The need to achieve large beta values in a limited space calls for quadrupole gradients up to 17 KG/cm at 70 GeV. Such gradients can only be achieved in an iron-poled magnet of rather small bore — in this case 0.5" diameter. The strongest magnet in this family is about 4 feet in length. Figures 3.5.5.1 and 3.5.5.2a show the cross sections of two possible designs. One magnet is assembled by bolting four quarter cores together, thereby accommodating conventional coils operating at a convenient maximum current of about 250 amperes. It is not clear that the very tight tolerances can be held. The other design is a magnet stacked with single piece laminations, not as subject to mechanical assembly errors, but through which single conductors must be inserted and brazed at their ends. (Figure 3.5.5.2b) These conductors run at a less convenient 2000 amps. The choice of design will be made after model tests have been conducted and power supply/bussing considerations have been evaluated.



23	PARKER 203 P-2	(UNION TEE (1/4" NPT))	SAE UNFIN
24	PARKER 203 P	NET NIPPLE (1/4" NPT)	SAE UNFIN
25	37° FLARED FIT	MALE ELBOW (BODY ONLY)	SAE UNFIN
26	NET	1/4" FLARED TUBE (1/4" NPT)	
27	PARKER 4 F/2 B	MALE CONNECTOR (BODY ONLY)	
28	PARKER 4 F/2 B	MALE CONNECTOR (BODY ONLY)	
29	CONN FITS ALL BRASS	MALE CONNECTOR (1/4" NPT)	
30	CONN FITS ALL BRASS	MALE ELBOW (1/4" NPT)	
31	PARKER 109 C-6-2	1/4" TUBE (1/4" NPT)	
32	PARKER 109 C-6-2	1/4" TUBE (1/4" NPT)	
33	PF 234-419-08	JUMPER TUBE 'L'	
34	1/2" REDUCED OD	WASHER, PLAIN, STL	
35	33 400-810-30	NUT, HEX, STL, 1/4"-20	
36	33 267-21-03	SCREW, PAN HD, SS 6-32x1/4 LG	
37	1/4"-20 x 1/4" LG	BOX, HEX HD, STL	
38	1/4"-20 x 1/4" LG	BOX, SOCKET HD, STL	
39	PF 235-419-21	PLATE, TERM. MTS. PLAIN	
40	SA 235-419-16	MAGNET COIL, CROSSED ENDS, B	
41	SA 235-419-15	MAGNET COIL, CROSSED ENDS, B	
42	SA 235-419-13	MAGNET COIL, PAINTED ENDS, B	
43	SA 235-419-12	MAGNET COIL, PAINTED ENDS, B	
44	SA 235-419-10	CORE ASSEMBLY	

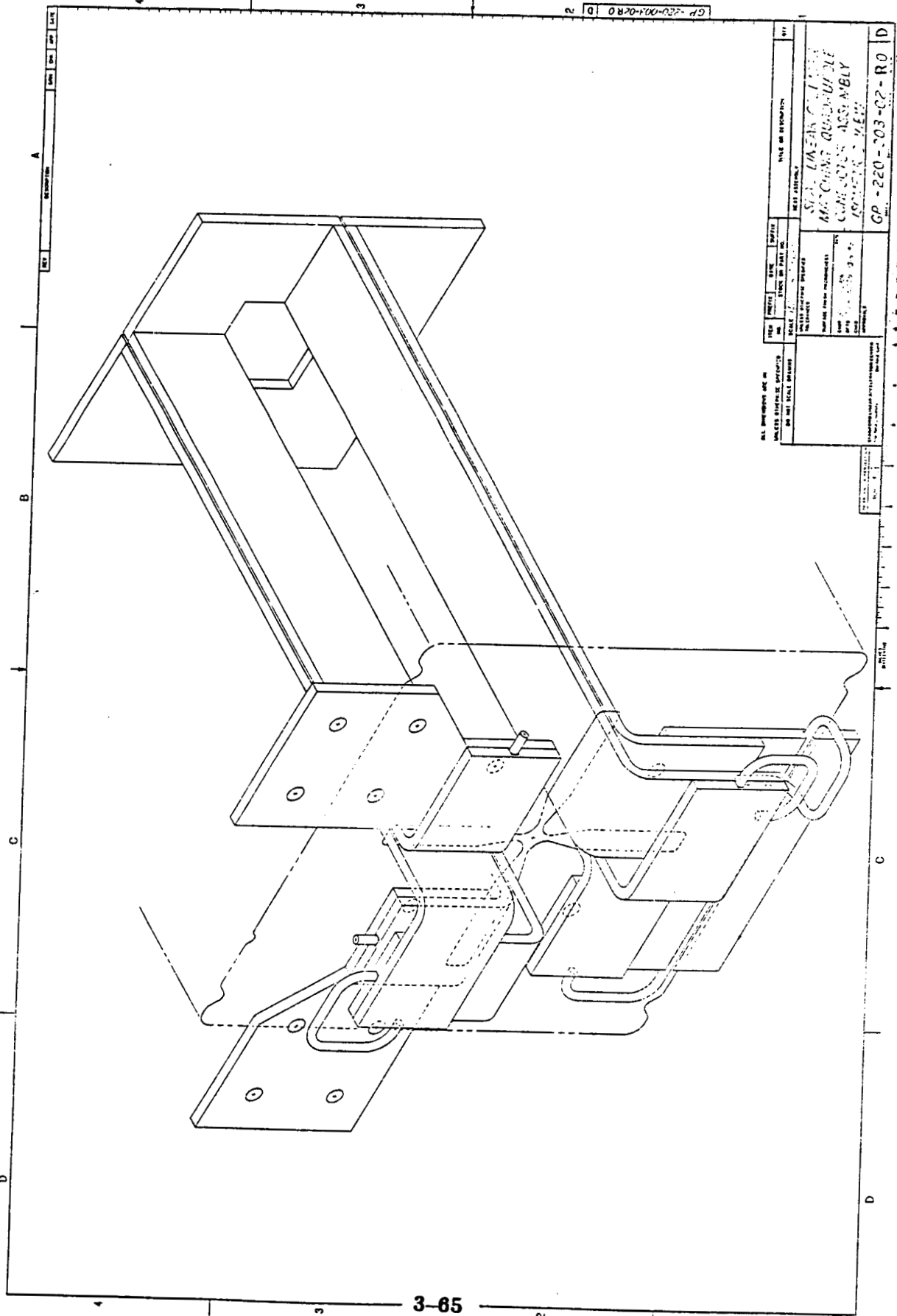
See MA 236-419-4  
See MA 236-419-1  
See MA 235-419-29

- NOTES:
- BORE TO BE INSPECTED UPON COMPLETION OF ASSEMBLY. VARIATION OF OPPOSITE POLE TIPS NOT TO EXCEED ±.0005
  - CHECK WATER FLOW @ 100 PSI (A.P.). FLOW = 1:1 GPM (MIN) FOR EACH COIL. IF FLOW IS LESS THAN 90% OF THIS VOLUME, EACH COIL MUST BE CHECKED SEPARATELY TO LOCATE THE OBSTRUCTION.

Figure 3.5.5.1 4-Part Special Quad

SLC MATCHING QUADRUPOLE  
50 46.5 MAGNET ASSY  
AD 236-419-00 R 1 E





GP-220-001-02-R0 D

ALL DIMENSIONS ARE IN UNLESS OTHERWISE SPECIFIED IN THIS SCALE DRAWING		DATE OF REVISION	
REV	DATE	BY	DESCRIPTION
1			ISSUE FOR FABRICATION
PART NAME		PART NUMBER	
SINGLE PIECE QUAD CONDUCTOR ASSEMBLY		GP-220-001-02-R0	
DRAWN BY		CHECKED BY	
DATE		DATE	
SCALE		SCALE	
MATERIAL		MATERIAL	
FINISH		FINISH	
TOLERANCES		TOLERANCES	
SURFACE FINISH		SURFACE FINISH	
TYPICAL DIMENSIONS		TYPICAL DIMENSIONS	
UNLESS OTHERWISE SPECIFIED		UNLESS OTHERWISE SPECIFIED	
IN THIS SCALE DRAWING		IN THIS SCALE DRAWING	

Figure 3.5.5.2b: Conductor Layout of Single Piece Quad

### 3.5.6 Power Supplies

**3.5.6.1 Main Supply** The conceptual diagram of the main arc supply and bussing is shown in Figure 3.5.6.1. Two supplies are used, each capable of running an arc separately or connected in series with a common current. The system is grounded at midpoint to limit the voltage to ground excursion. One or the other side may be trimmed to adjust for the energy imbalance that may exist between the two beams. It has been recently determined to be more economical and technically sounder to construct two new supplies and house them on the pump pad above the start of the BSY, than to use the existing old 5.8 MW supply and carry the current to the arcs via a rather long bus.

Polarities of AG arc magnets are described in Reference 26.<sup>26</sup>

**3.5.6.2 Special Magnet Supplies** Table 3.5.6.2 provides the present list of magnets and their supply requirements. Note that all 16 reverse bend and instrument matching quads are bussed in series.

**3.5.6.3 Trim Supplies** Assuming that centroid orbit corrections are accomplished via magnet movers, trim supplies will now be required for three functions.

1. Synchrotron radiation taper, one per achromat or 46 supplies.
2. Dispersion correction at the entrance to reverse bend and final focus matching sections, 8 parameters at 4 locations, or 32 supplies
3. Miscellaneous steering correctors in the front end and matching sections or 20 supplies.

TOTAL 98

### 3.5.7 Diagnostic Instruments

**3.5.7.1 Energy and Energy Spread Spectrometers** The purpose of this monitor and its location have already been mentioned in Section 3.2.3. In as much as this device should measure the centroid and width of the energy dispersed beam to provide the klystron phasing system with its feedback error signal on a pulse to pulse basis, it should be transparent to the beam. Transparency means

that when operational, it should cause no additional emittance growth. At the time of this writing (January 1984) several concepts for profile monitors have been proposed. The use of transition radiation from an extremely thin carbon foil (about 125 Angstroms) is one example.<sup>27</sup>

Figure 3.5.6.1 Main Arc P.S. Schematic

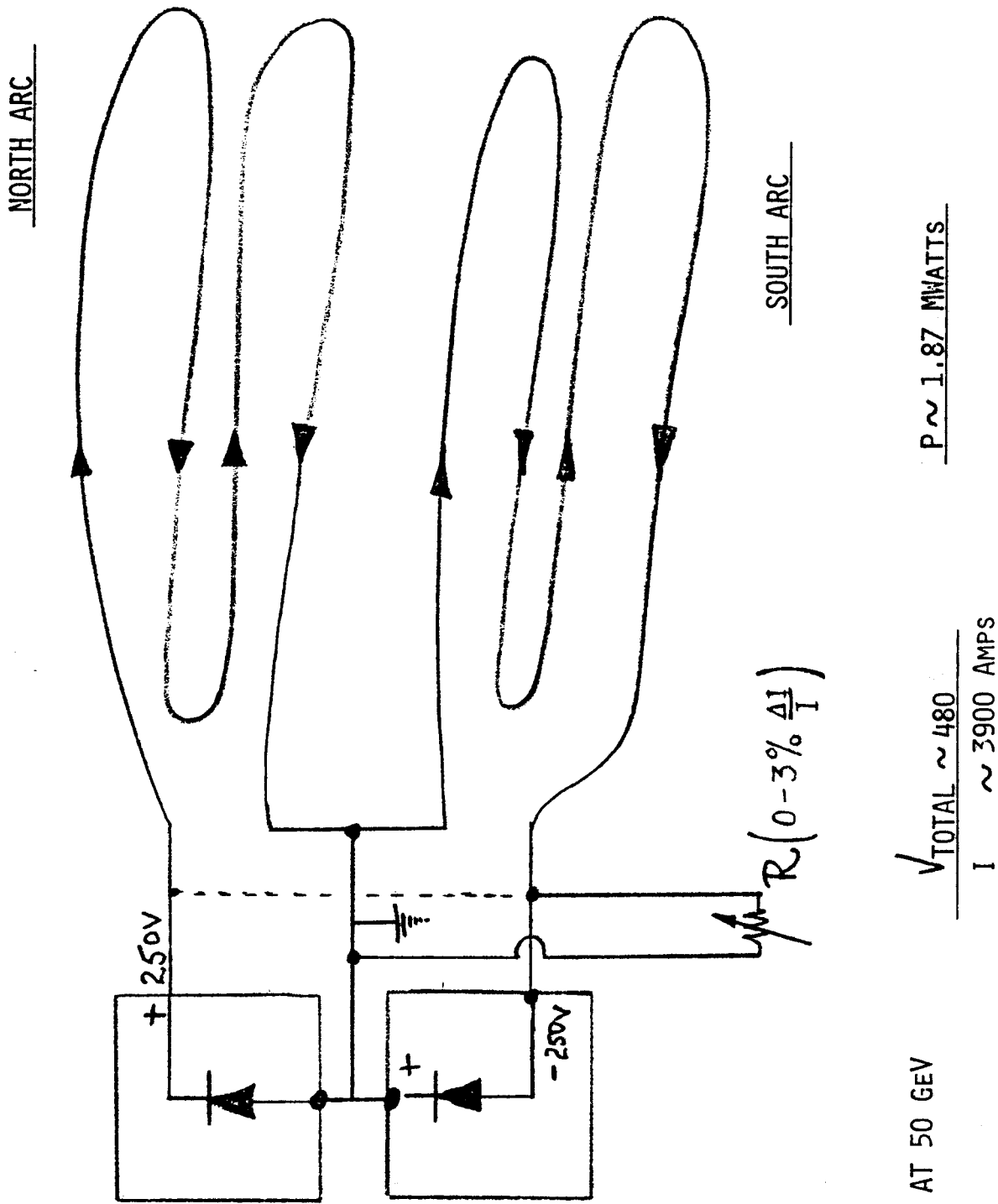


### Table 3.5.6.2 Magnet-Power Supply Cable Summary

E. K. Johnson  
January 19, 1984

#### Linac to Arc Matching

\*The following power supply distances are based upon placing the supplies in a support building in the vicinity of the vacuum pumping station across the street from the end of the Klystron Gallery.

Power Supply	Magnet(s)	Type	Current Amps	Voltage (Mag/Cable)	Power		Dist. from PS	Power Supply			Wire Size	Remarks
					KW	KW		Volts	Amps	KW		
1	50Q1 50Q2 50Q3	QDH QF QD	191.	14.	7.	.	150.	60	500	30.	4/0	
2	50B1	K1	620.	18.	7.	15.5	125.	40	800	32.	2-500MCM	
3a 3b	51AGF 52AGF		163. 163	9.	.	1.5	150.	?	?	?	3/0	
4	51Q2 51Q3 51Q4A 51Q4B	Q2 Q3 Q4 Q4	139.	78.	6.	.	200.	200	300	60.	4/0	
5	51B2	K2	482.	11.	10.	10.1	170.	40	800	32.	2-350MCM	
6	52Q2 52Q3 52Q4A 52Q4B	Q2 Q3 Q4 Q4	139.	78.	6.	.	200.	200	300	60.	4/0	
7	52B2	K2	482.	11.	10.	10.1	170.	40	800	32.	2-350MCM	

@- 0.6 P.F.= .KVA

#### South Arc Instrumentation Section

This data is prepared on the basis of power supplies located in the Main Control Center (MCC). The corresponding magnets are located almost directly below the MCC. DC leads will be quite short. The Tudor drawings indicate a 12" diameter penetration just outside of the entrance to the MCC. I propose to utilize this penetration for DC cables to the instrumentation section. It may also be the route for Trim and Steering cables to this portion of the Arc.

Power Supply	Magnet(s)	Type	Current Amps	Voltage (Mag/Cab.)	Power		Dist. from PS	Power Supply			Wire Size	Remarks
					KW	KW		Volts	Amps	KW		
1	51BI1 51BI4	B B	3.	10.	2.	.04	355	30	5	.15	#6	
2	51QI1 51QI2 51QI3 51QI4 51QI5 51QI6 51QI7 51QI8 51QI9 51QI10 51QI11 51QI12 51QI13 51QI14 51QI15 51QI16	Q Q Q Q Q Q Q Q Q Q Q Q Q Q Q Q	250.	44.	12.	13.	400	80	300	24.	350MCM	
3	51BI2 51BI3	B B	350.	21.	10.	10.9		60	500	30.	350MCM	

Table 3.5.6.2 continued

South Arc Reverse Bend Match

This data is based upon the installation of power supplies in a Research Yard type power supply building located adjacent to the shaft-head building.

Power Supply	Magnet(s)	Type	Current Amps	Voltage (Mag/Cab.)	Power KW	Dist. from 0.0	Power Supply Volts	Power Supply Amps	Power Supply KW	Wire Size	Remarks
1	51B3	BET	3.	10.	3.	.04	540.	30	5	.15	#6
	51B6	BET									
2	51Q5		250.	124.	18.	35.5	590.	60	500	30.	350MCM
	51Q6										
	51Q7										
	51Q8										
	51Q9										
	51Q10										
	51Q11										
	51Q12										
	51Q13										
	51Q14										
	51Q15										
	51Q16										
	51Q17										
51Q18											
51Q19											
51Q20											
3	51B4	BETP	350.	21.	21.	14.7	1410.	60	500	30.	
	51B5	BETP									

North Arc Reverse Bend Match

Distances referred to 0.0 are the start of the SLC Beam Lines in the Accelerator Housing. Distance to Power Supply must be added to these distances.

Power Supply	Magnet(s)	Type	Current Amps	Voltage (Mag/Cab.)	Power KW	Dist. from 0.0	Power Supply Volts	Power Supply Amps	Power Supply KW	Wire Size	Remarks
1	52B3	BET	3.	10.	—	.	1414.	30	5	.15	
	51B6	BET									
2	52Q5		250.	124.	—	.	1417.	60	500	30.	
	52Q6										
	52Q7										
	52Q8										
	52Q9										
	52Q10										
	52Q11										
	52Q12										
	52Q13										
	52Q14										
	52Q15										
	52Q16										
	52Q17										
52Q18											
52Q19											
52Q20											
3	52B4	BETP	350.	21.	—	.	1443.	60	500	30.	
	52B5	BETP									

If klystron stability is such as to permit the insertion now and then of an emittance destructive luminescent screen, then the readout problem has been solved by use of a recently developed high resolution optical digital scanner.

Any spectrometer should contain momentum defining collimators to limit the transmission of extreme off-momentum rays. The movable jaws (jaw opening for a 1% pass band is 1.5 mm) of the device will have to be designed to withstand full beam power (70 KW). Energy density considerations<sup>28-29</sup> may dictate the use of the "spoiler principle"<sup>30</sup> that is being employed in other areas of the SLC project to protect apertures from melting of failing thermal fatigue.

**3.5.7.2 Emittance Monitors and Collimators** On-line emittance monitors are called for to provide corrective error signals to the beam steering system of the linac so that wakefield effects are minimized. They are required in both arms of the arc because positrons and electrons are steered in opposite directions in the linac by dipole correcting coils.

As mentioned in Section 3.3.4, these monitors will be located in the reverse bend matching sections. Maximum beam size at beta values of 40 to 80 meters with  $\epsilon = 3 \times 10^{-10}$  radian meters is only about  $\pm 134$  micrometers or slightly less than 0.3 mm total. All of the monitor readout considerations of the section above apply. Moreover, it is not at all clear how to build emittance defining jaws with the required precision. The beam density considerations mentioned above are now serious and the use of the spoiler principle would be essential.

Emittance at a given place (phase) along the transport line is the product of the transverse spatial and angular extent of the beam. In contrast with a storage ring in which all phases are eventually traced out by the circulating beam, in principle it is, therefore, also necessary to measure angular spread. This could be accomplished by measuring the size of the beam at its smallest size, i.e., at beta minimum. This occurs at the center of the matching insertions. To limit angles by jaws at this point is beyond technology but may not be necessary if it can be accomplished in the final focus section, provided background conditions permit.

**3.5.7.3 Machine Protection** The concept of component protection is built on the principle that if the beam fails to arrive at a given point with sufficient intensity relative to its upstream current, it must have been lost by striking something on the way. Numerous toroid current comparators are planned for in the arcs to measure transmission on a pulse to pulse basis. The moment a given threshold of loss is sensed, the gun permissive trigger is inhibited, and the operator must lower both the gun current and repetition rate for diagnosis of where and how the loss occurred. Properly shielded protection collimators will be installed where applicable.

## REFERENCES

1. R. Stiening, CN-110 8/16/81
2. SLC Conceptual Design Report, SLAC-229, June 1980
3. G.E. Fischer, AATF/79/5 August 1979, H. Wiedemann CN-82 1981
4. H. Wiedemann, CN-84 1981, H. Wiedemann, CN-85 1981. During '82 and '83, this work was carried out by the members of the Beam Dynamics Task Force
5. J.J. Murray and R.V. Servranckx, CN-259 12/19/83
6. Readers are requested to contact the Beam Dynamics Task Force chairman to obtain the latest version of the lattice file or find them on Disk 191 JJMRA under the names ARCN FINAL and ARCS FINAL
7. D.C. Carey, K.L. Brown and Ch. Iselin, SLAC-246 March 1982
8. R.H. Helm and H. Wiedemann, PEP Note 303 (1979) and K.L. Brown, J. Murray private communication
9. Beam Dynamics Task Force private communication 1983
10. A. Chao and R. Helm, CN-201 10/20/82
11. J. Peterson, P.B. Wilson, CN-232 1983, R. Stiening, CN-20 3/13/80
12. K.L. Brown, SLAC-Pub-2257 (1979)
13. B. Richter, CN-202 (1982)
14. J. Matthews, CN-197 (1982)
15. A. Chao, CN-121 (1981), see also J.R. Rees, CN-243, 8/17/83
16. H. Wiedemann, AATF/12 (1979)
17. R. Stiening, CN-14 (1980)
18. G.E. Fischer, AATF/18 (1980); S. Whitaker, CN-223 4/28/83
19. H. Wiedemann, AATF/7 (1979); J.J. Murray, private communication
20. G.E. Fischer, CN-236, 6/16/83
21. K.L. Werner, CN-246, 9/15/83.

22. Beam Dynamics Task Force, and for some particular systems, see, for example, A. Chao, J. Jaeger, S. Kheifets and H. Shoaee, CN-252, Nov(1983)
23. E.D. Courant, M.S. Livingston, H. Snyder, Phys. Rev. 88,1190 (1952)
24. J.L. Pellegrin, CN-105 8/12/81
25. J.L. Pellegrin, CN-214, 1/14/83
26. M. Anderson CN-191, 7/26/82
27. E.W. Jenkins, CN-260 12/22/83)
28. W.R. Nelson and T.M. Jenkins, CN-235 7/7/83
29. S. Ecklund and R. Nelson, CN-135 12/8/81
30. W.R. Nelson and T.M. Jenkins, CN-262, 1/10/84

## **CHAPTER 4.**

### **THE FINAL FOCUS SYSTEM**

#### **4.1 INTRODUCTION**

#### **4.2 OPTICS**

- 4.2.1 Basic Building Blocks
- 4.2.2 Computational Tools
- 4.2.3 Chromatic Aberrations
- 4.2.4 Third Order Aberrations
- 4.2.5 Current Working Solution
- 4.2.6 S-Bend
- 4.2.7 Tolerances and Corrections
- 4.2.8 Dynamic Steering Corrections

#### **4.3 MAGNETS**

- 4.3.1 Conventional Magnets
- 4.3.2 Mounting
- 4.3.3 Detector Quadrupoles
  - 4.3.3.1 Superconducting Quadrupoles
  - 4.3.3.2 Conventional Quadrupoles
  - 4.3.3.3 SmCo<sub>5</sub> Quadrupoles
- 4.3.4 Power Supplies and Bussing

#### **4.4 EXTRACTION**

- 4.4.1 Introduction
- 4.4.2 Optics
- 4.4.3 Disrupted Beam

4.4.4 Polarization

4.4.5  $e^-/e^-$  Option

4.4.6 Beam Dumps

4.4.7 Kicker Magnets

4.4.8 Septum Magnets

4.5 VACUUM SYSTEM

4.6 INSTRUMENTATION

## 4. FINAL FOCUS SYSTEM

### 4.1 INTRODUCTION

The final focus system (FFS) must transform the beam envelope at the end of the collider arc to the small size needed for high luminosity beam collisions at the interaction region. The minimum beam size achievable is determined by the emittance and momentum spread of the entering beam and the optical quality of the FFS. In particular, the chromatic aberrations resulting from the finite momentum spread in the beam must be reduced to an acceptable level.

Two basic principles have been used to achieve the above objectives. The first is to design an optical system having small path length differences between the monoenergetic trajectories so as to minimize the chromatic distortions. The second is to correct for the residual second-order chromatic aberrations by introducing dipoles and sextupoles into the solution. The ultimate performance is then limited by the residual third-order geometric and chromatic aberrations introduced by the sextupoles.

The beam parameters dominating the design of the FFS are the beam emittance,  $\epsilon$ , the maximum design energy,  $E(\text{max})$ , the momentum spread of the beam,  $dp/p$ , the desired rms beam size at the interaction point,  $\sigma^*$ , and the maximum beam disruption angle,  $\theta_d$ , resulting from the beam-beam collisions.

The following values for these parameters are assumed for the purpose of this report:

$$\epsilon = 3 \times 10^{-10} \text{ radian-meters}$$

$$E(\text{max}) = 55 \text{ GeV}$$

$$(dp/p) = \pm 0.5\% (\pm 1\% \text{ if possible})$$

$$(\theta_d < 2.5 \text{ mrad for } \sigma^* = 1.2 \text{ } \mu\text{m})$$

$$(\theta_d < 1.0 \text{ mrad for } \sigma^* = 1.8 \text{ } \mu\text{m})$$

## 4.2 FINAL FOCUS OPTICS

### 4.2.1 The Basic Building Blocks for the FFS

Telescopic modules, similar to the one illustrated in Fig. 4.2.1.1 are used as the basic building blocks for the design of the final focus system. They provide simultaneous parallel-to-parallel and point-to-point imaging in both transverse planes. A sequence of telescopic modules has the important property that it minimizes the maximum amplitudes of the characteristic sine-like and cosine-like trajectories, which are two independent solutions of the second-order differential equation describing the linear optics. This tends to minimize the magnitude of the higher-order optical distortions.

The first-order transformation matrix of a telescopic module, like that shown in Fig. 4.2.1.1, is particularly simple. The notation used is that of TRANSPORT,<sup>1</sup> where

$$\begin{array}{ll}
 (x|x_o) = R_{11} = C_x & (y|y_o) = R_{33} = C_y \\
 (x|x'_o) = R_{12} = S_x & (y|y'_o) = R_{34} = S_y \\
 (x'|x_o) = R_{21} = C'_x & (y'|y_o) = R_{43} = C'_y \\
 (x'|x'_o) = R_{22} = S'_x & (y'|y'_o) = R_{44} = S'_y
 \end{array}$$

The matrix elements  $R_{11}$  and  $R_{33}$  are equal to the optical magnifications,  $M$ :

$$R_{11} = M_x = \sqrt{(\beta_2/\beta_1)_x}; \quad R_{33} = M_y = \sqrt{(\beta_2/\beta_1)_y}$$

where 1 and 2 are the beginning and end points of the module. For the  $x$ -plane the condition  $R_{12} = 0$  is equivalent to point-to-point imaging and  $R_{21} = 0$  is equivalent to parallel-to-parallel imaging. When both  $R_{12}$  and  $R_{21}$  are equal to zero, the orientation of the phase ellipse is an invariant; i.e., the Courant-Snyder parameter  $\alpha$  is the same at the end of the system as it is at the beginning. For example, an upright ellipse transforms to another upright ellipse (i.e., waist-to-waist imaging). For an upright ellipse, the monoenergetic beam envelope size is given by:<sup>2</sup>

$$\sigma_x = \sqrt{\beta_x \epsilon}$$

and the angular beam spread is:

$$\sigma'_x = \sqrt{\epsilon/\beta_x}$$

Similar relations apply to the  $y$ -plane optics.

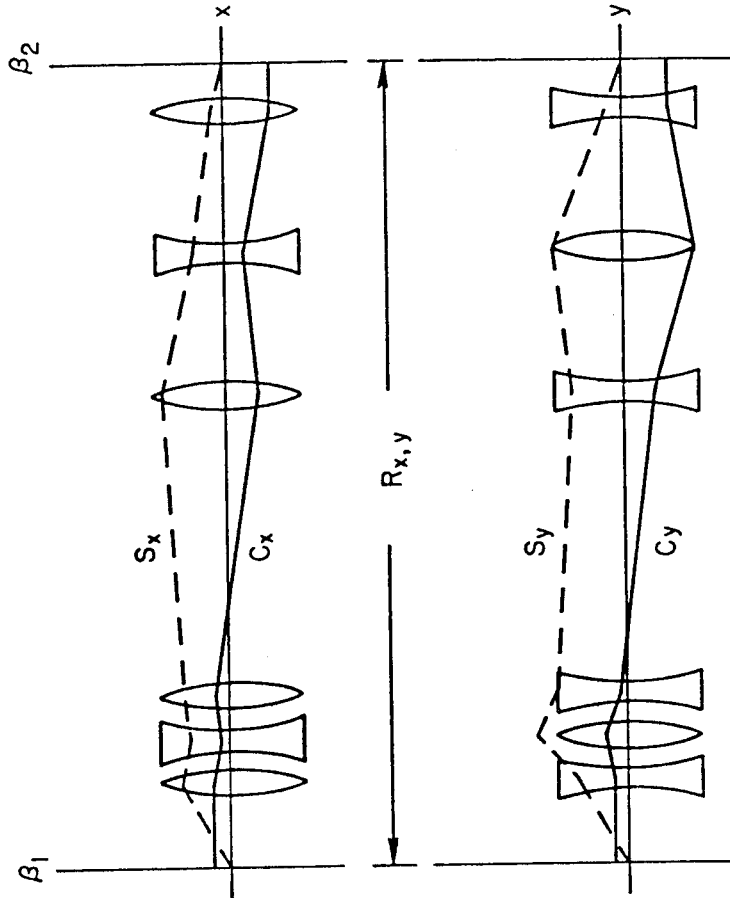
#### 4.2.2. Computational Tools Available for the Design

The optical configuration of the final focus system has been designed with the aid of the computer programs TRANSPORT<sup>1</sup>, TURTLE<sup>3</sup> and DIMAT.<sup>4</sup>

TRANSPORT is a second-order matrix multiplication program for designing the first and second-order optics of a proposed system. It is used to determine the quadrupole strengths required to minimize first-order optics and the sextupole strengths required to minimize the second-order chromatic distortions introduced by the quadrupoles.

TURTLE is an efficient ray tracing program that uses the second-order matrices from TRANSPORT to represent each element of the system. Individual rays are traced through each element separately so that higher-order cross coupling terms between elements are calculated in the computation, in contrast to TRANSPORT which truncates each matrix multiplication to second order. For example, the third and fourth-order cross coupling between sextupoles is calculated as the rays are traced through the system. TURTLE results are displayed in the form of histograms which show the density distribution of rays as a function of any of the phase space coordinates.

DIMAT is a differential ray tracing program which uses the second-order matrix formalism of TRANSPORT, but keeps higher-order effects due to the coupling between individual elements. This provides an independent check on the results obtained with TURTLE and yields information on other higher-order distortions not calculated by TURTLE. DINGBAT, a version of DIMAT implemented at SLAC, features automatic misalignment and field error simulation features, as well as provisions for representing beam position monitors (with their own errors). To facilitate the study of possible correction schemes, the fitting routines have been modified to incorporate information read from beam



$$R_{x,y} = \begin{bmatrix} -M_x & 0 & 0 & 0 \\ 0 & -\frac{1}{M_x} & 0 & 0 \\ 0 & 0 & -M_y & 0 \\ 0 & 0 & 0 & -\frac{1}{M_y} \end{bmatrix} = \begin{bmatrix} -\sqrt{(\beta_2/\beta_1)_x} & 0 & 0 & 0 \\ 0 & -\sqrt{(\beta_2/\beta_1)_x} & 0 & 0 \\ 0 & 0 & -\sqrt{(\beta_2/\beta_1)_y} & 0 \\ 0 & 0 & 0 & -\sqrt{(\beta_2/\beta_1)_y} \end{bmatrix}$$

Figure 4.2.1.1

position monitors.

### 4.2.3 Chromatic Aberration Theory

The second-order chromatic aberrations introduced by the quadrupoles nearest to the interaction point are a dominant factor in the design of a final focus system. Even though midplane symmetry is preserved in the basic design, forcing some elements of the T-matrix to zero, the following second-order chromatic aberrations may be non-zero:  $(x, x\delta)$ ,  $(x, x'\delta)$ , and  $(x, \delta\delta)$  in the  $x$ -plane, and  $(y, y\delta)$  and  $(y, y'\delta)$  in the  $y$ -plane, where  $\delta$  means  $dp/p$ . In TRANSPORT notation, the above aberration coefficients have the following equivalents:  $T_{116} = (x, x\delta)$ ,  $T_{126} = (x, x'\delta)$ ,  $T_{166} = (x, \delta\delta)$ ,  $T_{336} = (y, y\delta)$ , and  $T_{346} = (y, y'\delta)$ . Of these,  $(x, x\delta)$  and  $(y, y\delta)$  are usually unimportant for the FFS because of the small values of the phase space parameters  $\beta_x$  and  $\beta_y$  of the beam at the IP and because telescopic modules are used as the basic building blocks.  $(x, \delta\delta)$  can be made to vanish by choosing the appropriate optical symmetries.

This leaves  $(x, x'\delta)$  and  $(y, y'\delta)$  as the two principal second-order chromatic aberrations limiting the performance of the FFS. Both aberrations can be eliminated by the introduction of dipoles and sextupoles into the optics of the system. The magnitude of these two aberrations, before sextupole corrections are made, is calculated by an integral over the length of the FFS.<sup>5-6</sup> The result is the following:

$$T_{126} = M_x \int_1^2 (s'_x)^2 ds = \sqrt{(\beta_2/\beta_1)_x} \int_1^2 (s'_x)^2 ds \quad (1)$$

$$T_{346} = M_y \int_1^2 (s'_y)^2 ds = \sqrt{(\beta_2/\beta_1)_y} \int_1^2 (s'_y)^2 ds$$

where 1 and 2 are the beginning and the end points of the FFS. Note that the integrands in these expressions for these particular aberration coefficients are positive definite.

These integrals are related to the second-order path length differences be-

tween the monoenergetic particles and the central trajectory (normalized to the square of their initial angle) as follows:

$$\frac{2\Delta\ell}{(x'_o)^2} = \frac{2}{(x'_o)^2} \int_1^2 [1 - \cos x'(s)] ds \approx \int_1^2 \left[ \frac{x'(s)}{x'(o)} \right]^2 ds = \int_1^2 (s'_x)^2 ds$$

where we define

$$\frac{\Delta\ell}{(x'_o)^2} = T_{522}$$

So,

$$2T_{522} = \int_1^2 (s'_x)^2 ds, \quad (2)$$

and similarly:

$$2T_{544} = \int_1^2 (s'_y)^2 ds.$$

$T_{522}$  and  $T_{544}$  are the second-order path length aberrations (TRANSPORT notation). For an uncorrected system, the overall beam size is minimized by equating the monoenergetic beam size at the interaction point to the magnitude of the second-order chromatic distortion. For telescopic systems having waist to waist imaging, this condition yields the equation:

$$\sigma_x^* = \sqrt{\beta_x^*} \epsilon = \left( x'_L \frac{\Delta p}{p} \right) T_{126} = \sqrt{(\epsilon/\beta_L)_x} \left( \frac{\Delta p}{p} \right) \sqrt{(\beta_L/\beta^*)_x} \int_*^L (s'_x)^2 ds,$$

where \* is at the interaction point (IP), and  $L$  is at the (lattice) input to the final focus. Simplifying, one obtains:

$$\beta_x^* = \left( \frac{\Delta p}{p} \right) \int_*^L (s'_x)^2 ds = 2 \left( \frac{\Delta p}{p} \right) T_{522}, \quad (3)$$

and similarly:

$$\beta_y^* = 2 \left( \frac{\Delta p}{p} \right) T_{544}.$$

If no second-order chromatic corrections are made to the system, the above equations define the practical lower limits for  $\beta^*$  that may be achieved. Note that the effective rms beam size is  $\sqrt{2}$  larger than the monoenergetic beam size because both the monoenergetic beam size and the "chromatic beam size" are contributing to the total beam size at the interaction point.

For chromatically corrected systems, the magnitudes of  $T_{522}$  and  $T_{544}$  evaluated with the sextupoles turned off, are a measure of the degree of success to be expected from a system when the sextupoles are turned on. The smaller their values, the better the corrected system will perform.

#### 4.2.4 Third-Order Aberrations

If the system is chromatically corrected to second order, then the third-order aberrations introduced by the sextupoles usually become the principal source of the residual optical distortions limiting the system's performance. For the final focus design considered in this report, the dominant third-order aberrations in the  $x$ -plane are the geometrical terms  $(x, x'x'x')$  and  $(x, x'y'y')$  and the chromatic terms  $(x, x'\delta\delta)$  and  $(x, y'y'\delta)$ . Similar aberrations exist in the  $y$ -plane.

The ratios of the third-order chromatic aberrations to the third-order geometric aberrations are functions of the strengths of the dipoles used for the second-order chromatic corrections. By adjusting the dipole and sextupole strengths in inverse proportions, the total third-order optical distortion can, in general, be minimized without disrupting the second-order chromatic correction. This minimum value occurs when the angular dispersion introduced by the dipoles is approximately equal to the monoenergetic angular spread in the beam (at the dipole). This is expressed by the equation:

$$d'_x \left( \frac{\Delta p}{p} \right) = \sqrt{\frac{\epsilon}{\beta_D}}$$

and

$$d'_x = \alpha. \quad (4)$$

where  $\alpha$  is the angular dispersion introduced by the dipole, and  $\beta_D$  is the value of  $\beta_x$  at the dipole. Eq. 4 serves as an initial guess for  $\alpha$ . The final adjustment of the strengths of the dipoles is obtained by observing, in the computer simulations, the relative optical distortions introduced by the sextupoles for a monoenergetic beam versus those for a beam having a momentum spread of  $dp/p$ . It is typically found that the optimum value for  $\alpha$  is within 20% of that given by the above equation.

#### 4.2.5 Final Focus Optical Solution

The optical solution for the final focus is illustrated in Fig. 4.2.5.1. A transport listing is given in Table 4.2.5.1. The  $\beta$ ,  $\eta$ , and envelope functions are plotted in chapter 3 along with those of the arcs. While some details of the design have not yet been firmly set, the basic design has been established. Each side of the final focus will consist of five half-wave modules: an azimuthal bending section that immediately follows the arc and cancels the off-energy function,  $\eta$ , a telescopic  $\beta$ -matching section that accommodates the extraction system for the outgoing beam, two modules which together correct the second-order chromatic distortion of the system, and finally a transformer which demagnifies the beam to the final spot size and provides for fast precise steering. The performance of the SLC will depend on the focusing power of the final quadrupole array. With this in mind, the system has been designed to accommodate a diverse range of possibilities for the final transformer, allowing us to take advantage of the best magnets that become available, without having to modify the rest of the system.

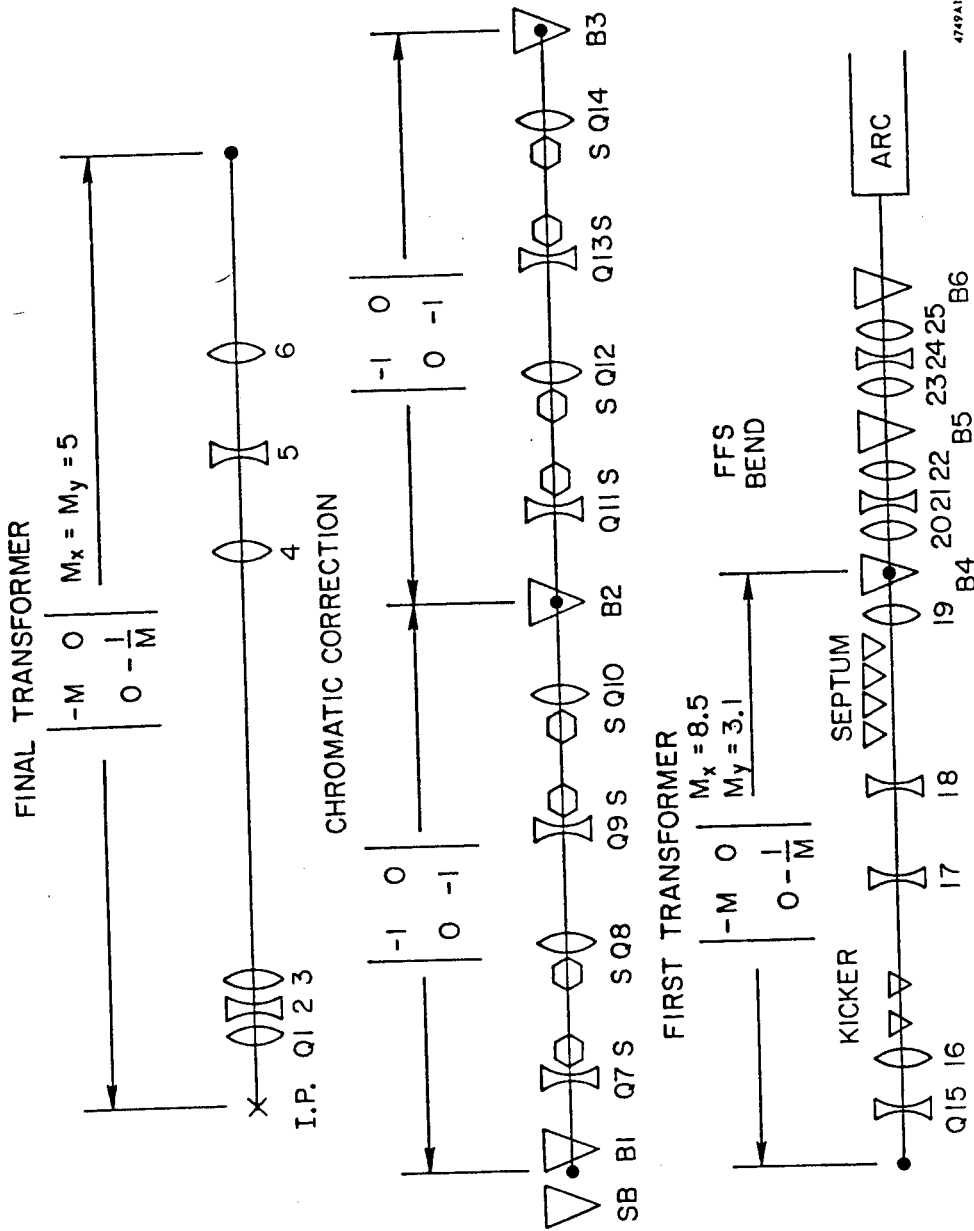
Beginning at the end of the arc, the first half-wave module consists of three dipoles separated by quadrupole triplets. The strength of the middle dipole, B5, is chosen so that its momentum dispersion cancels the residual  $\eta$  from the arcs by zeroing the  $\eta'$ , in effect, at the quarter-wave point. The first and third dipoles, B6 and B4, are identical and separated by a half wavelength. Thus, the additional dispersion introduced by B6 is exactly cancelled by B4. This module,

which is oriented in the rotated plane of the last arc magnet, has a net bend with a vertical component that brings the beam into the horizontal plane of the IP, and a horizontal component that aligns the dispersion-free beam with the first telescopic transformer.

The first telescopic module, consisting of quadrupoles Q15 through Q19, has demagnifications of 8.51 and 3.09 in the  $x$  and  $y$  planes, respectively. These values were chosen to match the  $\beta$  functions, and thus, to deliver a round beam with  $\sigma_x = \sigma_y \approx 6.0 \mu\text{m}$  to the chromatic correction section. Because the envelope of the incoming beam is a rotated ellipse in the  $xy$  plane, the magnets in this section must be mounted with a slight roll (approximately  $4.1^\circ$  on the north side,  $5.9^\circ$  on the south). Since the beam leaving this section is circular, all downstream elements can be oriented with a vertical  $y$  axis.

This module was designed with drift spaces long enough to accommodate the extraction magnets for the outgoing beam. The space between quadrupoles Q16 and Q17 ( $\approx 24$  ft) accommodates the pulsed kicker. The space between quadrupoles Q18 and Q19 (35 ft) accommodates the dc septum magnet. Quadrupoles Q17 and Q18, through which the outgoing beam must pass off-axis, are both horizontally defocusing, and thus assist in extracting the beam rapidly. The details of the extraction system are discussed in Section 4.4.

The second and third modules, used for the chromatic correction system, each have unity magnifications in the  $x$  and  $y$  planes. These two modules each consist of a FODO array of four identical quadrupole singlets, interspersed with sextupoles in a sequential symmetry arrangement. With this arrangement, the dominant optical distortions will tend to be third-order chromatic aberrations. Dipoles are introduced at the junctions between the modules to produce a symmetric momentum dispersion about the center of the chromatic correction section. The first and third dipoles are of the same strength; the second dipole, located between modules 2 and 3, has twice the strength of the others. Sextupole pairs are introduced in each transverse plane at the locations shown. The sextupole pairs are positioned so that the momentum dispersion is the same at each member of the pair. The  $R_{12}$  and the  $R_{34}$  matrix elements, the sine-like



3-84

4749A1

Figure 4.2.5.1

Table 4.2.5.1 Transport Listing

ARCN FINAL A 12-11-84 RELOC CORECS IN RB

*BEAM*	1.	*BEAM*	50.00000 GEV							
0.0 FT						0.0	51.116 MICR			
						0.0	5.869 MMRD	0.0		
						0.0	18.531 MICR	0.0	0.0	
						0.0	16.189 MMRD	0.0	0.0	0.0
						0.0	0.200 CM	0.0	0.0	0.0
						0.0	0.0 PM	0.0	0.0	0.0
*UPDATE*	6.	*TRNC*	(6.) 5.0							
*BETA*	16.		1. 0.0							
*DRIFT*	3.	*DB6 *	1.88972 FT							
1.890 FT										
*BEND*	4.	*B6 *	3.11028 FT	-14.00000 KG	0.0		( -390.847 FT ,	-0.456 DEG )		
5.000 FT										
*BEND*	4.	*B6 *	3.11028 FT	-14.00000 KG	0.0		( -390.847 FT ,	-0.456 DEG )		
8.110 FT										
*DRIFT*	3.	*DB6 *	1.63622 FT							
9.746 FT										
*DRIFT*	3.	*DFE *	0.10885 FT							
9.855 FT										
*DRIFT*	3.	*DQ25*	0.49018 FT							
10.346 FT										
*QUAD*	5.	*Q25 *	1.48070 FT	7.71064 KG	6350.00000 MICR	( 10.23583 FT )				
11.826 FT										
*DRIFT*	3.	*DDF *	1.63155 FT							
13.458 FT										
*DRIFT*	3.	*DQ24*	2.40715 FT							
15.865 FT										
*QUAD*	5.	*Q24 *	1.31359 FT	-7.71064 KG	6350.00000 MICR	( -11.03894 FT )				
17.179 FT										
*QUAD*	5.	*Q24 *	1.31359 FT	-7.71064 KG	6350.00000 MICR	( -11.03894 FT )				
18.492 FT										
*DRIFT*	3.	*DQ24*	2.40715 FT							
20.899 FT										
*DRIFT*	3.	*DDF *	1.63155 FT							
22.531 FT										
*QUAD*	5.	*Q23 *	1.48070 FT	7.71064 KG	6350.00000 MICR	( 10.23583 FT )				
24.012 FT										
*DRIFT*	3.	*DQ23*	0.49018 FT							
24.502 FT										
*DRIFT*	3.	*DFE *	0.10885 FT							
24.611 FT										
*DRIFT*	3.	*DB5 *	3.29269 FT							
27.903 FT										
*BEND*	4.	*B5 *	1.45381 FT	14.00000 KG	0.0		( 390.847 FT ,	0.213 DEG )		
29.357 FT										
*BEND*	4.	*B5 *	1.45381 FT	14.00000 KG	0.0		( 390.847 FT ,	0.213 DEG )		
30.811 FT										
*DRIFT*	3.	*DB5 *	3.29269 FT							
34.104 FT										
*DRIFT*	3.	*DFE *	0.10885 FT							
34.212 FT										
*DRIFT*	3.	*DQ22*	0.49018 FT							
34.703 FT										
*QUAD*	5.	*Q22 *	1.48070 FT	7.71064 KG	6350.00000 MICR	( 10.23583 FT )				
36.183 FT										
*DRIFT*	3.	*DDF *	1.63155 FT							
37.815 FT										
*DRIFT*	3.	*DQ21*	2.40715 FT							
40.222 FT										

Table 4.2.5.1 Transport Listing Continued

*QUAD*	5.	"Q21 "	1.31359 FT	-7.71064 KG	6350.00000 MICR (	-11.03894 FT )
41.536 FT						
*QUAD*	5.	"Q21 "	1.31359 FT	-7.71064 KG	6350.00000 MICR (	-11.03894 FT )
42.849 FT						
*DRIFT*	3.	"DQ21"	2.40715 FT			
45.256 FT						
*DRIFT*	3.	"DDF "	1.63155 FT			
46.888 FT						
*QUAD*	5.	"Q20 "	1.48070 FT	7.71064 KG	6350.00000 MICR (	10.23583 FT )
48.369 FT						
*DRIFT*	3.	"DQ20"	0.23668 FT			
48.605 FT						
*DRIFT*	3.	"DFE "	0.10885 FT			
48.714 FT						
*DRIFT*	3.	"DB4 "	1.88972 FT			
50.604 FT						
*BEND*	4.	"B4 "	3.11028 FT	-14.00000 KG	0.0	( -390.847 FT , -0.456 DEG )
53.714 FT						
*BEND*	4.	"B4 "	3.11028 FT	-14.00000 KG	0.0	( -390.847 FT , -0.456 DEG )
56.824 FT						
*DRIFT*	3.	"DB4 "	0.88972 FT			
57.714 FT						
*DRIFT*	3.	"DFX "	1.00000 FT			
58.714 FT						
*QUAD*	5.	"QFX5"	1.81738 FT	1.02362 KG	6350.00000 MICR (	61.58251 FT )
60.531 FT						
*DRIFT*	3.	"DFX "	19.50000 FT			
80.031 FT						
*DRIFT*	3.		8.00000 FT			
88.031 FT						
*DRIFT*	3.	"DFX "	7.50000 FT			
95.531 FT						
*QUAD*	5.	"QFX4"	1.95342 FT	-3.83460 KG	40005.00000 MICR (	-95.55298 FT )
97.485 FT						
*DRIFT*	3.	"DFX2"	29.41710 FT			
126.902 FT						
*QUAD*	5.	"QFX3"	1.95049 FT	-7.08798 KG	20638.00000 MICR (	-26.47679 FT )
128.852 FT						
*DRIFT*	3.	"DFX1"	15.46898 FT			
144.321 FT						
*DRIFT*	3.	"DFX "	8.60000 FT			
152.921 FT						
*QUAD*	5.	"QFX2"	2.89853 FT	9.00000 KG	10325.00000 MICR (	7.61252 FT )
155.820 FT						
*DRIFT*	3.	"DFX "	3.00000 FT			
158.820 FT						
*QUAD*	5.	"QFX1"	1.97272 FT	-9.00000 KG	10325.00000 MICR (	-10.11834 FT )
160.793 FT						
*DRIFT*	3.	"DQFX"	0.08333 FT			
160.876 FT						
*QUAD*	5.	"QFX1"	1.97272 FT	-9.00000 KG	10325.00000 MICR (	-10.11834 FT )
162.849 FT						
*DRIFT*	3.	"DFX "	1.00000 FT			
163.849 FT						
*DRIFT*	3.		4.00000 FT			
167.849 FT						
*DRIFT*	3.		-4.00000 FT			
163.849 FT						
*Z RO*	20.	"ROIP"	-4.10913 DEG			
163.849 FT						
*BEND*	4.	"B3 "	4.00000 FT	12.50000 KG	0.0	( 437.748 FT , 0.524 DEG )
167.849 FT						

Table 4.2.5.1 Transport Listing Continued

*BEND*	4.	"B3 "	4.00000 FT	12.50000 KG	0.0	( 437.748 FT , 0.524 DEG )
171.849 FT						
*DRIFT*	3.		10.35742 FT			
182.206 FT						
*QUAD*	5.	"QF "	3.00000 FT	7.68414 KG	20638.00000 MICR	( 16.58313 FT )
185.206 FT						
*DRIFT*	3.		0.50000 FT			
185.706 FT						
*SEXT*	18.	"SEXA"	2.50000 FT	2.06244 KG	20638.00000 MICR	
188.206 FT						
*DRIFT*	3.		8.85742 FT			
197.064 FT						
*SEXT*	18.	"SEXB"	2.50000 FT	-4.77772 KG	20638.00000 MICR	
199.564 FT						
*DRIFT*	3.		0.50000 FT			
200.064 FT						
*QUAD*	5.	"QD "	3.00000 FT	-7.68430 KG	20638.00000 MICR	( -15.58236 FT )
203.064 FT						
*DRIFT*	3.		10.35742 FT			
213.421 FT						
*DRIFT*	3.		8.00000 FT			
221.421 FT						
*DRIFT*	3.		10.35742 FT			
231.778 FT						
*QUAD*	5.	"QF "	3.00000 FT	7.68414 KG	20638.00000 MICR	( 16.58313 FT )
234.778 FT						
*DRIFT*	3.		0.50000 FT			
235.278 FT						
*SEXT*	18.	"SEXA"	2.50000 FT	2.06244 KG	20638.00000 MICR	
237.778 FT						
*DRIFT*	3.		8.85742 FT			
246.636 FT						
*SEXT*	18.	"SEXB"	2.50000 FT	-4.77772 KG	20638.00000 MICR	
249.136 FT						
*DRIFT*	3.		0.50000 FT			
249.636 FT						
*QUAD*	5.	"QD "	3.00000 FT	-7.68430 KG	20638.00000 MICR	( -15.58236 FT )
252.636 FT						
*DRIFT*	3.		6.10742 FT			
258.743 FT						
*BEND*	4.	"B2 "	8.00000 FT	12.50000 KG	0.0	( 437.748 FT , 1.047 DEG )
266.743 FT						
*DRIFT*	3.		0.25000 FT			
266.993 FT						
*DRIFT*	3.		0.25000 FT			
267.243 FT						
*BEND*	4.	"B2 "	8.00000 FT	12.50000 KG	0.0	( 437.748 FT , 1.047 DEG )
275.243 FT						
*DRIFT*	3.		6.10742 FT			
281.351 FT						
*QUAD*	5.	"QF "	3.00000 FT	7.68414 KG	20638.00000 MICR	( 16.58313 FT )
284.351 FT						
*DRIFT*	3.		0.50000 FT			
284.851 FT						
*SEXT*	18.	"SEXA"	2.50000 FT	2.06244 KG	20638.00000 MICR	
287.351 FT						
*DRIFT*	3.		8.85742 FT			
296.208 FT						
*SEXT*	18.	"SEXB"	2.50000 FT	-4.77772 KG	20638.00000 MICR	
298.708 FT						
*DRIFT*	3.		0.50000 FT			
299.208 FT						

Table 4.2.5.1 Transport Listing Continued

*QUAD*	5.	"QD "	3.00000 FT	-7.68430 KG	20638.00000 MICR (	-15.58236 FT )
302.208 FT						
*DRIFT*	3.		10.35742 FT			
312.566 FT						
*DRIFT*	3.		8.00000 FT			
320.566 FT						
*DRIFT*	3.		10.35742 FT			
330.923 FT						
*QUAD*	5.	"QF "	3.00000 FT	7.68414 KG	20638.00000 MICR (	16.58313 FT )
333.923 FT						
*DRIFT*	3.		0.50000 FT			
334.423 FT						
*SEXT*	18.	"SEXA"	2.50000 FT	2.06244 KG	20638.00000 MICR	
336.923 FT						
*DRIFT*	3.		8.85742 FT			
345.780 FT						
*SEXT*	18.	"SEXB"	2.50000 FT	-4.77772 KG	20638.00000 MICR	
348.280 FT						
*DRIFT*	3.		0.50000 FT			
348.780 FT						
*QUAD*	5.	"QD "	3.00000 FT	-7.68430 KG	20638.00000 MICR (	-15.58236 FT )
351.780 FT						
*DRIFT*	3.	"DSB1"	7.66489 FT			
359.446 FT						
*DRIFT*	3.	"DSB3"	2.40370 FT			
361.849 FT						
*BEND*	4.	"BSB "	7.59742 FT	12.50000 KG	0.0	( 437.748 FT , 0.994 DEG )
369.446 FT						
*DRIFT*	3.		1.00000 FT			
370.446 FT						
*BEND*	4.	"SB "	10.00000 FT	0.50000 KG	0.0	( 10943.704 FT , 0.052 DEG )
380.446 FT						
*DRIFT*	3.	"DSB2"	8.66258 FT			
389.109 FT						
*QUAD*	5.	"Q6X "	3.80156 FT	7.50000 KG	63500.00000 MICR (	40.62320 FT )
392.911 FT						
*DRIFT*	3.	"D6 "	14.65621 FT			
407.567 FT						
*QUAD*	5.	"Q5B "	3.38888 FT	-7.50000 KG	63500.00000 MICR (	-44.29149 FT )
410.956 FT						
*DRIFT*	3.		0.50000 FT			
411.456 FT						
*QUAD*	5.	"Q5A "	3.38888 FT	-7.50000 KG	63500.00000 MICR (	-44.29149 FT )
414.844 FT						
*DRIFT*	3.	"D5A "	10.00000 FT			
424.844 FT						
*DRIFT*	3.	"D5 "	4.65621 FT			
429.501 FT						
*QUAD*	5.	"Q4X "	3.80156 FT	7.50000 KG	63500.00000 MICR (	40.62320 FT )
433.302 FT						
*DRIFT*	3.	"D4 "	42.07563 FT			
475.378 FT						
*QUAD*	5.	"Q3X "	1.96006 FT	14.00000 KG	10000.00000 MICR (	6.88064 FT )
477.338 FT						
*DRIFT*	3.	"D3 "	1.00000 FT			
478.338 FT						
*QUAD*	5.	"Q2B "	1.78664 FT	-14.00000 KG	10000.00000 MICR (	-6.88784 FT )
480.125 FT						
*DRIFT*	3.	"D2AB"	0.0 FT			
480.125 FT						
*QUAD*	5.	"Q2A "	1.78664 FT	-14.00000 KG	10000.00000 MICR (	-6.88784 FT )
481.911 FT						

**Table 4.2.5.1 Transport Listing Continued**

*DRIFT*	3.	"D2 "	1.00000 FT																	
			482.911 FT																	
*QUAD*	5.	"Q1X "	1.96006 FT	14.00000 KG	10000.00000 MICR (	6.88064 FT )														
			484.871 FT																	
*DRIFT*	3.	"D1 "	7.25444 FT																	
			492.126 FT																	
*TRANSFORM 1*		"IP "																		
			-0.02343	0.00147	0.00464	-0.00004	0.0	1.11001												
			0.00005	-42.46343	-0.00000	1.10668	0.0	0.13036												
			-0.00168	-0.00014	-0.06458	-0.00069	0.0	0.07975												
			0.00000	-3.05053	-0.00006	-15.40415	0.0	0.00964												
			0.00000	-0.00000	0.00000	-0.00000	1.00000	-0.00001												
			0.0	0.0	0.0	0.0	0.0	1.00000												
									0.0	1.201 MICR										
									0.0	249.861 MMRD	-0.007									
									0.0	1.200 MICR	0.000	0.000								
									0.0	250.020 MMRD	0.000	-0.000	0.009							
									0.0	0.200 CM	-0.000	0.000	0.000	0.000						
									0.0	0.0 PM	0.0	0.0	0.0	0.0						
*DRIFT*	3.	"D1 "	7.25444 FT																	
*LENGTH*			499.38017 FT																	

functions, have the same magnitude but opposite sign at each of the conjugated elements of a given sextupole pair. This arrangement results in a natural cancellation of the second-order geometric aberrations which would otherwise be troublesome. The strengths of the sextupole pairs are then adjusted to eliminate the second-order chromatic aberrations,  $T_{126}$  and  $T_{346}$ , which are the main source of the optical distortions.

The function of the fourth and final telescopic module is to complete the beam envelope matching to the interaction point with an additional demagnification factor of five in both the  $x$  and  $y$  planes. In general, the higher the field gradient in the final quadrupole triplet, Q1, Q2, Q3, and the shorter the distance,  $L^*$ , from the IP to the face of the first quadrupole, the smaller is the achievable beam spot at the interaction point and the higher the luminosity. Of course, high quadrupole gradients can generally be obtained by using small apertures, but in practice this can only be done at the expense of the field quality, and in this application, a minimum aperture of about 38 mm is needed to clear the outgoing radiation. With this aperture, a gradient of 14 to 16 kG/cm can be reached by an extension of Fermilab's superconducting Tevatron technology. A design for such a magnet is described in Section 4.3.3.1 below.

Because of the complexity inherent in a superconducting system and the technical difficulties likely to be encountered in the initial operation of such a system, an alternate optical solution based on conventional iron and copper quadrupoles has been developed. This conventional solution, based on well-established engineering designs, would be a simple and reliable alternative to the superconducting solution. As of this writing, the conventional solution is being studied with the aim of finding an optical design that could be converted later to the full-performance superconducting quad solution with a minimum of changes to other components. It appears that the loss in peak luminosity may be at most on the order of 40% compared to the superconducting solution. This loss might easily be offset by the greater reliability and ease of operation of the conventional option during the first year. Thus, the conventional option is likely to yield a greater total integrated luminosity. On the other hand, the conventional iron quadrupoles would not be usable in the presence of an external

magnetic field. When the SLD detector is installed, this would force  $L^*$  to be increased to about 14 ft, resulting in about a factor of two loss in luminosity. Nevertheless, this conventional solution may be preferable during at least the first few months of SLC operation with the Mark II detector.

A variety of other solutions become available if the  $L^*$  or aperture requirements are relaxed. An interesting possibility being examined as a back-up or future option is based on  $\text{SmCo}_5$  permanent-magnets. Permanent magnet quadrupoles offer a smaller gradient than superconducting magnets but could be used to reach the full design luminosity if  $L^*$  were reduced to 0.75 m. No practical solution has been developed for tuning a permanent magnet system over a useful energy range, but the problem is being studied. Any small-aperture solution will introduce new complications in the already formidable background radiation problem discussed below.

Because of the technical uncertainties in constructing high-gradient superconducting quadrupoles, the final focus system as a whole has been designed to work with any gradient in the range of about 5 to 20 kG/cm in the final triplet with only a small degradation of the overall performance. Lowering the gradients in Q1, 2, and 3 requires changing the gradients in Q4, 5, and 6 and repositioning them longitudinally along the beam line, and changing the field strengths in the sextupoles. Table 4.2.5.2 lists the beam spot sizes that can be achieved (neglecting emittance growth due to synchrotron radiation and residual aberrations due to missalignments) for several values of the final triplet gradient. The last entry corresponds to the conventional quadrupole alternative.

Also listed is the sextupole strength required to cancel the chromatic aberrations, expressed as a pole tip field at a radius of 2.0638 cm. For a fixed total demagnification, the magnitude of the sextupole fields, and by implication the severity of the uncorrected chromatic effects, is seen to grow as the final triplet strength is reduced. In the conventional solution, the first-order demagnification factor has been reduced from 5 to 4, partly to keep the sextupole fields within practical limits. An important feature of this design is that construction and installation of all the conventional magnets in the matching and chromatic cor-

rection sections can proceed without an exact specification of the final triplet. Furthermore, if some future development leads to improved quadrupole technology, the final triplet could easily be replaced. The only other change needed would be in the positions of Q4, Q5, and Q6.

**Table 4.2.5.2.**

Spot Size and Sextupole Strength for Various Gradients in the Final Triplet

$L^*$ (m)	Q1, 2, 3 (kG/cm)	$\sigma_x^*$ ( $\mu\text{m}$ )	$S_B$ (kG at pole tip)
2.2	20	1.34	5.54
2.2	14	1.35	5.81
2.2	10	1.46	5.96
3.0	14	1.43	6.60
2.8	4.8	1.65	4.64

#### 4.2.6 S-Bend

A novel feature of the SLC final focus not found in conventional storage rings is the S-bend geometry formed by the antisymmetric bends of the north and south chromatic correction sections. Specifically, the final dipole on the north side bends the electron beam to the west, while the final dipole on the south side bends the positron beam to the east. This is illustrated in Fig. 4.2.6.1. This feature has been incorporated to ease the problem of masking off the dipole synchrotron radiation that would otherwise illuminate the experimental detector.

In a conventional storage ring, most of the dipole synchrotron radiation from both directions can be blocked by a pair of circular masks, symmetrically arranged on each side of the detector. Unavoidably, however, some of the radiation passing through the center hole of the first mask will strike the inside (detector side) surface of the second mask and back-scatter into the detector. With the beam energies and intensities planned for the SLC, these hot spots on the inside surfaces of the masks could be serious sources of hard x-ray background.

This problem has been curtailed by introducing the S-bend. With this ar-

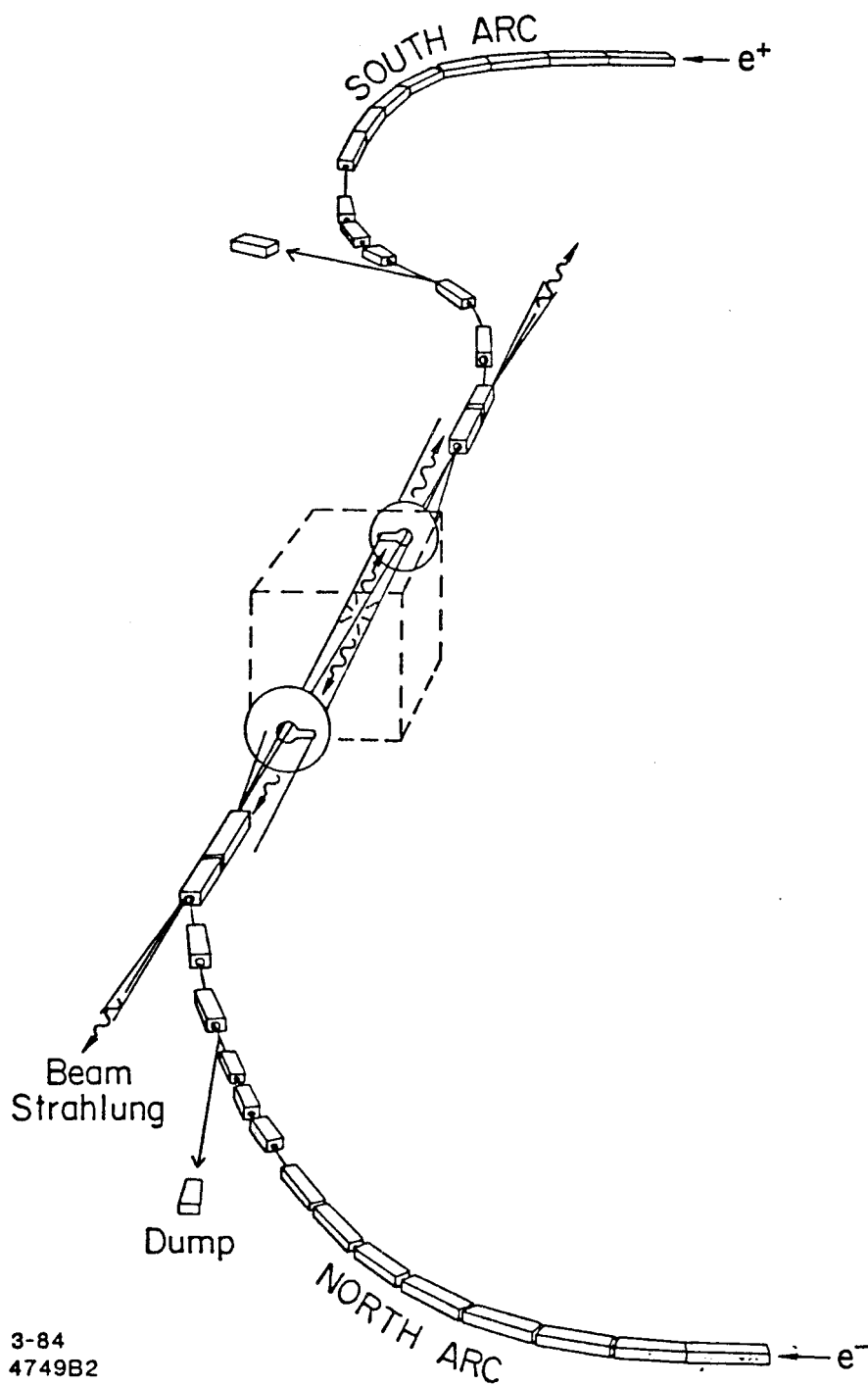
rangement, the synchrotron radiation from the electron beam (approaching from the north) is all in a thin horizontal sheet to the east of the beam itself. The radiation from the positron beam is all in a horizontal sheet to the west. Masks with open slots on one side can then be arranged anti-symmetrically to block the incoming radiation but pass the outgoing radiation from the other beam. Unfortunately, the S-bend does nothing to reduce the synchrotron radiation background expected from the quadrupoles. Backgrounds and masking are discussed in quantitative terms in Section 9.3 below.

#### 4.2.7 Tolerances and Corrections

At the time of this writing, the study of alignment tolerances and correction schemes for the final focus is in progress. An attempt to give a detailed description of this aspect of the design would be premature, but the general guidelines are clear. Not surprisingly, the performance of the system is extremely sensitive to misalignments of the optical axes of the magnets relative to the beams, both with respect to correcting the chromatic aberrations and to steering the beams into the final collision. The misalignment of a sextupole by a few tens of microns will enlarge the spot by a large factor; a misalignment of the final quadrupole triplet on one side by  $5 \mu\text{m}$  relative to the other will cause the incoming beams to miss each other completely if no correction is made.

An important distinction must be made, however, between static and time-dependent errors. Even as the beam is sensitive to alignment errors, it is also a powerful diagnostic tool itself. Given enough beam position monitors with resolution of the order of  $25 \mu\text{m}$  and enough trim dipoles, the beams can be cleanly threaded through the system. Studies show that static alignment errors of up to  $100 \mu\text{m}$  and rolls of up to  $\pm 1 \text{ mrad}$  can be tolerated. Figure 4.2.7.1 shows schematically the positions of the trim and steering magnets and the diagnostic instrumentation.

Time-dependent errors pose a more challenging problem. Such errors may be caused by natural or artificially generated ground movements, temperature changes, or the relaxation of mechanical support structures. These sources of errors can best be discussed in terms of three loosely defined (and overlapping)



3-84  
4749B2

Figure 4.2.6.1

time domains: slow ( $\tau > 10^2$  sec), intermediate ( $\tau \approx 1$  sec), and fast ( $\tau < 10^{-2}$  sec).

As suggested above, slow movements over a limited amplitude range can be compensated by trim dipoles, guided by BPM information. The final quadrupole triplets, however, will require special positioning considerations, because of their intimate mechanical relationship to the detector. Specifically, these triplets must be supported by structures that pass through the detector endcap holes and permit easy access to the drift chambers and other devices in the heart of the detector. Experience at PEP has shown that relative positioning tolerances for massive detector components is no better than several hundred microns. These errors are compounded by vertical floor movements on the order of 1 mm, expected when detectors (or even just the endcaps of a second-generation detector) are moved within the IR hall. To ensure that transverse alignment tolerances of  $< 100\mu\text{m}$  can be maintained, the triplets will be equipped with an alignment monitoring system and motorized translation devices to facilitate remotely-controlled positioning. The development of such a system is in progress.

Movements in the high-frequency time domain can be dealt with by designing support structures that passively damp vibrations. Man-made transient ground movements may perturb the beams enough to cause them to miss many times each day, but it is expected that the overall effect of these perturbations on the integrated luminosity can be kept small ( $< 10\%$ ). In the intermediate timescale, an active feedback system will be required to keep the opposing beams centered on each other. This is discussed in the next section.

The impact of the static magnetic field errors is being studied in parallel with the alignment tolerance problems. These studies indicate that the most severe field tolerances are about one part in  $10^4$  for some of the magnets. For others, static errors of one part in  $10^3$  will be acceptable if sufficient diagnostic instrumentation and trim magnets are provided. Distortions caused by field errors in the final focus quadrupoles can be corrected by a pair of small trim quadrupoles near Q4 and Q5 in the final transformer. In addition, skew quad-

ruipoles will be provided to correct for rotational errors in the final triplet and to compensate for  $xy$  mixing caused by the solenoid field of the detector. It has also been found that these trim magnets in the final transformer can, to a large extent, correct for misalignments of the sextupoles in the chromatic correction section. Any residual momentum dispersion can be cancelled with a pair of trim dipoles near Q6.

#### 4.2.8 Dynamic Steering Corrections

An array of small steering dipoles will be required to correct for small time-dependent variations in the positions or strengths of magnets or shifts in the trajectories of the beams entering from the arcs. Although some details of the design have not been completed, the general features are now understood.

The beam quality is sensitive to position errors at several points in the FFS. To avoid introducing aberrations, the incoming beam should be close to the optical axis of the quadrupoles as it enters the first telescope. Then, it must be centered in each of the eight sextupoles, and it must be centered in the final quadrupole triplet. Finally, the two incoming beams must meet at the IP where their dimensions are on the order of  $1\ \mu\text{m}$ .

Near each of these critical points will be a pair of BPMs with both  $x$  and  $y$  elements, spaced approximately one-quarter betatron wavelength apart. These pairs will be located at the ends of drift sections when possible, where they uniquely define a line in space. Upstream of each such BPM pair will be a pair of steering dipoles (both  $x$  and  $y$  at each position), also spaced a quarter wavelength apart. Although it is impractical to find an optical solution with functionally-orthogonal steering controls, the settings of each dipole pair can be determined by a simple matrix operation by a microprocessor. Separate microprocessors on the north and south sides could sequentially cycle through the corrector sets to independently optimize the  $e^+$  and  $e^-$  beams through their respective optical systems.

By instrumenting a few strategically located BPMs to measure the positions of both the incoming and outgoing beams, the steering can then be adjusted to bring the beams together at the IP. For example, two pairs of BPMs in the

chromatic correction section could be used in this way to take advantage of the magnification of the final telescope. If each BPM has a resolution of  $10\ \mu\text{m}$  for the relative centroid positions of the incoming and outgoing beams (measured a few hundred nanoseconds apart), the relative separation of the beams at the IP will be known to  $2\ \mu\text{m}$ .

The final steering will be accomplished by small dipoles in the final transformer, under the control of a dedicated microprocessor. Feedback information may come from any of several sources. The most promising are beamstrahlung monitors, devices which are sensitive to the gamma rays associated with the mutual disruption of the opposing beams, and which can be segmented to indicate the direction of the outgoing beam as well as the degree of disruption. A preliminary design for such a device is discussed in Section 4.6.

The beamstrahlung monitors will be located on each side of the IP along the line-of-sight. One possibility being considered is to position a small-angle beamstrahlung monitor behind (upstream of) the hard-bend dipole B1 on each side, where they are clear of the charged beams. They would be supplemented by wide-angle beamstrahlung monitors positioned near the soft-bend magnets, each with a center hole to pass the charged beams. The control algorithm would then steer to center the beamstrahlung cones on the monitors and maximize the disruption angles. The optimum frequency of steering updates will depend on the nature of the perturbations or drifts, and will have to be determined experimentally. In principle, it may be possible to correct once every six pulses.

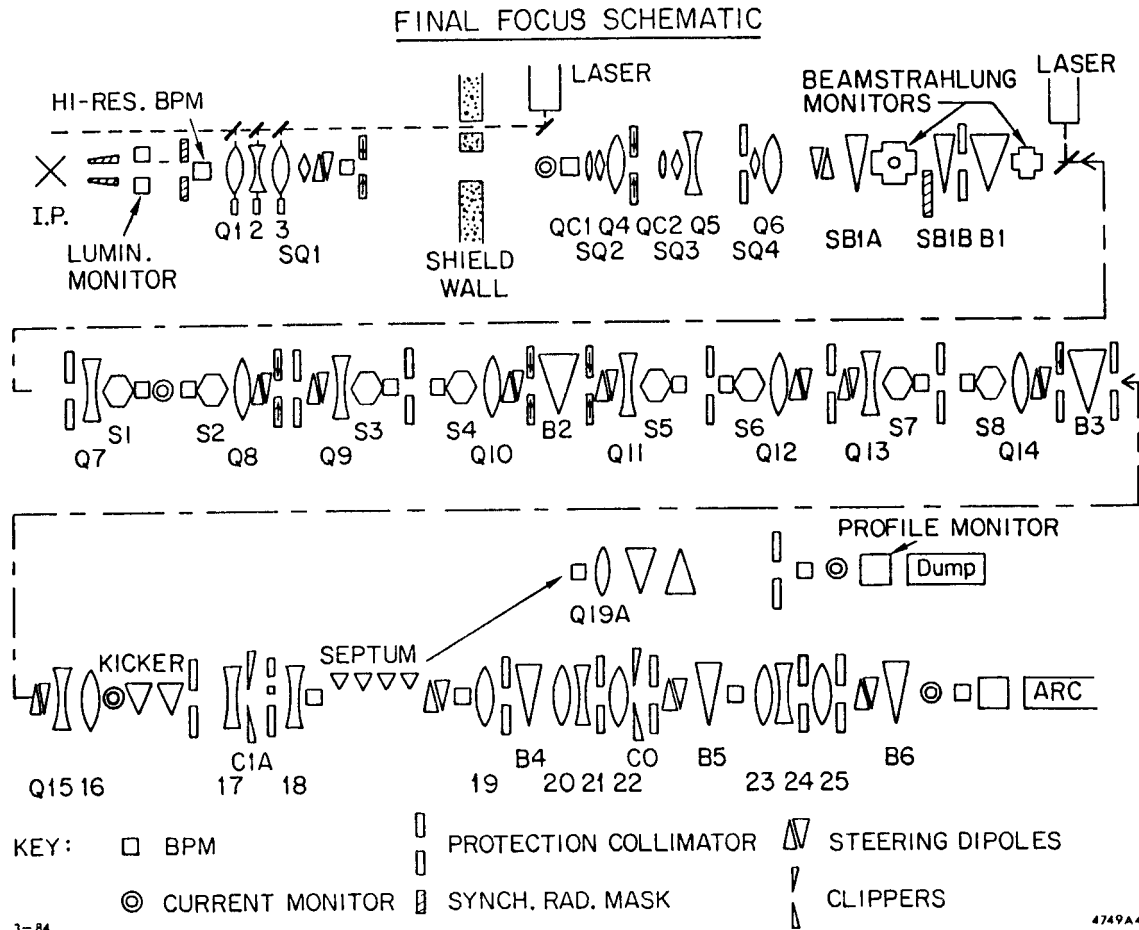


**Figure 4.2.7.1**

## 4.3 MAGNETS

### 4.3.1 Conventional Magnets

The current final focus optical design consists of 50 quadrupoles, 16 sextupoles, 14 dipoles and various steering and corrector magnets, as well as the kickers, septa, and superconducting triplet, which are described separately below. The specifications of the conventional magnets and their power supplies are given in Table 4.3.1 (for 55 GeV operation).

The cores of most quadrupoles will be made up of thin magnet steel laminations. The cores of all the bends and sextupoles will be fabricated from solid steel. The coils will be copper in all cases except for Q4, Q5, and Q6, for which they will be aluminum.

### 4.3.2 Mounting

Mounting on individual support stands is planned for most of the conventional magnets in the final focus system, because of the long drifts between magnets. However, magnets located close together, such as the quadrupole-sextupole pairs, will share the same support, in order to minimize alignment errors and reduce costs.

### 4.3.3 Detector Quadrupoles

As discussed in Section 4.2.5 above, the final telescope has been designed to accommodate a variety of possible magnets in the final quadrupole triplet. A triplet of high-gradient superconducting quadrupoles now appears to have the greatest potential for reaching the highest peak luminosity. For the reasons discussed above, however, a set of conventional iron quadrupoles may be preferable for the initial operation of the SLC.

**4.3.3.1 Superconducting Quadrupoles:** To develop superconducting magnets within the time frame of the SLC construction, SLAC has negotiated an agreement with Fermilab to design and test a superconducting quadrupole based on the technology developed for the Tevatron low-beta quads. The SLC quad, shown in Fig. 4.3.3.1, has the same general geometry as the FNAL design and can use the same type of cable (23 strands with Cu/NbTi = 1.3), but differs in

having a smaller aperture, higher gradient, and no iron.

The inner conductor diameter was chosen to be 2 inches. This diameter is a practical lower limit imposed by the geometry of the keystone-shaped superconducting cable. Allowing space for an inner helium passage and for the beam pipe, the clear aperture is 1.680 inches. This leaves about 2 mm of radial clearance at the upstream end of Q3 if a disruption angle of 2.2 mrad is achieved. The first prototype using low-beta cable was tested recently at Fermilab and reached a maximum gradient of 16.6 kG/cm at 5770 amps and 4.2°K. The SLC can tolerate a maximum deviation from a pure quadrupole field of  $10^{-4}$  at a radius of 1 mm. Preliminary results indicate that the prototype was well within that tolerance.

Proceeding in parallel with these efforts, the Fermilab magnet group is investigating a segmented conductor having an overall cross-section geometry similar to their standard low-beta cable, but segmented into five sub-cables of equal area. Coils using this type of cable are more difficult to fabricate, but will reduce the current requirement to 1200 amps, with a significant reduction in the refrigeration and power supply requirements and in the stray fields from the power supply cables.

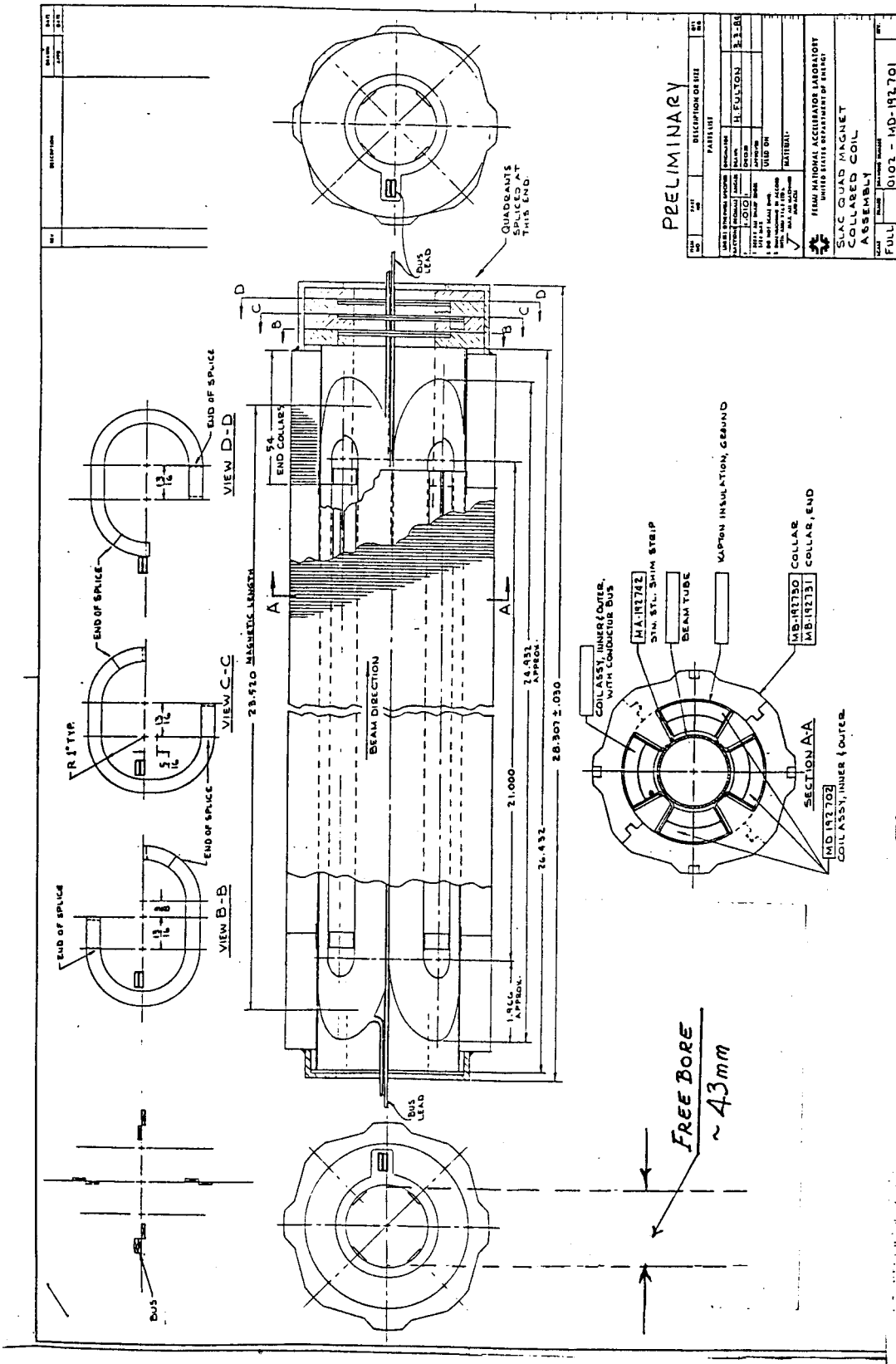
The SLC quadrupoles must be operable when immersed in the solenoid field of a large second generation detector (now estimated at 6 kG for the SLD), as well as with the smaller Mark II. This precludes the use of iron in these quadrupoles, because of the large magnetic forces and the uneven saturation effects. Apart from the question of iron, however, an external field of this magnitude is expected to lower the quench current by about 6%. One possibility for recovering the lost performance would be to cool the quads down to the 3°K range, and thus raise the quench current. This would require a more sophisticated cryogenic system.

The tentative schedule calls for the construction and testing of prototype collared quad coils by early 1985 using the low-beta and segmented cables. Final decisions on the design specifications will be made based on the performance of these prototypes. Procurement and fabrication will then proceed for two

Table 4.3.1

Proposed Magnet & Power Supply Specifications for the SLC Final Focus System at 55 GeV  
(Conventional Magnet Solution for Final Triplet)

Magnet	Voltage Per Magnet V	Current A	Power Per Magnet kW	Flow Per Magnet gpm	$\int$ Gdl-kG $\int$ Bdl-kGm $\int$ Gdl-/kG/cm	Pole Tip or Gap Flux kG	Aperture Gap cm cm	$L_{eff}$ cm	Voltage (total) V	Power (total) kW	Power Supply (V/A/kW)
Q1, Q3	55.6	291	16.2	2.6	624.762	11.000	4.128	117.21	213.4	62.2	250/300/75
Q2A&B	51.1	291	14.9	2.7	568.984	11.000	4.128	106.75			
Q4, Q6	27.3	1,254	34.2	7.2	150.542	9.78	12.7	97.79	100	131.6	135/3000/400
Q5A&B	25.2	1,254	31.6	7.6	134.200	9.78	12.7	86.55			
Q7-Q14	36.8	286	10.5	3.2	374.512	10.8	4.128	71.42	294.4	84.0	400/400/160
Q15	15.2	544	8.3	5.1	1145.05	10.15	2.065	116.45	26.8	14.7	50/600/30
Q16	11.6	544	6.4	2.0	841.215	10.15	2.065	85.57			
Q17	25.6	299	7.7	2.9	220.886	10.67	4.128	42.70	25.6	7.8	60/500/30
Q18	280	390	10.9	4.4	67.213	7.80	8.0	34.48	6.6	0.6	20/100/2
Q19	3.4	33.7	0.1	AIR COOLED	102.693	4.108	1.27	15.88	3.3	0.1	20/50/1
SB	Could be two magnets with different B				1.524	0.500	12.7	304.80	32.4	14.3	60/500/30
B1	44.5	520	23.2	~ 6	31.841	13.75	2.223	231.42	~ 171	~ 90	200/600/120
B2A,B2B, B3	47.0	520	24.4	~ 6	33.528	13.75	2.223	243.68			
Sz7,-9, -11,-13	16.5	109	1.8	0.7	91.129	5.091	4.128	76.2	66.1	2.8	100/200/20
Sz8,-10, -12,-14	Same magnets, same Power Supply, but magnets run at lower values than Sz7, Sz9, Sz11, Sz13										100/200/0
Kickers	14,000	2,500	?	AIR COOLED	0.306	0.402	2.54	76.2	14,000	?	12,000/ 0.45/5.4
Septa	20.7	762	15.8	2.1	7.505	6.156	2.032	121.9	82.8	63.2	100/800/80
Q20,-22 -23,-25	5.9	303	1.8	1.1	602.829	9.134	1.27	41.91	42.6	12.9	80/300/24
Q21,Q24	9.5	303	2.9	0.8	1069.582	9.134	1.27	74.36			
B4,B6	25.7	465	11.9	3.5	26.544	15.4	1.448	189.60	64.5	29.9	100/500/50
B5	13.1	465	6.1	5.3	13.648	15.4	1.448	88.62			
A3,A6(x,y)	11.9	100	1.2	0.4	0.500	1.23	12.7	40.64	11.9	1.2	15/100/1.5
A8,A9 A10,A11	15.9	9.6	0.15	AIR COOLED	0.500	1.23	4.128	40.64	15.9	0.15	20/10/0.2
A12,A13, A14,A15	15.9	9.6	0.15	AIR COOLED	0.500	1.23	4.128	40.64	15.9	0.15	20/10/0.2
A19,A22 A25(x,y)	9.5	3.8	0.04	AIR COOLED	0.500	1.23	1.429	40.64	9.5	0.04	12/4/0.05
QC's	Corrector quads, not yet designed.										
QSC's	Skew quads, not yet designed.										



PRELIMINARY

REVISIONS		REVISIONS	
NO.	DATE	DESCRIPTION OF REV.	BY
1		ISSUED FOR FABRICATION	REVLUNGN
2		ISSUED FOR FABRICATION	REVLUNGN
3		ISSUED FOR FABRICATION	REVLUNGN
4		ISSUED FOR FABRICATION	REVLUNGN
5		ISSUED FOR FABRICATION	REVLUNGN
6		ISSUED FOR FABRICATION	REVLUNGN
7		ISSUED FOR FABRICATION	REVLUNGN
8		ISSUED FOR FABRICATION	REVLUNGN
9		ISSUED FOR FABRICATION	REVLUNGN
10		ISSUED FOR FABRICATION	REVLUNGN

FROM NATIONAL ACCELERATOR LABORATORY  
 UNITED STATES DEPARTMENT OF ENERGY  
 SAC QUAD MAGNET  
 COLLARED COIL  
 ASSEMBLY  
 FULL 0102 - MD-192701

Figure 4.3.3.1

complete triplets plus spares, with the expectation that they will be assembled, measured, and delivered to SLAC within one year.

**4.3.3.2 Conventional Quadrupoles:** In any quadrupole design for the final triplet, it is desirable to keep the aperture as large as possible to minimize background radiation scattering into the detector. For the conventional option, a 1 5/8 in. aperture was chosen. With the pole-tip field conservatively set to 10 kG (for 50 GeV), a gradient of 4.85 kG/cm is reached. This can be scaled up to greater than 55 GeV before saturation effects become noticeable.

The design shown in Fig. 4.3.3.2.1 is based on laminated steel construction with water-cooled copper coils and can be fabricated by well established techniques. The outside dimensions are close to those of the cryostat for the superconducting option, and such magnets will fit through the hole in the Mark II end cap with a small margin of clearance. A mounting arrangement is shown in Fig. 4.3.3.2.2. Note that quadrupole Q2 is represented by two separate but identical adjacent magnets. Splitting Q2 in this way would be done to simplify fabrication and mounting and to avoid errors caused by sagging or bending.

**4.3.3.3 SmCo<sub>5</sub> Quadrupoles:** An interesting alternative to superconducting magnets in the final triplet would be SmCo<sub>5</sub> permanent magnets mounted inside the detector close to the IP, and possibly supplemented by conventional iron magnets outside the detector. Because of the small aperture and small  $L^*$  required, the permanent magnet approach is not part of the current working design. However, because of the extensive effort applied to this approach in the early phases of the SLC design, and because such magnets offer interesting possibilities for later improvements, the status of this study is summarized here. Each permanent magnet quadrupole in a practical design would consist of a large number of "mini-quad" layers. A quadrupole's focal length could be adjusted by rotating individual mini-quads (in pairs) relative to each other, or simply removing them, to allow for a continuum of collider energies. Another approach would be to slide mini-quad sections longitudinally to vary the net focusing strength of the set.

A prototype quadrupole consisting of seven layers, each 1.27 cm thick, was

Figure 4.3.3.2.1 Conventional Final Focus Quadrupole Option

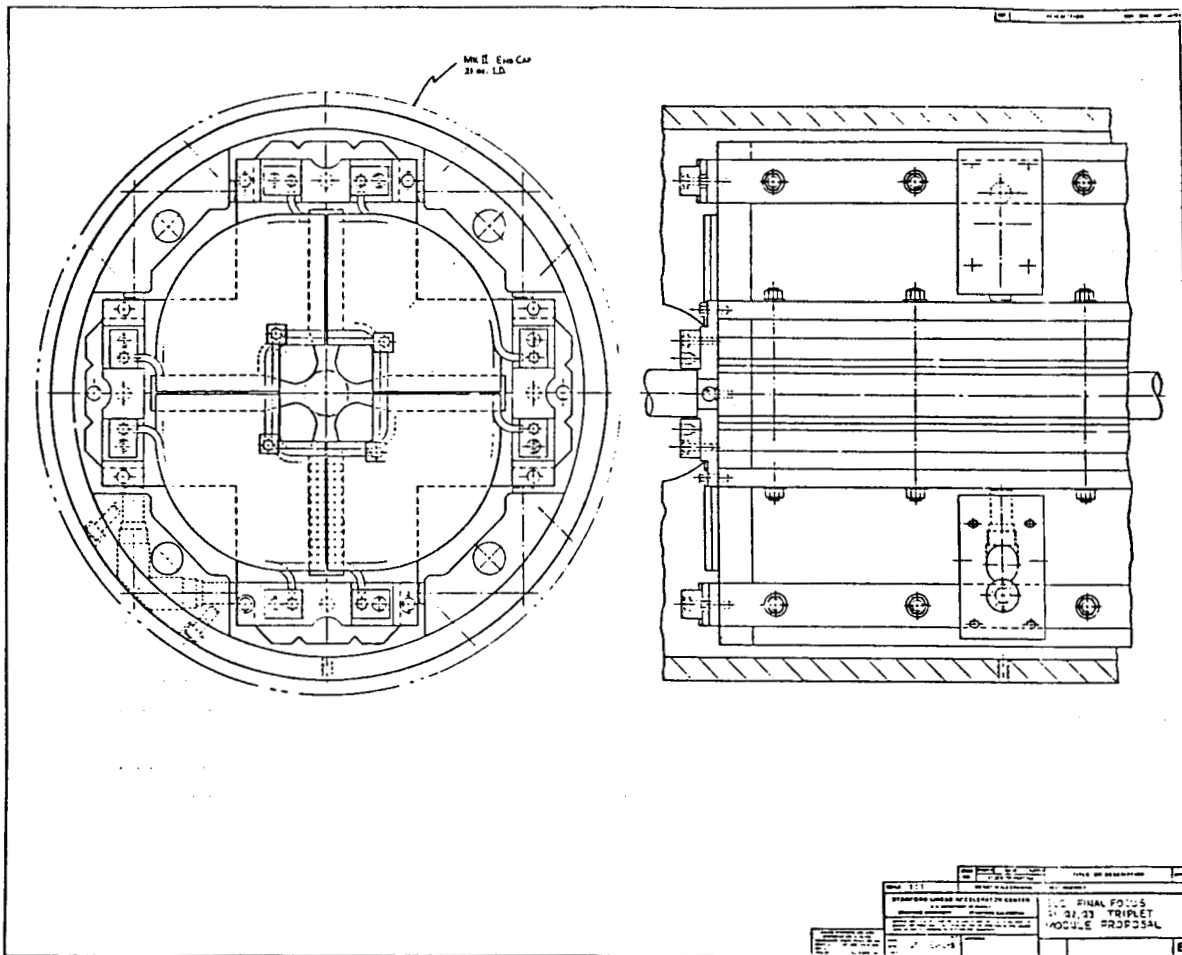
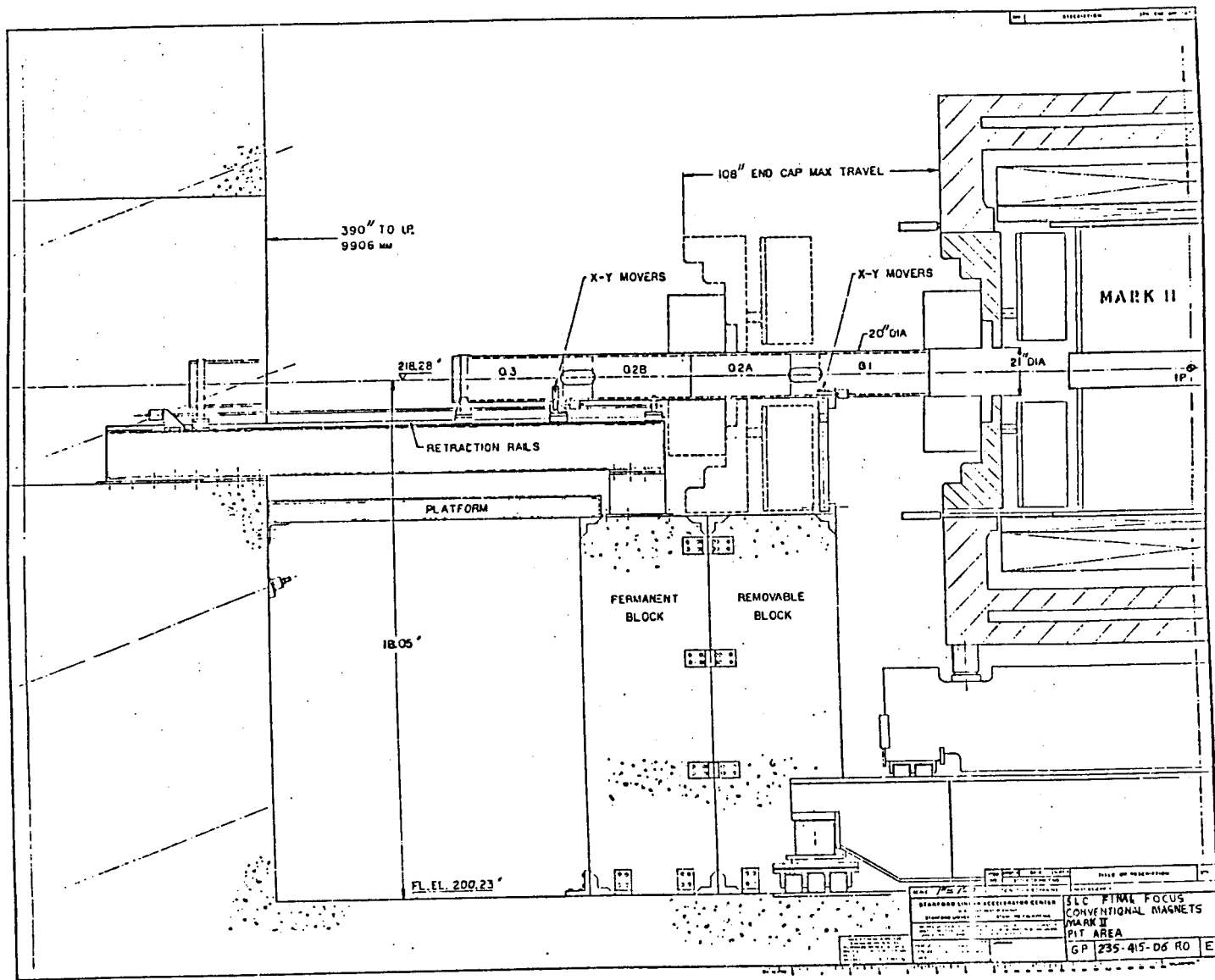


Figure 4.3.3.2.2

Mounting arrangement of conventional quadrupoles with Mark II detector.



fabricated and tested last year. Each layer consisted of 16 blocks of samarium cobalt,  $\text{SmCo}_5$ , with a coercive strength of  $H_c = 8.2$  kG, and a remanent induction of  $B_r = 9$  kG. The assembled quadrupole had a clear aperture of 2 cm diameter. Field measurements were done at a radius of 8 mm, or 80% of aperture. The results showed the 36-pole to be 0.09% of the quadrupole content. All other harmonics were less than that.

#### 4.3.4 Power Supplies and Bussing

Power supplies for the FFS will be located in two separate locations:

1. North arc power supplies will be located in a building on the utility pad north of the collider experimental hall. Alternating current power will be brought to the power supplies from a 12 kV/480 V substation on an adjacent pad. Three 24-in. diameter shafts will link the building to the north arc tunnel. One shaft is reserved for power supply circuits.
2. South arc power supplies will be located inside the collider experimental hall on the south side of the main floor between the structural columns. The power supplies will have ac from a 12 kV/480 V substation to the south of the experimental hall. A vault, with access to the main floor via a rectangular opening, will be linked to the south arc tunnel by three 24 in. diameter shafts. One of the shafts is reserved for power supply circuits. Cable trays will be installed for the support of the conductors in the power supply building, in the collider experimental hall, and in the arc tunnels.

Air cooled aluminum conductors will be used for most of the magnet bussing circuits. Conductors will be compact, with unidirectional stranding insulated for 600 V and suitable for installation in cable trays or conduits. Connectors will be either set-screw type or compression type, as required.

One of the quadrupole circuits will be bussed with a water-cooled aluminum conductor with the following characteristics:

1. Conductor Material	1060 H Aluminum
2. O.D. of Aluminum Conductor	1 in.
3. Cooling Passage	3/8 in. diameter
4. Insulation	1000 V

This conductor can be installed using conventional cable pulling methods. Terminations will be installed by welding "flags" to the conductor or by the use of power actuated devices which provide mechanical connections to the conductor. Connections to the LCW system for cooling of the bus will be accomplished using tapped fittings and hoses to manifolds.

Refer to Table 4.3.1 for the specifications of the power supplies. The larger power supplies will be air cooled, floor mounted, 480 V, three phase. Small power supplies will be rack mounted 208 V, single phase.

## 4.4 EXTRACTION SYSTEM AND BEAM DUMPING

### 4.4.1 Introduction

The function of the beam dumping system is to transport the outgoing beams to a location where the beam power (70 kW) can be safely dissipated and adequate radiation shielding can be provided. An important secondary function will be to provide conditions that will allow measurement of the electron polarization using Moeller scattering. The current final focus optics design consists of two telescopes separated by a chromatic correction section. Extraction does not begin until the exhaust beam has reached the outboard telescope.

### 4.4.2 Optics

Extraction is accomplished by perturbing the outgoing beam with a pulsed kicker, and allowing this perturbation to be magnified by succeeding FFS magnets, such that enough spatial offset is generated to allow room for a dc septum magnet to provide the main separation. The following conditions must be satisfactorily balanced to make this scheme work:

1. The distance between the pulsed kicker magnet and the IP must be sufficient to allow for attainable rise times.
2. The location of the kicker and septum must be chosen, such that the first order transfer matrix element,  $\langle y|y' \rangle$  or  $\langle x|x' \rangle$  is large between these magnets. The beam size must be small compared to the offset at the septum, and the kick angle must be large enough to provide sufficient offset at the septum, but small enough to keep the disrupted beams within FFS magnet apertures.
3. Finally, there must be sufficient drift space behind the septum to allow the extracted beam to clear the next FFS element.

At the present septum location, the clearance between the incoming beam axis and the outgoing (disrupted) beam axis is large enough to allow a choice between a Lambertson-type septum, which extracts in the vertical plane, and a current coil septum, which extracts in the horizontal plane. Moreover, the clearance is large enough so that the septum does not have to be in vacuum. To achieve the earliest possible separation between the arc magnets and the

extracted beam line for the Moeller polarimeter, it was desirable to choose extraction in the horizontal plane, to the outside of the arc. Choosing this option means that spin precession of the electrons coming backwards through the FFS is confined to the horizontal plane.

Figures 4.4.2.1 and 4.4.2.2 are sketches of the electron and positron extracted beam lines. The two sides differ, because the FFS S-bend scheme forces the arc-to-FFS matching sections and outboard telescopes to be different. Fortunately, the more rapid separation of the two beams on the electron extraction side allows space for the Moeller polarimeter without the need to lengthen the dump alcove. To control the horizontal dispersion function at the Moeller target, a small quadrupole, Q19A, is squeezed into the electron extraction line, just outboard the septum. This quad is not needed on the positron side; the extracted positrons simply drift approximately 200 ft from the septum to the north dump.

#### 4.4.3 Disrupted Beam Profile

The beam-stay-clear in the FFS and extraction line has been determined with the following outgoing beam parameters:

$$\begin{aligned}x_o &= y_o = 1.3 \text{ } \mu\text{m max,} \\ \theta_o &= \phi_o = \pm 2.5 \text{ mrad max,} \\ \text{Energy } e^+ &= 1.03 \times (\text{Energy } e^-), \\ \Delta E/E &= 0.6\% \text{ max.}\end{aligned}$$

The maximum disruption angles,  $\theta_o$  and  $\phi_o$ , are calculated to be 2.2 mrad with an arbitrary addition of 0.3 mrad.<sup>7</sup> With various combinations of the above input beam parameters, the ray tracing program TURTLE (second order) tracked the beam backwards through the FFS into the extraction line to the dump. The beam profiles in the FFS are shown in Figures 4.4.3.1–4.4.3.4. Figure 4.4.3.1 shows that, with no  $e^+ e^-$  energy difference, the disrupted beam stays within 10 mm radius quadrupoles and sextupoles; but, as seen in Figures 4.4.3.2–4.4.3.4, when the energy difference approaches 3%, the beam begins to scrape even 20 mm radius magnets. Based on these runs, the FFS quadrupole and sextupole apertures in the achromat have been chosen to have 20 mm radius. The calculated beam size at the electron dump assumes Q19A is operating

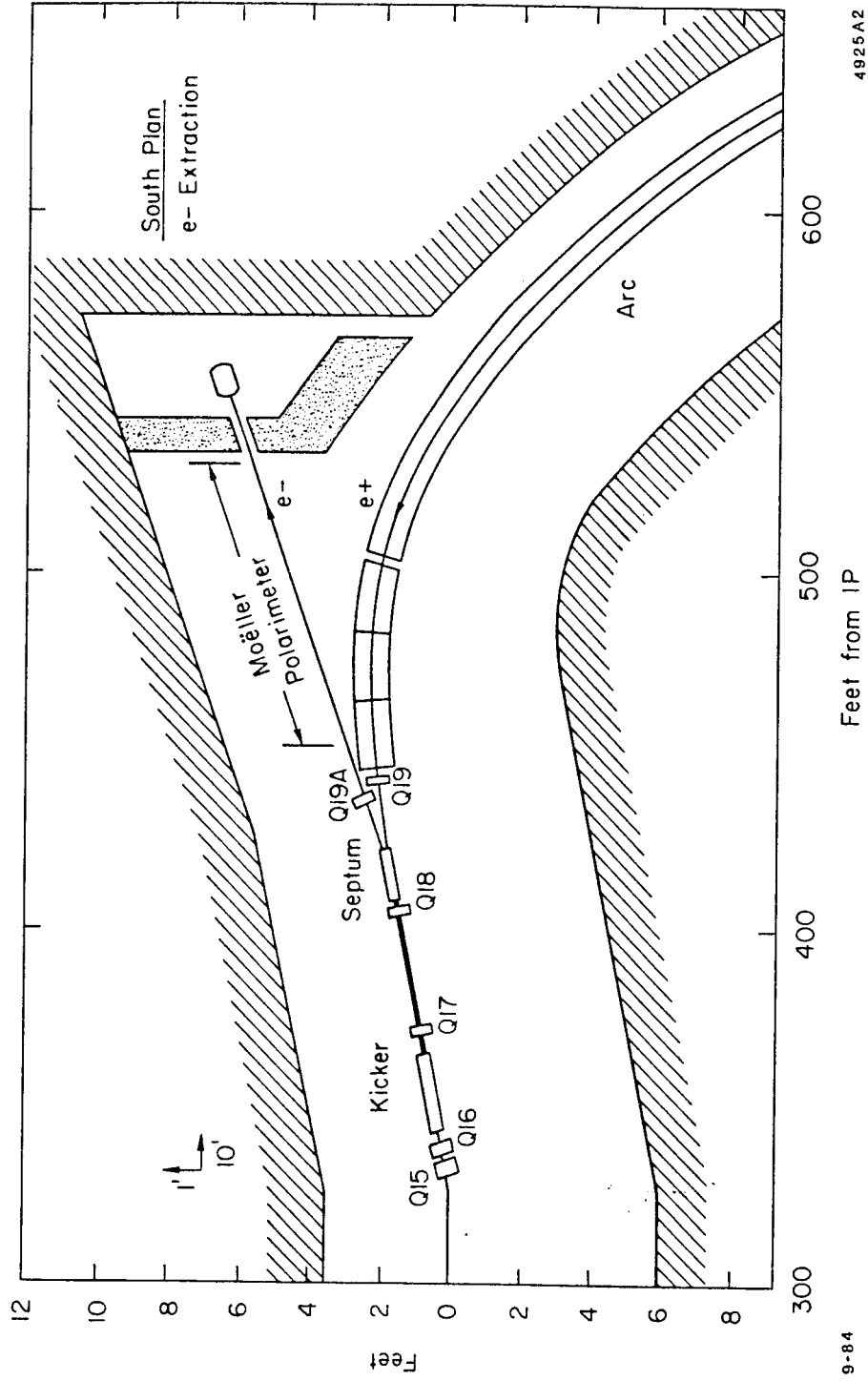
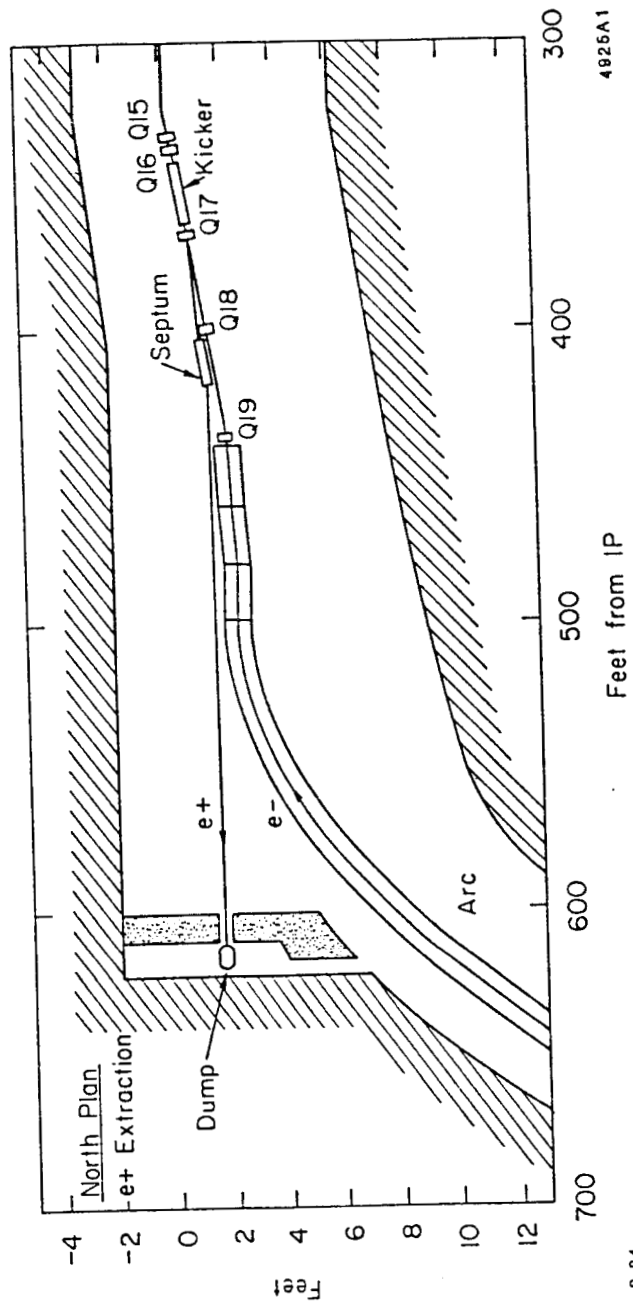


Figure 4.4.2.1 Electron Extraction



9-84

Figure 4.4.2.2 Positron Extraction

for the Moeller polarimeter; otherwise, the beam size is comparable to that on the positron side.

#### 4.4.4 Polarization

The measurement of the polarization of the beam at the IP, using a Moeller polarimeter in the exhaust electron beam, requires that the spin precess an integral multiple of  $\pi$  while traversing the FFS and extraction system for all energies of the outgoing beam. This requires that a spin rotator (horizontal dipole magnet) be placed in the extracted beam upstream of the Moeller scattering target (just outboard from Q19A in Figure 4.4.2.1). Following the Moeller target an equal-strength, opposite-polarity dipole is necessary to steer the extracted beam onto the dump. This second dipole (the corrector) then becomes part of the Moeller spectrometer. The strength of the rotator and corrector dipoles are dependent on the beam energy, and reach a maximum of 2.3 Tm, corresponding to  $90^\circ$  spin rotation, when  $E_{\text{beam}} = 38.2$ , and 53.5 GeV. The rotator and corrector are off when  $E_{\text{beam}} = 45.9$  GeV.

#### 4.4.5 Electron-Electron Scattering

Figure 4.4.5.1 shows the paths of like-sign outgoing beams in the FFS. They intercept the quadrupole immediately behind the first large bend. The separation of the two beams at that point is about 6 in. The quadrupole in question is one of a string of eight identical magnets in the FFS achromatic section; its strength is 346 kG at 50 GeV. Assuming it could be redesigned to allow clearance, it may be possible to fit in dumps, shielding and water handling equipment, without enlarging the tunnel. This is shown conceptually in Figure 4.4.5.1. Because of the S-bend FFS geometry, the extracted beam line must cross the aisle on the south side. That means the passage of people and equipment through the dump region is hampered, but probably not prohibited. This is only a preliminary look at like-sign beams, and a detailed engineering study still needs to be done.

#### 4.4.6 Beam Dumps

Two beam dumps are required to absorb and safely dissipate the spent



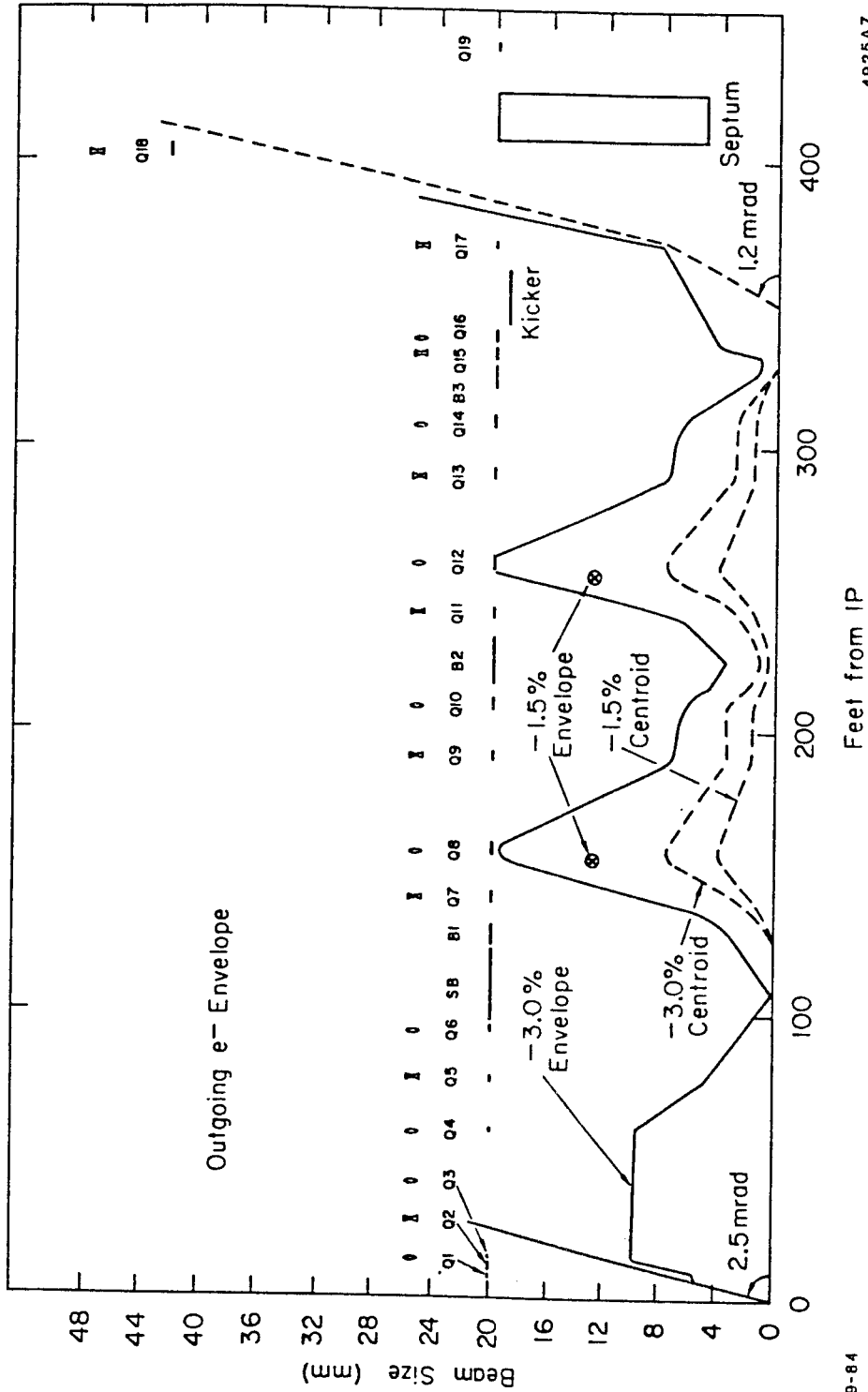


Figure 4.4.3.2

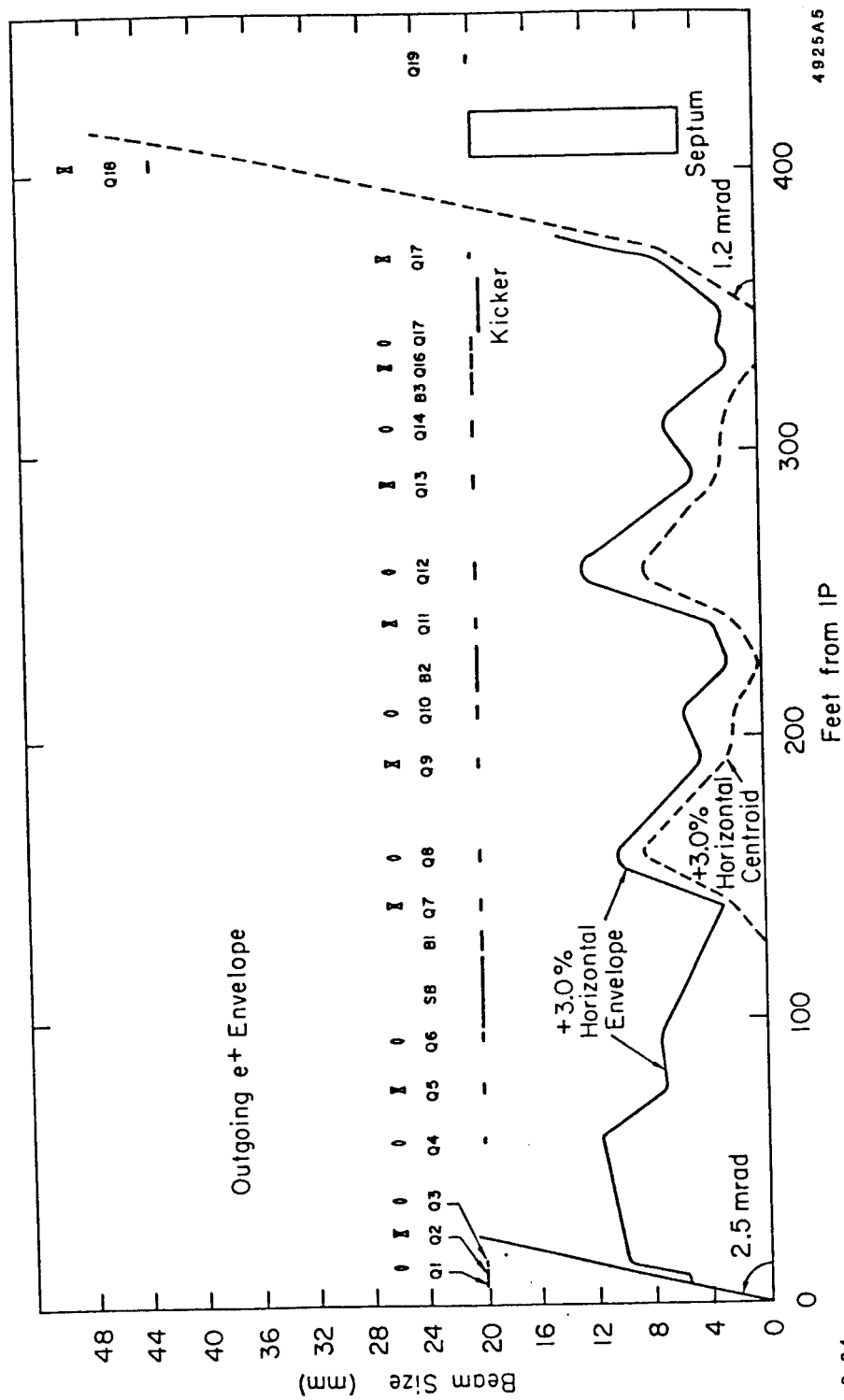


Figure 4.4.3.3

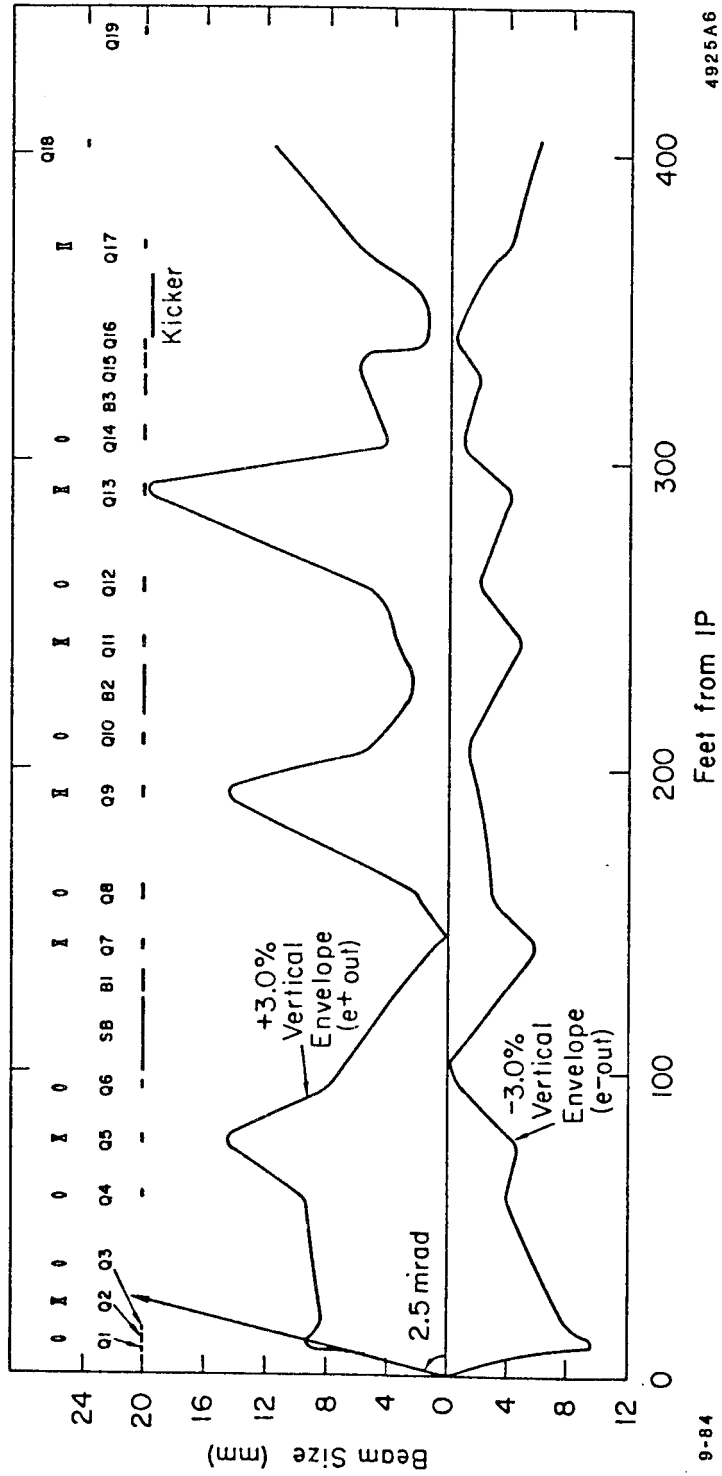


Figure 4.4.3.4

electron and positron beams after they leave the IR hall. With the nominal design flux at 50 GeV, the resulting average power is  $P_{ac} \sim 70$  kW, and  $I_{av} = 1.4 \mu\text{A}$  in each beam.

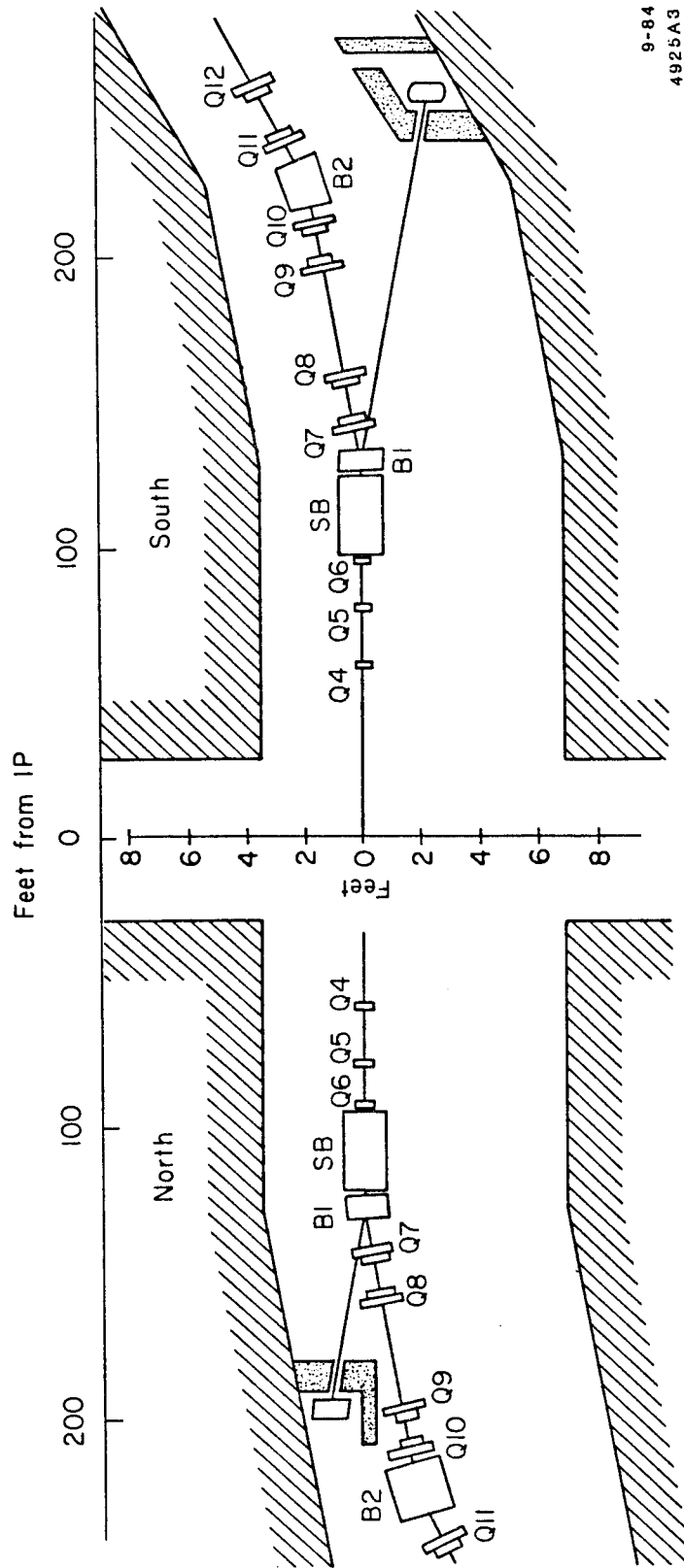
The proposed beam dump design is a SLAC sphere dump.<sup>8</sup> The required dump diameter for adequate attenuation of the radial shower is 25 cm, allowing for the expected excursion of the beam centroid. If the packed bed is made up of aluminum spheres, the dump will comfortably handle both the primary (undisrupted) and the disrupted beams. The dump window and the shell are also of aluminum. The window is 0.5 cm thick, and absorbs 3 W. The shower maximum for 50 GeV in aluminum occurs at  $T_{max} = 6.2$  r.l., and the shower multiplicity is  $\Pi_{max}^{e-} \sim 150$ . The rate of energy deposition at  $T_{max}$  is:

$$P_{max} = \rho \frac{dE}{dx} I_{av} \Pi_{max}^{e-} = 930 \text{ W/cm.}$$

The smallest expected spot size of the primary beam can be safely attenuated in a bed of 1-cm-dia, water-cooled spheres. Approximately 15 r.l. (= 175 cm) are needed to attenuate the longitudinal shower to a level where solid aluminum can be introduced. The packed bed is to be followed by 5 r.l. of solid aluminum ( $\sim 45$  cm), and then by 30 r.l. of a higher  $Z$  material, such as copper ( $\sim 45$  cm). This amounts to 50 r.l., and will adequately attenuate the longitudinal cascade; the resulting total dump length is 265 cm (= 8.7 ft).

The desirable water velocity over the surface of the spheres is 1 m/sec (3 ft/sec). For a good packing factor (0.74 hcp), the required flow rate is 4  $\ell$ /sec (65 gpm). This is dictated by heat transfer considerations, rather than by bulk temperature rise, which is a modest 4°C. The pressure drop in the dump for this flow rate is 7 psig.

For an average packing factor of 70%, approximately 11% of the incident beam power is directly dissipated in the cooling water. This causes radiolysis and results in evolution of free  $\text{H}_2$  at a rate<sup>9</sup> of 0.3  $\ell$ /(MW-sec), or  $2.3 \times 10^{-3}$   $\ell$ /sec. After saturation, the radiolytically evolved  $\text{H}_2$  collects principally in the gas space of the surge tank of the water system. For the required flow rate, and

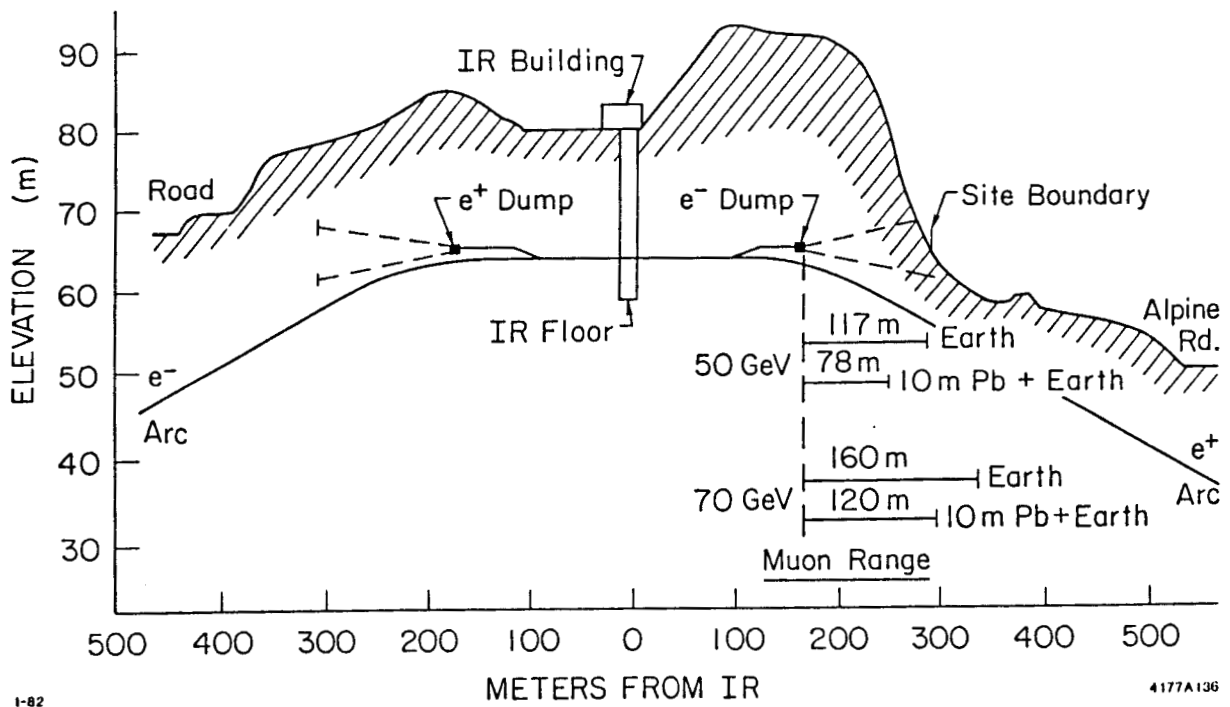


9-84  
4925A3

Figure 4.4.5.1

**Figure 4.4.6.1**

Cross section of the SLC at the final focus showing the muon ranges. Earth shielding will satisfy boundary dose limit for 50 GeV muons; 70 GeV requires "high-Z" material behind the dump.



1-82

4177A136

the size of the system, the surge tank might have a gas space of 100ℓ. The lower explosive limit (LEL) of H<sub>2</sub> in air is 4%. For practical operation, the concentration must never exceed 2%, and the trip level of the H<sub>2</sub> sensors in the SLAC H<sub>2</sub> recombiner circuits is set at 1%. For this system, the trip level will be reached in 7 minutes, and LEL in about 1/2 hour. A small H<sub>2</sub> recombiner is thus required. The water system, of course, must be a radioactive water system, separated from the LCW system by a heat exchanger. Also required is a demineralizer/deionizer.

Access to the collider areas, soon after beam operation has ceased, requires that the dump be shielded by the equivalent of a 0.5 m of concrete. The same amount of shielding is required between the dump and the components of the radioactive water systems requiring periodic maintenance. A substantial amount of shielding, perhaps as much as 3 m of concrete, will be necessary upstream of the dump to reduce background to the polarimeter and the IR hall.

Figure 4.4.6.1 shows a vertical cross-section at the FFS. Note that for 50 GeV beams, the muons from the electron dump are just barely contained within the earth. Calculations of radiation levels show that the muons must be completely ranged out to satisfy the site boundary conditions. Room has been provided to add lead or depleted uranium behind the dump, in case a beam of 70 GeV has to be absorbed. Bending the beam down before it enters the dump is also a possible solution, but would require 10 T-m, which is impractical. On the positron (north) side, the natural terrain is adequate to stop even 70 GeV muons.

#### **4.4.7 Kicker Magnets**

Two kicker magnet systems are currently being developed for the SLC, either of which could give the necessary 1.2 mrad kick to the spent beams. The available turn-on time, between the passage of the incoming beam and the return of the outgoing beam, is about 600 nsec. The current working design for the extraction lines is based on a current-loop kicker. A ferrite kicker has also been developed and could be used as a high-performance backup.

**4.4.7.1 Current Loop Kicker Magnet:** A prototype current-loop kicker,

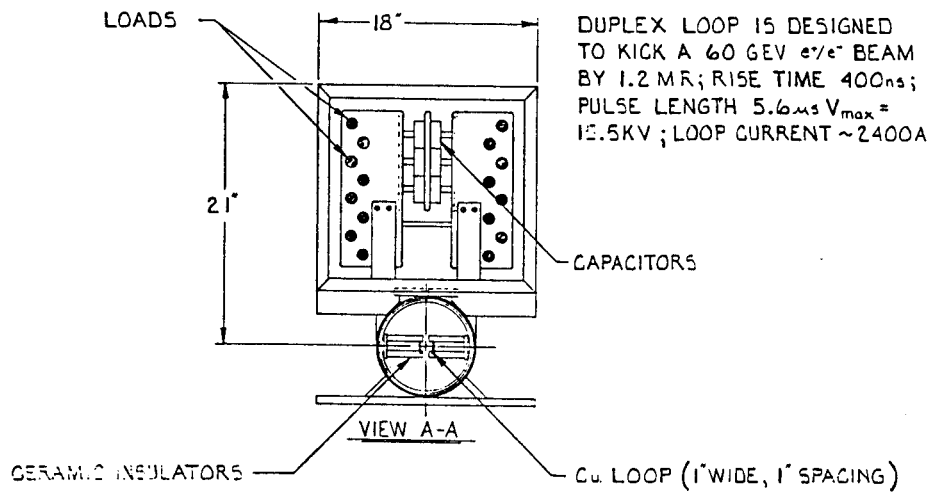
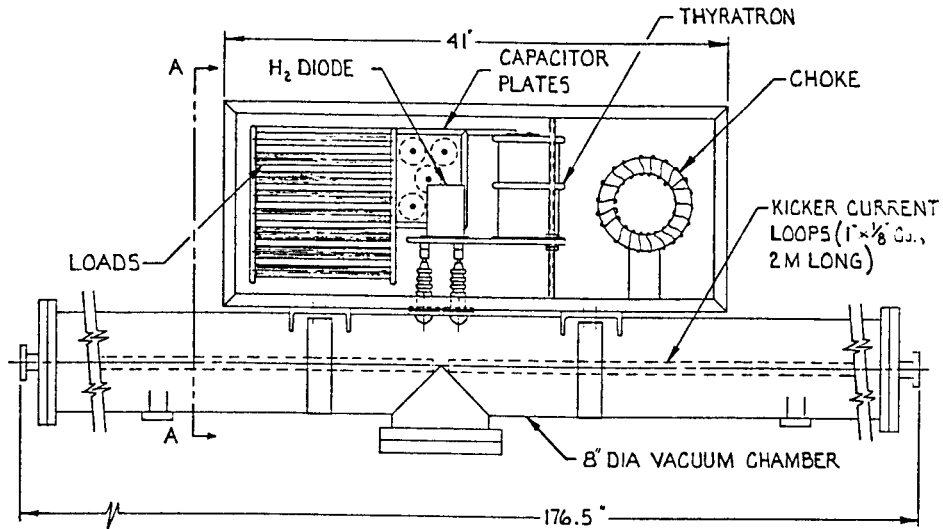
shown in Fig. 4.4.7.1, has been fabricated and is being tested. The actual kickers will consist of two (per side) copper current loops mounted in a vacuum chamber. Each loop has a magnetic length of 2 m, and should develop a field of 600 gauss at 25 kA, for a total of 2.4 kG-m, and a deflection of 1.2 mrad at 60 GeV. Two adjacent loops are driven in parallel by one thyatron. The design rise time is 400 nsec, and the total pulse length is 5.3  $\mu$ sec. The copper conductors have a 1/8 in.  $\times$  1 in. cross-section, and opposing conductors are separated by 1 in. The thyatron voltage is 15.5 kV, and the current is  $\sim$  5 kA. The power dissipated inside the vacuum chamber is 11.3 W per loop. The current loop approach has several advantages over the ferrite magnet design; it is shorter, works at a lower voltage, consumes less power, and costs less. It has the disadvantage that there are high-voltage feed-throughs into the vacuum system, and water may have to be brought in for cooling.

**4.4.7.2 Ferrite Kicker Magnets:** This approach would consist of two 3 m-long (magnetic length) magnets in each spent beam line, each of which is comprised of four 0.75 m-long modular sections. The magnet is designed as a transmission line of 50  $\Omega$  impedance. A full-size prototype of one such modular section was built using TDK M8C ferrite material (similar to 4C4). The cross-section is 3 in.  $\times$  3 in., with a 1 in.  $\times$  1 in. gap for a ceramic vacuum chamber. This prototype was successfully tested at low power with a pulse forming network (PFN), based on a hybrid Blumlein with a rise time of 30 nsec (10 – 90% ), followed by a flat top of 60 nsec. The magnetic pulse had a rise time of 55 nsec, followed by a 60 nsec flat top.

#### 4.4.8 Septum Magnets

The initial extraction kick angle of  $\sim$  1.2 mrad is complemented by an additional  $\sim$  15 mrad from a dc septum magnet located  $\sim$  15 m downstream of the kicker. The septum magnet is a coil septum magnet, or what might be called a modified current sheet septum. It allows for a separate vacuum chamber for the extracted beam, and contains no electrical hardware in the vacuum system, and thus, no power or water feed-throughs. A cross section of the magnet is shown in Figure 4.4.8.1.

Figure 4.4.7.1



**S.L.C. FINAL FOCUS**

**DUPLEX CURRENT LOOP DUMP KICKER**

36A

For convenience during fabrication and alignment, each magnet is made of four modular sections. One section is 52 in. long, with a core length of 48 in. The expected  $\int Bdl$  at 657A is  $\sim 7.5$  kGm (for a design beam energy of 60 GeV). The copper coil is a hybrid of two different conductor sizes (0.187 square inches in the septum, 0.340 square inches in the return leg), which are joined in the turnaround. The septum thickness is 0.60 in. for all sections, to simplify fabrication, even though the beam spacing requires this thickness only in the first module.

Figure 4.4.8.1

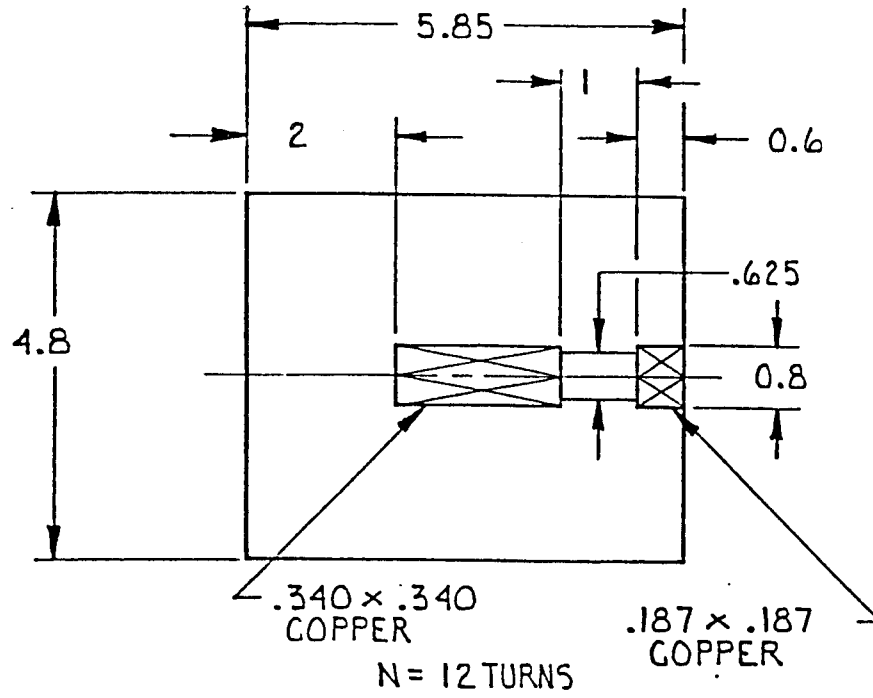


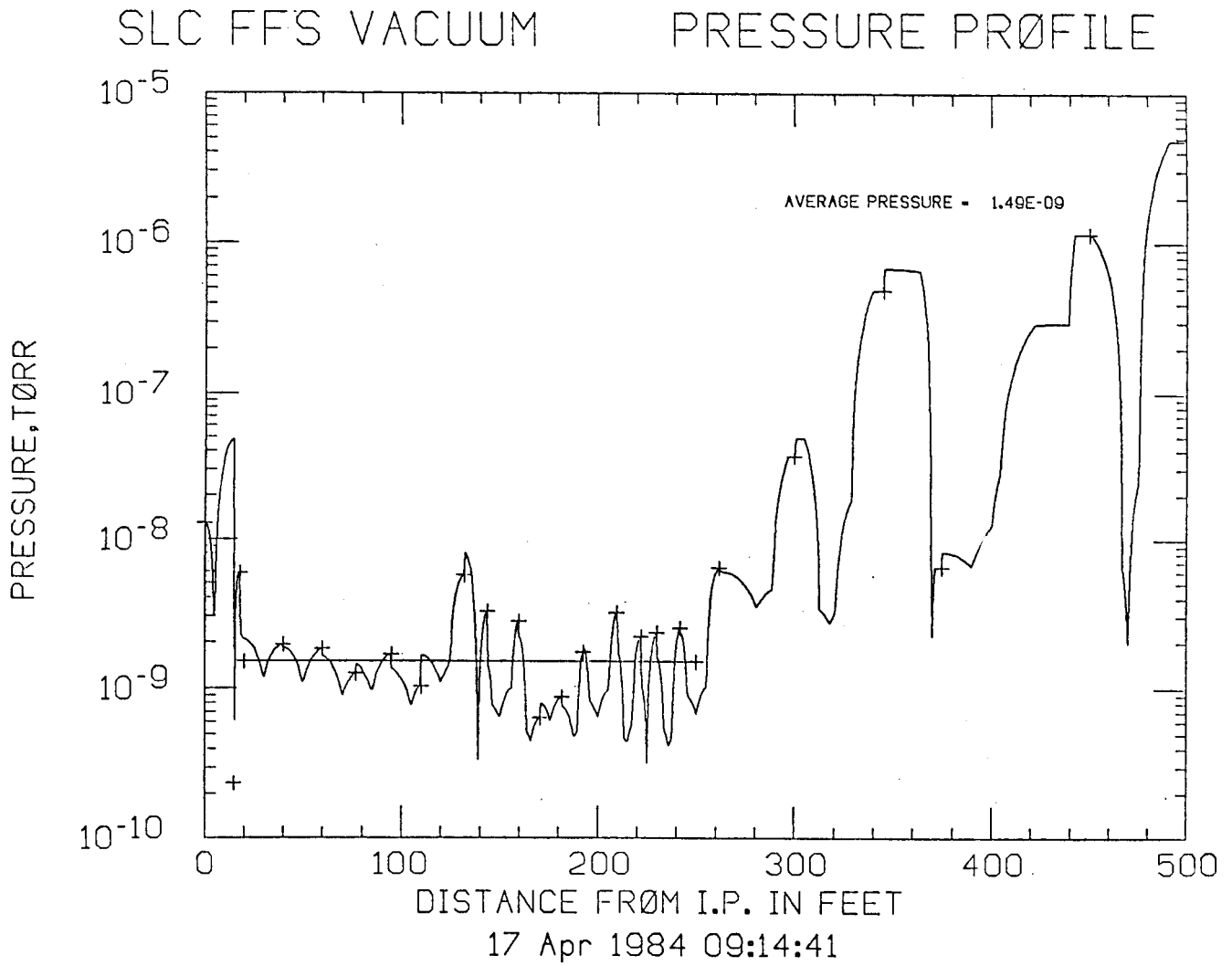
FIG. S.L.C. CURRENT COIL SEPTUM MAGNET

#### 4.5 VACUUM SYSTEM

The final focus vacuum system will consist of  $\approx 70$  flanged, stainless steel tubes varying between 0.5 in. and 5.0 inches in diameter, to fill the magnet apertures. The total length for the north and south arcs together will be  $\approx 1000$  ft, and the individual vacuum chambers will vary from 2 ft to 20 ft. For the purpose of this report, the vacuum chamber through the experiment is assumed to be 2 in. diameter tubing.

As shown in Figure 4.5.1, the pressure will be about  $3 \times 10^{-8}$  torr in the region from the IP to 20 ft,  $5 \times 10^{-9}$  torr from 20 ft to 250 ft and  $2 \times 10^{-8}$  torr from 250 ft out to the arcs. This pressure distribution will require fifteen 50 l/s, three 200 l/s, and two 400 l/s ion pumps in each section.

Figure 4.5.1



## **4.6 INSTRUMENTATION**

The number and approximate positions of the instruments as now envisioned are shown in Fig. 4.2.7.1. Design studies are in progress.

**REFERENCES**

1. K.L. Brown, D.C. Carey, Ch. Iselin, and F. Rothacker, *TRANSPORT, A Computer Program for Designing Charged Particle Beam Transport Systems*, SLAC-91, Rev. 2 (1977), CERN 80-04, and NAL-91.
2. K.L. Brown, *Beam Envelope Matching for Beam Guidance Systems*, SLAC Pub. 2370 (1980), and Nucl. Inst. and Methods 187, 51-65 (1981).
3. D.C. Carey, K.L. Brown, and Ch. Iselin, *TURTLE, A Computer Program for Simulating Charged Particle Beam Transport Systems, Including Decay Calculations*, SLAC-246 (1982), and Fermilab PM-31.
4. DIMAT has been implemented at SLAC by R. Servranckx. The documentation has not been published.
5. K.L. Brown, *A First and Second-Order Matrix Theory for the Design of Beam Transport Systems and Charged Particle Spectrometers*, SLAC Report No. 75; Adv. Part. Phys. 1 71-134 (1967)
6. K.G. Steffen, *High-Energy Beam Optics*, Interscience Monographs and Texts in Physics and Astronomy, Vol. 17, John Wiley and Sons, New York (1965).
7. R. Hollebeek, CN-39,d (1981).
8. D. Walz and L. Lucas, SLAC Pub-555.
9. D. Walz and E. Seppi, SLAC TN-67-29 (1967).